ISBN 978-82-326-3744-7 (printed version)
ISBN 978-82-326-3745-4 (electronic version)
ISSN 1503-8181

Doctoral Thesis

Eskil Aursand

Doctoral theses at NTNU, 2019:70

Eskil Aursand

Film boiling and rapid phase transition of liquefied natural gas

NTNU
Norwegian University of
Science and Technology
Faculty of Engineering
Department of Energy and Process Engineering

NTNU
Norwegian University of
Science and Technology

Doctoral theses at NTNU, 2019:70

NTNU

NTNU
Norwegian University of
Science and Technology

Eskil Aursand

Film boiling and rapid phase transition of liquefied natural gas

Thesis for the degree of Philosophiae Doctor

Trondheim, December 2018

Norwegian University of Science and Technology
Faculty of Engineering
Department of Energy and Process Engineering

NTNU
Norwegian University of
Science and Technology

NTNU
Norwegian University of Science and Technology

Thesis for the degree of Philosophiae Doctor

Faculty of Engineering
Department of Energy and Process Engineering

ISBN 978-82-326-3744-7 (printed version)
ISBN 978-82-326-3745-4 (electronic version)
ISSN 1503-8181

Doctoral theses at NTNU, 2019:70

Printed by Skipnes Kommunikasjon as

Abstract

When liquefied natural gas (LNG) is spilled onto water there is a possibility that explosive rapid phase transition (RPT) events occur. According to experiments, these vapor explosions are highly unpredictable, with yields up to several kilograms of TNT equivalent. The leading theory of RPT claims that triggering occurs due to a sudden and rapid chain of events involving film-boiling collapse, liquid superheating, rapid nucleation and explosive expansion. Still, after over four decades of research on the topic, it appears that there is no reliable and accepted method for quantitative LNG RPT risk-assessment. The main goal of the present thesis is to remedy this issue through theoretical means. According to the leading theory of RPT, prediction of the triggering event necessitates modelling of two properties: the *Leidenfrost temperature* and the *superheat limit temperature*, both of which were investigated herein.

The Leidenfrost temperature is by definition the surface temperature below which film-boiling collapse occurs. Therefore, it is necessary to understand film boiling and its stability. While much work has been done in the past on modelling the stability of thin liquid films with the long-wave approximation, these models are not directly applicable to film boiling. The equations describing a vapor film trapped between two dense phases of extremely different temperatures turn out to be different in subtle but important ways. In this project a new model for vapor-film dynamics has been developed within the long-wave approximation methodology. This model crucially involves a coupling to non-equilibrium evaporation models from kinetic theory, which allows for the inclusion of the thermocapillary effect at the evaporating interface. Based on stability analysis of this model, a novel and promising prediction method for the Leidenfrost temperature has been discovered. The method carries with it the surprising theoretical impli-

cation that film-boiling collapse occurs when the thermocapillary instability overpowers vapor-thrust stabilization. However, further experimental investigations of the Leidenfrost temperature is needed in order to draw strong conclusions regarding its validity.

The superheat limit may be estimated within the framework of classical nucleation theory (CNT). These predictions have been compared with a wide array of relevant experimental data on hydrocarbons, both for pure fluids and binary mixtures. The performance of the CNT model was deemed satisfactory, and thus, no further efforts to improve superheat limit modelling have been made in this project.

Finally, a framework for the prediction of RPT risk and consequence during LNG boil-off has been developed. This framework demonstrates how models for the Leidenfrost temperature and the superheat limit temperature as functions of LNG mixture composition may be combined with classical thermodynamics in order to predict when (and if) the conditions for RPT triggering may be met. Additionally, it has been shown how the predicted LNG composition at the time of triggering may be used to estimate the worst-case explosive pressure and energy yield through the use of a simplified thermodynamic model. While quite idealized, this framework represents an important step towards practical risk assessment and mitigation for LNG rapid phase transition. The thesis concludes with a series of suggestions on how the framework may be further improved.

Preface

The present thesis is the product of a three-year long journey of ups and downs, while learning either way. I stumbled into some frustrating dead-ends, but I also found quite a few fruitful paths. Having a background from a five-year Master's program completely devoid of fluid mechanics made for a particularly challenging start. I have learned that motivation can be a wonderful and unreliable friend, but discipline is always there for you. Those who know me well know that I certainly did not find this journey easy. Still, it has been a very interesting and rewarding endeavor that has changed me for the better, and I certainly don't regret starting it.

Two of these years were spent at the Department of Energy and Process Engineering at NTNU in Trondheim. I am grateful to my main supervisor Bernhard Müller, as well as my co-supervisors Morten Hammer, Svend Tollak Munkejord and Tor Ytrehus, for their support, feedback and patience. I would also like to thank all the wonderful PhD-students and Postdocs at the department for showing up to breaks and talking about all things besides work. In particular I would like to thank Marin for teaching me how embrace the sometimes frustrating process of science without going mad.

The remaining year was spent far away from home, as a Visiting Scholar in Chicago. I am extremely grateful to Stephen H. Davis for hosting me at Northwestern University, as well as granting me access to his remarkable knowledge and experience in the field, despite having no obligation to do so. My best work was done under his guidance, and it could not have happened elsewhere. Additionally, I would like to thank the people at the U.S.- Norway Fulbright Foundation for believing in me, supporting me financially during this visit, and providing indispensable practical support during the daunting task of moving alone to a different continent. It was truly an amazing and life-changing year, with repercussions far beyond my

PhD work.

I made it my goal to keep a healthy life outside of academia. I am grateful to my various groups of friends in Trondheim for accompanying me while going to the gym, watching silly TV shows, and taking video games far too seriously. I am grateful to my parents for raising and supporting me, and to my siblings for inspiring me. Last but not least, I would like to thank Kyle, Noy, and especially Hunter, for keeping me sane in between long bouts of writing in the many coffee shops of Lakeview, Chicago. Neither me nor this work would be same same without you.

Eskil Aursand
Trondheim, December 18th 2018

Acknowledgments

This work has been performed in relation to the project *Predict-RPT* at SINTEF Energy Research, which is funded under the research program for *Maritime activities and Offshore operations (MAROFF)*. I acknowledge the Research Council of Norway (244076/O80) and The Gas Technology Centre NTNU-SINTEF (GTS) for their financial support.

I would also like to thank the U.S.–Norway Fulbright Foundation for financially supporting my research visit to the United States.

What is success? To laugh often and much; to win the respect of intelligent people and the affection of children; to earn the appreciation of honest critics and endure the betrayal of false friends; to appreciate the beauty; to find the best in others; to leave the world a bit better, whether by a healthy child, a garden patch or a redeemed social condition; to know even one life has breathed easier because you have lived. This is to have succeeded!

Bessie A. Stanley[1] (1905)

[1] Often misattributed to Ralph W. Emerson. It's a long story...

Contents

Part I

Monograph

Chapter 1

Introduction

1.1 Project background and motivation

This PhD project is part of a larger project called *Predict-RPT*, which was initiated by SINTEF Energy Research in 2015. Its aim is to promote safety and risk quantification in large-scale transportation, refueling and production of liquefied natural gas (LNG). Specifically, it seeks to fill knowledge gaps in the understanding of an unpredictable and potentially dangerous phenomenon called Rapid Phase Transition (RPT).

RPT events, sometimes also called *vapor explosions*, are considered one of the main safety concerns of the LNG industry [1]. In maritime LNG operations, both in production and usage, there is a risk of spilling LNG onto water due to events such as ship collisions or loading-arm failures (see Fig. 1.1). When spilled into water, LNG will spread on top of the water while gradually boiling off, normally without incident. However, in some cases it is observed to suddenly, and seemingly at random, explosively vaporize in large quantities at once. This is an RPT event, whose explosive nature poses a danger to both people and equipment. Accurate prediction of if, when and where this will happen has seemingly eluded researchers for many years. Shedding light on this *triggering event* is the main goal of this thesis.

The methods behind this thesis have been theoretical and computational. As is often the case with such academic endeavors, the pursuit of knowledge has taken the project down many unforeseen avenues of research, including thin-film flow, stability analysis, molecular kinetic theory, nucleation theory and non-equilibrium thermodynamics.

1.2 Liquefied Natural Gas (LNG)

Natural gas is a common fossil fuel used for heating, cooking, propulsion and electricity-generation across the globe. Its main component is methane (about 90%), with the remainder consisting of progressively smaller amounts of the heavier alkanes ethane, propane, butane, etc. Small amounts of carbon dioxide, nitrogen and helium may also be present.

Natural gas is extracted from increasingly remote sources. This situation requires long-range transportation in order to reach the places where the fuel is needed. For this purpose, the natural gas is often cooled down below its boiling point ($-162\,°C$) to form liquefied natural gas (LNG) [2]. The purpose of liquefaction is to increase density, mainly in order to improve the convenience and economics of long-range transportation. LNG is transported across the world's oceans in large carriers, from points of production (liquefaction) to delivery (re-gasification), and a single carrier may carry up to about $260\,000\,m^3$ of LNG. Combined with the fact that there is an increasing trend towards both LNG processing and usage at sea, this means that there are many scenarios where LNG may inadvertently spill and come in contact with seawater.

In such a spill scenario, illustrated in Fig. 1.1, the cryogenic nature of LNG becomes a problem. Compared to the LNG, the seawater is extremely hot. Specifically, the water is far above the LNG boiling point, and if the LNG were to reach that temperature it would take up about 600 times its original volume. Due to film boiling, this phase transition usually happens at a relatively slow pace. When it does not, it is called an RPT event.

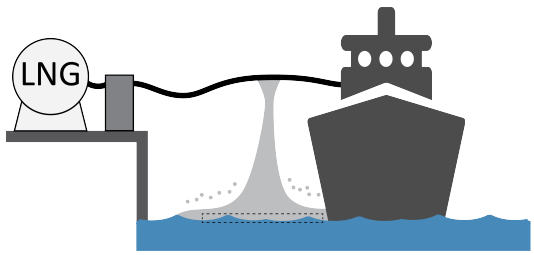

Figure 1.1: Illustration of a loading-arm failure while bunkering, causing LNG to spill onto seawater and thus creating the conditions for possible explosive RPT events. [1]

[1] Figure credits: SINTEF Energy Research

1.3 The rapid phase transition (RPT) event

In the LNG safety literature of the last couple of decades, RPT [3] is typically mentioned among the main concerns. This can range from giving it significant attention [4, 5, 1, 6], to little more than noting it as a concern [7, 8, 9, 10, 11]. While the exact microscopic mechanisms are very much up for debate, based on these reviews the general macroscopic chain of events for LNG RPT is as follows:

1. Due to some unintended event, LNG spills onto the sea.
2. Since LNG has about half the density of water, it floats on top and forms a spreading pool.
3. Due to *film boiling* the heat transfer is weak, and the LNG evaporates slowly and without incident. However, for some reason there may suddenly be a local dramatic increase in heat transfer rate.
4. This sudden event is observed as a vapor explosion, where a part of the liquid LNG undergoes a rapid phase transition into its vapor state.

RPT is not an explosion in the common sense of the word; i.e., it does not involve combustion or other chemical reactions. It is what is sometimes called a vapor explosion or a physical explosion. It is still destructive, as its peak pressures and released mechanical energy can be large enough to displace and damage heavy equipment [4, 1, 11] and could theoretically cause secondary structural damage and cascading containment failures [9].

As will be shown in Sec. 1.4, experimental tests have shown that both the triggering probability and consequences are highly unpredictable. We will see in Sec. 1.6 that these puzzling macroscopic observations seem to be due to a diverse array of subtle microscopic phenomena.

1.4 History of LNG RPT research

1.4.1 Discovery of an unexpected phenomenon (1960s)

While there were some minor incidents in the 1950s and 60s that were reported but largely ignored [3], LNG RPTs eventually started attracting significant interest due to the 1968–1969 US Bureau of Mines experiments [12]. During a set of large-scale spill tests, violent explosions were observed after LNG-water contact. The tests were mainly intended to study hazards associated with vapor clouds, and a vapor explosion originating from the

LNG pool was not expected. Due to this, proper equipment for the measurement of explosive events were not set up. Witnesses described the event as "comparable to the explosion from a stick of dynamite".

This unexpected discovery sparked several research programs in the decades to follow, dedicated partly or fully to the subject of LNG RPT. A chronological overview of the most significant contributions to the understanding of LNG RPT will follow below.

1.4.2 Formulation of a hypothesis (1971)

Due to the discovery of this explosive and potentially dangerous event at the Bureau of Mines tests, research groups scrambled to offer an explanation for the phenomenon and to determine any danger it might pose for the LNG industry. A few years later, in 1971, a hypothesis regarding the mechanisms behind the observed event emerged. It was put forward by three different groups almost simultaneously, and it is difficult to determine exactly who should be credited for its conception. These researchers were Katz & Sliepcevich [13, 14], Nakanishi & Reid [15] and Enger & Hartman [16, 17, 18, 19].

This was truly pioneering work, and introduced theories and terminology for LNG RPT that have been used to this day. The researchers correctly identified the phenomenon as a rapid phase transition as opposed to a chemical explosion, and thus coined the term "RPT". Furthermore, they formulated a new hypothesis for the microscopic chain of events behind the phenomenon. This included making the connection to concepts such as film boiling, superheating, the lack of nucleation sites at liquid–liquid interfaces, superheat limit (homogeneous nucleation limit) and rapid nucleation. Quantitatively, the work also included the discovery of the important "40% rule", due to the observation that LNG on water needed to boil down to 40 mol% methane in order to trigger an RPT event.

This early work left a lasting legacy, as the core hypothesis would serve as the base assumption in virtually all later RPT research. Its essential details will be described in Sec. 1.6, where we summarize the current consensus on the mechanisms and chain of events behind LNG RPT.

1.4.3 LNG Research Center at MIT (1970s)

Through the 1970s the *LNG Research Center* at Massachusetts Institute of Technology (MIT), led by Professor R.C. Reid, performed a significant amount of research to test the core hypothesis and provide the experimental data necessary to apply it. A diverse array of relevant experimental research

was performed on topics such as the spreading and boiling rate of cryogenic hydrocarbons on water [20, 21, 22, 23, 24], the superheat limit of hydrocarbons [25], and the conditions necessary for rapid phase transition [15, 26]. This all culminated in the summary by Reid [3] in 1983.

This important body of work elaborated and solidified the pioneering work of the early 1970s. Besides the useful quantitative data on boiling rates and superheat limits, a significant conclusion of this program was that in order for RPT to be triggered, the surface (water) temperature can neither be too high nor too low. Both of the following seemed to be necessary [26]:

- $T_{\mathrm{w}} > T_{\mathrm{SHL}}$: The water temperature (T_{w}) must be above the LNG superheat limit (T_{SHL}). If not, no amount of contact with water will be able to heat the LNG to its superheat limit.
- $T_{\mathrm{w}} < 1.1T_{\mathrm{SHL}}$: The water temperature must be below about 1.1 times the LNG superheat limit. If not, the heat transfer will be limited by stable film boiling, and no superheating occurs. We will call this the "1.1 rule". As we will see later, the value $1.1T_{\mathrm{SHL}}$ is essentially the *Leidenfrost temperature*.

Since the LNG superheat limit T_{SHL} is a function of the LNG composition [25], this also inevitably leads to the conclusion that the amount of methane is crucial. Naturally, this relates to the "40% rule" discovered earlier.

The experiments performed by the LNG Research Center were mostly small-scale. Other large industry-funded programs would follow up with large-scale spill tests.

1.4.4 LLNL large-scale spill tests (1980s)

During the 1980s, Lawrence Livermore National Laboratory (LLNL) conducted a research program on large-scale LNG spills [27]. These spill test series were code-named *Burro* (1980) [28], *Coyote* (1981) [29] and *Falcon* (1987) [30]. While some other large-scale LNG spill-tests had been performed earlier in the 1970s [4], the LLNL program was the first one with some tests run explicitly for the study of RPTs. This meant that they were more appropriately instrumented than generic spill tests, and thus could lead to more knowledge gain beyond merely noting that an RPT occurred. The main lessons learned from these tests were [27, 4, 31]:

- In large-scale spills, two distinct types of RPT events may occur:

  - *Early RPT*: These events occur close to the spill point (point of jet impact), at any time during the spill. The properties of these RPTs seem to correlate with impact conditions such as spill-rate.
  - *Delayed RPT*: These events occur some time after the spill, close to the edge of the spreading pool. Their probability seems to correlate with initial LNG composition.

- Large-scale spills may appear to break the 40%-rule: RPTs may occur when spilling LNG mixtures with up to 90% methane, likely due to boil-off (delayed RPT) or different mechanisms coming into play in the mixing-zone (early RPT).
- Probability: RPTs occur in about one third of the spills. The lower the initial methane fraction, the more likely it is. Overall, RPTs seem very unpredictable/random. It appears that the same LNG mixture may or may not lead to RPT, changing from one spill test to the next.
- Severity: RPTs in large-scale spills can be quite severe. One event was able to throw a 27kg object a distance of 50 m. The RPTs have estimated energy yields from a few grams to several kilograms of TNT equivalent. Overpressures in the order of 1 bar could be measured at a distance of 30 m. However, note that this would decay rapidly with distance, so the pressure right next to the source may be much larger.
- Secondary risk: Besides the direct danger of the vapor explosion, the RPT event may spread the vapor-cloud above the pool and significantly increase the potential burn-area in an unpredictable way.

1.4.5 Gaz de France and partners (1981-2003)

While a lot was learned from the LLNL program, the lessons were mostly qualitative. One significant issue remained: How can we quantitatively predict the risk and consequence of RPT in a given LNG release scenario? A consortium of partners including Gaz de France, British Gas, Shell, Statoil and the Norwegian University of Science and Technology set out to remedy this situation through a research program that would eventually span two decades. The program included small, medium and large-scale experiments, as well as considerable development of numerical simulation code [32, 33].

The program does not appear to have yielded significant new qualitative knowledge on the nature of LNG RPT. Its main contribution was the development and validation of models in the form of numerical computer codes. The model development appears to have been focused on early RPT, as much effort was spent on modeling mixing and detonation in the chaotic

mixing-zone beneath the point of LNG jet impact. This work was an adaptation of the considerable modeling work made on Fuel-Coolant Interactions (FCI) in nuclear safety research by a group led by D.F. Fletcher. Two simulation tools were developed [33]:

- CRYOMIX (based on CHYMES [34] for FCI): A numerical code for modeling the water/LNG mixing-zone. It allows the estimation of mixing volume and droplet distribution, which may be used as input parameters to models concerned with detonation and propagation (see CRYO-CULDESAC below).

- CRYO-CULDESAC (based on CULDESAC [35] for FCI): A numerical code for modeling spherically symmetric propagation and droplet fragmentation in the LNG/water mixing-zone after the initial triggering. This allows the estimation of total mechanical energy release, and thus the potential destructiveness of the early RPT event.

For estimating explosive energy release, the researchers in this project also recommended the Hicks and Menzies methodology [36, 32, 37]. This is a purely thermodynamic method developed in the context of FCIs, and it uses an idealized thermodynamic path with isentropic expansion. Like CRYO-CULDESAC, this method also requires input such as the amount of participating LNG.

While the final goal was to make a practically useful tool for the industry, it is unclear whether the project actually succeeded in this. Examples of CRYOMIX and CRYO-CULDESAC being used together as a unified predictive tool could not be found in the open literature.

1.4.6 Later developments and current status (2000–2018)

In the time since the research program of Gaz de France and partners there has been little new original research on LNG RPT. There are two notable exceptions, which are described in the following:

- In 2006, the company IoMosaic released a report [31] specifically focusing on the issue of LNG RPT. Besides providing a modern review of theory, experiments and the possible spill scenarios that may lead to RPT, they also appear to have developed a quantitative model for risk and consequence of delayed RPT based on their proprietary software SuperChems. The model tracks the gradual compositional change during boil-off until eventual departure from the film-boiling regime and subsequent RPT triggering. However, they do not reveal how

they model the transition point from film boiling to nucleate boiling (Leidenfrost point), which is crucial to the overall triggering prediction. This lack of completeness and transparency makes it difficult to assess the merits of the model. For the explosive yield they appear to use a Hicks & Menzies [36] methodology with a 50% reduction factor to account for non-idealities, and conclude that 38 kJ ($\approx$ 10 g TNT) per kg of triggered LNG may be expected.

- In 2009, Bubbico and Salzano [38] published an acoustic analysis of LNG RPT blast waves. The model yields a prediction of peak overpressure as a function of distance from a simplified point source. However, the strength of the point source is not predicted from the model itself and must be supplied as an input. In this work the source strength was adjusted to fit experimental data, and thus the model is unable to perform *ab initio* predictions of RPT severity. However, such a model gives valuable information on the pressure wave's rate of decay. Also, by measuring the peak pressure at one distance, one may estimate the peak pressure at another distance. When fitted to pressure measurements at specific distances, the model estimates a safety-distance of about 500 m for LNG RPT.

While there has been little new original research on LNG RPT published in the last two decades, there has been no lack of general LNG safety reviews from gas companies, consultants and academics.

Sandia National Laboratories (SNL) appears to have done significant work with compiling and reviewing LNG safety research [39, 8, 4]. While they have no reviews about RPT specifically, they always mention it as one of several potential risks. In particular, they made the following statement:

> *Energy releases equivalent to several kilograms of high explosive have been observed. Effects will be localized near the spill source and should not cause extensive structural damage.*
>
> (Hightower et al. [39], Sandia, 2004)

The above statement seems contradictory, as an explosion of several kg TNT equivalents is certainly quite dangerous. The second sentence cites no source and appears mostly speculative.

DNV, now DNV-GL, has similarly done extensive reviews on LNG safety, though none focusing specifically on RPT. Some of them acknowledge the risk of LNG RPT [5, 1], while some do not mention it at all [40, 41]. The DNV reviews mention the possibility of LNG in the following way:

> *DNV believes that RPT is unlikely to damage large structural elements of a ship. This argument is reasoned, but speculative*

> *and further experiments would be beneficial.*
>
> (Shaw, Baik, and Pitblado [5], DNV, 2005)

> *Of concern is the possibility of an RPT when LNG is discharged into the double hull space and washed down by inflowing sea water. The spill may be trapped next to the LNG tank and possibly contribute to a cascading event.*
>
> (Pitblado and Woodward [1], DNV, 2011)

Besides acknowledging the risk of RPT in the above fashion, they offer no recommendations or practical risk-assessment methods. The statement regarding RPT not posing significant risk to a ship does not refer to any sources and appears to be an educated guess.

Risk, Reliability and Safety Engineering published a paper titled "Introduction to LNG Safety" [7], which briefly mentions the danger of LNG RPT with the following:

> *These explosions can result in localized damage to equipment and a potential for escalation, leading to larger LNG spills.*
>
> (Alderman [7], 2005)

They do not address the issue further.

The public review by LLNL on their own research program from the 1980s was not published until 2007 [27]. This report summarizes the lessons already mentioned in Sec. 1.4.4, with particular attention to the discovery that RPTs will significantly increase the potential burn-area of the spill. Beyond this, they make no practical recommendations. Instead, they conclude by clearly stating that additional RPT tests are needed to quantify the upper limit of possible RPT explosive yield as well as to better understand the underlying mechanisms.

The *Chemical Hazards Research Center* at University of Arkansas published a review of the US regulations for LNG terminals in 2007 [9]. They mention that the regulations do not presently address RPT hazards and go on to state the following:

> *Although these hazards will not be discussed further here, it is noted that neither should be entirely dismissed. [...] For RPTs, the remaining concern is for the potential of RPTs to cause secondary structural damage, which might lead to cascading containment failures.*
>
> (Havens and Spicer [9], 2007)

Despite the stated concern for RPT, it is never mentioned again in this review.

Bureau Veritas published a LNG safety review in 2017 [11]. Their comment on RPT is the following:

> *An RPT can eject large amounts of liquid into the air, which will evaporate during the fall down. If RPTs occur because of an accident in an LNG Offshore Floating Unit, it could be quite violent and create blast waves that might cause damage to the surroundings. RPTs have been studied extensively but its occurrence was never documented in industry. Nevertheless, they can occur when there are rich mixtures of LNG with high proportions of ethane and propane.*
>
> (Forte and Ruf [11], Bureau Veritas, 2017)

Again, no advice is given for the assessment of risk and consequence. The final sentence is somewhat misleading, as it neglects to mention that almost any LNG mixture may reach the conditions for RPT given enough time to boil off, even if it is initially a high-methane mixture.

It is apparent that most LNG safety reviews will, if they even acknowledge RPT at all, simply state that there is a risk and leave it at that. Some essentially state that RPT is nothing to be worried about, but these appear speculative and without foundation in data beyond the lack of serious incidents in the past. All these recent reviews appear to have the following two things in common:

- They acknowledge the potential risk of explosive RPT events during LNG spills.
- They seem to lack any practical recommendations for the quantitative assessment of risk and consequence.

While the reviews do not state this outright, the above contradiction implicitly communicates the conclusion that **there are currently no established and trusted methods available for quantifying risk and consequence of LNG RPT.** Of course, this conclusion is based on published literature. We cannot know what is hiding in terms of proprietary research in the Oil & Gas industry.

1.5 Introduction to central concepts

Before we can clearly summarize the established consensus on the mechanisms behind LNG RPT, it is necessary to explain some central concepts in a bit more detail.

1.5.1 Thermodynamics: Equilibrium description of LNG

Classical thermodynamics is the description of equilibrium states and the possible transitions between them. An *equilibrium state* is the state of a system that is thermodynamically stable, which means that the system is in its global energy-minimum and will stay there indefinitely if the imposed conditions remain the same. In the present context of LNG, the *system* is a small but macroscopic amount of fluid, which may be liquid, gas or both.

Many of the thermodynamic equilibrium properties of a fluid may be represented in a temperature–pressure *phase diagram*, which is a map of possible thermodynamic states of given combinations of temperature (T) and pressure (p) applied to the fluid. Such diagrams usually indicate regions of qualitatively different states, and the crucial boundaries between them forming lines in T-p space. An example of such a phase diagram for LNG can be seen in Fig. 1.2. Note that this diagram is not universal for LNG, but will depend on the specific molar composition ($\boldsymbol{z}$), i.e. the relative amounts of the different hydrocarbons.

In Fig. 1.2 we may point out the following features:

- *Liquid region*: Region where the equilibrium state is purely liquid.
- *Vapor region*: Region where the equilibrium state is purely gaseous.
- *Two-phase region*: Region where the equilibrium state is a mixture of liquid and gas. Generally these two phases have different compositions from the overall composition $\boldsymbol{z}$. We label the liquid and gas compositions $\boldsymbol{x}$ and $\boldsymbol{y}$, respectively.
- *Bubble-line*: Boundary between the liquid region and the two-phase region. In more technical terms, when entering the two-phase region across this line the new (*incipient*) phase is less dense than the majority phase.
- *Dew-line*: Boundary between the vapor region and the two-phase region. In more technical terms, when entering the two-phase region across this line the new (*incipient*) phase is more dense than the majority phase.

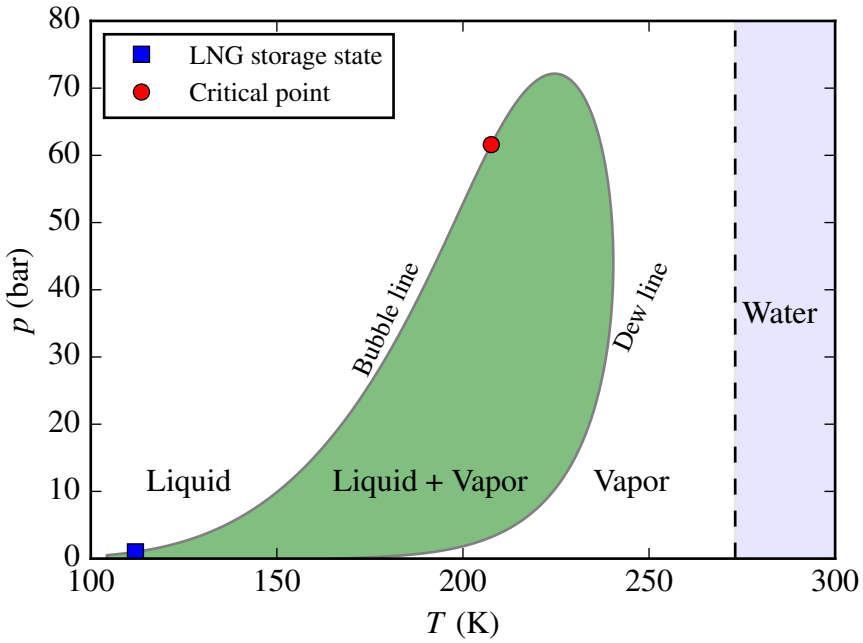

Figure 1.2: Phase diagram for an LNG mixture with 95% methane, 2% ethane, 2% propane and 1% n-butane, as computed when using the Peng–Robinson [42] equation of state. The possible temperatures of liquid water are also show.

- *Critical point*: This is the point where the bubble-line and the dew-line, as defined above, meet. When approaching this point from inside the two-phase region, the properties of the liquid and vapor phases converge continuously to form a single phase called the *critical state*. For more technical definitions, see the work of Reid and Beegle [43] or the original work of Gibbs [44].

Computation of the equilibrium state of a mixture such as LNG at given values of temperature and pressure requires two things:

- *Equation of State (EoS)*: An equation specifying a relation between the quantities temperature, pressure and density of a single phase of any given composition, and the ability to calculate state functions such as the Gibbs free energy of said phase.
- *Two-phase equilibrium algorithms*: An iterative algorithm that is able to use an EoS to search for the most stable state, given a total composition $\boldsymbol{z}$. The result may be pure liquid, pure vapor, or a two-phase state. In the latter case, the two resulting phases will generally have a composition that is different from $\boldsymbol{z}$. Once the equilibrium phase state is found, the EoS may be used to get properties such as density of any phase.

The phase diagram in Fig. 1.2 was generated using the Peng and Robinson [42] (PR) EoS in combination with the temperature–pressure equilibrium algorithms developed by Michelsen and Mollerup [45]. A wide variety of EoS and equilibrium algorithms are implemented in an in-house thermodynamics software developed at SINTEF Energy Research [46]. This code was used for all the numerical two-phase thermodynamics computations necessary in this thesis.

1.5.2 Non-equilibrium: Meta-stable states

As mentioned, phase diagrams such as Fig. 1.2 only indicate the equilibrium states. In reality it is possible to temporarily be in states that are different from the equilibrium state at the current temperature and pressure. We call these *meta-stable states*.

The type of meta-stable state relevant for LNG RPT is the *superheated liquid*. This is a state $(T, p, \boldsymbol{z})$ which is purely liquid despite the corresponding equilibrium state being a two-phase split between a liquid $(T, p, \boldsymbol{x})$ and a vapor $(T, p, \boldsymbol{y})$ of different compositions, or even a pure vapor state. In more technical terms, this means that there is a liquid solution to the EoS

at $(T, p, \boldsymbol{z})$, but this solution does not represent the state with the lowest possible energy.

The reason why such a meta-stable liquid may persist is due the energy barrier of nucleation. Even though there is a more energetically favorable state on a per-volume basis, there is a significant per-surface energy cost of creating new vapor bubbles (nuclei). The balance between these two effects constitutes an energy barrier that must be overcome.

A superheated liquid state may be obtained by starting with a thermodynamically stable liquid and then carefully heating it at constant pressure until entering the two-phase region, as illustrated in Fig. 1.3. If the conditions are right, the liquid will not immediately boil. A superheated liquid state will eventually transition into its equilibrium state if it is given enough time, is significantly disturbed, or put in contact with solid-surface nucleation sites. However, if the conditions are ideal it may be possible to heat the liquid far into the two-phase region without it boiling.

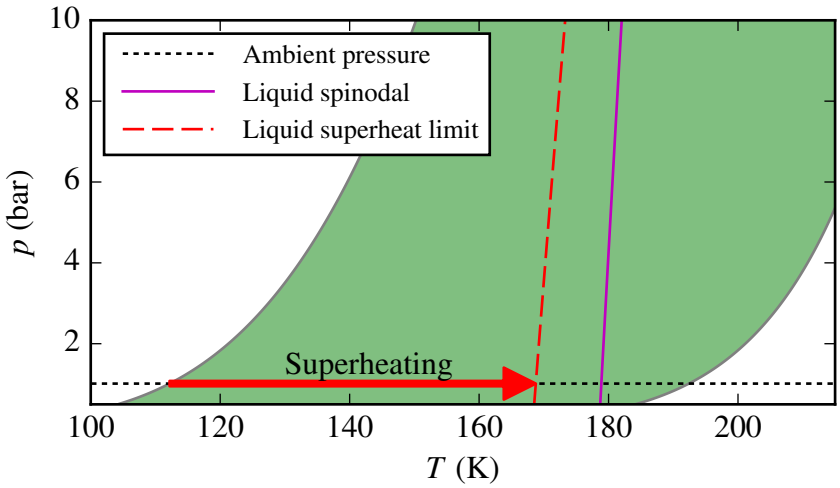

Figure 1.3: Zoomed in phase diagram, with spinodal and superheat limit, for a typical LNG mixture. The phase diagram and spinodal were computed using the Peng–Robinson [42] equation of state. The superheat limit was computed using classical nucleation theory in combination with the same equation of state.

Of course, the superheating cannot go on forever, and eventually nucleation of vapor must occur. In terms of an EoS, the temperature may become so high that a theoretical liquid solution for $(T, p, \boldsymbol{z})$ no longer exists at all. This is called the *spinodal*, or the *thermodynamic superheat limit*, and is theoretically the highest temperature that a pure liquid of composition $\boldsymbol{z}$ at

pressure p may exist. This may be viewed as the nucleation barrier going to zero.

In practice the spinodal is never reached because thermal fluctuations allow for the nucleation barrier to be overcome before it reaches zero. The temperature at which nucleation becomes very likely due to such fluctuations is called the *kinetic superheat limit*. Since this is the practical limit of superheat seen in experiments, we will refer to this as simply the *superheat limit* (SHL), and label it as T_{SHL}. Note that the SHL is sometimes referred to as the *homogeneous nucleation limit*. The superheat limit cannot be found from an EoS alone, since it also involves interface effects. However, classical nucleation theory (CNT) in combination with an EoS can make quite accurate predictions [47]. This is covered in more detail in Chapter 4.

1.5.3 Film boiling and the Leidenfrost point

When a liquid is put in contact with a surface that has a higher temperature than the liquid's boiling temperature, the mode of vaporization is called *boiling*. The driving force of this boiling is the *surface superheat*, $\Delta T_{\mathrm{w}} = T_{\mathrm{w}} - T_{\mathrm{s}}$, where T_{w} is the surface temperature and T_{s} is the boiling (saturation) temperature of the fluid. In the context of a mixture like LNG, T_{s} is on the bubble line shown in Fig. 1.2. A positive value of ΔT_{w} results in a *boiling heat flux*, $\dot{q}$. A plot of $\dot{q}$ against ΔT_{w} is called the *boiling curve* [48], sometimes called the *Nukiyama curve* after the person who first characterized it back in the 1930s [49]. An illustration of such a boiling curve may be found in Fig. 1.4.

At the lower end of wall superheat values we find the *nucleate boiling* regime, which most people would recognize as "normal" boiling. In this regime the heat flux intuitively increases as the surface temperature increases. However, this trend only continues to a certain point, when the *critical heat flux* is reached. Beyond, the heat flux dramatically decreases, as it transitions into the *film boiling* regime. In this regime the surface is covered by a continuous thin vapor film, allowing very little direct liquid–surface contact. The vapor-film acts as thermal insulation keeping the heat flux low despite the large surface superheat. When pure liquid methane or methane-rich LNG is spilled onto surfaces close to room temperature, the boiling will be in the film-boiling regime.

A particularly important point on the boiling curve is the *Leidenfrost point*, ΔT_{L}, which is the local minimum of $\dot{q}$ at the lower end of the film boiling regime. The corresponding critical wall temperature is called the *Leidenfrost temperature* (T_{L}), which means that $\Delta T_{\mathrm{L}} = T_{\mathrm{L}} - T_{\mathrm{s}}$. Thus, a wall temperature $T_{\mathrm{w}} > T_{\mathrm{L}}$ implies film boiling. Crossing the Leidenfrost

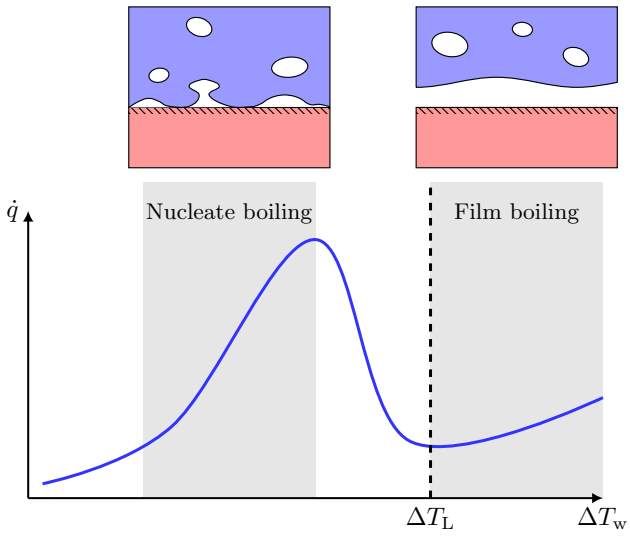

Figure 1.4: Illustration of a typical boiling curve, showing boiling heat flux ($\dot{q}$) as a function of surface superheat (ΔT_w). Also shown is the Leidenfrost point (ΔT_L), which marks the lower end of the film boiling regime.

point from the right to the left is called *film-boiling collapse* and causes a dramatic increase in heat flux. As will be explained in the next section, this is a crucial step in the theory of RPT triggering.

1.6 Overview of LNG RPT chain-of-events

As mentioned in Sec. 1.4, the core theory of LNG RPT was established in the 1970s and has remained relatively unchanged since. We are now in a position to make a detailed description of the chain-of-events implied by this theory. The steps are as follows:

1. **Film boiling**: The difference between the temperature of sea water and the bubble temperature of LNG (see Fig. 1.2) is so large that the LNG initially boils in the film boiling regime ($T_w \gg T_L$). This moderates the heat flux so that all the heat reaching the LNG is spent on evaporation and very little liquid superheating occurs.

2. **Enrichment**: While LNG is boiling it is mainly losing methane, as it is by far the most volatile component. This means that the molar

composition ($\boldsymbol{z}$) will gradually change towards the heavier components, and this is called *enrichment*.

3. **Film boiling collapse (Leidenfrost transition)**: While the water temperature (T_{w}) is relatively constant, the Leidenfrost temperature (T_{L}) depends on the molar composition. Specifically, T_{L} increases as the LNG is enriched. This means that the film-boiling criterion $T_{\mathrm{w}} > T_{\mathrm{L}}$ may eventually be broken, which causes film-boiling collapse. Film boiling collapse implies the transition into a regime with considerable direct liquid–liquid (LNG–water) contact and thus a dramatically larger heat flux.

4. **Superheating to the superheat limit**: Since the LNG–water interface does not have nucleation sites in the way that a liquid–solid interface typically has, it is presumed that evaporation is not initially able to proceed fast enough to spend the heat flux. The surplus thermal energy causes rapid superheating of the LNG. As indicated in Fig. 1.3, superheating of the LNG takes it from an equilibrium state at the bubble-line to a meta-stable state inside the two-phase region. If left relatively undisturbed, this will proceed until reaching the superheat limit, T_{SHL}.

5. **Rapid homogeneous nucleation**: After some quantity of LNG crosses the superheat limit, nucleation and growth of the new vapor phase becomes overwhelmingly likely throughout its volume. It is rapidly forced out of its meta-stable liquid state and towards an equilibrium state that contains considerable amounts of vapor.

6. **Explosive expansion**: If in mechanical equilibrium with its surroundings, the new state would take up over 100 times the volume of the original superheated liquid state. The fluid is initially forced to fit in the original volume, so the pressure increases dramatically before it has time to expand. Since this transition happens fast, it is observed as a loud and destructive vapor explosion, and was eventually named Rapid Phase Transition. The event involves high-pressure waves and considerable energy release through expansion work.

Note that in practical LNG spills, one would observe steps 1 and 2 and then a sudden skip to the macroscopic vapor explosion of step 6. In other words, steps 3 through 5 have so far been practically unobservable due to the small spatial and temporal scales involved. These steps must therefore be taken as a theoretical hypothesis, not certain fact.

During the enrichment phase, the two-phase region shown in Fig. 1.2 and the Leidenfrost temperature T_L gradually creep to higher temperatures. Once RPT is triggered, steps 3 through 6 occur almost instantaneously on the time-scale of enrichment. Thus, these steps may be illustrated in terms of a static phase diagram based on the composition at the time of film-boiling collapse, as shown in Fig. 1.5. This figure also introduces p^*, the highest pressure of the combined process of rapid nucleation and expansion. This may be interpreted as the peak pressure of the explosion, very close to the source.

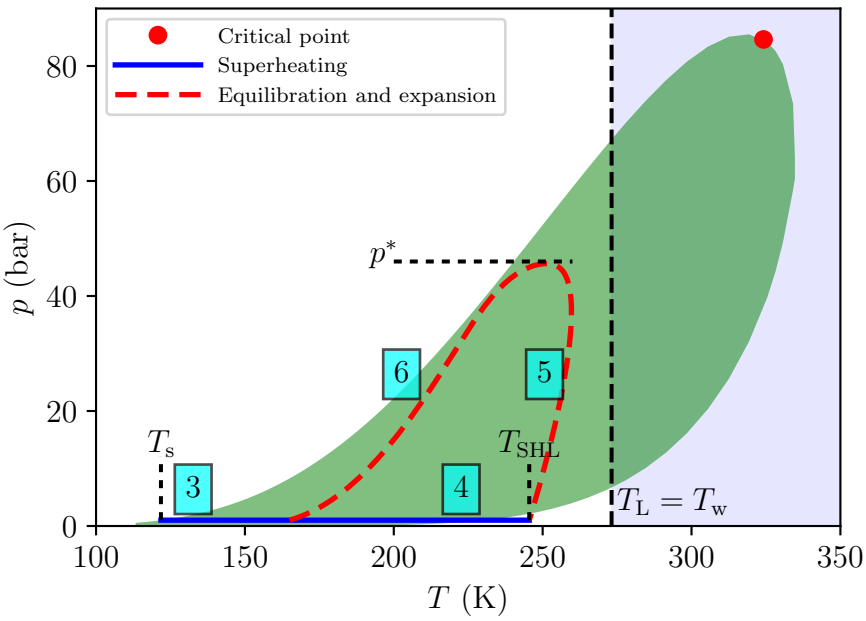

Figure 1.5: Steps 3 through 6 of the RPT process listed in Sec. 1.6, drawn on top of the phase-diagram of LNG that has been enriched to about 40% methane in order to meet the film-boiling collapse criterion ($T_\mathrm{L} \approx T_\mathrm{w}$). The green area is the liquid–vapor region and the blue area illustrates the temperatures possible for liquid water. The red dashed curve is not based on computation, but rather an educated guess for the actual thermodynamic path taken by steps 5 and 6 (see Chapter 4 for an idealized computation of this path). The peak of this line constitutes the maximum pressure of the event (p^*).

According to the chain-of-events outlined above, it follows logically that there are two necessary criteria for the delayed triggering of LNG RPT:

- The water temperature must be below the LNG's Leidenfrost temperature, as this is by definition necessary for film-boiling collapse and liquid–liquid contact.
- The water temperature must be above the LNG's superheat limit. If not, no amount of liquid–liquid contact will create the necessary degree of LNG superheating.

These two criteria for the water temperature (T_{w}) must be satisfied simultaneously, and may be written together concisely as

$$T_{\mathrm{SHL}}(\boldsymbol{z}) < T_{\mathrm{w}} < T_{\mathrm{L}}(\boldsymbol{z}), \tag{1.1}$$

where it has been emphasized that both the LNG superheat limit temperature (T_{SHL}) and the LNG Leidenfrost temperature (T_{L}) are functions of the LNG molar composition ($\boldsymbol{z}$). Finding ways to evaluate the criterion in Eq. (1.1) is the core motivation for most of the research efforts in this thesis. This criterion may be compared with the early discoveries by the LNG Research Center described in Sec. 1.4.3. Their empirical "1.1-rule" was likely found simply because $1.1T_{\mathrm{SHL}}$ is a decent approximation for T_{L}. Similarly, the "40% methane rule" for LNG is likely just a statement of the dependence of T_{L} on composition.

1.7 Why still study LNG RPT?

Since LNG has been transported in carriers at sea for roughly 50 years without major accidents, and is commonly stated to have an excellent safety record [7, 11], it is worth asking why we should expend this effort to study LNG RPT. The motivation for this project is based on the following few points: First, there is a record of actual unintended (though small scale) RPT incidents in the LNG industry [33]. Second, for reasons of maintaining a positive public perception, small accidents or near-accidents are not necessarily in the public record. Because of this, the true risks may be higher than what they appear to be. Third, the offshore activities of the LNG industry are starting to change. The industry is moving towards increased use of floating facilities for production, storage, offloading and re-gasification (see FPSO[2], FSRU[3] and FLNG[4] vessels) in order to make

[2]Floating production storage and offloading
[3]Floating Storage Re-gasification Unit
[4]Floating LNG

remote gas fields economically viable. Additionally, LNG is projected to see significantly increased usage as a marine fuel, which will necessitate more small-scale bunkering operations. These developments introduce additional scenarios for LNG leakage, as well as potentially more severe consequences due to the addition of passengers, workers and more sensitive equipment. Such operations may not necessarily inherit the good safety record of the traditional LNG carrier activities.

Overall, in the interest of preserving the excellent safety record of the industry, no significant theoretical risk should remain poorly understood. Based on the review of the research status in Sec. 1.4, we may conclude that the possibility of LNG RPT should be included among these risks.

1.8 Scope and outline of thesis

Based on the background given in Sec. 1.4, we may reasonably claim that the current state of knowledge is insufficient to reliably predict the risk and consequence of LNG RPT. However, this does not imply that we do not have a great body of work to build on. Central to all of this is the core hypothesis of RPT mechanisms, detailed in Sec. 1.6, which dates all the way back to the 1970s. While this foundational hypothesis is worth questioning, that endeavor is deemed outside the scope of the present work. Instead, we will take the hypothesis at face value and pursue its implications for prediction and quantification of LNG RPT. The approach will be theoretical and computational, but we will of course take into account the considerable body of available experimental data on both LNG RPT and the various relevant phenomena involved.

As we have shown in Sec. 1.6, the logical conclusion of the core hypothesis is a deceptively simple criterion for RPT triggering, namely Eq. (1.1). However, in order to apply this criterion in the context of an LNG spill, a series of questions must be answered:

- How can we predict the Leidenfrost temperature (T_{L}) of LNG, including its dependence on the changing composition? As explained in Sec. 1.5.3, this is the lower boundary of the film-boiling regime of the boiling curve, below which film boiling is no longer stable. Due to this, the major topic of study in this thesis is **film boiling**, which naturally also led down the path to a study of **evaporation models** for strong non-equilibrium evaporation.
- How can we predict the superheat limit (T_{SHL}) of LNG, including its dependence on the changing composition? As explained in Sec. 1.5.2,

this is the highest temperature a liquid may be superheated to before spontaneous nucleation becomes overwhelmingly likely. There is an established method of modeling this, **nucleation theory**, but for the purposes of LNG RPT it is necessary to evaluate how well it works for hydrocarbon mixtures.

- Given models for $T_{\mathrm{L}}(\boldsymbol{z})$ and $T_{\mathrm{SHL}}(\boldsymbol{z})$, how may we make quantitative predictions of RPT risk and consequence for a given LNG spill event? Answering this question requires the development of **LNG spill simulations** at some appropriate level of approximation. This is a complex multi-physics problem involving fluid mechanics, heat transfer and thermodynamics.

In this thesis we attempt to tackle all of these questions to varying depths. That being said, the most significant body of original research herein relates to the topic of film boiling and the stability thereof.

The monograph part of this thesis, **Part I**, is a self-contained summary of the research most relevant to LNG RPT. This includes introductions to the topics that are too established to be included in the research articles, but nevertheless very useful to a reader of this thesis. Following the present introductory chapter, **Chapter 2** contains background on non-equilibrium evaporation models based on kinetic theory, and the derivation of simplified forms that may be easily integrated in the subsequent film-boiling models. Then, **Chapter 3** covers the derivation of a new model for film-boiling, which crucially makes use of the kinetic theory evaporation models. Application of stability analysis on this model leads to a novel method for predicting the Leidenfrost temperature of pure fluids. Finally, **Chapter 4** demonstrates how models for the Leidenfrost temperature and superheat limit of hydrocarbon mixtures may be used to predict the risk and severity of delayed RPT. Many of the most significant results from this thesis have been published in or submitted to peer-reviewed journals. **Chapter 5** provides an overview of these articles, and summaries of their most significant results. The thesis is concluded by **Chapter 6**, which summarizes the findings in the context of LNG RPT, while identifying remaining knowledge gaps.

The preface of each chapter contains an overview of any journal articles it is based on. The full manuscripts of these articles are attached in **Part II**.

Chapter 2

Kinetic-theory evaporation models

2.1 Preface

In order to tackle the topic of film boiling, and specifically the problem of film boiling collapse (Leidenfrost point), it was necessary to look deeper into the process of evaporation across a liquid–vapor interface. The strong evaporation conditions present in film boiling necessitated modeling beyond the basic quasi-equilibrium approximation often used in conventional fluid mechanics, and this led to a study of kinetic theory. My work on this topic mainly consisted of:

- Obtaining a thorough understanding of kinetic theory, and in particular the origins of kinetic-theory evaporation models of varying complexity: Hertz–Knudsen, Schrage–Mills, and the Boltzmann Equation Moment Method.
- Implementing code to test and compare the above models, including an iterative numerical solver for the nonlinear Moment Method.
- Deriving the simplified and linearized form of these models that could be used in my efforts to model film boiling.

Most of this work, and more, may be found in the following journal article, which is included in Part II:

Paper E

Comparison of kinetic theory evaporation models for liquid thin-films

Eskil Aursand, Tor Ytrehus

Submitted to *International Journal of Multiphase Flow.*

2.2 The thermodynamic view of evaporation

In order to introduce the concepts of evaporation, we will take a step back from the complicated world of mixtures like LNG and consider a well-known pure fluid like water. In the case of a pure fluid, the two-phase region in Tp-space, as illustrated in Fig. 1.2, collapses from a region to a line. This line is called the *saturation line*, and is illustrated for the case of water in Fig. 2.1.

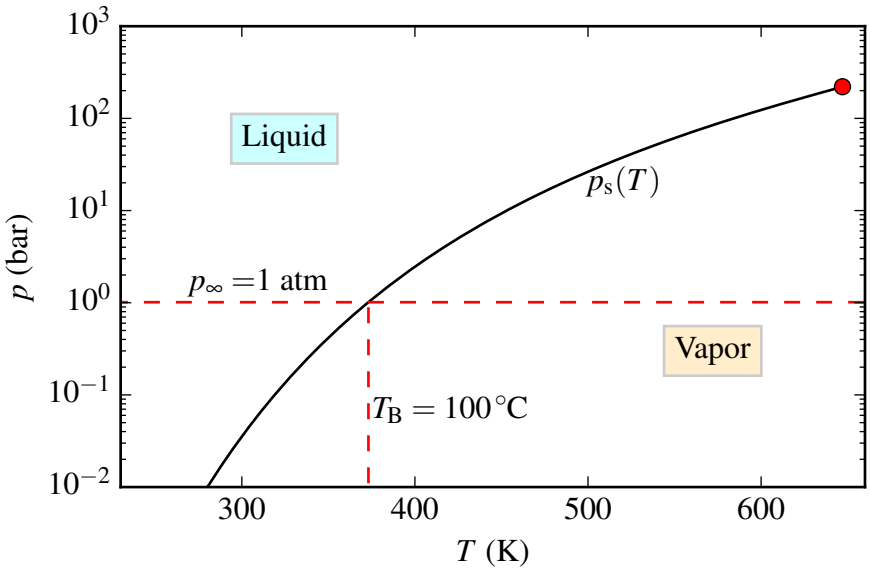

Figure 2.1: The temperature–pressure phase diagram of water, with the saturation line running from the triple point (not seen) to the critical point (red dot). Also shown is the conventional boiling temperature T_B, whish is the saturation temperature corresponding to atmospheric pressure.

The saturation line implies that at a given pressure there is only one discrete temperature where vapor and liquid may exist together in equilibrium. To the left and right of the line, the equilibrium state is purely liquid and vapor, respectively. The saturation line may be described by the function $p_s(T)$, or its inverse $T_s(p)$. A very useful relation from thermodynamics is the *Clausius–Clapeyron equation*, which approximates the slope of the saturation line at a given temperature as

$$\frac{\mathrm{d}p_s(T)}{\mathrm{d}T} = \frac{L\rho_s(T)}{T}, \tag{2.1}$$

where L is the *latent heat* of evaporation and $\rho_\mathrm{s}(T)$ is the vapor density at the saturation line.

Imagine an open container filled with liquid water, exposed to an atmosphere of pure water vapor. The atmosphere is large enough to impose a constant ambient pressure p_∞ regardless of what happens with the container. This means that we will always stay somewhere on the horizontal dashed line in Fig. 2.1,. If the system is initially at equilibrium, it is settled at the corresponding saturation temperature $T_\mathrm{s}(p_\infty)$. Imagine now that we attempt to increase the temperature of the liquid (T_l) by adding some energy (heat) to it for a short amount of time. This will have the immediate effect of increasing the liquid temperature so that $T_\mathrm{l} > T_\mathrm{s}(p_\infty)$. Due to the positive slope of $p_\mathrm{s}(T)$ the liquid's saturation pressure is now larger than the external pressure, and we may identify this as the fundamental driving force of evaporation. In fact, we may generally state that

$$p_\mathrm{s}(T_\mathrm{l}) \begin{cases} > p_\infty & \text{Evaporation} \\ = p_\infty & \text{Equilibrium} \\ < p_\infty & \text{Condensation} \end{cases} . \tag{2.2}$$

Once evaporation proceeds, there is a net flux of molecules from the liquid state to the vapor state. The vapor phase has a higher intrinsic energy (technically enthalpy) than the liquid phase, and this difference is the latent heat of evaporation (L). During evaporation this necessary energy is taken from the superheated liquid, thus cooling it until it reaches $T_\mathrm{s}(p_\infty)$, at which point the evaporation stops. We are then back in an equilibrium state at the exact same temperature and pressure as before, but with more vapor and less liquid than before.

Note that according to the driving force in Eq. (2.2), evaporation is fundamentally a non-equilibrium process, requiring the liquid to be in a superheated (meta-stable) state. The degree of superheat depends on the intensity of evaporation. A common way of avoiding the complications of meta-stable states in fluid mechanics problems with evaporation is to apply the *quasi-equilibrium approximation*. This essentially means assuming that the the liquid surface stays exactly at $T_\mathrm{s}(p_\infty)$ throughout the evaporation process. A consequence is that the added heat is immediately spent on evaporation. In technical terms, it means that if the rate of heat added per liquid surface area is $\dot{q}$, the resulting mass flux of evaporation across the liquid surface is $j_\mathrm{QE} = \dot{q}/L$, while the liquid surface stays exactly at $T_\mathrm{s}(p_\infty)$. Quasi-equilibrium is technically valid only in the limit of very weak/slow evaporation. Generally it predicts the correct evaporation flux in the case of a steady heat flux. However, it can not predict the degree to which the

liquid is superheated, nor can it predict the evaporation flux due to a highly transient heat flux.

As mentioned in Sec. 1.6, superheating is an essential mechanism behind RPT. Within the quasi-equilibrium approximation, no amount of added heat will lead to the liquid superheating because the evaporation process is too idealized. We need something that models the relationship between the driving force and the resulting evaporation flux, and this requires a closer look at the structure at and around the evaporating interface.

2.3 The microscopic view of evaporation

We consider the problem of determining the macroscopic boundary conditions appropriate at an evaporating liquid–vapor interface. While such an interface is commonly treated as having zero thickness in continuum fluid mechanics, the microscopic structure actually includes two layers of relatively small but nonzero thicknesses (see Fig. 2.2):

- **Interface transition**: A very rapid transition from a liquid-like density to a gas-like density across the distance of a few molecular diameters. Its thickness (δ_i in Fig. 2.2) is of the order of 1 nm.
- **Knudsen layer**: A layer very close to the interface, where the gas is in a non-equilibrium state and its behavior is dominated by interaction with the evaporating interface. Its thickness (δ_Kn in Fig. 2.2) is of the order of a few molecular mean free path lengths.

The quantities at the boundary between the Knudsen layer and the continuum bulk vapor are traditionally labeled with the subscript ∞ due to their large distance from the interface on the scale of the mean free path length.

The molecular mean free path referred to above is the average distance traveled by a molecule in the gas before colliding with another. For an equilibrium distribution of monatomic particles, kinetic theory finds that the mean free path is

$$\lambda = \frac{k_\mathrm{B} T}{\sqrt{2} p \pi d^2}, \tag{2.3}$$

where d is the effective particle diameter and k_B is the Boltzmann constant. For atoms or molecules with diameters in the range of 0.25 nm to 1 nm, Eq. (2.3) implies that the mean free path under standard conditions is in the range of 10 nm to 150 nm.

Consider now the case of an evaporating liquid in contact with an atmosphere of its own vapor holding a given pressure p_∞. According to Eq. (2.2)

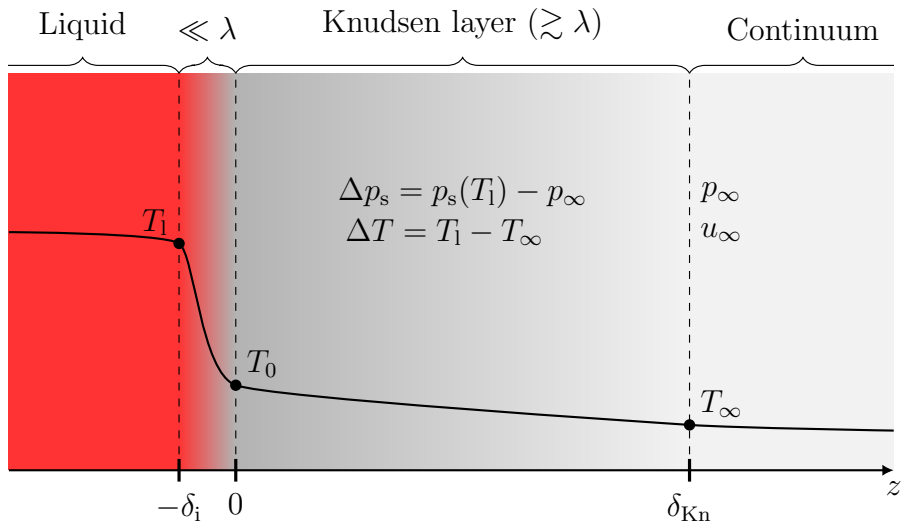

Figure 2.2: Illustration of an evaporating interface when zoomed in to the scale of the Knudsen layer.

there are two ways of driving this evaporation, either by heating up the liquid (increasing T_l) or by dropping the outside pressure (reducing p_∞). In either case we may define the driving force as

$$\Delta p_\mathrm{s} = p_\mathrm{s}(T_\mathrm{l}) - p_\infty, \tag{2.4}$$

which must be positive in the case of evaporation. While the state on the liquid side is (T_l, p_∞) and the state on the (bulk) vapor side is (T_∞, p_∞), Eq. (2.4) also makes use of a third *reference state*, $(T_\mathrm{l}, p_\mathrm{s}(T_\mathrm{l}))$. The latter state is not realized at any location in the system, but plays an important role in the qualitative formulation of the driving force, as shown in Eq. (2.2). Through certain foundational postulates in kinetic-theory evaporation modeling, the reference state will also play a quantitative role. These three states, and the resulting driving force Δp_s, are illustrated in relation to the saturation line in Fig. 2.3. The figure also shows the quantity ΔT,

$$\Delta T = T_\mathrm{l} - T_\infty, \tag{2.5}$$

which is the total temperature difference between the bulk liquid and the bulk vapor. While the temperature changes continuously on a microscopic

scale, the structure in Fig. 2.2 is so thin that the difference ΔT will appear as a temperature discontinuity on the macroscopic scale of fluid mechanics. As indicated in Fig. 2.2, and shown in more detail in Ytrehus [50], most of the temperature jump occurs across the interface transition, not the Knudsen layer.

The problem is now the following: Given a liquid at a temperature T_l in contact with its vapor held at a pressure p_∞ (and thus a driving force Δp_s), what is the resulting evaporation rate (j) and temperature of the outgoing vapor (T_∞)? One method of tackling this problem is kinetic theory, which will be introduced in the next section.

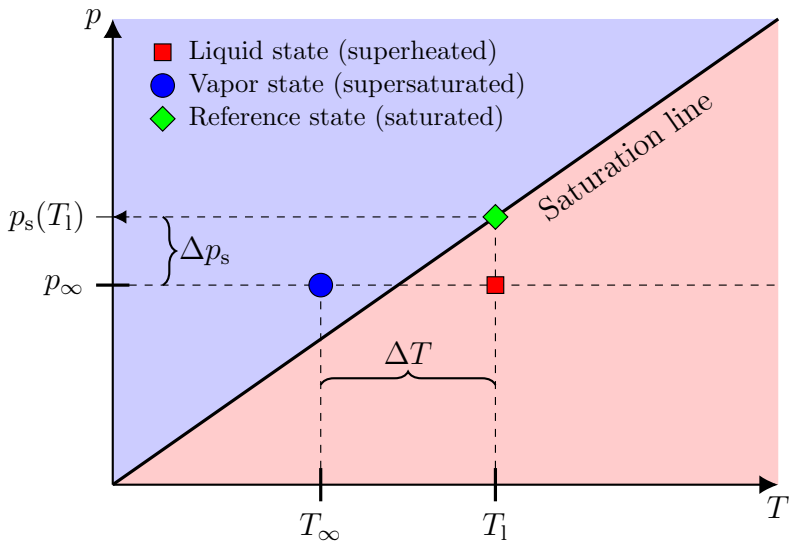

Figure 2.3: The bulk liquid and vapor states on either side of the Knudsen layer shown on a phase diagram in relation to the evaporating fluid's saturation line. Also shown is the reference state, which by definition is a saturated state with the same temperature as the liquid. Note that in this case the vapor state is shown as being supersaturated, but that need not always be the case.

2.4 Kinetic gas theory

2.4.1 History of kinetic-theory evaporation models

The endeavor to apply kinetic theory to evaporation and condensation problems was pioneered by Hertz [51] and Knudsen [52]. Their focus was on evaporation between two opposing surfaces with a near-vacuum between, but the base concepts were useful stepping stones for the more general evaporation models that would follow. The next step came with Schrage [53], who extended the model to represent evaporation from a surface into a bulk gas phase at atmospheric pressure.

However, the models remained incomplete in the sense that they did not provide a complete specification of the state on either side of the evaporating interface. The reason was that they only considered the conservation of mass across the interface, not the conservation of momentum and energy. This was eventually remedied from the 1970s and onwards through more detailed considerations of the dynamics within the Knudsen layer: the submicrometer kinetic boundary-layer of vapor between the evaporating liquid surface and the external bulk vapor. Due to its non-equilibrium nature, this layer cannot be described by typical continuum equations. Instead, it is described by the *Boltzmann equation* from kinetic theory, which is an integro-differential equation for the evolution of the statistical distribution of molecular velocities. This problem has been solved to various degrees of approximation throughout the years, as reviewed by Kogan [54], Ytrehus [50] and Frezzotti and Barbante [55]. Initially, linear models for weak phase-transfer rates were derived by authors such as Patton and Springer [56], Shankar and Marble [57], Pao [58] and Pao [59]. Then, non-linear treatments for strong flow rates were considered by Kogan and Makashev [60], Sone and Onishi [61], using numerical methods, and by Ytrehus [62] using a moment method to obtain analytical solutions.

2.4.2 Background on kinetic theory

In kinetic theory we deal with the dynamics of velocity distribution functions $f(\boldsymbol{x}, t, \boldsymbol{\xi})$, where $\boldsymbol{x}$ is position, t is time, and $\boldsymbol{\xi}$ is a molecular velocity vector. The distribution represents the number of molecules at a given point $(\boldsymbol{x}, t)$ having a specific velocity. In technical terms, $f\mathrm{d}^3\boldsymbol{\xi}$ gives the number density of particles within the element of velocity space $\mathrm{d}^3\boldsymbol{\xi}$.

The evolution of the distribution function $f(\boldsymbol{x}, t, \boldsymbol{\xi})$ is governed by the

Boltzmann equation [63], which may be written as

$$\frac{\partial f}{\partial t} + \xi_x \frac{\partial f}{\partial x} + \xi_y \frac{\partial f}{\partial y} + \xi_z \frac{\partial f}{\partial z} = Q(\boldsymbol{\xi}). \tag{2.6}$$

For every point in real space (x, y, z), this equation describes change in the number of molecules belonging to every point in velocity space (ξ_x, ξ_y, ξ_z). Thus, it is essentially an equation in six-dimensional phase-space, in addition to time.

The true complexity of Eq. (2.6) lies in its right hand side, Q, which is the *collision term*. The collision term represents the rate of change in the distribution $f(\boldsymbol{x}, t, \boldsymbol{\xi})$ due to binary collisions, some taking molecules out of the state $\boldsymbol{\xi}$ and some bringing molecules into the same state $\boldsymbol{\xi}$. Technically, the term is an integral over all such possible collisions, thus making Eq. (2.6) an integro-differential equation. The details of the collision term depends on the *collision model* used, which contains assumptions about the detailed nature of the binary collisions between molecules.

Regardless of the specific collision model used, as long as the binary collisions obey fundamental conservation laws, the Boltzmann equation will always evolve an isolated ideal gas towards the same type of equilibrium distribution. This follows from *Boltzmann's H-theorem*, and the equilibrium distribution is called the *Maxwell–Boltzmann* distribution. When allowing for some macroscopic drift velocity u along the z-axis, it may be written as

$$f_{\mathrm{M}}(\boldsymbol{\xi}; T, n, u) = \frac{n}{(2\pi RT)^{3/2}} \exp\left(-\frac{(\boldsymbol{\xi} - u\hat{\boldsymbol{z}})^2}{2RT}\right), \tag{2.7}$$

Here $n = p/(k_{\mathrm{B}}T)$ is the total number density (particles per volume) corresponding to the state (T, p) that the gas is kept at, and R is the specific gas constant of the particles.

While Eq. (2.7) is technically the distribution of an isolated gas at uniform temperature and pressure, in the more general non-uniform case we may still find that the distribution $f(\boldsymbol{x}, \boldsymbol{\xi}, t)$ is locally very similar to the Maxwell–Boltzmann distribution corresponding to the local temperature and pressure. This is called *local equilibrium*, and is a very common approximation made in fluid mechanics.

When close to local equilibrium one may perform a so-called *Chapman–Enskog* expansion of the Boltzmann equation [50], with a small parameter representing deviation from local equilibrium. Remarkably, at zeroth and first order one retains the well-known continuum fluid mechanics equations, the Euler equations and the Navier–Stokes equations, respectively. In the

latter case one may also find transport coefficients (viscosity and thermal conductivity) according to the intermolecular interaction law.

In the context of the evaporation illustrated in Fig. 2.2, the bulk vapor phase outside the Knudsen layer is close to equilibrium, and may thus be described by continuum models like the Navier–Stokes equations. However, within the Knudsen layer the gas is so far from local equilibrium that the Chapman–Enskog expansion does not apply [50]. Because of this we must resort to the more fundamental Boltzmann equation.

2.4.3 Properties of the Maxwell–Boltzmann distribution

For every drifting Maxwell–Boltzmann distribution like Eq. (2.7) there is a corresponding dimensionless *speed ratio*, defined as

$$S(T,u) = \frac{u}{\sqrt{2RT}}. \tag{2.8}$$

This is the ratio between the macroscopic flow speed (u) and the most probable molecular speed of the corresponding stationary distribution ($\sqrt{2RT}$). Note that since the speed-of-sound of a monatomic ideal gas is $\sqrt{(5/3)RT}$, S is closely related to the Mach number ($\mathrm{Ma} = \sqrt{(6/5)}S$).

A Maxwell–Boltzmann distribution is a statement on the various molecular velocities present at that location. Each of these molecules carries with it conserved quantities such as mass, momentum and kinetic energy, and thus a distribution contains information on the local fluxes of these quantities in different directions. In the case of the Knudsen layer, as illustrated in Fig. 2.2, we are due to symmetry mainly concerned with z-momentum and variations of quantities along the z-axis. We define the following shorthands for the mass, z-momentum and kinetic energy of molecules,

$$\Psi = \left(m, m\xi_z, \frac{1}{2}m\boldsymbol{\xi}^2\right), \tag{2.9}$$

where m is the mass of a single molecule. Given this, the net fluxes into the $z > 0$ half-plane due to a Maxwell-Boltzmann distribution are

$$\int_{\xi_z>0} \xi_z \Psi_i f_{\mathrm{M}} \mathrm{d}\boldsymbol{\xi} \quad = \begin{cases} \rho\sqrt{\frac{RT}{2\pi}}F^+(S) & , \quad i=1 \\ \rho\frac{RT}{2}G^+(S) & , \quad i=2\,, \\ 2\rho RT\sqrt{\frac{RT}{2\pi}}H^+(S) & , \quad i=3 \end{cases} \tag{2.10}$$

and similarly the net fluxes into the $z < 0$ half-plane are

$$\int_{\xi_z<0} \xi_z \Psi_i f_{\mathrm{M}} \mathrm{d}\boldsymbol{\xi} = \begin{cases} -\rho\sqrt{\frac{RT}{2\pi}} F^-(S) & , \quad i = 1 \\ \rho\frac{RT}{2} G^-(S) & , \quad i = 2 \\ -2\rho RT\sqrt{\frac{RT}{2\pi}} H^-(S) & , \quad i = 3 \end{cases}. \tag{2.11}$$

The functions $F^{\pm}(S)$, $G^{\pm}(S)$ and $H^{\pm}(S)$ are defined in Eqs. (2.54) to (2.56) in Sec. 2.A. They all approach unity as $S \to 0$, which leads to the expected equality of fluxes in the two directions due to symmetry. The presence of a non-zero drift speed ($S \neq 0$) breaks this symmetry.

The fluxes defined and calculated in Eqs. (2.10) and (2.11) will be crucial building blocks in the kinetic-theory evaporation models that follow.

2.5 Evaporation models from kinetic theory

Given a liquid temperature (T_l) and an outside applied pressure (p_∞), we may define the following dimensionless driving force for evaporation,

$$\Delta\mathcal{Z} = \frac{\Delta p_\mathrm{s}}{p_\infty}. \tag{2.12}$$

Given a value for $\Delta\mathcal{Z}$, the goal of these evaporation models is then to predict the resulting dimensionless temperature jump,

$$\Delta\mathcal{Y} = \frac{\Delta T}{T_\mathrm{l}}, \tag{2.13}$$

and evaporation rate in terms of downstream speed ratio,

$$S_\infty = S(T_\infty, u_\infty). \tag{2.14}$$

Here u_∞ is the bulk z-directed flow speed outside the Knudsen layer, as illustrated in Fig. 2.2. All three quantities $\Delta\mathcal{Z}$, $\Delta\mathcal{Y}$ and S_∞ approach zero when the evaporation rate approaches zero. The evaporation mass flux (j) is proportional to S_∞, with a small correction due to the temperature jump,

$$j = \rho_\infty u_\infty = \frac{p_\infty}{\sqrt{RT_\mathrm{l}}}\sqrt{\frac{2}{1-\Delta\mathcal{Y}}} S_\infty. \tag{2.15}$$

In the second step we have used the ideal gas law ($p_\infty = \rho_\infty R T_\infty$) as well as the definitions in Eqs. (2.8), (2.13) and (2.14).

It is worth commenting on why $\Delta\mathcal{Y}$, and thus the downstream temperature T_∞, is considered an output instead of an input to the problem. As

will be shown later by considering conservation of mass, momentum and energy across the Knudsen layer, specification of both $\Delta\mathcal{Z}$ and $\Delta\mathcal{Y}$ would constitute an overdetermination of the problem. In other words, we are not free to specify the two of them independently, and setting one determines the other. In the following treatment we choose to consider $\Delta\mathcal{Z}$ as the independent variable.

2.5.1 Schrage-Mills (SM)

The first truly realistic kinetic-theory evaporation model for non-vacuum conditions was developed by Schrage [53] in the 1950s as an elaboration on the similar but more primitive model by Hertz [51] and Knudsen [52]. These models do not really solve the Boltzmann equation inside the Knudsen layer, but they make important use of the equilibrium (Maxwell–Boltzmann) solution Eq. (2.7) at the boundaries.

With reference to Fig. 2.2, these models make the following crucial postulate: The liquid surface ejects molecules into the Knudsen layer according to the $\xi_z > 0$ half of a stationary Maxwell–Boltzmann distribution corresponding to the reference state shown in Fig. 2.3,

$$f_\mathrm{e} = f_\mathrm{M}(T_\mathrm{l}, n_\mathrm{e}, 0). \tag{2.16}$$

Here n_e is the total number density corresponding to the reference state $(T_\mathrm{l}, p_\mathrm{s}(T_\mathrm{l}))$. Similarly, the bulk vapor sends molecules into the Knudsen layer according to the $\xi_z < 0$ half of a Maxwell–Boltzmann distribution drifting out at some unknown speed u_∞,

$$f_\infty = f_\mathrm{M}(T_\infty, n_\infty, u_\infty). \tag{2.17}$$

This need not be thought of as a postulate, as we may merely define the outer edge of the Knudsen layer at the point where this local-equilibrium approximation applies. Here n_∞ is the total number density corresponding to the bulk vapor state (T_∞, p_∞).

These two distributions may then be used to express the net flux of molecules from the liquid to the bulk vapor. After multiplying with an ad-hoc evaporation–condensation coefficient $\alpha \in [0, 1]$, to be discussed later,

the evaporation mass flux is found to be

$$\begin{aligned} j &= \alpha \left[\int_{\xi_z>0} \xi_z \Psi_1 f_\mathrm{e} \mathrm{d}\boldsymbol{\xi} \quad + \int_{\xi_z<0} \xi_z \Psi_1 f_\infty \mathrm{d}\boldsymbol{\xi} \quad \right], \\ &= \alpha \left[\rho_\mathrm{s}(T_\mathrm{l}) \sqrt{\frac{RT_\mathrm{l}}{2\pi}} - \rho_\infty \sqrt{\frac{RT_\infty}{2\pi}} F^-(S_\infty) \right], \\ &= \alpha \left[\frac{p_\mathrm{s}(T_\mathrm{l})}{\sqrt{2\pi RT_\mathrm{l}}} - \frac{p_\infty}{\sqrt{2\pi RT_\infty}} F^-(S_\infty) \right]. \end{aligned} \tag{2.18}$$

Here Eqs. (2.10) and (2.11) have been used to evaluate the integrals, and the ideal gas law has been used to change between densities and pressures. Unfortunately, since j and S_∞ are dependent through Eq. (2.15), Eq. (2.18) is actually an implicit equation for j. This may be remedied by considering the weak-evaporation limit, which we may formally define as

$$S_\infty \ll 1, \qquad \Delta\mathcal{Z} \ll 1, \qquad \Delta\mathcal{Y} \ll 1. \tag{2.19}$$

In this case $F^-(S_\infty) \approx 1 - \sqrt{\pi} S_\infty$, and Eq. (2.18) may be solved explicitly for j and yield the more useful Schrage–Mills formula [64],

$$\begin{aligned} j &= \frac{\alpha}{1 - \frac{1}{2}\alpha} \left[\frac{p_\mathrm{s}(T_\mathrm{l})}{\sqrt{2\pi RT_\mathrm{l}}} - \frac{p_\infty}{\sqrt{2\pi RT_\infty}} \right], \\ &= \frac{\alpha}{1 - \frac{1}{2}\alpha} \frac{p_\infty}{\sqrt{2\pi RT_\mathrm{l}}} \left[1 - \frac{1}{2} \frac{\Delta\mathcal{Y}}{\Delta\mathcal{Z}} \right] \Delta\mathcal{Z}. \end{aligned} \tag{2.20}$$

One remaining issue for the application of Eq. (2.20) is that $\Delta\mathcal{Y}$ is unknown. As mentioned in Sec. 2.4.1, models like Schrage–Mills lack a complete specification of the problem due to ignoring momentum and energy, and is thus unable to make a prediction for the downstream temperature T_∞. In order to make a prediction for j given T_l and p_∞ we must either ignore the temperature jump ($\Delta\mathcal{Y} \approx 0$), or make some additional ad-hoc assumption regarding the downstream vapor. One such option is to assume that the vapor leaves the Knudsen layer in a saturated state, so that

$$T_\infty = T_\mathrm{s}(p_\infty). \tag{2.21}$$

According to the Clausius–Clapeyron relation Eq. (2.1) we may then relate the temperature jump to Δp_s. In the weak-evaporation limit this means that

$$\Delta\mathcal{Y} \approx \frac{RT_\mathrm{l}}{L} \Delta\mathcal{Z}. \tag{2.22}$$

By inserting Eq. (2.22) into Eq. (2.20) we finally find a practically useful version of the Schrage-Mills formula,

$$j = \frac{\alpha}{1 - \frac{1}{2}\alpha}\left[1 - \frac{1}{2}\frac{RT_\mathrm{l}}{L}\right]\frac{p_\infty}{\sqrt{2\pi RT_\mathrm{l}}}\Delta\mathcal{Z}. \tag{2.23}$$

2.5.2 Boltzmann equation moment method (BEMM)

As mentioned previously, models like Schrage–Mills (SM) only considers mass conservations, and as a result they arrive at an incomplete description of the Knudsen layer boundaries. The Boltzmann Equation Moment Method (BEMM) [62, 50] is a way of resolving this issue by also considering conservation of z-momentum and energy across the Knudsen layer.

Governing equations

In this method we start by assuming that the governing equation in the Knudsen layer is the one-dimensional steady-state form of the Boltzmann equation Eq. (2.6),

$$\xi_z\frac{\partial f}{\partial z} = Q(\boldsymbol{\xi}). \tag{2.24}$$

This still leaves the complexity of the collision term Q, but the BEMM model may in fact make predictions for the evaporation rate and temperature jump without choosing a specific collision model. This is made possible by noting the fact that regardless of the specific details, individual collisions should always conserve mass, momentum and energy. In technical terms, the quantities Ψ_i in Eq. (2.9) are *collision invariants* [50], and this fact may be expressed as

$$\int \Psi_i(\boldsymbol{\xi})Q(\boldsymbol{\xi})\mathrm{d}\boldsymbol{\xi} = 0, \tag{2.25}$$

for all three components of Ψ in Eq. (2.9). We may now multiply Eq. (2.24) by Ψ_i before integrating throughout velocity space, and thanks to Eq. (2.25) the right-hand side vanishes. Since the only z-dependence on the left-hand side is in f, we may pull the differentiation outside the integral, leaving us with

$$\frac{\partial}{\partial z}\left[\int \Psi_i\xi_z f(z,\boldsymbol{\xi})\mathrm{d}\boldsymbol{\xi}\right] = 0. \tag{2.26}$$

In words, the three moments $\Psi_i \xi_z$ of the unknown distribution f are independent of z. This must mean that they are equal on either side of the Knudsen-layer (ref. Fig. 2.2), i.e.

$$\left[\int \Psi_i \xi_z f(z, \boldsymbol{\xi}) \mathrm{d}\boldsymbol{\xi}\right]_{z=0} = \left[\int \Psi_i \xi_z f(z, \boldsymbol{\xi}) \mathrm{d}\boldsymbol{\xi}\right]_{z\to\infty} \tag{2.27}$$

Eq. (2.27) for every i yields the three *moment equations* that now constitute the governing equations of our problem. However, we also need boundary conditions for the distribution function f.

Boundary condition on the right-hand side

Just like in the Schrage–Mills model, by definition the outer edge of the Knudsen layer has a drifting Maxwell–Boltzmann distribution,

$$f|_{z\to\infty} = f_{\mathrm{M}}(T_\infty, n_\infty, u_\infty). \tag{2.28}$$

Boundary condition on the left-hand side

We wish to construct a realistic boundary condition for the distribution function f at the liquid surface, $z = 0$. This will be done separately for the outgoing ($\xi_z > 0$) and incoming ($\xi_z < 0$) part of the distribution, labeled f^+ and f^-, respectively.

Just like in the Schrage–Mills model, we construct the outgoing part based on the Maxwell–Boltzmann distribution of the reference state, f_{e}. However, this only accounts for emission from the liquid, and we also want to account for the reflection of vapor molecules at the surface. The combination of the two yields

$$f^+\big|_{z=0} = \alpha_{\mathrm{e}} f_{\mathrm{e}}^+ + (1 - \alpha_{\mathrm{c}}) f_{\mathrm{r}}^+, \tag{2.29}$$

using ad-hoc weighing with an evaporation-coefficient ($\alpha_{\mathrm{e}} \in [0, 1]$) and a condensation-coefficient ($\alpha_{\mathrm{c}} \in [0, 1]$). The incoming part is assumed to be proportional to the incoming part of the distribution at the other side of the Knudsen layer,

$$f^-\big|_{z=0} = \beta f_\infty^-, \tag{2.30}$$

with β being some unknown parameter to be solved for.

The reflection contribution f_{r}^+ in Eq. (2.29) is assumed to be the outgoing part of a Maxwell-Boltzmann distribution at the liquid temperature, but with a different unknown number density n_{r},

$$f_{\mathrm{r}}^+ = f_{\mathrm{M}}^+(T_{\mathrm{l}}, n_{\mathrm{r}}, 0). \tag{2.31}$$

The number density n_r can be found through the *flux-condition*, which states that the maximum (condensation-coefficient zero) reflected mass flux must be equal to the incoming mass flux at $z = 0$. When combining this principle with the assumption in Eq. (2.30), it may be written as

$$\int_{\xi_z>0} \xi_z f_\mathrm{r}^+ \mathrm{d}\boldsymbol{\xi} = \beta \int_{\xi_z<0} |\xi_z| f_\infty^- \mathrm{d}\boldsymbol{\xi}. \tag{2.32}$$

According to Eq. (2.28) and Eq. (2.31) both distributions in Eq. (2.32) are Maxwell–Boltzmann distributions, and thus we may use Eqs. (2.10) and (2.11) to evaluate the integrals. This simplifies the flux-condition to a relation between the densities n_r and n_∞,

$$n_\mathrm{r}\sqrt{\frac{RT_\mathrm{l}}{2\pi}} = \beta\sqrt{\frac{RT_\infty}{2\pi}}F^-(S_\infty)n_\infty. \tag{2.33}$$

In summary, the boundary condition at the left-hand side of the Knudsen layer may be written as

$$f|_{z=0} = \begin{cases} \left(\alpha_\mathrm{e} + (1-\alpha_\mathrm{c})\frac{n_\mathrm{r}}{n_\mathrm{e}}\right) f_\mathrm{e}^+ & \xi_z > 0 \\ \beta f_\infty^- & \xi_z < 0 \end{cases} \tag{2.34}$$

with n_r according to Eq. (2.33). Of course, this boundary condition depends on the new unknown β that we have introduced. However, this is not a problem. Since there are three equations in Eq. (2.27), we have enough information to solve for the three unknowns S_∞, $\Delta\mathcal{Y}$ and β when specifying a driving force $\Delta\mathcal{Z}$.

Complete solution

We may now combine the three moment equations in Eq. (2.27) with the boundary conditions Eqs. (2.28) and (2.34), while using Eqs. (2.10) and (2.11) to evaluate the integrals. After a significant amount of manipulation that will not be shown here, this yields a set of three coupled nonlinear equations,

$$\alpha_\mathrm{e}\mathcal{Z}\sqrt{\mathcal{Y}} + (1-\alpha_\mathrm{c})\beta F^- - \beta F^- = 2\sqrt{\pi}S_\infty \tag{2.35}$$

$$\alpha_\mathrm{e}\mathcal{Z} + (1-\alpha_\mathrm{c})\sqrt{\frac{1}{\mathcal{Y}}}\beta F^- + \beta G^- = 4S_\infty^2 + 2 \tag{2.36}$$

$$\alpha_\mathrm{e}\mathcal{Z} + (1-\alpha_\mathrm{c})\sqrt{\frac{1}{\mathcal{Y}}}\beta F^- - \sqrt{\mathcal{Y}}\beta H^- = \sqrt{\mathcal{Y}}\sqrt{\pi}S_\infty\left(S_\infty^2 + \frac{5}{2}\right) \tag{2.37}$$

which represent conservation of mass, momentum and energy, respectively. Note that we have introduced the following quantities,

$$\mathcal{Z} = 1 + \Delta\mathcal{Z} = \frac{p_\mathrm{s}(T_\mathrm{l})}{p_\infty}, \qquad \mathcal{Y} = 1 - \Delta\mathcal{Y} = \frac{T_\infty}{T_\mathrm{l}}, \tag{2.38}$$

and that the functions F^-, G^- and H^- are implicitly evaluated at $S = S_\infty$.

Given a driving force $\Delta\mathcal{Z}$ and assumed values for the coefficients α_e and α_c, the three equations Eqs. (2.35) to (2.37) may be solved numerically for the three unknowns S_∞, $\Delta\mathcal{Y}$ and β. This solution may then be used to find the evaporation mass flux through Eq. (2.15). This constitutes a solution to the evaporation problem as stated.

Linearized solution

If we assume weak evaporation as defined as Eq. (2.19), as well as equality of the evaporation and condensation coefficient, we may find an explicit first-order solution of Eqs. (2.35) to (2.37) in terms of S_∞,

$$\Delta\mathcal{Y} = \frac{\sqrt{\pi}}{4} S_\infty, \tag{2.39}$$

$$\Delta\beta = \sqrt{\pi}\left[\frac{2}{\pi} - \frac{9}{16}\right] S_\infty, \tag{2.40}$$

$$\Delta\mathcal{Z} = \frac{32\pi + 32\alpha - 23\pi\alpha}{16\sqrt{\pi}\alpha} S_\infty, \tag{2.41}$$

with α as the combined evaporation/condensation coefficient. We may solve Eq. (2.41) for S_∞ to get

$$S_\infty = \frac{1}{2\sqrt{\pi}} \left(\frac{\alpha}{1 - \left(\frac{\gamma-1}{\gamma}\right)\alpha} \right) \Delta\mathcal{Z}. \tag{2.42}$$

with the shorthand γ defined as

$$\gamma = \frac{32\pi}{32 + 9\pi} \approx 1.67. \tag{2.43}$$

If we insert Eq. (2.42) into the weak-evaporation approximation of Eq. (2.15) we find the mass flux as

$$j = \left(\frac{\alpha}{1 - \left(\frac{\gamma-1}{\gamma}\right)\alpha} \right) \frac{p_\infty}{\sqrt{2\pi R T_\mathrm{l}}} \Delta\mathcal{Z} \tag{2.44}$$

which is directly comparable to the Schrage–Mills formula in Eq. (2.23). Similarly, by combining Eq. (2.39) with Eq. (2.42) we find that the interfacial temperature jump is

$$\frac{\Delta T}{T_\mathrm{l}} = \Delta\mathcal{Y} = \frac{1}{8}\left(\frac{\alpha}{1-\left(\frac{\gamma-1}{\gamma}\right)\alpha}\right)\Delta\mathcal{Z}. \tag{2.45}$$

If the vapor is exactly saturated we know from the Clausius–Clapeyron relation Eq. (2.1) that the temperature jump must be $\Delta\mathcal{Y} \approx (RT_\mathrm{s}/L)\Delta\mathcal{Z}$. By comparing with Eq. (2.45) we then find that the vapor will be supersaturated if α is high, and superheated if α is low. The exact boundary between the two regimes will be fluid dependent, but generally around $\alpha \approx 0.5$.

2.5.3 Model comparison

The most straight-forward comparison we can make against evaporation experiments is the relationship between the downstream speed-ratio (S_∞) and the dimensionless driving force ($\Delta\mathcal{Z}$). For the case of weak evaporation, both the Schrage–Mills model and the linearized BEMM model take the same form,

$$S_\infty = \frac{r(\alpha)\delta(T_\mathrm{l})}{\sqrt{4\pi}}\Delta\mathcal{Z}. \tag{2.46}$$

For Schrage–Mills these functions are

$$r_\mathrm{SM} = \frac{\alpha}{1-\frac{1}{2}\alpha}, \qquad \delta_\mathrm{SM} = \left[1-\frac{1}{2}\frac{RT_\mathrm{l}}{L}\right], \tag{2.47}$$

and for linearized BEMM they are

$$r_\mathrm{BEMM} = \frac{\alpha}{1-\left(\frac{\gamma-1}{\gamma}\right)\alpha}, \qquad \delta_\mathrm{BEMM} = 1 \tag{2.48}$$

A third option is the full nonlinear BEMM model, which implies solving the set of equations in Eqs. (2.35) to (2.37) numerically for every given value of the driving force $\Delta\mathcal{Z}$.

The evaporation rates predicted by the three models are compared with each other in Fig. 2.4, together with experimental data from Ytrehus [62] (also shown in Ytrehus [50, Sec. 4.4]). The plot does not go beyond the driving force that yields $S_\infty \approx 0.9$, as it is known that the 1D evaporative flow in the Knudsen layer is restricted to the subsonic regime [65, 50]. The

evaporation–condensation coefficient is kept at $\alpha = 1$ for simplicity. The parameter RT_l/L, needed by the SM model, is set to 0.1 according to Trouton's rule. From Fig. 2.4 it is clear that the full nonlinear BEMM model is the most accurate one throughout the range of weak to strong evaporation. However, as expected, the linearization is a good approximation for weak evaporation.

The predicted interfacial temperature jumps from the BEMM model and its linearization are shown in Fig. 2.5. We see that in this case ($\alpha = 1$) the downstream vapor is supersaturated for weak and moderate evaporation, but superheated for very strong evaporation.

2.5.4 Simplification by linearizing the saturation line

In fluid mechanics problems it is some times very convenient to model the evaporation rate directly from the liquid temperature, without requiring an exact representation of the saturation line $p_\mathrm{s}(T)$ to find the corresponding driving force $\Delta\mathcal{Z}$. Such a representation may be derived in the weak-evaporation case, where Δp_s is so small that the saturation-line can be linearized by the Clausius–Clapeyron relation Eq. (2.1),

$$p_\mathrm{s}(T) = p_\infty + \frac{L\rho_\mathrm{s}}{T_\mathrm{s}}\left[T - T_\mathrm{s}\right]. \tag{2.49}$$

Here ρ_s and T_s are short-hands for $\rho_\mathrm{s}(p_\infty)$ and $T_\mathrm{s}(p_\infty)$, respectively. This means that the driving force can be approximated as a linear function of the liquid superheat,

$$\Delta\mathcal{Z} = \frac{L}{RT_\mathrm{s}}\left[\frac{T_\mathrm{l} - T_\mathrm{s}}{T_\mathrm{s}}\right]. \tag{2.50}$$

If we combine Eq. (2.50) with Eq. (2.46) and Eq. (2.15), take the weak-evaporation limit again, and assume that $RT_\mathrm{l}/L \ll 1$, the SM and linearized BEMM model both take the simple form of

$$\frac{\tilde{K}}{r(\alpha)} j = T_\mathrm{l} - T_\mathrm{s} \tag{2.51}$$

Here $\tilde{K}$ is defined as

$$\tilde{K} = \frac{\sqrt{2\pi R}T_\mathrm{s}^{3/2}}{\rho_\mathrm{s} L}. \tag{2.52}$$

The constant $\tilde{K}$ depends on both fluid properties and applied pressure, and is a measure of the importance of non-equilibrium evaporation effects. In a sense $\tilde{K}/r$ is an interfacial resistance, indicating how much thermal driving force $(T_\mathrm{l} - T_\mathrm{s})$ is necessary to obtain an evaporation flux (j).

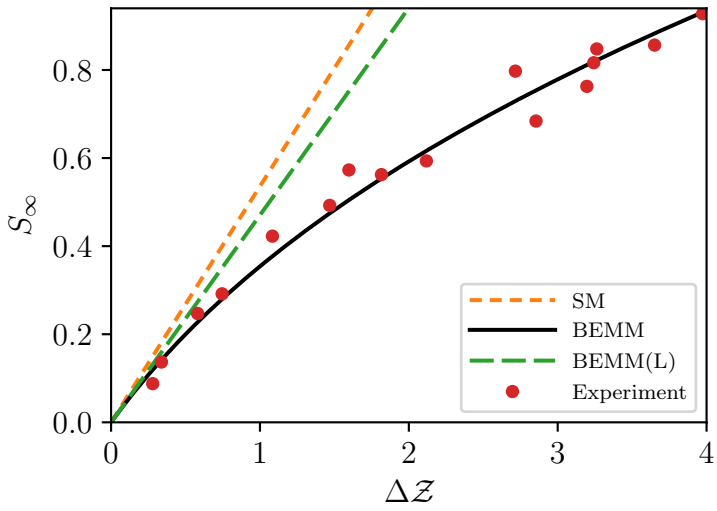

Figure 2.4: Predicted downstream speed-ratio (S_∞) as a function of driving force ($\Delta\mathcal{Z}$), for the SM model, the BEMM model and the linearized BEMM model. Parameters are set to $\alpha = 1$ and $RT_\mathrm{l}/L = 0.1$. Also shown are experimental data from Ytrehus [62].

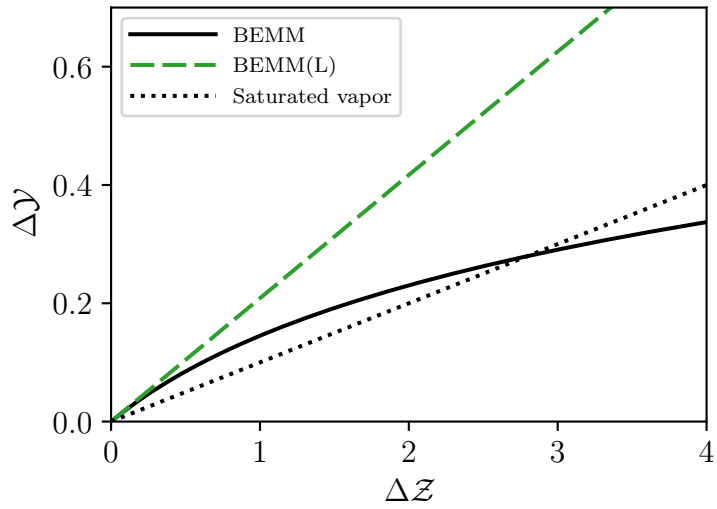

Figure 2.5: Predicted dimensionless interfacial temperature jump ($\Delta\mathcal{Y}$) as a function of driving force ($\Delta\mathcal{Z}$), for the BEMM model and its linearized form. Parameters are set to $\alpha = 1$ and $RT_\mathrm{l}/L = 0.1$. The dotted line shows the $\Delta\mathcal{Y}$ that follows from the assumption of saturated vapor. A value of $\Delta\mathcal{Y}$ above this line implies supersaturated vapor.

2.5.5 The evaporation coefficient

In the derivation of the Schrage–Mills model the ad-hoc coefficient $\alpha \in [0, 1]$ was introduced in Eq. (2.18) as a pre-factor that, if less than one, reduces the evaporation rate from what the idealized derivation implies. Then, in the derivation of the BEMM model we separately introduced an evaporation coefficient ($\alpha_e \in [0, 1]$) and a condensation coefficient ($\alpha_c \in [0, 1]$) in Eq. (2.29). The former represented the probability of molecule emission relative to the ideal Maxwell–Boltzmann distribution, and the latter represented the probability of adsorption (as opposed to reflection) of incoming molecules from the Knudsen layer. The exact values that these coefficients should take is usually uncertain, and for simplicity they are commonly taken to be equal [50, 66]. This common value is often referred to as the evaporation–condensation coefficient. Since we in the present work are mainly concerned with evaporation, we will continue to refer to this value as simply the *evaporation coefficient*, and label it as α.

The evaporation coefficient is introduced in the boundary conditions in a rather ad-hoc way, and cannot be determined from within kinetic theory itself. Its value is the subject of much uncertainty, debate and active research to this date. Water is the only somewhat well studied fluid, and even there the experiments show a large scatter from 0.1 to 1.0, as seen in e.g. [67, Tab. 1]. Besides experiments, a common way of estimating the coefficient is by molecular dynamics simulations (MD). These methods show somewhat more consistent results, and generally give values quite close to unity unless the temperatures are very high. Overall, MD simulations from the last decade seem to generally agree on the following trends [66, 67, 68, 69, 70, 71, 72]:

- For a given fluid, the evaporation/condensation coefficient decreases as liquid temperature is increased.
- As long as the liquid temperature is less than 0.7 times the critical temperature (T_c), we can expect $\alpha \in (0.7, 1.0)$ for a considerable variety of fluids.

In the cases considered here the liquid surface temperatures are very close to the saturation temperatures, and every liquid considered here satisfies $T_s < 0.7T_c$. Thus, we may expect that $\alpha_e \in (0.7, 1.0)$.

2.6 Conclusions

The main take-away results from this chapter are the highly simplified evaporation models derived in Sec. 2.5.4. They take the very convenient form of a constitutive relation,

$$\hat{K} j = T_\mathrm{l} - T_\mathrm{s}, \tag{2.53}$$

with $\hat{K} = \tilde{K}/r(\alpha)$ being the interfacial resistance to evaporation (j) due to a driving force based on liquid superheat ($T_\mathrm{l} - T_\mathrm{s}$). At this level of approximation, the effect of choosing either Schrage–Mills or BEMM simply manifests as a slight change in the function $r(\alpha)$. Eq. (2.53) allows for a very practical way of including non-equilibrium evaporation effects in fluid mechanics problems. However, it comes with the cost of introducing a new parameter: the evaporation coefficient (α).

The relation in Eq. (2.53) will be crucial in the following modeling of film boiling, as it provides the necessary closure when the liquid interface temperature (T_l) is allowed to be a variable as opposed to the constant value (like in the quasi-equilibrium approximation). Allowing the interface temperature to be a variable enables the inclusion of phenomena like the thermocapillary effect, which will turn out to play an important role in the model.

2.A Appendix: Kinetic-theory details

The short-hands introduced in Eqs. (2.10) and (2.11), including their expansions for $S \ll 1$, are

$$\begin{aligned} F^{\pm}(S) &= \sqrt{\pi} S \left(\operatorname{erf}(S) \pm 1\right) + \mathrm{e}^{-S^2} \\ &= 1 \pm \sqrt{\pi} S + \mathcal{O}\left(S^2\right), \end{aligned} \tag{2.54}$$

$$\begin{aligned} G^{\pm}(S) &= \left(2S^2 + 1\right)\left(1 \pm \operatorname{erf}(S)\right) \pm \frac{2}{\sqrt{\pi}} S \mathrm{e}^{-S^2} \\ &= 1 \pm \frac{4}{\sqrt{\pi}} S + \mathcal{O}\left(S^2\right), \end{aligned} \tag{2.55}$$

$$\begin{aligned} H^{\pm}(S) &= \frac{\sqrt{\pi} S}{2}\left(S^2 + \frac{5}{2}\right)\left(\operatorname{erf}(S) \pm 1\right) + \frac{1}{2}(S^2 + 2)\mathrm{e}^{-S^2} \\ &= 1 \pm \frac{5\sqrt{\pi}}{4} S + \mathcal{O}\left(S^2\right). \end{aligned} \tag{2.56}$$

Chapter 3

Film boiling stability

3.1 Preface

According to the theory of LNG RPT presented in Sec. 1.6, crossing of the Leidenfrost point is the crucial first step that leads to superheating and subsequent vapor explosion. As shown in Fig. 1.4, crossing the Leidenfrost point is equivalent to film-boiling collapse, and thus the prediction of such a transition is key to predicting LNG RPT triggering. This reasoning led to the main bulk of original work in this thesis being related to the phenomenon of film boiling and in particular the stability thereof.

This work was performed with two simplifications compared to the case of LNG film boiling on water: Firstly, only pure fluids were considered. This choice was made due to the availability of evaporation models (see Chapter 2) and experimental data on the Leidenfrost point. As will be discussed later, a further extension to mixtures is likely necessary before the model is directly applicable to LNG. Secondly, the hot surface was assumed to act like a stationary solid, not a liquid. This choice was made to not over-complicate the model and also make it more comparable to the existing body of correlations and experimental data. It is likely quite accurate for boiling on quiescent water.

My original work on this topic may be summarized as:

- The long-wave thin-film modeling methodology reviewed by Oron, Davis, and Bankoff [73], particularly the model of Burelbach, Bankoff, and Davis [74], was extended to the case of film boiling. The necessity to modify the model came from the fact that these works regarded thin liquid films, while the case of film boiling contains a thin vapor

film. Since film boiling has a film that is less dense than the bulk, free-surface assumptions were not possible, and a new approach had to be developed. Based on this, a new set of long-wave governing equations were derived, for arbitrary orientation and Reynolds number.

- It was discovered that the common low-Reynolds version of such equations are unable to capture the observed instabilities in vertical film boiling. A moderate-Reynolds version of the long-wave model was developed to remedy this.

- Based on the low-Reynolds limit of the general equations, which are valid for horizontal film boiling, a single partial differential equation (PDE) for the film-thickness function was derived.

- Examination of the stability properties of uniform horizontal base states showed that very long and very short waves were unconditionally stable. Further, the examination showed that the stability of intermediate wavelengths is conditional, and divided into three distinct regimes based on film thickness.

- It was found that the critical wall superheat for the stability of intermediate wavelengths is a surprisingly good predictor for the Leidenfrost point. The theoretical implication of this is that film-boiling collapse occurs when the destabilizing thermocapillary effect overpowers the stabilizing vapor thrust effect.

The following chapter shows a concise derivation of the long-wave equations for film boiling, initially on a generalized form valid for any Reynolds number. Then, the stability analysis of horizontal low-Reynolds film boiling is treated in detail, leading to the novel model for the Leidenfrost point based on the stability conditions of intermediate waves.

All of the main results on film boiling covered in this chapter have been published already. The relevant papers, which are attached in full in Part II, are:

Paper A
Thermocapillary instability as a mechanism for film boiling collapse
Eskil Aursand, Stephen H. Davis, Tor Ytrehus
Published in *Journal of Fluid Mechanics*.
(2018) Vol. 852, pp. 283–312
https://doi.org/10.1017/jfm.2018.545

Paper B

Inclination dependence of planar film boiling stability

Eskil Aursand

Published in *International Journal of Multiphase Flow.*
(2018) Vol. 106, pp. 243–253
https://doi.org/10.1016/j.ijmultiphaseflow.2018.05.010

Paper C

Inclined film boiling: Film stability and heat transfer

Eskil Aursand, Stephen H. Davis

Published in *International Journal of Multiphase Flow.*
(2019) Vol. 111, pp. 175–187
https://doi.org/10.1016/j.ijmultiphaseflow.2018.11.017

3.2 Film-boiling model

3.2.1 Background

As illustrated in Fig. 1.4, film boiling involves a continuous thin vapor film between two bulk dense phases. In the present work we attempt to describe the dynamics of this vapor film within the framework of the long-wave approximation. This approach typically leads to a single scalar highly nonlinear equation for the film-thickness function, and has been thoroughly reviewed by Oron, Davis, and Bankoff [73], Myers [75] and Craster and Matar [76] for the case of liquid films. However, for the purposes of studying film boiling stability the approach had to be modified in several ways.

The model developed herein is heavily inspired by two previous original works, which both consider thin film flow with phase transition: the model for evaporating liquid films by Burelbach, Bankoff, and Davis [74], and the model for horizontal film boiling by Panzarella, Davis, and Bankoff [77]. However, neither model is identical to the one developed herein. While Panzarella, Davis, and Bankoff [77] consider a vapor film, their model did not capture the thermocapillary effect [78], which will appear quite crucial in the present work. As we shall show, this is due to the assumption of maximum liquid drag (zero tangential interface velocity), which effectively decouples the model from any thermocapillary forces. Burelbach, Bankoff, and Davis [74], on the other hand, do include the thermocapillary effect. However, their model could not be applied to film boiling due to the fact that the densest phase is no longer the thin-film itself, but in the bulk outside. This disallowed the free-surface type approximation that for liquid films allows a pretty straightforward path to a so-called one-sided model for the film thickness.

The following work starts with a derivation of the first thin-film model to include van der Waals, thermocapillary, vapor thrust and non-equilibrium evaporation effects in the context of film boiling. This model is then applied to predict the Leidenfrost point. There has been a large variety of efforts to pinpoint the Leidenfrost point of boiling fluids. Some are based on simplified fluid mechanical considerations, such as the efforts of Zuber [79] and Berenson [80]. Others estimate it by the supposed upper bounds of the spinodal (Spiegler et al. [81]) or the superheat limit from nucleation theory (Yao and Henry [82]). However, as concluded by Bernardin and Mudawar [83], none of the older models appears to predict the Leidenfrost point in a satisfactory manner for an arbitrary fluid. Also, the ones that are reasonably accurate for conventional fluids are semi-empirical, which provides less physical insight and is dubious for extrapolation to unconventional fluids.

3.2.2 Problem description

We restrict the treatment herein to saturated film-boiling of pure fluids with no forced convection. The following core assumptions are made in order to construct the model:

- The equations of Newtonian incompressible flow apply to the vapor.
- Thermophysical properties such as density, viscosity and thermal conductivity are assumed constant within each phase.
- The saturation temperature of the fluid is treated as a constant. In other words, the pressure variations in the flow are insignificant on a thermodynamic scale.
- The onset of thin-film instabilities may be captured by a two-dimensional model.

The problem to be modeled is illustrated in Fig. 3.1: A fluid is put in contact with a flat solid wall at some angle of inclination (α_{w}). By the definition of saturated film boiling, the liquid is kept at its saturation temperature (T_{s}) some significant distance away from the wall. The internal bulk of the solid is kept at a constant temperature (T_{w}), which leads to a characteristic temperature difference across the system,

$$\Delta T_{\mathrm{w}} = T_{\mathrm{w}} - T_{\mathrm{s}}. \tag{3.1}$$

This value ΔT_{w} then sets the position along the horizontal axis of the boiling curve in Fig. 1.4. Here we assume that ΔT_{w} is in the film-boiling regime. The result is that a continuous vapor film forms between the liquid and the wall, at $z = h(x,t)$.

The purpose of the modeling efforts herein is in general to predict the spatiotemporal dynamics of the film thickness function $h(x,t)$. Specifically, knowledge of this allows for predictions of film-boiling stability. The problem is first treated generally with an arbitrary inclination angle, and later elaborated within two categories: horizontal (low-Reynolds) and non-horizontal (moderate-Reynolds) film boiling.

The variables of the problem are summarized in Tab. 3.1. Field variables will by default refer to the vapor phase. In the case that they refer to the liquid phase a subscript "l" is used. When the subscripts x, z or t are used, differentiation with respect to that variable is implied. The input parameters of the case are shown in Tab. 3.2. When applicable, subscripts "l" and "v" will then be used to indicate liquid or vapor, respectively.

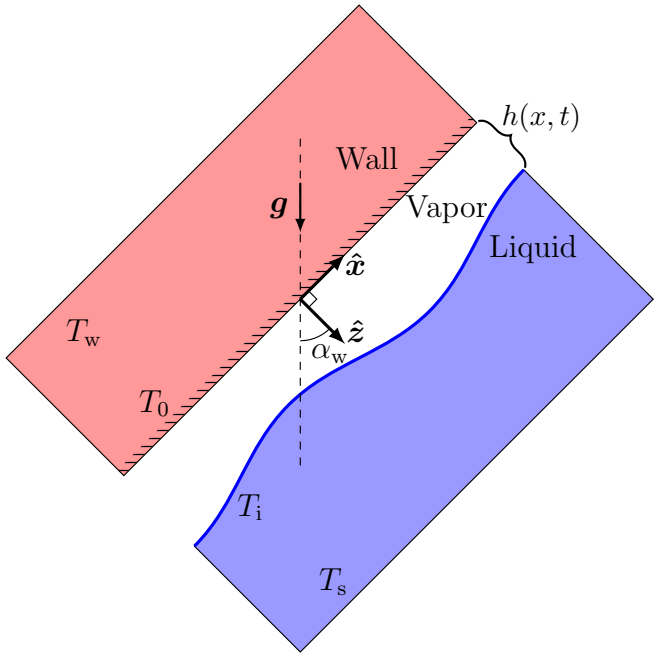

Figure 3.1: Illustration of the film-boiling case to be modeled: A heated solid surface is submerged in a liquid at some angle α_w with respect to the direction of gravity. The coordinate system is aligned with the solid surface, as indicated by the unit vector $\hat{\boldsymbol{x}}$ for the spatial variable x and the unit vector $\hat{\boldsymbol{z}}$ for the spatial variable z. The solid bulk is kept at a temperature T_w and the liquid bulk is kept at its saturation temperature T_s. The difference $\Delta T_\mathrm{w} = T_\mathrm{w} - T_\mathrm{s}$ is so large that the film boiling regime applies, and thus, a continuous vapor film forms between the liquid and the solid surface. The general purpose of the model herein is to predict the dynamics of the resulting film-thickness function $h(x,t)$ as a function of lateral position x and time t.

Table 3.1: Variables and functions in the film-boiling case.

Symbol	Description	Unit
x	Position tangential to wall	m
z	Position normal to wall	m
t	Time	s
$h(x,t)$	Vapor-film thickness	m
$j(x,t)$	Evaporation mass flux	$\mathrm{kg\,m^{-2}\,s^{-1}}$
$T_0(x,t)$	Solid surface temperature	K
$T_\mathrm{i}(x,t)$	Interface temperature	K
$p(x,z,t)$	Pressure	Pa
$T(x,z,t)$	Temperature	K
$u(x,z,t)$	Velocity x-component	$\mathrm{m\,s^{-1}}$
$w(x,z,t)$	Velocity z-component	$\mathrm{m\,s^{-1}}$
$\phi(x,z,t)$	Body-force potential	Pa
$\sigma(T)$	Surface tension	$\mathrm{N\,m^{-1}}$

Table 3.2: Constant input-parameters in the film-boiling case.

Symbol	Description	Unit
α_w	Angle of solid surface	–
T_w	Solid bulk temperature	K
T_s	Fluid saturation temperature	K
g	Gravitational acceleration	$\mathrm{m\,s^{-2}}$
ρ	Density	$\mathrm{kg\,m^{-3}}$
μ	Dynamic viscosity	$\mathrm{Pa\,s}$
c_p	Heat capacity	$\mathrm{J\,kg^{-1}\,K^{-1}}$
k	Thermal conductivity	$\mathrm{W\,m^{-1}\,K^{-1}}$
$\tilde{A}$	Effective liquid–solid Hamaker constant	J
σ_0	Surface tension at saturation temperature	$\mathrm{N\,m^{-1}}$
γ	Temperature sensitivity of surface tension	$\mathrm{N\,m^{-1}\,K^{-1}}$
L	Latent heat of evaporation	$\mathrm{J\,kg^{-1}}$
$\mathcal{H}_\mathrm{w}$	Heat-transfer coefficient (solid bulk to surface)	$\mathrm{W\,m^{-2}\,K^{-1}}$
$\mathcal{H}_\mathrm{l}$	Heat-transfer coefficient (interface to liquid bulk)	$\mathrm{W\,m^{-2}\,K^{-1}}$

3.2.3 Interface description

The liquid–vapor interface illustrated in Fig. 3.1 is located at $z = h(x,t)$, and its local shape may be characterized by a unit normal vector ($\hat{\boldsymbol{n}}$), a unit tangent vector ($\hat{\boldsymbol{t}}$) and a curvature (κ). These may be formally written as

$$\hat{\boldsymbol{n}} = \frac{1}{\sqrt{1+h_x^2}}\left(\hat{\boldsymbol{z}} - h_x\hat{\boldsymbol{x}}\right), \tag{3.2}$$

$$\hat{\boldsymbol{t}} = \frac{1}{\sqrt{1+h_x^2}}\left(\hat{\boldsymbol{x}} + h_x\hat{\boldsymbol{z}}\right), \tag{3.3}$$

$$\kappa = \frac{h_{xx}}{(1+h_x^2)^{3/2}}, \tag{3.4}$$

where the latter has units of inverse length.

The motion of the interface itself is described by the interface velocity, $\boldsymbol{v}_\mathrm{i} = u_\mathrm{i}\hat{\boldsymbol{x}} + w_\mathrm{i}\hat{\boldsymbol{z}}$. We define its tangential component as being equal to the tangential velocities of the two phases on either side, which are equal to each other due to the no-slip condition. Based on basic kinematics and geometry the interface velocity must have the following relationship to the film-thickness function $h(x,t)$,

$$h_t = w_\mathrm{i} - u_\mathrm{i}h_x \tag{3.5}$$

With the help of Eqs. (3.2) and (3.5) we then find that the normal component of the interface velocity may be found directly from derivatives of $h(x,t)$,

$$\begin{aligned}\boldsymbol{v}_\mathrm{i}\cdot\hat{\boldsymbol{n}} &= \left[u_\mathrm{i}\hat{\boldsymbol{x}} + w_\mathrm{i}\hat{\boldsymbol{z}}\right]\cdot\left[\frac{1}{\sqrt{1+h_x^2}}\left(\hat{\boldsymbol{z}} - h_x\hat{\boldsymbol{x}}\right)\right]\\ &= \frac{1}{\sqrt{1+h_x^2}}\left[w_\mathrm{i} - u_\mathrm{i}h_x\right]\\ &= \frac{h_t}{\sqrt{1+h_x^2}},\end{aligned} \tag{3.6}$$

In addition, mass conservation at the interface demands that any normal component of vapor velocity (in the frame of the interface) on either side is accounted for by an evaporation mass flux (j),

$$\rho_\mathrm{v}\left[(\boldsymbol{v}_\mathrm{i} - \boldsymbol{v})\cdot\hat{\boldsymbol{n}}\right]_{z=h} = j = \rho_\mathrm{l}\left[(\boldsymbol{v}_\mathrm{i} - \boldsymbol{v}_\mathrm{l})\cdot\hat{\boldsymbol{n}}\right]_{z=h}. \tag{3.7}$$

If we now use Eq. (3.6) to substitute for $\boldsymbol{v}_\mathrm{i} \cdot \hat{\boldsymbol{n}}$ and Eq. (3.2) to substitute for $\hat{\boldsymbol{n}}$, the left-hand equality Eq. (3.7) turns into the following useful *kinematic boundary condition*,

$$\rho_\mathrm{v} \frac{[h_t + u h_x - w]_{z=h}}{\sqrt{1+h_x^2}} = j. \tag{3.8}$$

The interface temperature T_i is simply defined as

$$T_\mathrm{i}(x,t) = [T(x,z,t)]_{z=h}\,. \tag{3.9}$$

Assuming continuity of temperature, its x-derivative is related to the tangential gradient of the temperature-field by

$$\begin{aligned}(T_\mathrm{i})_x &= [T_x + T_z h_x]_{z=h} \\ &= \sqrt{1+h_x^2}\left[\nabla T \cdot \hat{\boldsymbol{t}}\right]_{z=h}.\end{aligned} \tag{3.10}$$

In the following model derivation it will be necessary to express some specific components from the stress tensor ($\mathcal{T}$) of a Newtonian incompressible fluid [84]. By utilizing the definitions of the interface unit vectors in Eqs. (3.2) and (3.3), as well as the continuity equation ($u_x + w_z = 0$), these may be written as

$$\begin{aligned}(\mathcal{T} \cdot \hat{\boldsymbol{n}}) \cdot \hat{\boldsymbol{n}} &= -p + \frac{2\mu}{1+h_x^2}\left[h_x^2 u_x + w_z - h_x\,(u_z + w_x)\right] \\ &= -p + \frac{2\mu}{1+h_x^2}\left[u_x(h_x^2 - 1) - h_x\,(u_z + w_x)\right],\end{aligned} \tag{3.11}$$

and

$$\begin{aligned}(\mathcal{T} \cdot \hat{\boldsymbol{n}}) \cdot \hat{\boldsymbol{t}} &= \frac{\mu}{1+h_x^2}\left[(u_z + w_x)\left(1 - h_x^2\right) - 2h_x(u_x - w_z)\right] \\ &= \frac{\mu}{1+h_x^2}\left[(u_z + w_x)\left(1 - h_x^2\right) - 4u_x h_x\right].\end{aligned} \tag{3.12}$$

These may apply on either side of the interface by using the appropriate flow velocity vector.

3.2.4 Equations of film boiling

Governing equations

In accordance with the the assumptions listed in Sec. 3.2.2 the governing equations of the vapor film are the two-dimensional continuity equation, momentum equations, and energy equation of incompressible flow [84],

$$u_x + w_z = 0, \tag{3.13}$$

$$\rho_\mathrm{v}\left(u_t + uu_x + wu_z\right) = -p_x + \mu_\mathrm{v}\left(u_{xx} + u_{zz}\right) - \phi_x, \tag{3.14}$$

$$\rho_\mathrm{v}\left(w_t + uw_x + ww_z\right) = -p_z + \mu_\mathrm{v}\left(w_{xx} + w_{zz}\right) - \phi_z, \tag{3.15}$$

$$\rho_\mathrm{v} c_{pv}\left(T_t + uT_x + wT_z\right) = k_\mathrm{v}\left(T_{xx} + T_{zz}\right). \tag{3.16}$$

Since this is meant to describe thin-film flow, the body-force potential ϕ includes not only the gravitational potential, but also a *disjoining pressure* term [73] that represents the van der Waals interaction between the liquid surface and the solid wall,

$$\phi = \phi_0 + \rho_\mathrm{v} g\left(ax + bz\right) + \frac{\tilde{A}}{6\pi h^3(x)}. \tag{3.17}$$

Here ϕ_0 is a constant reference potential whose value is irrelevant. The symbols a and b are short-hands for the inclination dependence,

$$a = \sin(\alpha_\mathrm{w}), \qquad b = -\cos(\alpha_\mathrm{w}). \tag{3.18}$$

In addition to these fluid mechanical equations we use two supplementary equations. The first describes the temperature dependence of surface tension. This is approximated as a linearization around the value σ_0 at T_s [78],

$$\sigma(T) = \sigma_0 - \gamma\left[T - T_\mathrm{s}\right], \tag{3.19}$$

which makes the constant parameter γ the negative temperature derivative of σ. The second describes the connection between evaporation rate and interface superheat. According to the main result in Chapter 2, Eq. (2.53), this may be approximated by

$$\hat{K} j = T_\mathrm{i} - T_\mathrm{s}, \tag{3.20}$$

where $\hat{K} = \tilde{K}/r(\alpha)$ may be calculated from the other case parameters through Eq. (2.52). A closure such as Eq. (3.20) is necessary because the interface temperature T_i has been set free as a variable. If we were to use the quasi-equilibrium approximation, we would simply eliminate the variable by setting $T_\mathrm{i} = T_\mathrm{s}$, and there would be no need for an evaporation model.

Boundary conditions: Wall

At the vapor–solid boundary, two simple principles apply: First there is the no-slip condition, which in the case of a stationary wall implies zero velocity,

$$[\boldsymbol{v}]_{z=0} = 0. \tag{3.21}$$

Second there is the energy balance, which states that the heat flux exiting from the surface to the vapor must be equal to the heat flux entering from the bulk solid to the wall,

$$-k_{\mathrm{v}} [T_z]_{z=0} = \mathcal{H}_{\mathrm{w}} (T_{\mathrm{w}} - T_0). \tag{3.22}$$

Here, the internal heat transfer of the solid has been simply abstracted through the heat transfer coefficient $\mathcal{H}_{\mathrm{w}}$.

Boundary conditions: Liquid–vapor interface

The no-slip condition also applies to the liquid–vapor interface, but since this is not a stationary wall it instead manifests as a required continuity of tangential velocity

$$\left[(\boldsymbol{v} - \boldsymbol{v}_{\mathrm{l}}) \cdot \hat{\boldsymbol{t}}\right]_{z=h} = 0, \tag{3.23}$$

The relevant principle of mass conservation at the interface is found from Eq. (3.7),

$$\rho_{\mathrm{v}} [(\boldsymbol{v}_{\mathrm{i}} - \boldsymbol{v}) \cdot \hat{\boldsymbol{n}}]_{z=h} = j \tag{3.24}$$

which may also be written on the convenient form of Eq. (3.8). The stress balance at the interface yields the conditions

$$[j (\boldsymbol{v}_{\mathrm{l}} - \boldsymbol{v}) \cdot \hat{\boldsymbol{n}} - ([\mathcal{T} - \mathcal{T}_{\mathrm{l}}] \cdot \hat{\boldsymbol{n}}) \cdot \hat{\boldsymbol{n}}]_{z=h} = -\kappa\sigma, \tag{3.25}$$

$$\left[((\mathcal{T} - \mathcal{T}_{\mathrm{l}}) \cdot \hat{\boldsymbol{n}}) \cdot \hat{\boldsymbol{t}} - \nabla\sigma \cdot \hat{\boldsymbol{t}}\right]_{z=h} = 0, \tag{3.26}$$

for the normal and tangential stress components, respectively. The relevant components of the stress tensor ($\mathcal{T}$) are written out in Eqs. (3.11) and (3.12). Finally, conservation of energy demands that all the energy conducted into the interface from the vapor must be either spent on evaporation or conducted into the liquid bulk,

$$-k_{\mathrm{v}} [\nabla T \cdot \hat{\boldsymbol{n}}]_{z=h} = jL + \mathcal{H}_{\mathrm{l}} (T_{\mathrm{i}} - T_{\mathrm{s}}). \tag{3.27}$$

So far the governing equations and boundary conditions above follow the standard approach shown by Burelbach, Bankoff, and Davis [74] and Oron,

Davis, and Bankoff [73] for the case of liquid thin-films, with some subtle changes due to the liquid–vapor role-reversal. A simplifying aspect of the liquid thin-film case is that the outside bulk phase has much smaller values for density, viscosity and thermal conductivity, which makes the liquid–vapor interface essentially act like a free surface. This significantly simplifies the boundary conditions, and allows them to immediately arrive at the so called *one-sided* models.

In the present case of film boiling the outside bulk phase is the densest phase, and such immediate simplification is not possible. Specifically, the issue is the liquid-side stress tensor ($\mathcal{T}_\mathrm{l}$) in the interface stress balance of Eqs. (3.25) and (3.26), which may no longer be neglected. If we want to avoid having to solve a separate set of differential equations for the liquid phase, additional assumptions must be made regarding the flow and pressure in the liquid.

The first of these we call the *liquid pressure closure*. This is basically the assumption that the liquid pressure at a given position may be approximated by the hydrostatic pressure corresponding to that position. The liquid-side interface pressure is then

$$[p_\mathrm{l}]_{z=h} = -\rho_\mathrm{l} g(ax + bh). \tag{3.28}$$

The second and perhaps more controversial assumption we will call the *liquid shear closure* and is based on the following argument: The presence of the stationary liquid bulk acts as drag, slowing down the tangential interface velocity and therefore the overall vapor film velocity. Additionally, the strength of this drag effect should increase monotonically with the liquid viscosity (μ_l). It follows that the tangential interface velocity should approach zero in the limit $\mu_\mathrm{l} \to \infty$, and approach some maximum value in the limit $\mu_\mathrm{l} \to 0$. These limits are of course hypothetical, but serve to define the range of possible interface velocities in any given case. This is very useful because each extreme case may be solved for with relative ease. We then introduce a factor $\eta \in [0, 1]$ to denote where the actual value of the tangential interface velocity lies within this range of possible values. We formally write this principle as

$$\left[\boldsymbol{v} \cdot \hat{\boldsymbol{t}}\right]_{z=h} = \eta u_\mathrm{m}, \tag{3.29}$$

where u_m is the maximum tangential interface velocity found from the hypothetical case of $\mu_\mathrm{l} \to 0$. The factor η is left unknown for now, with the knowledge that it must obey the limits

$$\eta = \begin{cases} 0, & \mu_\mathrm{l} \to \infty \\ 1, & \mu_\mathrm{l} \to 0 \end{cases}, \tag{3.30}$$

and be a monotonic function of μ_l within this range. As discussed in Sec. 3.A, η will typically be quite small, in the range of 0.01–0.05.

3.2.5 Non-dimensionalization

A central aspect of the long-wave approximation is the thin-film *aspect-ratio* (ϵ), which is defined as the ratio of the film-thickness scale (h_0) and a longitudinal length scale (x_0),

$$\epsilon = \frac{h_0}{x_0}. \tag{3.31}$$

We may define the length scale x_0 in relation to the wavelengths (λ) of the film disturbances, $x_0 = \lambda/(2\pi)$. The scale h_0 is chosen based on which film-thickness we want to study the stability of. These two length scales are used to define dimensionless equivalents of the spatial parameters and the film thickness,

$$X = \frac{x}{x_0}, \qquad Z = \frac{z}{h_0}, \qquad H = \frac{h}{h_0}. \tag{3.32}$$

The unknown scale of the velocity's x-component is labeled u_0. Continuity then implies that the scale of the z-component must be ϵu_0 [73]. This allows us to define the dimensionless velocity components as

$$U = \frac{u}{u_0}, \qquad W = \frac{w}{\epsilon u_0}. \tag{3.33}$$

We define the time-scale from the longitudinal length-scale and velocity-scale, $t_0 = x_0/u_0$, so that the dimensionless time is

$$\tau = \frac{t}{t_0} \tag{3.34}$$

The pressure scale is set according to the viscous pressure-drop in a channel, $p_0 = \mu_\mathrm{v} u_0/(\epsilon h_0)$, which allows the definition of the dimensionless pressure and the dimensionless body-force potential,

$$P = \frac{p}{p_0}, \quad \Phi = \frac{\phi}{p_0} \tag{3.35}$$

The evaporation mass flux is scaled according to the quasi-equilibrium evaporation rate expected across a uniform and stationary vapor film, $j_0 = k_\mathrm{v}\Delta T_\mathrm{w}/(h_0 L)$, where L is the latent heat of vaporization. This defines a dimensionless evaporation mass flux as

$$J = \frac{j}{j_0} \tag{3.36}$$

The dimensionless temperature is defined as the normalized position on the interval between T_s and T_w,

$$\theta = \frac{T - T_\mathrm{s}}{\Delta T_\mathrm{w}}. \tag{3.37}$$

3.2.6 Dimensionless equations of film boiling

Based on h_0, u_0 and the case properties in Tab. 3.2 we may define a set of dimensionless numbers, as shown in Tab. 3.3. These may then be used to formulate dimensionless version of the equations in Sec. 3.2.4, which are shown below.

Governing equations

The dimensionless versions of the continuity, momentum and energy equations Eqs. (3.13) to (3.16) become

$$U_X + W_Z = 0, \tag{3.38}$$

$$\epsilon \mathrm{Re}\left(U_\tau + UU_X + WU_Z\right) = -\left(P_X + \Phi_X\right) + \left(\epsilon^2 U_{XX} + U_{ZZ}\right), \tag{3.39}$$

$$\epsilon^3 \mathrm{Re}\left(W_\tau + UW_X + WW_Z\right) = -\left(P_Z + \Phi_Z\right) + \epsilon^2\left(\epsilon^2 W_{XX} + W_{ZZ}\right), \tag{3.40}$$

$$\epsilon \mathrm{Re}\,\mathrm{Pr}\left(\theta_\tau + U\theta_X + W\theta_Z\right) = \epsilon^2\theta_{XX} + \theta_{ZZ}, \tag{3.41}$$

where Re is the Reynolds number and Pr is the vapor Prandtl number. The dimensionless body-force potential, Eq. (3.17), is

$$\Phi = \Phi_0 + G_\mathrm{v}\left(aX + \epsilon bZ\right) + \frac{\epsilon A}{H^3}, \tag{3.42}$$

where G_v is the vapor gravity number and A is the Hamaker number. The dimensionless equivalent of the evaporation model, Eq. (3.20), is

$$KJ = \theta_\mathrm{i}, \tag{3.43}$$

where K is the non-equilibrium number.

Boundary conditions: Wall

The dimensionless equivalents of Eqs. (3.21) and (3.22) are

$$[U]_{Z=0} = [W]_{Z=0} = 0, \tag{3.44}$$

$$-[\theta_Z]_{Z=0} = \mathrm{Bi}_\mathrm{w}\left(1 - \theta_0\right), \tag{3.45}$$

where Bi_w is the wall Biot number. The magnitude of its inverse represents the relative impact of solid surface cool-down due to the cold liquid on the other side of the vapor film. In other words, if $\mathrm{Bi}_\mathrm{w}^{-1} \to 0$ we have perfect surface temperature control ($\theta_0 = 1$ and thus $T_0 = T_\mathrm{w}$).

Table 3.3: Dimensionless numbers used in the film-boiling model.

Definition	Name
$\mathrm{Re} = \dfrac{\rho_\mathrm{v} u_0 h_0}{\mu_\mathrm{v}}$	Reynolds number
$E = \dfrac{k_\mathrm{v} \Delta T_\mathrm{w}}{\rho_\mathrm{v} u_0 h_0 L}$	Evaporation number
$\mathrm{Ca} = \dfrac{\mu_\mathrm{v} u_0}{\sigma_0}$	Capillary number
$K = \dfrac{\hat{K} k_\mathrm{v}}{h_0 L}$	Non-equilibrium number
$M = \dfrac{\Delta T_\mathrm{w} \gamma}{\mu_\mathrm{v} u_0}$	Marangoni number
$S = \dfrac{k_\mathrm{v} \Delta T_\mathrm{w}}{\mu_\mathrm{v} L}$	Vapor-thrust number
$A = \dfrac{\tilde{A}}{6\pi \mu_\mathrm{v} u_0 h_0^2}$	Hamaker number
$\mathrm{Pr} = \dfrac{\mu_\mathrm{v} c_{p\mathrm{v}}}{k_\mathrm{v}}$	Vapor Prandtl number
$\mathrm{Bi}_\mathrm{w} = \dfrac{\mathcal{H}_\mathrm{w} h_0}{k_\mathrm{v}}$	Wall Biot number
$\mathrm{Bi}_\mathrm{l} = \dfrac{\mathcal{H}_\mathrm{l} h_0}{k_\mathrm{v}}$	Liquid Biot number
$G_\mathrm{v} = \dfrac{\rho_\mathrm{v} g h_0^2}{\mu_\mathrm{v} u_0}$	Vapor gravity number
$G_\mathrm{l} = \dfrac{\rho_\mathrm{l} g h_0^2}{\mu_\mathrm{v} u_0}$	Liquid gravity number
$G = \dfrac{(\rho_\mathrm{l} - \rho_\mathrm{v}) g h_0^2}{\mu_\mathrm{v} u_0}$	Buoyant gravity number
$\Psi = \dfrac{\mu_\mathrm{v}}{\mu_\mathrm{l}}$	Viscosity ratio
$D = \dfrac{\rho_\mathrm{v}}{\rho_\mathrm{l}}$	Density ratio

Boundary conditions: Liquid–vapor interface

In dimensionless form the interface no-slip condition, Eq. (3.23), becomes

$$\left[U - U_{\mathrm{l}} + \epsilon^2 H_X \left(W - W_{\mathrm{l}}\right)\right]_{Z=H} = 0. \tag{3.46}$$

and the mass flux condition, Eq. (3.24), becomes

$$\epsilon \frac{\left[H_\tau + U H_X - W\right]_{Z=H}}{\sqrt{1+\epsilon^2 H_X^2}} = EJ, \tag{3.47}$$

where E is the evaporation number. Then, by using Eqs. (3.10), (3.19), (3.25) and (3.26) we find that the interfacial stress conditions, Eqs. (3.25) and (3.26), may be written as

$$\begin{aligned}
&\epsilon S E \left[1 - D\right] J^2 + \left[P - P_{\mathrm{l}}\right]_{Z=H} \\
&- \epsilon^2 \frac{2}{1+\epsilon^2 H_X^2} \left[U_X(\epsilon^2 H_X^2 - 1) - H_X \left(U_Z + \epsilon^2 W_X\right)\right]_{Z=H} \\
&+ \epsilon^2 \frac{2\Psi^{-1}}{1+\epsilon^2 H_X^2} \left[U_{\mathrm{l},X}(\epsilon^2 H_X^2 - 1) - H_X \left(U_{\mathrm{l},Z} + \epsilon^2 W_{\mathrm{l},X}\right)\right]_{Z=H} \\
&= -\frac{\epsilon^3}{\left(1+\epsilon^2 H_X^2\right)^{3/2}} H_{XX} \left(\mathrm{Ca}^{-1} - M\theta_{\mathrm{i}}\right),
\end{aligned} \tag{3.48}$$

and

$$\begin{aligned}
&\frac{1}{\sqrt{1+\epsilon^2 H_X^2}} \left[\left(U_Z + \epsilon^2 W_X\right)\left(1 - \epsilon^2 H_X^2\right) - 4\epsilon^2 U_X H_X\right]_{Z=H} \\
&- \frac{\Psi^{-1}}{\sqrt{1+\epsilon^2 H_X^2}} \left[\left(U_{\mathrm{l},Z} + \epsilon^2 W_{\mathrm{l},X}\right)\left(1 - \epsilon^2 H_X^2\right) - 4\epsilon^2 U_{\mathrm{l},X} H_X\right]_{Z=H} \\
&= -\epsilon M \theta_{\mathrm{i},X},
\end{aligned} \tag{3.49}$$

respectively. Here S is the vapor-thrust number, Ca is the capillary number, M is the (thermocapillary) Marangoni number, D is the density ratio and Ψ is the viscosity ratio. The energy balance in Eq. (3.27) reduces to

$$-\frac{\left[\theta_Z - \epsilon^2 \theta_X H_X\right]_{Z=H}}{\sqrt{1+\epsilon^2 H_X^2}} = \mathrm{Bi}_{\mathrm{l}} \theta_{\mathrm{i}} + J, \tag{3.50}$$

where Bi_{l} is the liquid Biot number. Finally, the liquid closures Eqs. (3.28) and (3.29) reduce to

$$\left[P_{\mathrm{l}}\right]_{Z=H} = -G_{\mathrm{l}} \left(aX + \epsilon b H\right), \tag{3.51}$$

and

$$\frac{\left[U + \epsilon^2 W H_X\right]_{Z=H}}{\sqrt{1 + \epsilon^2 H_X^2}} = \eta U_{\mathrm{m}}, \tag{3.52}$$

respectively, where G_{l} is the liquid gravity number and U_{m} is the dimensionless equivalent to the idealized tangential interface velocity defined in Eq. (3.29).

3.3 The general long-wave approximation

We now simplify the full dimensionless equations by performing the *long-wave approximation*. This involves assuming that the film thickness is generally much smaller than the length scale of any changes along the x-axis. Formally this means assuming that ϵ, as defined in Eq. (3.31), is very small,

$$\epsilon \ll 1. \tag{3.53}$$

This allows us to neglect all terms of order $\mathcal{O}\left(\epsilon^2\right)$ and higher, unless multiplied with some other very large number. We assume that surface tension effects are so strong compared to viscous effects that the following is true:

$$\begin{aligned} \epsilon^3 \mathrm{Ca}^{-1} &\sim \mathcal{O}\left(1\right), \\ \epsilon M &\sim \mathcal{O}\left(1\right). \end{aligned} \tag{3.54}$$

In the typical long-wave approach to thin-film flow modeling [73], it is also assumed that the Reynolds number is so small that terms of order $\mathcal{O}\left(\epsilon \mathrm{Re}\right)$ may also be neglected. This is often called the *lubrication approximation*. We will refrain from making this assumption at this stage, so that the result may also be valid for larger Reynolds numbers. We call this the *general long-wave approximation*.

3.3.1 Equations of long-wave film boiling

Given the assumptions of Eqs. (3.53) and (3.54) the full dimensionless equations of Sec. 3.2.6 are significantly simplified. In a few cases the equations are unaffected, but these are still repeated in the overview below for completeness.

Governing equations

The continuity, momentum and energy equations Eqs. (3.38) to (3.41) may now be written as

$$U_X + W_Z = 0, \tag{3.55}$$

$$\epsilon \mathrm{Re}\left(U_\tau + UU_X + WU_Z\right) = -\left(P + \Phi\right)_X + U_{ZZ}, \tag{3.56}$$

$$0 = -\left(P + \Phi\right)_Z, \tag{3.57}$$

$$\epsilon \mathrm{Re}\,\mathrm{Pr}\left(\theta_\tau + U\theta_X + W\theta_Z\right) = \theta_{ZZ}, \tag{3.58}$$

The dimensionless body-force potential and the evaporation mode, Eqs. (3.42) and (3.43), are still written as

$$\Phi = \Phi_0 + G_\mathrm{v}\left(aX + \epsilon bZ\right) + \frac{\epsilon A}{H^3}. \tag{3.59}$$

and

$$KJ = \theta_\mathrm{i}. \tag{3.60}$$

Boundary conditions: Wall

The boundary conditions of the wall, Eqs. (3.44) and (3.45), are unchanged:

$$[U]_{Z=0} = [W]_{Z=0} = 0, \tag{3.61}$$

$$-[\theta_Z]_{Z=0} = \mathrm{Bi_w}\left(1 - \theta_0\right). \tag{3.62}$$

Boundary conditions: Liquid–vapor interface

The interface boundary conditions Eqs. (3.46) and (3.47) simplify to

$$[U - U_\mathrm{l}]_{Z=H} = 0, \tag{3.63}$$

$$\epsilon\left[H_\tau + UH_X - W\right]_{Z=H} = EJ. \tag{3.64}$$

The stress balances Eqs. (3.48) and (3.49) simplify to

$$[P - P_\mathrm{l}]_{Z=H} = -\epsilon SE\left[1 - D\right]J^2 - \epsilon^3 \mathrm{Ca}^{-1} H_{XX}, \tag{3.65}$$

and

$$\left[U_Z - \Psi^{-1} U_{\mathrm{l},Z}\right]_{Z=H} = -\epsilon M(\theta_\mathrm{i})_X, \tag{3.66}$$

and the energy balance Eq. (3.67) simplifies to

$$-\left[\theta_Z\right]_{Z=H} = \mathrm{Bi_l}\theta_\mathrm{i} + J. \tag{3.67}$$

Finally, the liquid pressure closure Eq. (3.51) remains as

$$[P_\mathrm{l}]_{Z=H} = -G_\mathrm{l}\left(aX + \epsilon bH\right), \tag{3.68}$$

and the liquid shear closure Eq. (3.52) simplifies to

$$[U]_{Z=H} = \eta U_\mathrm{m}. \tag{3.69}$$

Comparison to previous models

In the $\epsilon\mathrm{Re} \to 0$ limit, these long-wave approximation equations have many similarities with the ones presented in Burelbach, Bankoff, and Davis [74, Eq. 5.5–5.10]. However, there are significant differences. Besides some sign changes, these differences all relate to the fact that the bulk phase outside the thin film is different. In Burelbach, Bankoff, and Davis [74], the normal-stress condition (here Eq. (3.65)) does not include a term for the pressure outside the thin film as it could conveniently be set constant and equal to zero. In the tangential-stress condition (here Eq. (3.66)), the bulk phase shear rate was set to zero, as the interface could be treated as a free surface. Neither simplification is possible in the present work, as the liquid and vapor have switched places. As explained previously, the liquid pressure- and shear closures, Eqs. (3.68) and (3.69), have to be assumed in order to enable a "one-sided" model like in Burelbach, Bankoff, and Davis [74].

3.3.2 Derived relations

Regardless of whether or not we choose to neglect the inertial $\epsilon\mathrm{Re}$-terms, certain general results may be derived at this stage. These are shown below.

Driving force of flow

Note that according to Eq. (3.57) the *reduced pressure*, defined as

$$\overline{P} = P + \Phi, \tag{3.70}$$

is independent of Z. This means that for a given X it may be evaluated at any Z. By evaluating it at $Z = H$, inserting the expression for the body-force potential in Eq. (3.59), and applying the normal-stress balance Eq. (3.65) with the liquid pressure closure Eq. (3.68), we find that the

reduced pressure is

$$\begin{aligned}\overline{P}(X) &= \left[\overline{P}(X,Z)\right]_{Z=H}, \\ &= [P]_{Z=H} + [\Phi]_{Z=H}, \\ &= \Phi_0 - G\left(aX + \epsilon bH\right) - \epsilon^3 \mathrm{Ca}^{-1} H_{XX} - \epsilon SE\left[1-D\right]J^2 + \frac{\epsilon A}{H^3}.\end{aligned} \tag{3.71}$$

The right-hand side of Eq. (3.56) requires the X-derivative of $\overline{P}$, which may be interpreted as the driving-force for lateral flow. By differentiating Eq. (3.71) we find that

$$\overline{P}_X(X) = -\underbrace{G\left(a + \epsilon b H_X\right)}_{\text{gravity}} - \underbrace{\epsilon^3 \mathrm{Ca}^{-1} H_{XXX}}_{\text{capillary}} - \underbrace{\epsilon SE\left[1-D\right](J^2)_X}_{\text{vapor thrust}} - \underbrace{3\frac{\epsilon A}{H^4}H_X}_{\text{vdW}}, \tag{3.72}$$

where we have labeled the four physical contributions.

Mass conservation

We may integrate Eq. (3.55) across the film while applying Leibniz's integral rule and the boundary conditions Eqs. (3.61) and (3.64) to find the general mass conservation PDE,

$$\epsilon\left[H_\tau + \left(\int_0^H U \mathrm{d}Z\right)_X\right] = EJ. \tag{3.73}$$

Eq. (3.73) is exactly what we need: a partial differential equation (PDE) for the film thickness $H(X,\tau)$. However, it requires two additional pieces: The velocity profile U and the evaporation rate J, both as functions of H. In general these functions must be found by solving the X-momentum equation (Eq. (3.56)) and the energy equation (Eq. (3.58)). The way to proceed depends on the assumed magnitude of $\epsilon\mathrm{Re}$:

- $\epsilon\mathrm{Re} \ll 1$ (low-Re film boiling): This allows further simplification of the momentum and energy equations, and leads to a single PDE for $H(X,\tau)$. This is covered in Sec. 3.4.
- $\epsilon\mathrm{Re} \sim \mathcal{O}(1)$ (moderate-Re film boiling): This significantly complicates the procedure, and leads to a set of two coupled PDEs. This is covered in Sec. 3.5.

As we shall see, the second approach is necessary to correctly predict the stability of non-horizontal film boiling.

3.4 Low-Re film boiling

We now make the assumption that the Reynolds number is small enough that the following is true:

$$\epsilon \mathrm{Re} \ll 1. \tag{3.74}$$

Such an assumption allows for major simplifications to the x-momentum equation and the energy equation, Eqs. (3.56) and (3.58).

3.4.1 Velocity profile and mass flow rate

Given the assumption of Eq. (3.74) we may neglect the inertial terms of the x-momentum equation, Eq. (3.56), and it simply reduces to

$$U_{ZZ} = \overline{P}_X. \tag{3.75}$$

If we integrate Eq. (3.75) twice across the film and apply the no-slip wall condition Eq. (3.61), we find that the velocity profile is

$$U = \frac{1}{2}\overline{P}_X \left(Z^2 - HZ\right) + \frac{Z}{H}\left[U\right]_{Z=H}. \tag{3.76}$$

$$= \frac{1}{2}\overline{P}_X \left(Z^2 - 2HZ\right) + Z\left[U_Z\right]_{Z=H}, \tag{3.77}$$

Here we have written it on two forms, by either collecting $[U]_{Z=H}$ or $[U_Z]_{Z=H}$ in the final term. Setting the final term of either Eq. (3.76) or Eq. (3.77) to zero corresponds to the commonly used assumptions of zero velocity and zero shear stress, respectively. Choosing either extreme would avoid the necessity of a liquid-shear closure like Eq. (3.69), but in the present generalization they simply correspond to the extremes of $\eta = 0$ and $\eta = 1$.

How do we apply the liquid shear closure in practice? Eq. (3.69) expresses the actual interface velocity as a fraction of the hypothetical interface velocity (U_m) that would follow in the case of vanishing liquid drag/viscosity, i.e. in the limit of $\Psi \to \infty$. In this limit Eq. (3.66) tells us that

$$\lim_{\Psi\to\infty}\left[U_Z\right]_{Z=H} = -\epsilon M(\theta_\mathrm{i})_X, \tag{3.78}$$

By combining Eq. (3.78) with Eq. (3.77) we find that the velocity profile in this limit is

$$\lim_{\Psi\to\infty}\left[U\right] = \frac{1}{2}\overline{P}_X \left(Z^2 - 2HZ\right) - \epsilon M(\theta_\mathrm{i})_X Z \tag{3.79}$$

The quantity U_m is by definition the tangential interface velocity corresponding to this case, which means that

$$U_\mathrm{m} = -\frac{1}{2}\overline{P}_X H^2 - \epsilon M(\theta_\mathrm{i})_X H \tag{3.80}$$

By combining Eq. (3.80) with the the shear-closure expression in Eq. (3.69) we find the generalized interface velocity, which may then be inserted into Eq. (3.76) to yield the velocity profile,

$$U = -\frac{1}{2}\overline{P}_X \left[(1+\eta)HZ - Z^2\right] - \epsilon\eta M(\theta_\mathrm{i})_X Z \tag{3.81}$$

Note how $\eta = 0$ leads right back to Eq. (3.76) with $[U]_{Z=H} = 0$, and how $\eta = 1$ leads right back to Eq. (3.77) with the normal derivative given by Eq. (3.78).

With Eq. (3.81) we are now in a position to calculate the total vapor-film flow rate required in the vapor-film PDE (Eq. (3.73)),

$$\int_0^H U \mathrm{d}Z = -\frac{\xi}{12}\overline{P}_X H^3 - \frac{1}{2}\epsilon\eta M H^2 (\theta_\mathrm{i})_X \tag{3.82}$$

with the short-hand

$$\xi = 1 + 3\eta. \tag{3.83}$$

3.4.2 Temperature profile and evaporation rate

With the approximation of Eq. (3.74), assuming that $\mathrm{Pr} \sim \mathcal{O}(1)$ or smaller, Eq. (3.58) reduces to

$$\theta_{ZZ} = 0. \tag{3.84}$$

This means that the temperature profile across the vapor film must be linear,

$$\theta(Z) = \theta_0 - \left(\frac{\theta_0 - \theta_\mathrm{i}}{H}\right) Z. \tag{3.85}$$

Such a profile satisfies the energy-balance boundary conditions Eqs. (3.62) and (3.67) and the evaporation relation Eq. (3.60) if and only if the evaporation rate is

$$J = \frac{1}{K + \left(\mathrm{Bi}_\mathrm{w}^{-1} + H\right) C}, \tag{3.86}$$

the wall surface temperature is,

$$\theta_0 = \frac{K + HC}{K + \left(\mathrm{Bi}_\mathrm{w}^{-1} + H\right) C}, \tag{3.87}$$

and the interface temperatures is

$$\theta_\mathrm{i} = \frac{K}{K + \left(\mathrm{Bi}_\mathrm{w}^{-1} + H\right) C}. \tag{3.88}$$

Here we have introduced the new constant C, which is defined as

$$C = 1 + \mathrm{Bi}_\mathrm{l} K = 1 + \frac{\mathcal{H}_\mathrm{l} \hat{K}}{L}. \tag{3.89}$$

We see that setting either $\mathrm{Bi}_\mathrm{l} = 0$ (no liquid conductivity) or $K = 0$ (saturated interface), both of which would imply no liquid heat transport, leads to $C = 1$. In other words, any departure of C from unity represents the relative effect of heat transported from the interface to the liquid bulk. Note that the value of C is independent of the film-thickness scale. While a thinner film would lead to more interface superheat, and thus a potentially higher liquid heat transport, it would also lead to a larger heat transport through the vapor. In the end, the relative impact of liquid heat transport is left unchanged. In realistic cases the actual magnitude of C is very close to unity. Thus, the heat lost into the saturated liquid is negligible regardless of the vapor film thickness.

By inspecting Eqs. (3.87) and (3.88) we see that any combination of parameters satisfy

$$0 < \theta_\mathrm{i} < \theta_0 < 1, \tag{3.90}$$

which is equivalent to stating that $[T_\mathrm{w} > T_0 > T_\mathrm{i} > T_\mathrm{s}]$. In other words, all temperatures stay within the range set by the outer boundary conditions in the liquid bulk (T_s) and the solid bulk (T_w), cf. Fig. 3.1.

We see that as the film thickness goes to zero ($H \to 0$) the wall surface and interface temperatures approach the same value, somewhere within this range. In this limit, we see from Eq. (3.86) that the evaporation rate is prevented from diverging due to a combination of finite wall conductivity ($\mathrm{Bi}_\mathrm{w}^{-1} > 0$) and non-equilibrium evaporation effects ($K > 0$).

Note that since H is dependent on the lateral position X, so are all three quantities J, θ_0 and θ_i. The evaporation rate J is required on the right-hand side of Eq. (3.73), while the X-derivatives of both J and θ_i

are required on the left-hand side through Eq. (3.72) and Eq. (3.82). The interface temperature's X-derivative may be written as

$$(\theta_\mathrm{i})_X = -CK\frac{F^2(H)H_X}{H^2} \tag{3.91}$$

with the short-hand $F(H)$ defined as

$$F(H) = \frac{H}{K + C\left(\mathrm{Bi}_\mathrm{w}^{-1} + H\right)}. \tag{3.92}$$

Separating $F(H)$ is convenient because it is very close to unity in most cases. According to the evaporation model in Eq. (3.60) the X-derivative of the evaporation rate is simply $J_X = (\theta_\mathrm{i})_X/K$.

From Eq. (3.91) it is apparent that a decrease in film thickness comes with a corresponding increase in interface temperature. As we will show, this may have important consequences through the thermocapillary effect.

3.4.3 PDE for the film-thickness function

We are now in a position to obtain a partial differential equation for the film thickness H. We start with the mass conservation PDE Eq. (3.73) and insert the flow rate from Eq. (3.82) with the driving force from Eq. (3.72). By then using the evaporation model Eq. (3.60) and the tangential interface temperature gradient from Eq. (3.91), we finally arrive at the following equation:

$$\begin{aligned}\left(\frac{\epsilon}{E}\right)H_\tau + \underbrace{\frac{\epsilon\xi G}{12E}\left[H^3\left(a+\epsilon bH_X\right)\right]_X}_{\text{gravity}} + \underbrace{\frac{\xi\epsilon^4\mathrm{Ca}^{-1}}{12E}\left[H^3H_{XXX}\right]_X}_{\text{capillary}} \\ \underbrace{-\frac{\xi\epsilon^2SC\left(1-D\right)}{6}\left[F^3(H)H_X\right]_X}_{\text{vapor thrust}} + \underbrace{\frac{\xi\epsilon^2A}{4E}\left[\frac{H_X}{H}\right]_X}_{\text{van der Waals}} \\ \underbrace{+\frac{\epsilon^2\eta MCK}{2E}\left[F^2(H)H_X\right]_X}_{\text{thermocapillary}} = \underbrace{\frac{F(H)}{H}}_{\text{evaporation}}.\end{aligned} \tag{3.93}$$

The factor (ϵ/E) in front of the time-derivative simply constitutes a re-scaling from the lateral-flow time-scale t_0 to an evaporative time-scale. Besides this term, there is in fact no dependence on the unknown velocity scale u_0, since the factors G/E, Ca^{-1}/E, S, A/E and M/E are all independent of it. Note also that the power of the ϵ-factors in the gradient terms

correspond exactly to the order of X-derivatives of H present, and thus they may simply be seen as a re-scaling of x from x_0 to h_0.

Eq. (3.93) is a scalar highly nonlinear fourth-order differential equation for the film thickness $H(X,\tau)$. It follows the common structure of a conservation equation with a flux-term ($\mathcal{F}$) and a source term ($\mathcal{S}$),

$$H_\tau + [\mathcal{F}(H)]_X = \mathcal{S}(H) \tag{3.94}$$

but with a very complicated (nonlinear and high-order) flux-term.

The behavior of this class of equations has been reviewed by authors such as Myers [75]. While Eq. (3.93) could in principle be solved numerically in its full nonlinear form, the fourth-order capillary term and the source term would require an unreasonably small time-step when using a straightforward explicit method. In order to get around this, implicit methods may be used [85], though this comes with a different set of challenges due to the strong non-linearity.

In the following analysis we will not solve Eq. (3.93) numerically, but rather find some simplified solutions (base states), and then investigate under which conditions they are stable.

3.4.4 Uniform non-steady solution

The first type of base state is a solution that is uniform, in the sense that no property varies along X. From the velocity profile in Eq. (3.81) we see that such uniformity implies zero lateral velocity throughout the vapor film. Due to continuity, this means that the vapor is completely stationary ($U = W = 0$). For non-zero evaporation rates, such solutions must necessarily give a time-dependent film thickness H, since the film must grow to accommodate the added vapor. Since there is no variation along X the lateral length scale x_0 is ill-defined, which also causes the time scale t_0 to be ill-defined. We switch to the *evaporative time scale* by defining a new dimensionless time $\tilde{\tau}$,

$$\tilde{\tau} = \frac{t}{t_\mathrm{e}} \tag{3.95}$$

where

$$t_\mathrm{e} = \frac{h_0}{(j_0/\rho_\mathrm{v})} = \frac{\rho_\mathrm{v} h_0^2 L}{k_\mathrm{v} \Delta T_\mathrm{w}}. \tag{3.96}$$

The ratio between the new time scale and the old one is then $t_\mathrm{e}/t_0 = \epsilon/E$, and thus, the change gets rid of the factor in front of H_τ in Eq. (3.93).

Then, with all X-derivatives set to zero, Eq. (3.93) reduces simply to

$$\frac{\partial \bar{H}}{\partial \tilde{\tau}} = \frac{1}{K + C\left(\mathrm{Bi}_{\mathrm{w}}^{-1} + \bar{H}\right)}, \tag{3.97}$$

where we have labeled these special solutions as $\bar{H}(\tilde{\tau})$. If we define the scale h_0 such that the initial condition is $H(0) = 1$, the analytical solution to Eq. (3.97) is

$$\bar{H}(\tilde{\tau}) = \frac{\sqrt{2C\tilde{\tau} + \left(\mathrm{Bi}_{\mathrm{w}}^{-1}C + K + C\right)^2} - \left(\mathrm{Bi}_{\mathrm{w}}^{-1}C + K\right)}{C}. \tag{3.98}$$

The initial growth rate of this solution is reduced by all three non-ideal effects: non-equilibrium ($K > 0$), finite solid heat transfer ($\mathrm{Bi}_{\mathrm{w}}^{-1} > 0$), and heat loss into liquid ($C > 1$). If all these effects are negligible, we get the upper-bound ideal solution $\bar{H}(\tilde{\tau}) = \sqrt{1 + 2\tilde{\tau}}$. In any case the solution will grow monotonically, as expected with evaporation.

3.4.5 Stability of uniform solution

We now seek to understand under which conditions the uniform time-dependent solution in Eq. (3.98) is stable. In other words, when does it remain uniform as opposed to being sensitive to small spatial disturbances. We formally do this by investigating the time-evolution of a state that is the sum of the uniform base state from Eq. (3.98) and a small perturbation,

$$H(X, \tilde{\tau}) = \bar{H}(\tilde{\tau}) + c\hat{H}(X, \tilde{\tau}). \tag{3.99}$$

Here $\hat{H} \sim \mathcal{O}(1)$, and c is the smallness parameter of the perturbation. If we insert Eq. (3.99) into the PDE Eq. (3.93), and collect the terms that are first-order in c, we get a linear PDE for $\hat{H}(X, \tilde{\tau})$. This may be written as

$$\frac{\partial}{\partial \tilde{\tau}}\hat{H} + \mathcal{L}\left[\hat{H}\right] = 0 \tag{3.100}$$

where $\mathcal{L}$ is the linear spatial differential operator with time-dependent coefficients,

$$\begin{aligned}\mathcal{L} = &\left[\frac{C\bar{F}^2}{\bar{H}^2}\right] + \left[\frac{\xi Ga\bar{H}^2}{4E}\right]\epsilon\frac{\partial}{\partial X} + \left[\frac{\xi \mathrm{Ca}^{-1}\bar{H}^3}{12E}\right]\epsilon^4\frac{\partial}{\partial X^4} \\ &+ \left[\frac{Gb\xi\bar{H}^3}{12E} + \frac{A\xi}{4E\bar{H}} - \frac{CS\xi(1-D)\bar{F}^3}{6} + \frac{CKM\eta\bar{F}^2}{2E}\right]\epsilon^2\frac{\partial}{\partial X^2}.\end{aligned} \tag{3.101}$$

Here $\bar{F}$ is simply $F(\bar{H})$, and thus also time-dependent through $\bar{H}(\tilde{\tau})$. A linear PDE for $\hat{H}(X,\tilde{\tau})$ with time-dependent coefficients opens up for normal-mode analysis in the X-dimension, which we shall now perform.

Consider a small initial spatial disturbance with an arbitrary shape given by $\hat{H}_0(X)$. If this is a localized disturbance, its shape may be represented by a Fourier integral over spatial normal-modes, each with its dimensionless and real wavenumber k,

$$\hat{H}_0(X) = \frac{1}{2\pi}\int_{-\infty}^{\infty} f(k)\mathrm{e}^{ikX}\mathrm{d}k \tag{3.102}$$

where $f(k)$ is the Fourier transform of $\hat{H}_0(X)$,

$$f(k) = \int_{-\infty}^{\infty} \hat{H}_0(X)\mathrm{e}^{-ikX}\mathrm{d}X. \tag{3.103}$$

We now suggest a full solution for the perturbation $\hat{H}(X,\tilde{\tau})$ of the form

$$\hat{H}(X,\tilde{\tau}) = \frac{1}{2\pi}\int_{-\infty}^{\infty} \tilde{H}_k(\tilde{\tau})f(k)\mathrm{e}^{ikX}\mathrm{d}k, \tag{3.104}$$

where each mode has an unknown complex time-dependent amplitude $\tilde{H}_k(\tilde{\tau})$. If they initially are $\tilde{H}_k(0) = 1$ for all k, Eq. (3.104) satisfies the initial condition $\hat{H}(X,0) = \hat{H}_0(X)$. The solution in Eq. (3.104) must also satisfy the governing equation, Eq. (3.100), and this sets constraints on the time-evolution of the amplitudes. A crucial point used in the following is that the functions $\exp(ikX)$ are eigenfunctions of any linear spatial differential operator. For the case of our operator, this is written as

$$\mathcal{L}\left[\mathrm{e}^{ikX}\right] = \ell_k(\tilde{\tau})\mathrm{e}^{ikX}, \tag{3.105}$$

where $\ell_k(\tilde{\tau})$ are the complex time-dependent eigenvalues. Given this, if we insert Eq. (3.104) into the governing equation Eq. (3.100) we get

$$\int_{-\infty}^{\infty} f(k)\left[\frac{\partial}{\partial\tilde{\tau}}\tilde{H}_k(\tilde{\tau}) + \ell(\tilde{\tau},k)\tilde{H}_k(\tilde{\tau})\right]\mathrm{e}^{ikX}\mathrm{d}k = 0. \tag{3.106}$$

Due to the orthogonality of the functions $\exp(ikX)$ it is not only sufficient but also necessary that the square bracket of Eq. (3.106) is zero individually for each value of k. Thus, we may treat each mode separately, and solve the equation

$$\frac{\partial}{\partial\tilde{\tau}}\tilde{H}_k(\tilde{\tau}) + \ell_k(\tilde{\tau})\tilde{H}_k(\tilde{\tau}) = 0, \tag{3.107}$$

for all k. Eq. (3.107) is an ordinary differential equation for the mode amplitudes $\tilde{H}_k(\tilde{\tau})$. If all amplitudes decay in time, the system is stable. If at least one mode grows, the system is unstable. Note that this analysis is independent of the Fourier transforms $f(k)$, and thus the conclusion on stability is unaffected by the shape of the real initial disturbance, $\hat{H}_0(X)$, as long as it is small.

The eigenvalues $\ell_k(\tilde{\tau})$ may readily be found by evaluating the left-hand side of Eq. (3.105) with the operator in Eq. (3.101). This allows us to write Eq. (3.107) as

$$\begin{aligned}\frac{\frac{\partial}{\partial\tilde{\tau}}\tilde{H}_k(\tilde{\tau})}{\tilde{H}_k(\tilde{\tau})} = &-\left[\frac{C\bar{F}^2}{\bar{H}^2}\right] - \left[i\frac{\xi Ga\bar{H}^2}{4E}\right](\epsilon k) - \left[\frac{\xi \mathrm{Ca}^{-1}\bar{H}^3}{12E}\right](\epsilon k)^4 \\ &+ \left[\frac{Gb\xi\bar{H}^3}{12E} + \frac{A\xi}{4E\bar{H}} - \frac{CS\xi(1-D)\bar{F}^3}{6} + \frac{CKM\eta\bar{F}^2}{2E}\right](\epsilon k)^2.\end{aligned} \tag{3.108}$$

The terms in Eq. (3.108) are each proportional to some power of (ϵk). Since k is the dimensionless wavenumber with the scale x_0, (ϵk) is simply the dimensionless wavenumber scaled with the film-thickness h_0.

The effect of the time-evolution of the mode amplitude $\tilde{H}_k(\tilde{\tau})$ is seen when inserting it into Eq. (3.104). Since it is a complex number, a time-dependent magnitude gives growth or decay of the mode, and a time-dependent phase gives traveling wave behavior. We see that in the case of a horizontal plane ($a = 0$), $\tilde{H}_k(\tilde{\tau})$ remains real and there are no traveling waves.

We now turn to the question of stability. The system is stable if the magnitude of $\tilde{H}_k(\tilde{\tau})$, which obeys Eq. (3.108), decays for all wavenumbers. The right-hand side of Eq. (3.108) is time-dependent due to $\bar{F}$ and $\bar{H}$ being time-dependent. However, we may reduce the problem to only evaluating it at the initial time when $\bar{H} = 1$, and inspect its dependence on film-thickness scale h_0. If the system is initially stable, but later grows into an unstable state, this new situation may be analyzed as a initial stability problem by simply changing h_0 to the new film thickness.

At the initial time, Eq. (3.108) reduces to

$$\left[\frac{\frac{\partial}{\partial\tilde{\tau}}\tilde{H}_k(\tilde{\tau})}{\tilde{H}_k(\tilde{\tau})}\right]_{\tilde{\tau}=0} = -\underbrace{\left[CF_0^2\right]}_{\text{evap.}} - \underbrace{\left[i\frac{\xi Ga}{4E}\right](\epsilon k)}_{\text{gravity}} - \underbrace{\left[\frac{\xi \mathrm{Ca}^{-1}}{12E}\right](\epsilon k)^4}_{\text{capillary}} + \underbrace{\left[\frac{Gb\xi}{12E}\right](\epsilon k)^2}_{\text{gravity}} - \underbrace{\left[\frac{CS\xi(1-D)F_0^3}{6}\right](\epsilon k)^2}_{\text{vapor thrust}} + \underbrace{\left[\frac{CK\eta MF_0^2}{2E}\right](\epsilon k)^2}_{\text{thermocapillary}} + \underbrace{\left[\frac{A\xi}{4E}\right](\epsilon k)^2}_{\text{van der Waals}}, \tag{3.109}$$

where F_0 is simply F from Eq. (3.92) evaluated at the initial state $\bar{H} = 1$,

$$F_0 = \frac{1}{K + C\left(1 + \mathrm{Bi}_{\mathrm{w}}^{-1}\right)}. \tag{3.110}$$

Regardless of the parameters it is always the case that $F_0 \in [0, 1]$. It approaches zero at very small film thicknesses according to $F_0 \sim h_0$, but approaches unity asymptotically as the film grows. For most relevant fluids and thicknesses it is quite accurate to say that $F_0 \approx 1$.

In addition to F_0, the effect of film-thickness scale on the terms of the stability analysis in Eq. (3.109) enters through the dimensionless numbers $G \propto h_0^2$, $E \propto h_0^{-1}$, $K \propto h_0^{-1}$, $A \propto h_0^{-2}$. Once again, none of the terms in Eq. (3.109) are dependent on the unknown velocity scale u_0.

Stability of a horizontal film is determined by the real part of Eq. (3.109). A positive real part implies instability (growing disturbances) and a negative real part implies stability (decaying disturbances). Note the following observations from Eq. (3.109):

- Very long waves ($k \to 0$) are unconditionally stable due to the evaporation term.
- Very short waves ($k \to \infty$) are unconditionally stable due to the capillary term.
- In between these two extremes, the stability of intermediate waves is dependent on the balance between the k^2-terms, some of which are stabilizing and some of which are destabilizing. The magnitudes of these terms are dependent on both case properties and the film thickness scale h_0:

– **Gravity term**: Destabilizing in the cases where the liquid is on top of the solid surface ($b > 0$). Magnitude increases with film thickness according to h_0^3.

$$\frac{Gb\xi}{12E}$$

– **van der Waals term**: Destabilizing in all cases. Magnitude decreases with film thickness according to h_0^{-1}.

$$\frac{A\xi}{4E}$$

– **Thermocapillary term**: Destabilizing in all cases. Magnitude is independent of film thickness in the regime where $F_0 \sim 1$. For very thin films, magnitude increases with film thickness according to h_0^2 through the influence of F_0.

$$\frac{CK\eta MF_0^2}{2E}$$

– **Vapor-thrust term**: Stabilizing in all cases. Magnitude is independent of film thickness in the regime where $F_0 \sim 1$. For very thin films, magnitude increases with film thickness according to h_0^3 through the influence of F_0.

$$-\frac{CS\xi(1-D)F_0^3}{6}$$

Thus, all k^2-terms are destabilizing except for the vapor-thrust term. This is in contrast to the case of an evaporating liquid film, where also the vapor thrust effect is destabilizing [73, 74].

To get an understanding of the relative importance of these four k^2-terms, we may plot their magnitude as a function of h_0. We consider the case of water boiling on top of a horizontal ($a = 0$ and $b = 1$) surface with a superheat of $\Delta T_\mathrm{w} = 200\,\mathrm{K}$. The wall Biot number ($\mathrm{Bi_w}$) is set according to a copper solid that is temperature-controlled at a depth of 1 mm. All vapor properties are evaluated at the average film temperature ($T = T_\mathrm{s} + \Delta T_\mathrm{w}/2$). The parameter η is estimated according to the model described in Sec. 3.A, the liquid heat transfer is neglected ($C \approx 1$), and the evaporation coefficient (α) is set to 0.85.

Fig. 3.2 shows the result of plotting the magnitude of the four k^2-terms as a function of film thickness scale (h_0) in the case described above. Based on this plot, we observe that there seems to be three distinct film-thickness regimes. These are:

- **The vdW regime**: For films of thickness less than 100 nm, the destabilizing influence of the van der Waals term dominates.
- **The gravity regime**: For films of thickness more than 10 µm, the destabilizing influence of the gravity term dominates.
- **Intermediate regime**: For films of thickness in the range of 0.1 µm to 10 µm, stability appears to be decided by a remarkably balanced struggle between the stabilizing vapor-thrust term and the destabilizing thermocapillary term. The outcome of the struggle depends on both fluid parameters and wall superheat ΔT_w.

The results of this stability analysis will be an important part of Sec. 3.6. We will find that the particular value of ΔT_w that gives an even balance in the intermediate regime is a remarkably good predictor for the Leidenfrost temperature of the fluid.

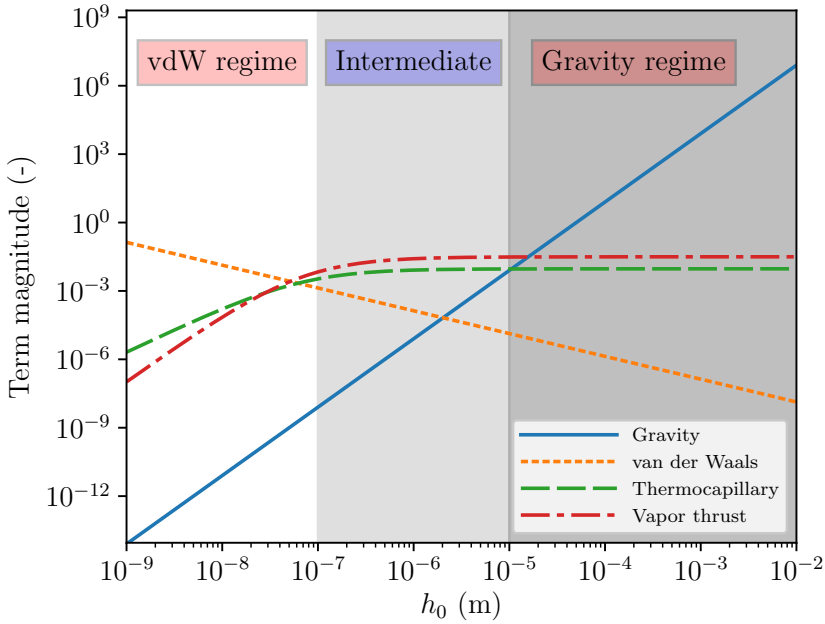

Figure 3.2: Magnitude of the k^2-terms (brackets in front of $(\epsilon k)^2$ in Eq. (3.109)) as a function of film-thickness scale h_0. Other parameters are set according to the case of water film-boiling on a horizontal surface with $\Delta T_w = 200$ K. The domain is divided into three regimes: the van der Waals regime (very thin films), the gravity regime (thick films), and the intermediate regime where the vapor-thrust and thermocapillary effects compete for dominance. In this particular example the vapor-thrust term is the strongest, but this depends on parameters such as ΔT_w.

3.4.6 Steady non-uniform solution

The second type of base state is the steady (time-independent) solution. For nonzero evaporation rates such solutions must necessarily be asymmetric (non-uniform), since the added vapor must escape along either the positive or the negative X-direction. We make two assumptions in order to find approximate solutions to such steady states:

- The film is very smooth: This is represented by a value of ϵ that is much smaller than previously assumed, so that $\epsilon G \ll 1$, $\epsilon A \ll 1$, $\epsilon S \ll 1$, $\epsilon M \ll 1$ and $\epsilon^3 \mathrm{Ca}^{-1} \ll 1$. Note that the last two imply that Eq. (3.54) is no longer true in this case.
- The film is so thick that the evaporation is very weak: This is represented by a value of E that is so small that $\epsilon/E \sim \mathcal{O}(1)$.

When we apply these two assumptions to Eq. (3.93) and retain only the terms that are $\mathcal{O}(1)$, the result is

$$\frac{\epsilon \xi a G}{12E} \left[\bar{H}^3\right]_X = \frac{F(\bar{H})}{\bar{H}}. \tag{3.111}$$

where we have labeled these special solutions as $\bar{H}(X)$. If we then also neglect certain non-ideal effects so that $F(H) \to 1$, we get a relatively simple ordinary differential equation (ODE),

$$\frac{\mathrm{d}\bar{H}}{\mathrm{d}X} = \frac{4E}{\epsilon \xi a G} \frac{1}{\bar{H}^3}. \tag{3.112}$$

With an assumed boundary condition of $\bar{H} = 0$ at the leading edge $X = 0$, Eq. (3.112) may be integrated to find the explicit expression

$$\bar{H}(X) = \left(\frac{16E}{\xi G a} \frac{X}{\epsilon}\right)^{1/4}. \tag{3.113}$$

The corresponding dimensional form is

$$\bar{h}(x) = \left(\frac{16 \mu_\mathrm{v} k_\mathrm{v} \Delta T_\mathrm{w}}{\xi a \rho_\mathrm{v} \Delta\rho g L} x\right)^{1/4}, \tag{3.114}$$

where $\Delta\rho = \rho_\mathrm{l} - \rho_\mathrm{v}$. We see that these steady solutions are only possible in non-horizontal cases, as they diverge in the horizontal ($a \to 0$) limit.

As opposed to the uniform solutions in Sec. 3.4.4, these solution have a net lateral flow of vapor, essentially directed and driven by buoyancy.

For a steady solution such as Eq. (3.114), the rate of vapor flowing out laterally at position x must be balanced by the total rate of vapor entering by evaporation from the leading edge to the position x. Formally, this means that the following must be satisfied at all positions x:

$$\int_0^h \rho_\mathrm{v} u(x,z)\mathrm{d}z = \int_0^x j(x')\mathrm{d}x'. \tag{3.115}$$

Under the approximations used in this section, the dimensionless evaporation rate is simply $J = 1/H$, which means that the dimensional evaporation rate is $j = k_\mathrm{v}\Delta T_\mathrm{w}/(L\bar{h})$. According to Eq. (3.115) the average velocity at position x is then

$$\begin{aligned}\overline{u}(x) &\equiv \frac{1}{\bar{h}(x)}\int_0^h u(x,z)\mathrm{d}z \\ &= \frac{1}{\rho_\mathrm{v}\bar{h}(x)}\int_0^x \frac{k_\mathrm{v}\Delta T_\mathrm{w}}{L\bar{h}(x')}\mathrm{d}x' \\ &= \frac{k_\mathrm{v}\Delta T_\mathrm{w}}{L\rho_\mathrm{v}\bar{h}(x)}\int_0^x \frac{1}{\bar{h}(x')}\mathrm{d}x'\end{aligned} \tag{3.116}$$

The integral above may be evaluated by inserting Eq. (3.114), which leads to the result

$$\begin{aligned}\overline{u}(x) &= \frac{4}{3}\frac{k_\mathrm{v}\Delta T_\mathrm{w}}{L\rho_\mathrm{v}}\left(\frac{16\mu_\mathrm{v}k_\mathrm{v}\Delta T_\mathrm{w}}{\xi a\rho_\mathrm{v}\Delta\rho g L}\right)^{-1/2} x^{1/2} \\ &= \frac{a\xi\Delta\rho g}{12\mu_\mathrm{v}}\bar{h}^2(x)\end{aligned} \tag{3.117}$$

In the last line of Eq. (3.117) it may seem counterintuitive that a larger film thickness should cause a higher velocity, since one would think that causes weaker evaporation and a higher cross-section for the vapor to escape through. This is explained by the fact that $\bar{h}$ in Eq. (3.117) is not any general film thickness, but specifically the solution in Eq. (3.114). Because of this, a higher $\bar{h}$ implies a much larger x and thus a much higher total evaporation rate from 0 to x that is not compensated for by the slowly growing cross section. As we see from the first line of Eq. (3.117), the velocity in fact grows with x according to $\overline{u} \propto \sqrt{x}$.

The model in Eq. (3.93) was derived under the assumption that the Reynolds number was so small that the terms $\mathcal{O}(\epsilon\mathrm{Re})$ could be neglected. It is thus interesting to calculate the Reynolds number corresponding to the simplified steady state derived from it. We define this Reynolds number by

using $\bar{h}$ and $\overline{u}$ from Eq. (3.114) and Eq. (3.117), and find that

$$\overline{\mathrm{Re}} \equiv \frac{\rho_\mathrm{v}\overline{u}\bar{h}}{\mu_\mathrm{v}} = a\xi\frac{\rho_\mathrm{v}\Delta\rho g}{12\mu_\mathrm{v}^2}\bar{h}^3 \propto x^{3/4}. \tag{3.118}$$

We see that the Reynolds number grows almost linearly with distance from the leading edge, and thus it is clear that the underlying assumption of smallness will inevitably be broken at some point downstream. This has important implications for the validity of the low-Re approximation in vertical and inclined film boiling, and this will be explored further in Sec. 3.5.

3.5 Moderate-Re film boiling

The results of Sec. 3.4 were all derived under the assumption that the Reynolds number is so small that the $\epsilon\mathrm{Re}$-terms could be neglected. While this assumption is appropriate for horizontal film boiling, as we will show below, it does not appear to be appropriate in vertical/inclined film boiling due to the large lateral velocities induced by buoyancy.

This section includes a more formal explanation of why the low-Re assumption breaks down and follows up with a derivation of a new long-wave model that includes the inertial terms. The film aspect-ratio is still assumed to be small, so that higher order terms in ϵ may be neglected. However, the Reynolds number is allowed to be so large that the following product,

$$\epsilon\mathrm{Re} \sim \mathcal{O}(1) \tag{3.119}$$

is not negligible. As shown in Paper C [86], such a model may be used to predict the stability and heat transfer coefficient of non-horizontal film boiling.

3.5.1 The necessity of keeping inertial terms

According to Sec. 3.4.6, in cases of non-horizontal film boiling ($a \neq 0$) there is the possibility of steady non-uniform solutions of the kind shown in Eq. (3.113). Consider a case where we wish to investigate the stability of the steady state film thickness $\bar{h}(x)$ with respect to some localized disturbance at a position $x = \overline{x}$. It is then reasonable to define the scales h_0 and u_0 in a way that closely matches the steady state at that location. Here we choose the scales to be

$$h_0(\overline{x}) = \left(\frac{16\mu_\mathrm{v}k_\mathrm{v}\Delta T}{\rho_\mathrm{v}\Delta\rho g L}\overline{x}\right)^{1/4}, \tag{3.120}$$

and

$$u_0(\overline{x}) = \frac{g\Delta\rho h_0^2(\overline{x})}{12\mu_\mathrm{v}}. \tag{3.121}$$

Note that we have defined the scales using the case of a vertical surface ($a = 1$) and zero interface velocity ($\eta = 0$) as a reference. By inserting Eqs. (3.120) and (3.121) into the definition for the Reynolds number in Tab. 3.3, we find that

$$\mathrm{Re}(\overline{x}) = \frac{\rho_\mathrm{v}\Delta\rho g}{12\mu_\mathrm{v}^2} h_0^3(\overline{x}) \propto \overline{x}^{3/4} \tag{3.122}$$

In other words, the Reynolds number grows as we move downstream, almost linearly with with distance from the leading edge. The aspect ratio ϵ, as defined in Eq. (3.31), is additionally dependent on the longitudinal scale of the disturbances (x_0),

$$\epsilon(\overline{x}, x_0) = \frac{h_0(\overline{x})}{x_0}. \tag{3.123}$$

If we multiply Eq. (3.122) by Eq. (3.123), we find

$$\begin{aligned} \epsilon\mathrm{Re} &= \frac{\rho_\mathrm{v}\Delta\rho g}{12\mu_\mathrm{v}^2}\left[\frac{h_0^4(\overline{x})}{x_0}\right] \\ &= \frac{4}{3}S\left[\frac{\overline{x}}{x_0}\right], \end{aligned} \tag{3.124}$$

where the constant S is defined in Tab. 3.3. Since we have no ab initio knowledge on the wavelength of the arising disturbances, the value of the last square bracket in Eq. (3.124) remains unknown. However, we may say something about its minimum possible value. Any wavelike disturbance arising at position $\overline{x}$ must fit between that position and the leading edge where $h = 0$. In other words, any disturbance arising at position $\overline{x}$ must have a longitudinal scale x_0 that approximately satisfies $x_0 < \overline{x}$. If we combine this observation with Eq. (3.124), we find that

$$\epsilon\mathrm{Re} > \frac{4}{3}S. \tag{3.125}$$

Importantly, this remains valid for any position $\overline{x}$. As we go closer to the leading edge (decrease $\overline{x}$), the Reynolds number decreases. However, the allowable wavelengths also decrease, and thus, the lower bound on ϵ increases. The end result is that the lower bound on the product $\epsilon\mathrm{Re}$ is given by Eq. (3.125) regardless of position.

The lower bound implied by Eq. (3.125) will depend on the choice of fluid and ΔT_{w}. For realistic film boiling cases, the value of S is generally of the order of

$$S \sim \mathcal{O}\left(10^{-1}\right). \tag{3.126}$$

For the steady-state solutions themselves, which have the effective longitudinal scale of $x_0 \sim \overline{x}$, Eq. (3.124) tells us that the inertial terms are reasonably small ($\epsilon\mathrm{Re} \sim S$). However, as indicated by Eq. (3.125), when using the ϵ corresponding to a wavelike disturbance of this state there is no guarantee that the ϵRe-terms will be small.

The conclusion for non-horizontal film boiling is the following: The steady-state solution in Sec. 3.4.6 that was obtained from the low-Re approach is valid on its own. However, any stability analysis thereof must include ϵRe-terms. In Sec. 3.5.2 we derive a model that includes these inertial terms in the momentum equation.

3.5.2 Moderate-Re long-wave model

The general long-wave model of Sec. 3.3 was derived without making any assumptions regarding the magnitude of the inertial terms ϵRe. Thus, the expression for the driving force in Eq. (3.72) and the general mass conservation PDE in Eq. (3.73) remain valid. However, the velocity profile $U(X, Z)$ required in Eq. (3.73) is not as easily obtained, since the assumptions leading to Eq. (3.75) are no longer valid.

The present goal is to retain the inertial terms from the momentum equation, Eq. (3.56), while still arriving at a relatively simple one-dimensional model like in the low-Re case, Eq. (3.93). The method that will be applied to achieve this is the *Momentum-Integral Method* (MIM), sometimes also referred to as the Kármán-Pohlhausen *integral boundary-layer method* [73, 76]. This is a method that has been applied to falling thin-films for decades, starting with Shkadov [87, 88], and later by authors such as Alekseenko, Nakoryakov, and Pokusaev [89], Prokopiou, Cheng, and Chang [90], Lee and Mei [91], Ruyer-Quil and Manneville [92, 93, 94], Bestehorn, Han, and Oron [95] and Bestehorn [96]. However, these results can not be applied directly to the present case because they are all derived for the case of a falling liquid film, not a buoyant vapor film. Just like in the low-Re case earlier, the present case introduces additional complications due to the inability to make free-surface assumptions for the liquid–vapor interface. The results herein allow for a more generalized interface, and will be most similar to the liquid-film results in the $\eta = 1$ limit.

In principle the momentum-integral method entails expanding the unknown velocity profile $U(X,Z)$ in a basis of Z-dependent polynomials with X-dependent expansion coefficients. In its simplest (lowest order) form, which is the one applied herein, this reduces to calculating the parabolic profile resulting from the $\epsilon\mathrm{Re} \to 0$ limit and recognizing that this yields the first term of the expansion. This is then inserted back into the more general governing equations in order to compute a correction for the $\epsilon\mathrm{Re} \neq 0$ case.

Integrated momentum equation

In order to arrive at a one-dimensional model, it is necessary to integrate the X-momentum equation Eq. (3.56) across the vapor film, just like we did with the continuity equation earlier. First, we need the following useful relation,

$$\begin{aligned} UU_X - UW_Z &= U\left(2U_X - \underbrace{[U_X + W_Z]}_{=0}\right) \\ &= 2UU_X \\ &= \left(U^2\right)_X, \end{aligned} \tag{3.127}$$

where the square bracket above could be set to zero due to the continuity equation, Eq. (3.55).

Now, with the help of Leibniz's integral rule, integration by parts, the relation in Eq. (3.127), the wall boundary condition (Eq. (3.61)) and the interface mass balance (Eq. (3.64)), we find the integral of the left-hand side of Eq. (3.56) to be:

$$\begin{aligned} &\int_0^H (U_\tau + UU_X + WU_Z)\,\mathrm{d}Z \\ &\quad= \left(\int_0^H U\mathrm{d}Z\right)_\tau - [U]_{Z=H}\,H_\tau + \int_0^H \underbrace{(UU_X - UW_Z)}_{=(U^2)_X \text{ (Eq. (3.127))}}\,\mathrm{d}Z \\ &\qquad + [UW]_{Z=H} - \underbrace{[UW]_{Z=0}}_{=0 \text{ Eq. (3.61)}} \\ &\quad= \left(\int_0^H U\mathrm{d}Z\right)_\tau + \left(\int_0^H U^2\mathrm{d}Z\right)_X - [U]_{Z=H}\underbrace{(H_\tau + UH_X - W)_{Z=H}}_{=EJ/\epsilon \text{ (Eq. (3.64))}} \\ &\quad= \left(\int_0^H U\mathrm{d}Z\right)_\tau + \left(\int_0^H U^2\mathrm{d}Z\right)_X - \frac{E}{\epsilon}\,[U]_{Z=H}\,J. \end{aligned} \tag{3.128}$$

Since Eq. (3.57) shows that $\overline{P}$ is independent of Z, the integral of the right-hand side of Eq. (3.56) is simply

$$\int_0^H \left(-\overline{P}_X + U_{ZZ}\right) \mathrm{d}Z = -\overline{P}_X H + [U_Z]_{Z=H} - [U_Z]_{Z=0} \ . \tag{3.129}$$

If we now integrate Eq. (3.56) and insert Eqs. (3.128) and (3.129) we find that the complete integrated momentum equation is

$$\begin{aligned} &\epsilon\mathrm{Re}\left(\left[\int_0^H U \mathrm{d}Z\right]_\tau + \left[\int_0^H U^2 \mathrm{d}Z\right]_X - \frac{E}{\epsilon}[U]_{Z=H} J\right) \\ &= -\overline{P}_X H + [U_Z]_{Z=H} - [U_Z]_{Z=0} \ . \end{aligned} \tag{3.130}$$

Note how the low-Re parabolic velocity profile in Sec. 3.4.1 is easily retained if we neglect the left-hand side inertial correction ($\epsilon\mathrm{Re} \to 0$).

The result in Eq. (3.130) is somewhat similar to the one for liquid films by Alekseenko, Nakoryakov, and Pokusaev [89, Eq. 15]. However, the present version is significantly more complicated due to the inclusion of evaporation (J), interface drag ($[U_Z]_{Z=H}$) and a more comprehensive driving-force term $\overline{P}_X$, cf. Eq. (3.72).

The integrated form in Eq. (3.130) is convenient because it is independent of Z, in contrast to Eq. (3.56). In other words, it is a PDE in the space of X and τ only. However, the terms are dependent on certain properties of the velocity profile $U(Z)$ at any given X. In order to proceed we must make an assumption regarding the shape of this profile.

Approximations

Before proceeding we make certain assumptions that considerably simplify the following treatment while retaining its core message. We assume that the vapor film being analyzed has grown sufficiently thick that the effects of van der Waals forces, non-equilibrium evaporation and solid surface cool-down are all negligible,

$$A \to 0 \qquad K \to 0, \qquad \mathrm{Bi}_\mathrm{w}^{-1} \to 0. \tag{3.131}$$

The quasi-equilibrium approximation ($K = 0$) has the effect of forcing the interface temperature to be saturated ($\theta_\mathrm{i} = 0$), and thus also eliminates the thermocapillary effect (term with M in Eq. (3.66)). A more general form of the following derivation, including thermocapillary effects, is found in Paper C [86].

Assumed parabolic velocity profile

In the low-Re results of Sec. 3.4 we were able to find an explicit expression for the velocity profile, Eq. (3.81). We now assume that the general velocity profile has the same parabolic shape (but with unknown magnitude) and use it to compute the new inertial contributions in Eq. (3.130).

We want to propose a parabolic velocity profile that also satisfies the liquid-shear closure, Eq. (3.69). This implies that the interface velocity should monotonically increase from zero with the parameter $\eta \in [0, 1]$, and that the maximum at $\eta = 1$ should correspond to the hypothetical state of zero interface shear stress. Such a profile may be written as

$$U = \frac{6Q}{\xi H}\left[(1+\eta)\frac{Z}{H} - \left(\frac{Z}{H}\right)^2\right], \tag{3.132}$$

where we have introduced a new variable $Q(X, \tau)$ which is defined as the flow rate at a given position X,

$$Q(X,\tau) = \int_0^H U \mathrm{d}Z. \tag{3.133}$$

We are now in a position to calculate the integrals on the left hand side of the integrated momentum equation, Eq. (3.130), in terms of the X-dependent quantities Q and H. According to Eq. (3.133) the first integral is simply Q, by definition. The second integral is

$$\int_0^H U^2 \mathrm{d}Z = \frac{6}{5}\zeta\frac{Q^2}{H} \tag{3.134}$$

with a new short-hand ζ defined as

$$\zeta = \frac{10\eta^2 + 5\eta + 1}{\xi^2} \tag{3.135}$$

The interface velocity required on the left-hand side of Eq. (3.130) is

$$[U]_{Z=H} = \frac{6\eta Q}{\xi H}, \tag{3.136}$$

and the friction term on the right-hand side is simply

$$[U_Z]_{Z=H} - [U_Z]_{Z=0} = -\frac{12Q}{\xi H^2}. \tag{3.137}$$

Temperature profile

The application of Eq. (3.130) requires a model for the evaporation rate J, explicitly on the left-hand side and through $\overline{P}_X$ on the right-hand side.

The low-Re solutions for the temperature profile and evaporation rate in Sec. 3.4.2 were found after neglecting the left-hand side of the energy equation, Eq. (3.58), by virtue of $\epsilon\mathrm{Re}$ being very small. In the present case of non-horizontal film boiling we have shown that $\epsilon\mathrm{Re}$ is in fact not small. However, as shown in the appendices (Sec. 3.B) the inertial effects on the energy equation may still be negligible. Thus, we assume that the results of solving the energy equation are unaffected by inertial effects, and simply use Eq. (3.86). Under the simplifying assumptions of Eq. (3.131) this reduces to

$$J = \frac{1}{H}. \tag{3.138}$$

3.5.3 Coupled PDEs of moderate-Re film boiling

With the assumptions of Eq. (3.131) and the simplified evaporation rate of Eq. (3.138), the driving force in Eq. (3.72) reduces to

$$\overline{P}_X(X) = -G\left(a + \epsilon b H_X\right) - \epsilon^3 \mathrm{Ca}^{-1} H_{XXX} + 2\epsilon S E\left[1 - D\right]\frac{H_X}{H^3} \tag{3.139}$$

Now, if we use Eqs. (3.133) and (3.138) in combination with the general mass conservation equation Eq. (3.73), we get

$$\epsilon\left[H_\tau + Q_X\right] = E\frac{1}{H}. \tag{3.140}$$

Similarly, if we use Eqs. (3.133), (3.134) and (3.136) to (3.138) in combination with the integrated momentum equation in Eq. (3.130) we get

$$\epsilon\mathrm{Re}\left(Q_\tau + \frac{6}{5}\zeta\left[\frac{Q^2}{H}\right]_X\right) = \mathrm{Re}\frac{6\eta E}{\xi}\frac{Q}{H^2} - \overline{P}_X H - \frac{12Q}{\xi H^2} \tag{3.141}$$

Eqs. (3.140) and (3.141) together form a set of coupled nonlinear partial differential equations for the quantities $H(X,\tau)$ and $Q(X,\tau)$, which may in principle be solved numerically in order to study the dynamics of inclined or vertical film boiling.

Note how Eq. (3.141) may be solved explicitly for Q in the limit of $\mathrm{Re} \to 0$. If we then substitute this expression for Q in Eq. (3.140) we retain the single low-Re PDE of Eq. (3.93) under the approximations Eq. (3.131).

In Paper C [86] the model represented by Eqs. (3.140) and (3.141) with Eq. (3.139) was used to examine the stability of the approximate steady state derived in Sec. 3.4.6. Based on this the critical Reynolds number for the onset of inertial instabilities was calculated, and the results were used to predict the heat transfer coefficient of vertical film boiling. While this is interesting in its own right, and serves as validation for the generalized long-wave methodology, it is less relevant to the central issue of this thesis. This is because LNG RPT is mainly concerned with horizontal film boiling. Thus, further analysis of non-horizontal film boiling is not covered here, but left to Paper C, which is attached in full in Part II.

3.6 Predicting the Leidenfrost point

This section goes back to the case of horizontal film boiling, where the low-Re result of Sec. 3.4 still applies. In particular we use the stability analysis of Sec. 3.4.5 in order to uncover an intriguing possible connection between the thermocapillary effect, the vapor thrust effect, and the Leidenfrost point introduced in Chapter 1. This essentially covers the most important result of Paper A [97].

3.6.1 Stability condition in the intermediate regime

We now consider the conditions for stability of the intermediate regime, as it is identified in Fig. 3.2. We see that this regime is dominated by a struggle between the stabilizing vapor thrust effect and the destabilizing thermocapillary effect. The other two terms (gravity and van der Waals) are usually at least two orders of magnitude smaller in this regime, so we neglect them from the consideration. By inspecting Eq. (3.109) we see that the vapor thrust effect exactly balances the thermocapillary effect when

$$\frac{CS\xi(1-D)F_0^3}{6} = \frac{CK\eta MF_0^2}{2E}. \tag{3.142}$$

We now make the approximation $F_0 \approx 1$, which is good in most of the intermediate regime. Eq. (3.142) is then satisfied at a specific value of the wall superheat,

$$\Delta T_\mathrm{w} = \left(\frac{3\eta}{1+3\eta}\right)\frac{\sqrt{2\pi R}T_\mathrm{s}^{3/2}\gamma}{r(\alpha)k_\mathrm{v}}\left(1+\frac{\rho_\mathrm{v}}{\rho_\mathrm{l}}\right)\frac{\rho_\mathrm{v}}{\rho_\mathrm{s}}, \tag{3.143}$$

where we have also simplified slightly by assuming that the density ratio is small, i.e. $D \ll 1$. We have inserted the definitions of the dimensionless

parameters according to Tab. 3.3. We then brought in the main result from kinetic-theory, Chapter 2, namely $\hat{K} = \tilde{K}/r(\alpha)$ with $\tilde{K}$ according to Eq. (2.52). As opposed to ρ_v, the quantity ρ_s from the kinetic-theory evaporation model is the vapor density evaluated at T_s.

While Eq. (3.143) may appear to be an explicit equation for ΔT_w, it is in fact implicit. This is due to the fact that the vapor properties on the right hand side are in reality temperature dependent and should be evaluated at the *film temperature*,

$$T_\mathrm{f} = T_\mathrm{s} + \frac{1}{2}\Delta T_\mathrm{w}. \tag{3.144}$$

Thus, solving Eq. (3.143) generally involves iteratively searching for a value of ΔT_w that satisfies the equation. We label this critical wall superheat value as ΔT_c, and note that

$$\begin{aligned} \Delta T_\mathrm{w} > \Delta T_\mathrm{c} \quad &\Longrightarrow \text{Stable intermediate regime.} \\ \Delta T_\mathrm{w} < \Delta T_\mathrm{c} \quad &\Longrightarrow \text{Unstable intermediate regime.} \end{aligned} \tag{3.145}$$

If we ignore the temperature-dependence of vapor properties we may set $\rho_\mathrm{v} = \rho_\mathrm{s}$ and $k_\mathrm{v} = k_\mathrm{s}$, where k_s is the thermal conductivity of saturated vapor. In this case Eq. (3.143) reduces to an explicit approximation for ΔT_c,

$$\frac{\Delta T_\mathrm{c}}{T_\mathrm{s}} \approx \underbrace{\frac{\sqrt{2\pi}}{r(\alpha)}}_{\approx 2} \underbrace{\left(1 + \frac{\rho_\mathrm{s}}{\rho_\mathrm{l}}\right)}_{\approx 1} \underbrace{\left(\frac{3\eta}{1+3\eta}\right)}_{\approx 0.04} \underbrace{\frac{\sqrt{RT_\mathrm{s}}}{k_\mathrm{s}}\gamma}_{\approx 3}. \tag{3.146}$$

The estimated values for the terms in Eq. (3.146) are based on water with saturated vapor and $\alpha \approx 0.8$. Values for a wider range of fluids are shown in Tab. 3.4. As will be shown later, the approximation in Eq. (3.146) generally yields a moderate over-prediction compared to the value of ΔT_c found from numerically solving the implicit equation in Eq. (3.143). However, Eq. (3.146) gives an important clue regarding the magnitude of $\Delta T_\mathrm{c}/T_\mathrm{s}$.

3.6.2 The Leidenfrost temperature

The important clue from Eq. (3.146) is essentially that ΔT_c, the critical wall superheat that balances the vapor-thrust effect with the thermocapillary effect, is generally in the range of

$$0.1 < \frac{\Delta T_\mathrm{c}}{T_\mathrm{s}} < 0.5 \tag{3.147}$$

Table 3.4: Values of the fluid dependent terms in Eq. (3.146) for a variety of fluids, based on saturated vapor properties. Thermophysical data was taken from the NIST Webbook database [98], and Eq. (3.152) was used to approximate the value of η. All values are for pressure $p = 1\,\text{atm}$.

Fluid	$1 + \frac{\rho_s}{\rho_l}$	$\frac{3\eta}{1+3\eta}$	$\frac{\sqrt{RT_s}}{k_s}$ (mK/N)	γ (N/(mK))
Water	1.0006	0.039	16537	0.000192
Freon-113	1.0049	0.054	12549	0.000110
Pentane	1.0049	0.061	12346	0.000108
Freon-11	1.0040	0.053	15951	0.000128
Methane	1.0043	0.060	20768	0.000250
Nitrogen	1.0057	0.062	20190	0.000229
Hydrogen	1.0188	0.100	16965	0.000162

for the fluids listed in Tab. 3.4. This is noteworthy because it is the range in which the experimental Leidenfrost point (ΔT_L) is usually found. As explained back in Sec. 1.5.3, this is the limiting wall superheat (ΔT_w) below which film boiling collapse occurs.

The above observation suggests a further investigation into whether ΔT_c may be a good predictor for ΔT_L. Experimental data on the Leidenfrost point for a series of fluids are shown in Tab. 3.5. These fluids cover a large range of boiling (saturation) temperatures, from cryogenic hydrogen (20 K) to water (373 K).

Table 3.5: Fluids for which both experimental data for T_L and complete vapor/liquid thermophysical data could be found. Where multiple measurements could be found for T_L, the average value is displayed. All values are for pressure $p = 1\,\text{atm}$.

Fluid	T_s (K)	T_L (K)	$\frac{\Delta T_L}{T_s}$	Sources for T_L
Water	373.15	462.78	0.24	[99, 82, 100, 101, 83]
Freon113	320.74	378.03	0.18	[99, 102, 103]
Pentane	309.21	367.00	0.19	[80]
Freon11	296.92	346.50	0.17	[99, 102]
Methane	111.70	163.33	0.46	[104, 105]
Nitrogen	77.36	100.00	0.29	[99, 102]
Hydrogen	20.27	28.77	0.42	[106]

The experimental values for $\Delta T_L = T_L - T_s$ may now be compared with the critical value of stability (ΔT_c) obtained by solving the implicit

equation Eq. (3.143) for each fluid. The latter depends on thermophysical properties, including the temperature dependence of the vapor properties. It also depends on the evaporation coefficient (α), which is essentially unknown but likely in the range of $\alpha \in [0.5, 1.0]$.

A straightforward dimensional comparison is shown in Fig. 3.3, from which we observe the following points:

- For all fluids the average experimental value of ΔT_{L} falls within the range of ΔT_{c} calculated for $\alpha \in [0.5, 1]$.
- The spread/uncertainly in the experimental ΔT_{L} data seems to be very large. Interestingly, this spread appears to be equivalent to the spread in ΔT_{c} due to the uncertainty in α.
- The approximation in Eq. (3.146) yields an over-prediction compared to the full solution of Eq. (3.143).

Of course, one could claim that most differences in ΔT_{L} are accounted for by differences in T_{s}. We may control for this by comparing the dimensionless quantities $\Delta T_{\mathrm{c}}/T_{\mathrm{s}}$ (model) and $\Delta T_{\mathrm{L}}/T_{\mathrm{s}}$ (experiments), which should yield a stronger test of predictive power. To make a well defined prediction we use the mid-point value of the expected interval for the evaporation coefficient, $\alpha = 0.75$. We compare this with the average experimental value for the Leidenfrost point, while accounting for the fact that the data points for ΔT_{L} generally show a random spread of $\pm 10\%$ (relative to T_{s}). The result is shown in Fig. 3.4.

We observe the following points:

- The computed $\Delta T_{\mathrm{c}}/T_{\mathrm{s}}$ agree with the data for $\Delta T_{\mathrm{L}}/T_{\mathrm{s}}$ for all fluids within the typical $\pm 10\%$ uncertainty. Most of them agree quite closely, while nitrogen appears somewhat anomalous (but still within a $\pm 10\%$ uncertainty margin).
- The range of different $\Delta T_{\mathrm{L}}/T_{\mathrm{s}}$ values from these fluids is not wide enough to provide a strong test for the predictive power of $\Delta T_{\mathrm{c}}/T_{\mathrm{s}}$. Measurements from a wider variety of fluids are needed to properly validate ΔT_{c} as a model for ΔT_{s}.

The results herein seem to give preliminary support for the hypothesis that ΔT_{c}, the critical superheat that balances vapor-thrust stabilization with thermocapillary destabilization, is a good predictor for the Leidenfrost point.

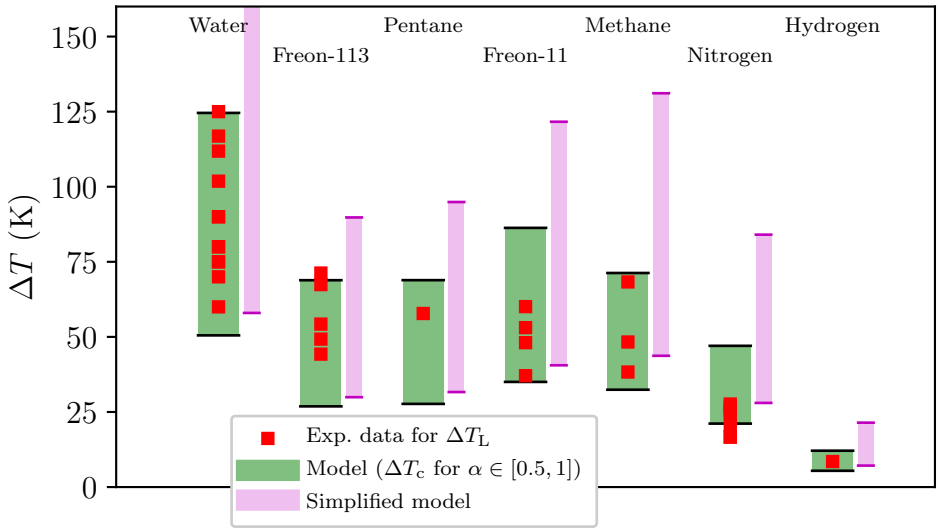

Figure 3.3: Comparison of the theoretical ΔT_c (green bars) with experimental Leidenfrost temperature ΔT_L (red squares). The green bars show ΔT_c according to a solution of Eq. (3.143) with the range of evaporation coefficients $\alpha \in [0.5, 1]$. The thinner bars show the corresponding approximation from Eq. (3.146).

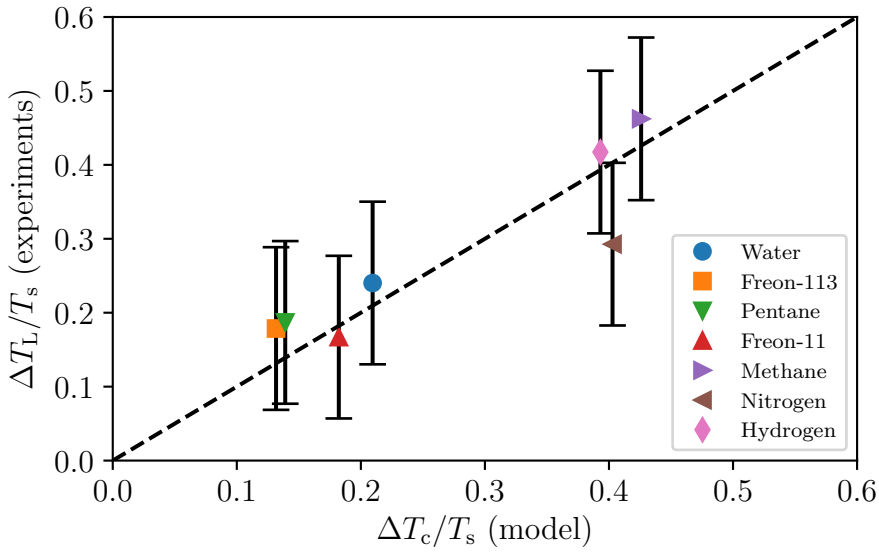

Figure 3.4: Comparison of computed $\Delta T_c/T_s$ (Eq. (3.143) with $\alpha = 0.75$) with experimental $\Delta T_L/T_s$. The dashed line represents exact correspondence. Error bars represent the typical $\pm 10\%$ uncertainty seen from the data.

3.7 Conclusions

Besides the possible applications of the general low-Re film-thickness PDE in Eq. (3.93), the most important result in the context of LNG RPT relates to the Leidenfrost point (film-boiling collapse). According to the common theory of LNG RPT presented in Sec. 1.6, crossing the Leidenfrost point is the crucial first step that leads to superheating and subsequent vapor explosion.

As shown in Figs. 3.3 and 3.4, there seems to be a remarkable correspondence between the critical superheat (ΔT_{c}) for stability in the intermediate regime of Fig. 3.2 and the experimental Leidenfrost point (ΔT_{L}). If this correspondence proves to be more than mere coincidence, it means that the Leidenfrost point may be estimated by solving Eq. (3.143). Beyond this practical benefit, the conclusion also comes with a novel theoretical implication: The thermocapillary instability is the cause of film-boiling breakdown. However, as mentioned, additional Leidenfrost-point data from a wider range of fluids would be necessary to conclude this with certainty.

Note that the derivation of Eq. (3.143) for ΔT_{c} was absolutely dependent on certain important nuances in the model. It may be tempting to use the quasi-equilibrium approximation ($K \to 0$) or the maximum liquid drag assumption ($\eta \to 0$), but using either would eliminate the thermocapillary effect and lead to $\Delta T_{\mathrm{c}} \to 0$. In other words, both including the kinetic-theory results from Chapter 2 as well as postulating the liquid shear closure in Eq. (3.29) proved to be absolutely essential for reaching the results herein.

In the context of LNG RPT a significant issue still remains: The model for film boiling derived in this chapter is technically only valid for the boiling of pure fluids, not mixtures. A simple and practical kinetic-theory evaporation model on the form of Eq. (3.20) has yet to be developed for the case of mixtures. However, if the present model for the Leidenfrost point proves to be accurate for a wide array of pure fluids, an extension to mixtures would certainly be worth the effort.

3.A Appendix: Estimating the value of η

For a very smooth ($\epsilon \to 0$) solution on a non-horizontal surface, Eq. (3.81) implies that the velocity profile of the vapor film is

$$U = \frac{Ga}{2}\left((1+\eta)HZ - Z^2\right). \tag{3.148}$$

This profile has a maximum velocity and an interface velocity of

$$[U]_{\max} = \frac{(1+\eta)^2}{4}\frac{GaH^2}{2}, \qquad [U]_{Z=H} = \eta\frac{GaH^2}{2}, \tag{3.149}$$

respectively. The ratio of interface to maximum velocity is then

$$\frac{[U]_{Z=H}}{[U]_{\max}} = 4\frac{\eta}{(1+\eta)^2} \overset{\eta\ll 1}{\approx} 4\eta + \mathcal{O}\left(\eta^2\right). \tag{3.150}$$

According to the results of Koh [107] on the velocity profile in smooth and steady film-boiling, we find the correlation

$$\frac{[U]_{Z=H}}{U_{\max}} \approx \frac{3}{4}\left(\frac{\rho_{\mathrm{v}}\mu_{\mathrm{v}}}{\rho_{\mathrm{l}}\mu_{\mathrm{l}}}\right)^{1/4}. \tag{3.151}$$

By equating Eq. (3.150) with Eq. (3.151), we find that the value of η may be approximated from

$$\eta \approx \frac{3}{16}\left(\frac{\rho_{\mathrm{v}}\mu_{\mathrm{v}}}{\rho_{\mathrm{l}}\mu_{\mathrm{l}}}\right)^{1/4}. \tag{3.152}$$

Note that this explicit expression is only valid for $\eta \ll 1$, since it used the rightmost part of Eq. (3.150). If we avoid making that assumption we arrive at an implicit equation for η which predicts that $\eta \ll 1$ is true for most fluids. Thus, the simplified form of Eq. (3.152) is equally valid and much more convenient.

While the basis for Eq. (3.152) is not very strong, it should give a reasonable estimate for η. The model has the advantage of only being dependent on two dimensionless fluid properties: the viscosity ratio and the density ratio. Due to the small power (1/4), the variation between different fluids is quite small. We find a typical range of

$$\eta \in [0.01, 0.05]. \tag{3.153}$$

3.B Appendix: The moderate-Re energy equation

In Sec. 3.5.1 we showed how the steady-state solutions for inclined film boiling found in Sec. 3.4.6 resulted in Reynolds numbers that were quite large. In fact, they were so large that any disturbances of these solutions could not satisfy the assumption of $\epsilon\mathrm{Re} \ll 1$. This issue was remedied in Sec. 3.5 by deriving more general equations that included the $\epsilon\mathrm{Re}$-terms from the momentum equation. However, the solution for the evaporation

rate in Sec. 3.4.2 was still used. This essentially means that the inertial effects on the energy equation were assumed to be negligible even when they were not negligible in the momentum equation. The purpose of the present section is to defend this assumption.

We simplify the following analysis by assuming that the vapor film is sufficiently thick so that

$$K \to 0, \qquad \mathrm{Bi}_{\mathrm{w}}^{-1} \to 0. \tag{3.154}$$

Just like in the case of the momentum equation in Sec. 3.5.2, we may now apply the continuity equation and the boundary conditions of Eqs. (3.61) and (3.64) in order to find an integrated form of the energy equation, Eq. (3.58), without assuming that $\epsilon\mathrm{Re} \to 0$. The steady-state result is

$$\epsilon\mathrm{Re}\,\mathrm{Pr}\left[\int_0^H \theta U \,\mathrm{d}Z\right]_X = [\theta_Z]_{Z=H} - [\theta_Z]_{Z=0}\,. \tag{3.155}$$

The low-Re results in Sec. 3.4.2, which yielded a relatively simple linear expression for the temperature profile $\theta(Z)$, were essentially obtained by neglecting the left-hand side of Eq. (3.155). We now wish to examine this result for self-consistency by using it to evaluate the magnitude of the left-hand term. The right-hand side terms of Eq. (3.155) are of the order $\mathcal{O}\,(1)$, so if the left-hand side term is considerably smaller the right-hand θ_Z terms must approximately cancel each other out. Such a result would thus be consistent with the linear temperature profile.

In order to evaluate the left-hand side of Eq. (3.155) we need a velocity profile $U(Z)$ and a temperature profile $\theta(Z)$. For the smooth steady solution considered here the velocity profile is once again a parabolic profile given by Eq. (3.148). Then, under the assumptions of Eq. (3.154) the linear temperature profile of Sec. 3.4.2 simply reduces to $\theta = 1 - Z/H$.

By using the derivative H_X from Eq. (3.112) and the fact that $E\mathrm{Re} = S$ we then find that the left-hand term of Eq. (3.155) is

$$\begin{aligned}\epsilon\mathrm{Re}\,\mathrm{Pr}\left[\int_0^H \theta U \,\mathrm{d}Z\right]_X &= \epsilon\mathrm{Re}\,\mathrm{Pr}\left[\frac{Ga}{2}\frac{(1+2\eta)}{12}H^3\right]_X \\ &= \frac{1}{2}S\,\mathrm{Pr}\,\frac{(1+2\eta)}{1+3\eta}\frac{1}{H}.\end{aligned} \tag{3.156}$$

In other words, the term is of order $\mathcal{O}\,(S\,\mathrm{Pr})$ when the film-thickness scale h_0 is set appropriately ($H \sim \mathcal{O}\,(1)$). Since

$$S\,\mathrm{Pr} = \frac{c_{p\mathrm{v}}\Delta T_{\mathrm{w}}}{L} \tag{3.157}$$

is much smaller than unity for most fluids if the wall superheat (ΔT_{w}) is moderate, the term is small and the result is consistent with a linear temperature profile.

Chapter 4

Prediction of delayed LNG RPT in spills

4.1 Preface

We now take a step back from the microscopic world and tackle the main problem of the project described in Chapter 1, namely prediction of LNG Rapid Phase Transition (RPT). The fundamental theoretical RPT triggering criterion of Eq. (1.1) requires the modeling of two quantities: The superheat limit of the LNG (T_{SHL}), and the Leidenfrost temperature (T_{L}) of the LNG. Since the composition changes during boil-off in an LNG spill, both quantities must be modeled as a function of composition. In other words, numbers simply calculated from the storage-composition of LNG are not sufficient.

As we will show herein, the issue of the superheat limit is resolved rather quickly. In Paper F we show that classical nucleation theory is quite successful in predicting this quantity for hydrocarbon mixtures. The issue of the Leidenfrost temperature is much more complicated. As mentioned in the conclusion of Chapter 3, a lot more work is needed before the new model developed in this thesis can be used on mixtures like LNG. In the present chapter we use a simplified placeholder model for the Leidenfrost temperature in order to proceed. This allowed for the development of a modeling framework that may predict how much LNG boil-off is necessary before the conditions for triggering are met, and the severity of the subsequent vapor explosion. Plugging in an improved Leidenfrost model into this framework at a later stage would likely be straightforward.

My original contributions to this topic may be summarized as:

- The classical nucleation theory (CNT) approach to predicting the superheat limit was generalized to mixtures, and implement numerically. In Paper F, it was confirmed that such a model is sufficiently accurate for pure hydrocarbons as well as binary hydrocarbon mixtures.
- A model was developed for the prediction of LNG RPT risk as a function of methane molar fraction during boil-off. It was discovered that the point of triggering, and the relative LNG amount remaining at that time, strongly correlate with a single scalar property of the initial mixture. We called this property the *alkane factor*. This contribution was published in D.
- An approximation of the explosion process illustrated in Fig. 1.5 was developed. Based on the composition of the LNG remaining at the time of triggering, thermodynamic routines were then used to estimate the worst-case pressure and energy-yield of the RPT vapor-explosion. This contribution was also published in D.

All of the work described in this chapter has been published. The relevant papers, which are attached in full in Part II, are:

Paper D
Predicting triggering and consequence of delayed LNG RPT
Eskil Aursand, Morten Hammer
Published in *Journal of Loss Prevention in the Process Industries.*
(2018) Vol. 55, pp. 124–133
https://doi.org/10.1016/j.jlp.2018.06.001

Paper F
The spinodal of single- and multi-component fluids and its role in the development of modern equations of state
Peder Aursand, Magnus Gjennestad, Eskil Aursand, Morten Hammer, Øivind Wilhelmsen
Published in *Fluid Phase Equilibria.*
(2017) Vol. 436, pp. 98–112
https://doi.org/10.1016/j.fluid.2016.12.018

4.2 RPT triggering criterion

As explained in Sec. 1.6, the theory behind RPT implies that the following must be satisfied in order for triggering to occur:

$$T_{\mathrm{SHL}}(\boldsymbol{z}) < T_{\mathrm{w}} < T_{\mathrm{L}}(\boldsymbol{z}). \tag{4.1}$$

Here T_{w} is the temperature of the sea water, which is assumed to be relatively constant and close to freezing. Eq. (4.1) expresses two separate necessary criteria for triggering:

1. T_{w} must be less than the LNGs Leidenfrost temperature, T_{L}. If not, film boiling is stable and the heat flux is presumably too small to cause superheating of the LNG.
2. T_{w} must be larger than the LNGs superheat limit, T_{SHL}. If not, no amount of film-boiling collapse may sufficiently superheat the LNG.

See Sec. 1.5.2 and Sec. 1.5.3 for more background on the superheat limit and the Leidenfrost temperature, respectively.

While both the superheat limit and the Leidenfrost point are quite complicated issues, they are usually quite proportional to (but less than) the critical temperature (T_{c}), and usually satisfy $T_{\mathrm{SHL}} < T_{\mathrm{L}}$. This means that there is a *triggering window* $[T_{\mathrm{SHL}}, T_{\mathrm{L}}]$ that lies somewhere below the critical temperature. According to Eq. (4.1), if the surface (water) temperature falls within this interval, the theory predicts RPT triggering.

As we showed back in Fig. 1.2, the critical temperature of LNG is around 210 K and therefore the whole triggering window is far below freezing. In other words, we are well within the stable film boiling regime, and no triggering may occur according to the theory. However, as reviewed in Chapter 1, experiments show that RPT does eventually happen, even in relatively undisturbed LNG pools.

The reason why RPT triggering eventually does happen in LNG spills is due to *enrichment*. This refers to the process in which the composition of the LNG changes over time, mainly due to loss of methane through boil-off. Removing methane from the mixture shifts the two-phase region (and the critical point) towards higher temperatures. Since the T_{SHL} and T_{L} generally seem to follow the critical temperature, the triggering window is also moved to higher temperatures. An example of this enrichment process is shown in Fig. 4.1. We see that while LNG has a triggering window far below the water temperature, once the methane fraction is reduced to about 40% the triggering window has moved up to envelop the water temperature, thus making RPT theoretically possible.

In order to arrive at a quantitative prediction of LNG RPT, our goals are now to:

- Model the triggering window as a function of composition.
- Quantify the methane fraction at which the triggering window meets the water temperature, and how this depends on case parameters.
- Quantify the possible consequences of explosive RPT, given the calculated enriched composition at the time of triggering.

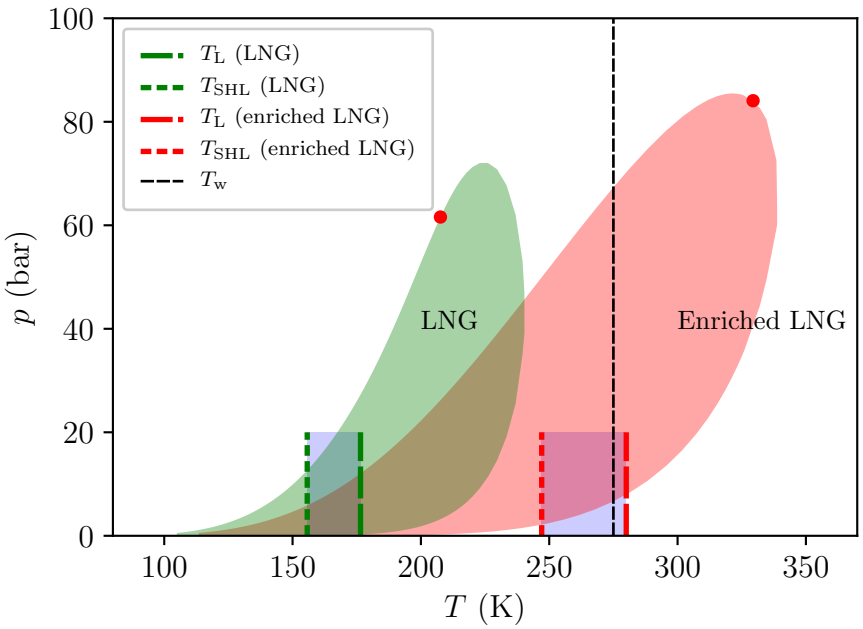

Figure 4.1: Illustration of how the triggering window is initially far below the water temperature, and how it may eventually move up to envelop the water temperature through enrichment, i.e. loss of methane. In this example the LNG is enriched from 95% methane to 40% methane.

4.3 LNG boil-off

We approximate the LNG as a mixture of the first four alkanes. The composition at any given time is formally specified in the *composition vector*,

$$\boldsymbol{z} = [z_1, z_2, z_3, z_4], \tag{4.2}$$

where each number z_i represents the molar fraction of methane (C1), ethane (C2), propane (C3), and n-butane (C4), respectively. The basic properties of these components are shown in Tab. 4.1.

A typical LNG mixture is very high in methane, with compositions such as $\boldsymbol{z} = [0.95, 0.02, 0.02, 0.01]$. As illustrated in Fig. 1.2, when mixing these four alkanes we no longer have the single atmospheric saturation temperature that pure fluids have. Instead we get a two-phase temperature range stretching from the atmospheric bubble-point to the atmospheric dew-point, which will approximately stretch from the lowest to the highest saturation temperatures among the components in the mixture.

When stored in a cryogenic tank for transport or usage, LNG is kept at its atmospheric bubble-point, approximately at 112 K. When the LNG is exposed to a heat flux, such as when spilled onto water, it will start to boil. As long as this heat flux is relatively moderate, as is the case in the film boiling regime, the temperature remains at the bubble point while all the heat is spent on evaporation (latent heat). The vapor leaving the LNG during boiling will not have the same composition as the liquid. Since methane is both the majority component and by far the most volatile, we may to a good approximation assume that the vapor leaving the LNG is purely methane [19]. If we label the original composition as $\boldsymbol{z}^{(0)}$, a current methane fraction of z_1 implies that the remaining components of the current composition are

$$z_i(z_1) = z_i^{(0)} \frac{1 - z_1}{1 - z_1^{(0)}} \quad \forall \quad i \neq 1. \tag{4.3}$$

Eq. (4.3) gives the full composition vector as a function of current methane fraction (z_1), and shows how the molar fractions of the heavier components increase linearly as the methane fraction decreases.

During boil-off the methane fraction decreases at some unknown rate that depends on the rate of heat transfer. For now we avoid complicating the picture with heat-flux uncertainty by considering the decreasing methane fraction as the progress parameter, not time. Thus, the goal is to evaluate the triggering criterion in Eq. (4.1) as a function of methane fraction. This requires estimates for the Leidenfrost temperature (T_{L}) and superheat limit (T_{SHL}) as functions of composition $\boldsymbol{z}$, and this will be reviewed the following two sections.

Table 4.1: Basic properties of the alkanes considered in this work: atmospheric boiling (saturation) temperature (T_s), critical temperature (T_c) and molar mass (M). Data from the NIST database [98].

Name		T_s (K)	T_c (K)	M ($kg\,mol^{-1}$)
Methane	("C1", CH_4)	112	191	0.01604
Ethane	("C2", C_2H_6)	185	305	0.03007
Propane	("C3", C_3H_8)	231	370	0.04410
n-Butane	("C4", C_4H_{10})	273	425	0.05812

4.4 Estimating the Leidenfrost temperature

As shown in Fig. 1.4, the Leidenfrost temperature T_L is the surface temperature below which film boiling breaks down. While Chapter 3 culminated in a novel model for predicting this quantity, the problem remains that this model is so far only applicable to pure fluids. Since LNG is a mixture, we must for now use a simpler placeholder model in order to illustrate how to use such models to predict RPT.

It has been suggested by authors such as Spiegler et al. [81] that the Leidenfrost temperature can be roughly estimated from the critical temperature according to

$$T_L(\boldsymbol{z}) = \frac{27}{32} T_c(\boldsymbol{z}). \tag{4.4}$$

It is difficult to assess how accurate Eq. (4.4) is for LNG mixtures, because it does not appear that the LNG boiling curve has ever been fully mapped. Additionally, even when some authors partially map it [108], that curve would correspond to one specific composition, and the composition dependence of the Leidenfrost point would remain unknown.

Since LNG is mainly methane, at least initially, we may use the Leidenfrost point of pure methane to gain some confidence in the use of Eq. (4.4). As seen in Tab. 3.5, the average Leidenfrost point found for methane in the literature is $T_L \approx 163\,K$. With the critical temperature also listed in Tab. 4.1, Eq. (4.4) predicts $T_L = 161\,K$, which is remarkably close.

Given the above, we proceed with the assumption that Eq. (4.4) is a decent enough approximation of the Leidenfrost temperature $T_L(\boldsymbol{z})$ for alkane mixtures like LNG when using the mixture's thermodynamic critical point. Note that evaluating Eq. (4.4) for mixtures is significantly more complicated than for pure fluids. For every composition $\boldsymbol{z}$ the critical point must

be solved for with the combination of an equation of state and iterative algorithms [45, 46], as opposed to simply looking up the pure fluid T_c in a table.

4.5 Estimating the superheat limit

In Paper F [47] we demonstrated how the superheat limit for alkanes, both pure and mixture, may be quite accurately estimated through classical nucleation theory (CNT). For completeness we will repeat the main principles of the model here. First we present it for the case of pure fluids, and then we explain how we generalize it for mixtures.

Due to random thermal fluctuations there is some probability of spontaneously creating vapor nuclei (tiny bubbles) within a superheated liquid. Such an event has two distinct effects on the energy of the system:

- **The energy decrease from creating a volume** of the thermodynamically preferred vapor phase. This is quantified by the thermodynamic driving force for evaporation, $p_s(T) - p$.
- **The energy increase from creating a new interface** around the new vapor nucleus. This is quantified by the surface tension of the liquid in contact with its own vapor, $\sigma(T)$.

As a general principle, systems on average seek to decrease their internal energy. Since this is a struggle between a volume-effect and a surface-effect, there must exist some critical nucleus size beyond which the volume-effect will overpower the surface-effect, and thus allow for a stable and growing vapor bubble. We call this the *critical nucleus size*. The energy required to spontaneously create a nucleus of this size is the *energy barrier*, ΔG. The probability of random thermal fluctuations overcoming a given energy barrier is typically quantified with a classical Arrhenius rate law,

$$\mathcal{J}(T) = \mathcal{J}_0 \exp\left(-\frac{\Delta G}{k_B T}\right), \tag{4.5}$$

where T is the temperature of the superheated liquid. The barrier ΔG is also temperature dependent, and may be modeled as [47]

$$\Delta G = \frac{16\pi\sigma^3(T)}{3\left[p_s(T) - p\right]^2}, \tag{4.6}$$

where p is the actual pressure applied to the liquid. The reference rate ($\mathcal{J}_0$) in Eq. (4.5) can be estimated from [47],

$$\mathcal{J}_0 = \frac{\rho_\mathrm{l}}{m^{3/2}}\sqrt{\frac{2\sigma}{\pi}}, \tag{4.7}$$

where ρ_l is the liquid density and and m is the mass of a single molecule.

The expression in Eq. (4.5) merely predicts a nucleation rate. In order to find the superheat-limit temperature it is necessary to define a critical nucleation rate $\mathcal{J}_\mathrm{c}$ which corresponds to sudden macroscopic phase change. It turns out that the result is very insensitive to the chosen value of $\mathcal{J}_\mathrm{c}$. Here we use the value of $\mathcal{J}_\mathrm{c} = 1 \times 10^{12}\,\mathrm{s^{-1}m^{-3}}$, similar to previous works [83, 47]. Thus, the procedure to find the superheat limit temperature (T_SHL) is to solve the implicit equation

$$\mathcal{J}(T) = \mathcal{J}_\mathrm{c} \tag{4.8}$$

for temperature, while using Eq. (4.5) to represent the function $\mathcal{J}(T)$. Note that it is critical to include the temperature dependence of σ. Simply using the surface tension at the saturation temperature yields a very different answer for T_SHL.

As it turns out, the result of solving Eq. (4.8) is very insensitive to the values of both $\mathcal{J}_\mathrm{c}$ and $\mathcal{J}_0$, and this allows for considerable simplification. We find that $\ln(\mathcal{J}_0/\mathcal{J}_\mathrm{c}) \approx 64$, which means that the critical nucleation rate is reached when the nucleation barrier ΔG drops below approximately $64 k_\mathrm{B} T$. Thus, to a very good approximation to the full solution of Eq. (4.8) we may instead solve

$$\frac{[p_\mathrm{s}(T) - p]^2\, k_\mathrm{B} T}{\sigma^3(T)} = \frac{\pi}{12}, \tag{4.9}$$

for temperature. This is very convenient, because it only requires knowledge of two functions:

- $p_\mathrm{s}(T)$: The saturation line of the fluid.
- $\sigma(T)$: The temperature dependent surface tension of the fluid.

The above theory is technically only valid for pure fluids, while LNG is a mixture. We assume that Eq. (4.9) may be generalized for mixtures by making the following two changes:

- Replace the saturation pressure $p_\mathrm{s}(T)$ by the closest analogue found in a mixture: the bubble-line pressure, shown in Fig. 1.2. This a function of both temperature (T) and composition ($\boldsymbol{z}$), and may be computed with the help of an equation of state.

- Replace the pure fluid surface tension $\sigma(T)$ with the mole-fraction average of the surface tension of the individual components of the liquid at that temperature. When above a component's critical temperature, that component has zero contribution. We compute the functions $\sigma(T)$ for the individual components based on interpolations of data from the NIST Webbook database [98].

While this generalization is somewhat crude, we showed in Paper F [47] that it is able to predict the experimental superheat limit of binary alkane mixtures quite well.

Based on this model, we find that the atmospheric-pressure superheat limits for the relevant mixtures are generally in the range from $0.6T_\mathrm{c}$ to $0.9T_\mathrm{c}$. In order to be more specific, Eq. (4.9) must be solved for every composition vector $\boldsymbol{z}$ as necessary.

4.6 RPT triggering: The Leidenfrost fraction

We now have models for both ends of the triggering window, $T_\mathrm{SHL}(\boldsymbol{z})$ from Eq. (4.9) and $T_\mathrm{L}(\boldsymbol{z})$ from Eq. (4.4), as functions of composition $\boldsymbol{z}$. Additionally, from Eq. (4.3) we have estimated the composition $\boldsymbol{z}$ as a function of the methane fraction z_1 and some initial composition $\boldsymbol{z}^{(0)}$. Overall, this enables us to track the triggering window as a function of decreasing z_1 during boil-off. For every case, which is defined by initial composition $\boldsymbol{z}^{(0)}$, there is a certain first (maximum) methane fraction z_1 where the triggering criterion Eq. (4.1) becomes satisfied. We call this the *Leidenfrost fraction*, z_L. When this methane fraction is reached, the total amount of LNG remaining is small compared to what was initially present before boil-off, and this is quantified by the *reduction factor*, ν. We formally define these two quantities as follows:

Definition. *Leidenfrost fraction (z_L): For an LNG boil-off case, the Leidenfrost fraction is the molar fraction of methane (z_1) where $T_\mathrm{L}(z_1) = T_\mathrm{w}$, i.e. where the RPT triggering criterion of Eq.* (4.1) *starts being satisfied.*

Definition. *Reduction factor (ν): For an LNG boil-off case, the reduction factor is the total moles of LNG remaining when the Leidenfrost fraction is reached, divided by the initial moles of LNG.*

With the help of some algebra, and the assumption that only methane is lost during boil-off, we find that the reduction factor may be simply

expressed from the Leidenfrost fraction and the initial methane fraction,

$$\nu = \frac{1 - z_1^{(0)}}{1 - z_\mathrm{L}}. \tag{4.10}$$

Since $z_\mathrm{L} < z_1^{(0)}$ (methane is lost in boil-off), we see that $\nu \in [0, 1]$.

An example of how the triggering window moves during boil-off is shown in Fig. 4.2, including the identification of the Leidenfrost fraction. This result, including the value of z_L, is independent of the initial methane fraction $z_1^{(0)}$. Changing the latter would not change how the process in Fig. 4.2 proceeds, but simply move our starting point. However, the result is very much dependent on the relative amounts of the non-methane components, $z_2/(1 - z_1)$ etc. Due to the approximation in Eq. (4.3), these relative amounts are unchanged throughout the boil-off process.

In principle we must solve for z_L throughout all possible values, which in this case would constitute a three-dimensional parameter space. However, by solving this problem throughout this parameter space we discovered that most of the dependence could be represented by a single scalar parameter. This was named the *alkane factor*. It is defined as

$$\zeta(\boldsymbol{z}) = \frac{M_2 z_2 + M_3 z_3 + M_4 z_4}{M_2(1 - z_1)}, \tag{4.11}$$

and is essentially the average molar mass of the non-methane part of the mixture, relative to the molar mass of pure ethane (M_2). By using Eq. (4.3) to substitute for z_2, z_3 and z_4 in Eq. (4.11), we see that it does not matter when ζ is evaluated. Thus, we may see it as a derived property of the initial composition. The value of ζ starts at unity for a binary mixture of methane and ethane, and increases as one adds heavier alkanes. Typical LNG mixtures generally yield values in the range $\zeta \in [1.1, 1.4]$.

By solving cases like Fig. 4.2 throughout the relevant composition space, it was found that z_L correlates remarkably well with the scalar ζ. The correlation is

$$z_\mathrm{L}(\zeta) \approx 1 - \frac{0.36}{\zeta - 0.73}, \tag{4.12}$$

By inserting this correlation into the reduction factor, Eq. (4.10), we get

$$\nu = \left(1 - z_1^{(0)}\right) \frac{\zeta - 0.73}{0.36} \tag{4.13}$$

We make the following observations from Eqs. (4.12) and (4.13):

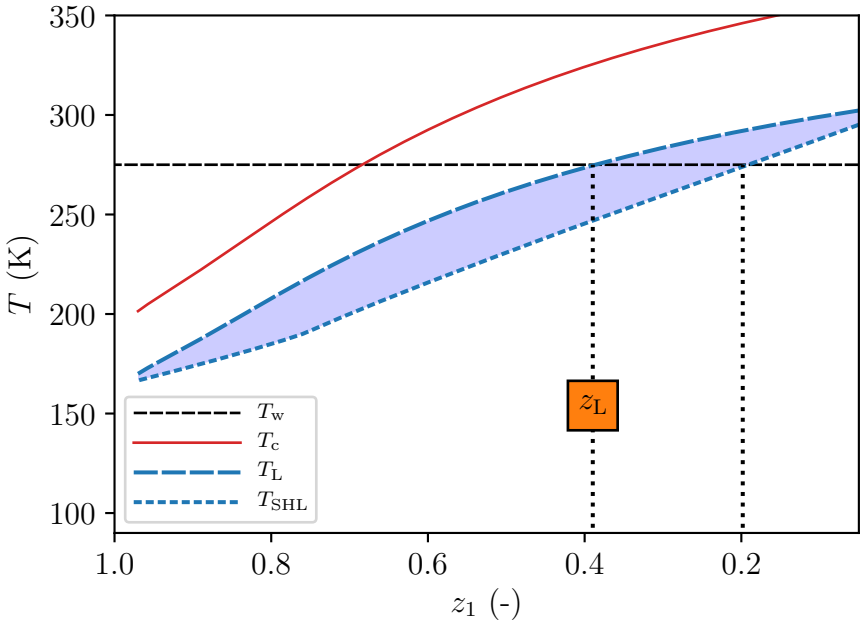

Figure 4.2: Example of how the *triggering window*, as illustrated in Fig. 4.1, moves to higher temperatures as the methane fraction (z_1) decreases due to boil-off. In this particular example, the non-methane part consists of 50% ethane, 30% propane and 20% butane. Also shown is the *Leidenfrost fraction* (z_L), which is the methane fraction where $T_L = T_w$, and thus the first methane fraction in the boil-off where the triggering criterion of Eq. (4.1) is satisfied. The region between the two vertical lines represents the zone of methane fractions where RPT triggering is theoretically possible.

- If $\zeta < 1.1$, we get $z_{\mathrm{L}} \to 0$. The interpretation of this is that the Leidenfrost temperature will never reach the water temperature, and RPT is not possible. Since both methane and ethane have $T_{\mathrm{L}} < T_{\mathrm{w}}$, no amount of methane loss from a binary methane/ethane mixture can make it reach $T_{\mathrm{L}} = T_{\mathrm{w}}$. If $\zeta < 1.1$, the LNG is simply too close to a binary methane/ethane mixture for RPT to occur.

- The typical range of $\zeta \in [1.1, 1.4]$ yields Leidenfrost fractions of $z_{\mathrm{L}} \in [0, 0.5]$. This means that the LNG will have to boil down to less than 50% methane before the conditions for RPT triggering are met.

- For an LNG mixture starting at 90% methane, the typical range of $\zeta \in [1.1, 1.4]$ yields $\nu \in [0.1, 0.2]$. This means that only 10%–20% of the original liquid amount (on a molar basis) remains when the conditions for RPT triggering are met.

4.7 RPT consequence quantification

The previous section was concerned with prediction of triggering, i.e., the conditions that must be met for RPT to occur. A second problem to consider is what happens after, when the macroscopic vapor explosion occurs. This is not completely separate from the question of triggering, because the mixture that undergoes the vapor explosion is not the original LNG, but rather the mixture corresponding to the Leidenfrost fraction.

According to the RPT chain-of-events described in Sec. 1.6, after film-boiling collapse (Leidenfrost transition) there is rapid superheating, homogeneous nucleation and explosive expansion. These steps were illustrated schematically in Fig. 1.5. It is now time to describe these processes quantitatively, and we do this by approximating the final two steps (red dashed curve in Fig. 1.5) by the following idealized two-step process:

1. **Equilibration**: Calculate the energy and density of the the mixture exactly when it reaches the superheat limit after film-boiling collapse. The temperature of this state is the superheat limit (T_{SHL}) corresponding to the Leidenfrost fraction (z_{L}). Then, find the corresponding quasi-equilibrium state, with the same energy, density and composition. This yields a new high-pressure intermediate state (T^*, p^*).
2. **Isentropic expansion**: The intermediate state (T^*, p^*) is called a quasi-equilibrium state because while it is in local equilibrium, it is not in mechanical equilibrium with the surroundings ($p^* \gg 1\,\mathrm{atm}$). This leads to a rapid expansion, which is approximated as an isentropic

process. The end-state of this expansion may then be found as the state at atmospheric pressure that has the same entropy as the high-pressure intermediate state.

Even with these simplifying assumptions, making such a calculation involves a set of quite complex thermodynamic algorithms. Generally these involve iteratively searching for the most stable two-phase state with certain constrained parameters, given that both phases are described by the chosen equation of state [45, 46]. For the equilibration stage one needs to implement an algorithm for energy and density as the given parameters, and for the expansion stage one needs to implement an algorithm for entropy and pressure as the given parameters.

The results from implementing and running such algorithms based on an LNG boil-off scenario is shown in Fig. 4.3. This involves first calculating the Leidenfrost fraction corresponding to the initial LNG mixture, calculating the corresponding superheat limit temperature, and then performing the above listed steps of equilibration and expansion. There are two significant numbers to take away from such a calculation:

- **Peak pressure** (p^*): This is found as the pressure of the intermediate state before expansion. The value may be interpreted as an estimate for the peak pressure seen in the vapor-explosion event.
- **Explosive yield/energy** (E): This is found as the mechanical work done by the expansion process. Since the process is assumed to be isentropic (reversible and adiabatic), it follows from classical thermodynamics that the work done by the process is simply the difference in total enthalpy between the initial and final states of the expansion. Note that this merely yields an energy per amount triggered (i.e. per mole or kilogram), not a total amount.

In Paper D, such calculations were run throughout the relevant range of ζ, and the results for p^* and E were correlated with this parameter. The general findings were:

- Peak pressure is predicted to be in the range of 20–60 bar, and increases with increasing alkane factor ζ.
- Explosive yield per triggered mass is generally in the range of 50–80 $\mathrm{kJ\,kg^{-1}}$. This is equivalent to about 10–20 g TNT per kg LNG.

Note that the numbers for explosive yield are calculated as energy per mass of triggered LNG. This amount of LNG is at most the amount remaining at the time of triggering, which is much less than the original amount spilled.

Thus, to consider total potential yield from a given amount of spilled LNG, the reduction factor (ν) in Eq. (4.13) must also be considered. Details of these considerations may be found in Paper D[109].

Note that while this two-stage explosion may be seen as a rough approximation, it is the combination of an isolated and an isentropic process. Any other real process with the same initial and final states will imply irreversible loss of energy, and thus the present calculation should yield a conservative (worst-case) bound for the explosive yield.

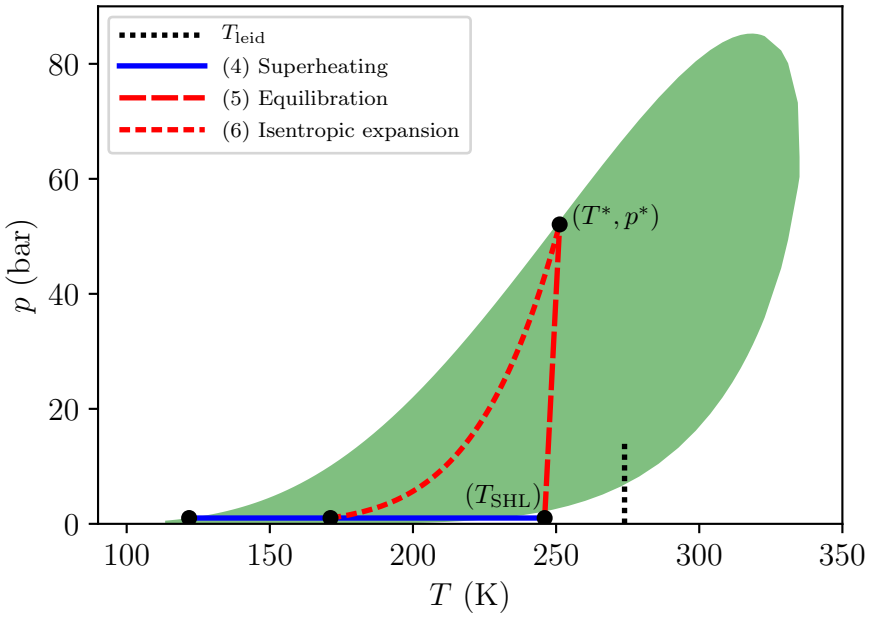

Figure 4.3: Example result from an approximate equilibration and expansion calculation as described in Sec. 4.7, based on the Leidenfrost fraction of a mixture where the non-methane part is 50% ethane, 30% propane and 20% butane. The numbering of each process is in reference to the list in Sec. 1.6: Once the methane fraction is reduced to the Leidenfrost fraction, the Leidenfrost temperature is equal to the water temperature. By definition, this means that film-boiling collapse occurs, and the LNG is rapidly superheated (4). This proceeds until the superheat limit (T_{SHL}), where the liquid is forced to equilibrate (5). Since the resulting quasi-equilibrium state is of very high pressure, it rapidly expands to reach mechanical equilibrium with the atmosphere (6).

4.8 Conclusions

Based on a highly simplified model for the Leidenfrost temperature and a validated model for the superheat limit temperature, we were able to quantify the fundamental RPT triggering criterion from Chapter 1, Eq. (1.1). The quantification was made in terms of the decreasing methane fraction as the progress parameter of LNG boil-off. The most useful results from this analysis are Eqs. (4.12) and (4.13). These equations quantify the critical methane-fraction of triggering, and the amount of LNG remaining once this fraction is reached, as functions of a single scalar case parameter, ζ. The implications of this model is thoroughly explored in Paper D [109], and the most important discoveries may be summarized as:

- Spilled LNG will typically boil down to about 10–20% of the original amount before RPT triggering is possible. At this point, the mixture is usually less than 50% methane.
- The RPT explosive yield per triggered LNG mass will generally be in the range $50\,\mathrm{kJ\,kg^{-1}}$ to $80\,\mathrm{kJ\,kg^{-1}}$. This yield is equivalent to 10 g to 20 g TNT per kg LNG.
- The peak explosive pressure will generally be in the range of 20 bar to 60 bar, but this is very dependent on the alkane factor, ζ.
- Potential explosive yield and pressure may be reduced by decreasing the alkane factor, ζ. This is achieved by removing the alkanes heavier than ethane from the LNG (e.g. propane and butane).
- The relative amount of LNG remaining at the time of triggering may be reduced by increasing the initial fraction of methane. This should be done in a way that does not increase the value of ζ.

The weakest point of the triggering prediction is that it is highly dependent on the simplified Leidenfrost model, Eq. (4.4). This model does not have a strong theoretical basis. Also, while quite accurate for pure methane, there seems to be insufficient data in the literature to validate it for hydrocarbon mixtures like LNG.

Regarding the RPT consequence predictions, one significant issue remains: The estimates for explosive yield obtained herein from thermodynamics are in terms of energy per triggered amount. However, we have no way of estimating how much LNG participates in each individual explosive event. We could assume that all the LNG remaining when the triggering conditions are met undergoes RPT simultaneously, but this will likely overestimate the explosive yield of the event.

Finally, note that Eq. (1.1) must be taken as a criterion for *delayed* RPT, as defined by the LLNL large-scale spill program described in Sec. 1.4.4. Early RPT, which is triggered somewhere in the chaotic mixing region at the point of impact between an LNG jet and a the water surface, likely depends on a whole other set of complex fluid dynamical consideration. This is considered outside the scope of this thesis.

Chapter 5

Overview of research articles

This chapter serves as an overview of the academic journal articles published (or submitted) as part of the work on this thesis. Their complete manuscripts are attached in Part II. The most relevant results, and my contribution to them, are summarized below:

Paper A
Thermocapillary instability as a mechanism for film boiling collapse
Eskil Aursand, Stephen H. Davis, Tor Ytrehus
Published in *Journal of Fluid Mechanics*.
(2018) Vol. 852, pp. 283–312
https://doi.org/10.1017/jfm.2018.545

Significance to thesis: Derivation of a new long-wave model for horizontal film-boiling, and the discovery of a novel model for the Leidenfrost temperature of pure fluids.

Role: Main author. Wrote the manuscript with guidance and feedback from the co-authors.

Status: Accepted and published.

Paper A [97] covers the derivation of a long-wave model for horizontal film-boiling using a non-equilibrium evaporation model in order to allow for thermocapillary effects. We obtained a highly nonlinear PDE for the film-thickness function, and by applying linear stability analysis we identified

three distinct stability regimes based on film thickness. Of particular interest was the intermediate regime, whose stability was seemingly dependent on a struggle between a stabilizing vapor-thrust effect and a destabilizing thermocapillary effect. We discovered that the wall superheat that causes a balance between the two effects is a remarkably good predictor for the Leidenfrost point. While the available experimental data was insufficient for making a definite conclusion, this constitutes a possible new model for the Leidenfrost temperature of pure fluids. This has profound implications for the apparent importance of thermocapillary instabilities in film-boiling collapse.

Paper B
Inclination dependence of planar film boiling stability
Eskil Aursand
Published in *International Journal of Multiphase Flow.*
(2018) Vol. 106, pp. 243–253
https://doi.org/10.1016/j.ijmultiphaseflow.2018.05.010

Significance to thesis: The discovery that low-Reynolds long-wave models are not sufficient for predicting the dominant inertial instabilities in vertical film boiling.

Role: Sole author.

Status: Accepted and published.

Paper B [110] describes the discovery that the low-Reynolds (lubrication approximation) long-wave models are incapable of predicting the inertial (Kelvin–Helmholtz type) instabilities that are seen in experiments on inclined and vertical film boiling. In this work, I developed a hybrid model involving potential-flow theory in order to predict inertial instabilities.

Paper C
Inclined film boiling: Film stability and heat transfer
Eskil Aursand, Stephen H. Davis
Published in *International Journal of Multiphase Flow.*
(2019) Vol. 111, pp. 175–187
https://doi.org/10.1016/j.ijmultiphaseflow.2018.11.017

Significance to thesis: Expansion of the long-wave film-boiling model from Paper A to include inertial terms.

Role: Main author. I wrote the manuscript with guidance and feedback from the co-author.

Status: Accepted and published.

Paper C [86] was sparked by the unsatisfactory nature of the hybrid model that I resorted to in Paper B. We wanted to capture the inertial instabilities of vertical and inclined film-boiling consistently within the long-wave framework. This required us to generalize the approach from Paper A by retaining the inertial (ϵRe) terms in the governing equations. By averaging both the continuity and momentum equations across the vapor film, we arrived at a set of two coupled PDEs describing the vapor film dynamics. This model was then used to successfully predict the heat transfer coefficient for a wide range of fluids in vertical film boiling.

Paper D
Predicting triggering and consequence of delayed LNG RPT
Eskil Aursand, Morten Hammer
Published in *Journal of Loss Prevention in the Process Industries.* (2018) Vol. 55, pp. 124–133
https://doi.org/10.1016/j.jlp.2018.06.001

Significance to thesis: Developed a practical framework for quantitative RPT risk-assessment in simplified spill scenarios.

Role: Main author. I wrote the manuscript with guidance and feedback from the co-author. I implemented the top-level code for spill-progression and RPT triggering prediction, while the co-author wrote a large part of the underlying thermodynamic algorithms.

Status: Accepted and published.

Paper D [109] essentially covers the topic of Chapter 4, but with considerably more detailed discussions on the implications for risk-assessment. In this paper we developed a model for RPT prediction in LNG spills based on thermodynamics, nucleation theory and a simplified Leidenfrost model. We discovered that the model predictions may be accurately characterized by two independent parameters alone: the initial fraction of methane and the

molar mass of the remaining non-methane part. Based on this model we developed correlations for risk assessment which may be used without access to the underlying thermodynamic algorithms, and we discussed practical advice for risk mitigation.

Paper E
Comparison of kinetic theory evaporation models for liquid thin-films
Eskil Aursand, Tor Ytrehus
Submitted to *International Journal of Multiphase Flow.*

Significance to thesis: Assessment of the possible choices for non-equilibrium evaporation model, and the derivation of linearizations suitable for use in the long-wave film-boiling models.

Role: Main author. I wrote most of the manuscript and all of the code, while the co-author wrote some sections of the manuscript.

Status: Submitted.

Paper E [111] was sparked by the observation that many of the developments done by the kinetic-theory community on evaporation have seen very slow adoption in the fluid mechanics and heat transfer communities. This article was an attempt at bringing the two fields together by demonstrating how the microscopic evaporation models may be applied in macroscopic cases and by highlighting when such models are necessary and useful. The first part of this paper has significant overlap with the overview and derivation of kinetic-theory evaporation models found in Chapter 2. The second part, which was not included in Chapter 2, is an application and comparison of these models to the case of an evaporating liquid film.

Paper F

The spinodal of single- and multi-component fluids and its role in the development of modern equations of state

Peder Aursand, Magnus Gjennestad, Eskil Aursand, Morten Hammer, Øivind Wilhelmsen

Published in *Fluid Phase Equilibria*.
(2017) Vol. 436, pp. 98–112
https://doi.org/10.1016/j.fluid.2016.12.018

Significance to thesis: Validating the ability of classical nucleation theory to accurately predict the superheat limit of hydrocarbon mixtures like LNG.

Role: Co-author (minor contribution). I participated in the validation of the superheat limit predictions against experimental data, and helped with the general quality-assurance of the manuscript.

Status: Accepted and published

Paper F [47] covers several interesting thermodynamic concepts both theoretical and practical. However, its significance for this thesis (and my contribution) mainly lies in the experimental validation of the superheat-limit predicted by classical nucleation theory. In particular, the work showed that our relatively ad-hoc extension of the model to mixtures was reasonably accurate for hydrocarbon mixtures. This was a significant conclusion, as it essentially resolved one half of the fundamental RPT triggering criterion in Eq. (1.1). The validated superheat-limit model was then used to construct the LNG RPT prediction framework of Chapter 4 and Paper D.

Chapter 6

Conclusions and Outlook

6.1 Summary of findings

As shown in Chapter 1, a thorough review of the literature on LNG RPT led to the conclusion that no satisfactory method for quantitative risk-assessment seemed to exist. With the goal of improving this situation in mind, the research in the present thesis achieved the following:

- An overview of the leading theory for the mechanisms behind LNG RPT was presented, and it was shown how its statements on the requirements for triggering may be summarized in one remarkably simple form: Eq. (1.1). However, evaluation of Eq. (1.1) required models for the *superheat-limit temperature* and the *Leidenfrost temperature* as functions of hydrocarbon composition.

- It was shown how Classical Nucleation Theory (CNT) with a simple extension to mixtures was able to predict the superheat limit of hydrocarbon mixtures with satisfactory accuracy. This settled one of the inequalities in Eq. (1.1).

- For the purposes of thin-film modeling, various non-equilibrium evaporation models from kinetic theory were analyzed and reduced to useful approximations. Then, the established long-wave formalism for modeling of thin-film flow was adapted to the case of film boiling. Beyond the resulting nonlinear model itself, linear stability analysis led to a novel model for the Leidenfrost temperature of pure fluids. While current experimental data is insufficient to draw firm conclusions, if

valid, this model would indicate that thermocapillary instabilities play a crucial role in instigating film-boiling collapse.

- Finally, it was demonstrated how models for the superheat limit and Leidenfrost temperature may be combined with thermodynamic algorithms to construct a framework for quantitative assessment of LNG RPT. This model was able to predict RPT triggering risk as a function of methane fraction during LNG boil-off. Based on the predicted composition at the time of triggering, a secondary thermodynamic model for the worst-case consequence of the RPT vapor explosion was also developed. Simplified correlations were derived based on these models, and practical recommendations for risk mitigation were made.

6.2 Knowledge gaps and open questions

There are two major missing pieces that must be in place in order to achieve the ultimate goal of predicting delayed RPT in LNG spills:

- A realistic and validated model for the Leidenfrost temperature of hydrocarbon mixtures. While a new Leidenfrost model was developed herein, it is not applicable to mixtures in its present form. This poses the following questions:
  - Is the critical wall superheat for stability in the intermediate regime truly a predictor for the Leidenfrost temperature, or does it fit the limited available data by mere coincidence?
  - If the former is true, how can this model be extended to mixtures?
- A model for how the LNG composition develops in space and time during realistic LNG spill scenarios with spreading and boil-off. Such a model could then be coupled to the new framework for predicting triggering as a function of composition. This poses the following questions:
  - What is the rate of heat transfer from water to LNG, and what is the resulting evaporation rate of each hydrocarbon component?
  - How does LNG spread from a localized source when it is film boiling on top of a water surface, and how does the composition vary in time and space?
  - Once RPT is triggered, how much LNG participates in each distinct explosive event?

6.3 Suggestions for further research

Based on the above mentioned open questions, we may suggest the following avenues of research in order to come closer to the goal of LNG RPT prediction:

Project A (experimental)

For the purposes of supporting or disproving the new Leidenfrost model in Sec. 3.6, it would be very useful to measure the Leidenfrost temperature for a wider array of pure fluids. As seen in Fig. 3.4, the fluids with sufficient data only cover a relatively narrow range of relative Leidenfrost temperature ($\Delta T_{\mathrm{L}}/T_{\mathrm{s}}$). According to the predictions of the present model, more extreme values can be expected to be found from fluids with abnormal values of γ, i.e. an unusually low or high temperature dependence of their surface tension.

Project B (theoretical)

If Project A yields positive results for the Leidenfrost model herein, efforts should be made to extend its validity to mixtures. Firstly, this would entail going back to Chapter 2 and generalizing the kinetic-theory evaporation models to mixtures. Secondly, the film-boiling model in Chapter 3 must be generalized to mixtures. Beyond plugging in the new evaporation models, complications are likely to arise due to variable liquid enrichment along the vapor film. In such a case Marangoni forces (tangential surface-tension gradients) may occur from the solutocapillary effect in addition to the already included thermocapillary effect.

Project C (experimental)

If a model resulting from Project B is ever to be validated, experimental data on the Leidenfrost temperature of LNG-like hydrocarbon mixtures is needed, and this appears to be lacking in the open literature. Efforts should be made to measure the Leidenfrost temperature for a number of such mixtures.

Project D (experimental)

It would be useful to experimentally measure the heat-transfer coefficient of LNG-on-water film boiling as a function of composition and water temperature. This could then be used to select the most accurate heat-transfer model among the various available ones, or to develop a new one.

Project E (theoretical/computational)

Once a reliable model for the boiling curve of LNG mixtures (including the Leidenfrost point) is in place, one could develop a multi-physics model for simulating the evolution of an LNG spill while estimating the risk of RPT triggering. This could involve developing a spreading model based on the shallow-water equations, which could then be coupled to models for heat flux and evaporation rate as functions of local composition. During the spill event, the triggering model of Chapter 4 may be applied locally using the current local composition as input. This project (using a simplified Leidenfrost model) is already in progress at SINTEF Energy Research.

Bibliography

[1] R. M. Pitblado and J. L. Woodward. "Highlights of LNG risk technology". In: *Journal of Loss Prevention in the Process Industries* 24.6 (2011), pp. 827 –836. DOI: 10.1016/j.jlp.2011.06.009.

[2] S. Kumar, H.-T. Kwon, K.-H. Choi, W. Lim, J. H. Cho, K. Tak, and I. Moon. "LNG: An eco-friendly cryogenic fuel for sustainable development". In: *Applied Energy* 88.12 (2011), pp. 4264–4273. DOI: 10.1016/j.apenergy.2011.06.035.

[3] R. C. Reid. "Rapid phase transitions from liquid to vapor". In: 12 (1983), pp. 105–208. DOI: 10.1016/S0065-2377(08)60252-5.

[4] A. Luketa-Hanlin. "A review of large-scale LNG spills: Experiments and modeling". In: *Journal of Hazardous Materials* 132 (2006), pp. 119 –140. DOI: 10.1016/j.jhazmat.2005.10.008.

[5] Stephen Shaw, John Baik, and Robin Pitblado. "Consequences of underwater releases of LNG". In: *Process Safety Progress* 24.3 (2005), pp. 175–180. DOI: 10.1002/prs.10088.

[6] P. Cleaver, M. Johnson, and B. Ho. "A summary of some experimental data on LNG safety". In: *Journal of Hazardous Materials* 140.3 (2007), pp. 429–438. DOI: 10.1016/j.jhazmat.2006.10.047.

[7] J. A. Alderman. "Introduction to LNG safety". In: *Process Safety Progress* 24.3 (2005), pp. 144–151. DOI: 10.1002/prs.10085.

[8] M. Hightower, L. Gritzo, and A. Luketa-Hanlin. "Safety implications of a large LNG tanker spill over water". In: *Process safety progress* 24.3 (2005), pp. 168–174. DOI: 10.1002/prs.10089.

[9] J. Havens and T. Spicer. "United states regulations for siting LNG terminals: Problems and potential". In: *Journal of Hazardous Materials* 140.3 (2007), pp. 439 –443. DOI: 10.1016/j.jhazmat.2006.10.020.

[10] P. K. Raj and L. A. Bowdoin. "Underwater LNG release: Does a pool form on the water surface? What are the characteristics of the vapor released?" In: *Journal of Loss Prevention in the Process Industries* 23.6 (2010), pp. 753 –761. DOI: 10.1016/j.jlp.2010.06.003.

[11] K. Forte and D. Ruf. "Safety Challenges of LNG Offshore Industry and Introduction to Risk Management". In: *ASME 2017 36th International Conference on Ocean, Offshore and Arctic Engineering*. American Society of Mechanical Engineers. 2017, V03BT02A016–V03BT02A016. DOI: 10.1115/OMAE2017-61027.

[12] D.S Burgess, J.N. Murphy, and M.G. Zabetakis. "Hazards of LNG spillage in marine transportation". In: *U.S. Department of Interior, Bureau of Mines, SRS Report No. S4105, February 1970.* (1970).

[13] D. L. Katz and C. M. Sliepcevich. "LNG/Water Explosions: Cause & Effect". In: *Hydrocarbon processing* 50.11 (1971).

[14] D. L. Katz. "Superheat-limit explosions". In: *Chemical Engineering Progress* 68.5 (1972), p. 68.

[15] E. Nakanishi and R.C. Reid. "Liquid Natural Gas - Water Reactions". In: *Chem. Eng. Progress* Vol. 67 (12) (1971), pp. 36 –41.

[16] T. Enger. "Explosive Boiling of Liquefied Gases on Water". In: *Proceeding of the conference on LNG import and terminal safety*. Boston, 1972.

[17] T. Enger and D.E. Hartman. "Mechanics of the LNG-water interaction". In: *AGA Distribution Conference, Atlanta*. 1972.

[18] T. Enger and D. E. Hartman. "Explosive boiling of liquefied gases on water". In: *Proceeding of the conf. on LNG import and terminal safety, Boston*. 1972.

[19] T. Enger, D. E. Hartman, and E. V. Seymour. "Explosive Boiling of Liquefied Hydrocarbon/Water Systems". In: *Advances in Cryogenic Engineering: Proceedings of the 1972. Cryogenic Engineering Conference. National Bureau of Standards. Boulder, Colorado. August 9–11, 1972*. Ed. by K. D. Timmerhaus. Boston, MA: Springer US, 1973, pp. 32–41. ISBN: 9781468431117. DOI: 10.1007/978-1-4684-3111-7_4.

[20] E.M. Drake, A.A. Jeje, and R.C. Reid. "Transient boiling of liquefied cryogens on a water surface: I. Nitrogen, Methane and Ethane". In: *International Journal of Heat and Mass Transfer* 18.12 (1975), pp. 1361 –1368. DOI: 10.1016/0017-9310(75)90249-5.

[21] E. M. Drake, A. A. Jeje, and R. C. Reid. "Transient boiling of liquefied cryogens on a water surface: II. Light hydrocarbon mixtures". In: *International Journal of Heat and Mass Transfer* 18.12 (1975), pp. 1369–1375. DOI: 10.1016/0017-9310(75)90250-1.

[22] A. K. Dincer, E. M. Drake, and R. C. Reid. "Boiling of liquid nitrogen and methane on water. The effect of initial water temperature". In: *International Journal of Heat and Mass Transfer* 20.2 (1977), pp. 176–177. DOI: 10.1016/0017-9310(77)90011-4.

[23] J.A. Valencia-Chavez and R.C. Reid. "The effect of composition on the boiling rates of liquefied natural gas for confined spills on water". In: *International Journal of Heat and Mass Transfer* 22.6 (1979), pp. 831 –838. DOI: 10.1016/0017-9310(79)90023-1.

[24] H.-R. Chang, R. C. Reid, and J. A. Fay. "Boiling and spreading of liquid nitrogen and liquid methane on water". In: *International Communications in Heat and Mass Transfer* 10.3 (1983), pp. 253–263. DOI: 10.1016/0735-1933(83)90010-6.

[25] W. M. Porteous and M. Blander. "Limits of superheat and explosive boiling of light hydrocarbons, halocarbons, and hydrocarbon mixtures". In: *AIChE Journal* 21.3 (1975), pp. 560–566. DOI: 10.1002/aic.690210319.

[26] W. M. Porteous and R. C. Reid. "Light hydrocarbon vapor explosions". In: *Chem. Eng. Prog.* Vol. 72:5 (1976), pp. 83–89.

[27] R.P. Koopman and D.L. Ermak. "Lessons learned from LNG safety research". In: *Journal of Hazardous Materials* 140 (2007), pp. 412 –428. DOI: 10.1016/j.jhazmat.2006.10.042.

[28] R. P. Koopman, J. Baker, R. T. Cederwall, H. C. Jr. Goldwire, W. J. Hogan, L. M. Kamppinen, R. D. Kiefer, J. W. McClure, T. G. McRae, and D. L. Morgan. *Burro Series Data Report. LLNL/NWC 1980 LNG Spill Test, UCID 19075.* Tech. rep. LLNL, 1982.

[29] H.C. Goldwire Jr, H.C. Rodean, R.T. Cederwall, E.J. Kansa, R.P. Koopman, J.W. McClure, T.G. McRae, L.K. Morris, L. Kamppinen, and R.D. Kiefer. *Coyote series data report LLNL/NWC 1981 LNG spill tests dispersion, vapor burn, and rapid-phase-transition, UCID-19953, Vol. 1.* Tech. rep. LLNL, 1983.

[30] T.C. Brown, R.T. Cederwall, S.T. Chan, D.L. Ermak, R.P. Koopman, K.C. Lamson, J.W. McClure, and L.K. Morris. *Falcon series data report: 1987 LNG vapor barrier verification field trials*. Tech. rep. LLNL, 1990.

[31] G.A. Melhem, S. Saraf, and H. Ozog. "LNG Properties and Hazards, Understanding LNG Rapid Phase Transitions (RPT)". In: *An ioMosaic Corporation Whitepaper* (2006).

[32] P. Cleaver, C. Humphreys, M. Gabillard, D. Nédelka, R. Heiersted, and J. Dahlsveen. "Rapid Phase Transition of LNG". In: *12th International Conference on Liquefied Natural Gas, LNG12*. Perth, Australia, 1998.

[33] D. Nédelka, V. Sauter, J. Goanvic, and R. Ohba. "Last developments in rapid phase transition knowledge and modeling techniques". In: *Offshore Technology Conference*. 2003. DOI: 10.4043/15228-MS.

[34] D. F. Fletcher and A. Thyagaraja. "The CHYMES coarse mixing model". In: *Progress in Nuclear Energy* 26.1 (1991), pp. 31 –61. DOI: 10.1016/0149-1970(91)90031-J.

[35] D. F. Fletcher. "Propagation investigations using the CULDESAC model". In: *Nuclear Engineering and Design* 155 (1995), pp. 271 – 287. DOI: 10.1016/0029-5493(94)00877-2.

[36] E. P. Hicks and D. C. Menzies. "Theoretical studies on the fast reactor maximum accident". In: *Proceedings of Conference on Safety, Fuels and Core Design in Large Fast Power Reactors (ANL–7120)*. 1965, pp. 654–670.

[37] G. Berthoud. "Vapor Explosions". In: *Annual Review of Fluid Mechanics* 32.1 (2000), pp. 573–611. DOI: 10.1146/annurev.fluid.32.1.573.

[38] R. Bubbico and E. Salzano. "Acoustic analysis of blast waves produced by rapid phase transition of LNG released on water". In: *Safety Science* 47.4 (2009), pp. 515–521. DOI: 10.1016/j.ssci.2008.07.033.

[39] M. Hightower, L. Gritzo, A. Luketa-Hanlin, J. Covan, S. Tieszen, G. Wellman, M. Irwin, M. Kaneshige, B. Melof, C. Morrow, and D. Ragland. *Guidance on risk analysis and safety implications of a large liquified natural gas (LNG) spill over water*. Tech. rep. Sandia Report SAND2004-6258. Albuquerque, New Mexico: Sandia National Laboratories, 2004.

[40] R. M. Pitblado, J. Baik, G. J. Hughes, C. Ferro, and S. J. Shaw. "Consequences of liquefied natural gas marine incidents". In: *Process Safety Progress* 24.2 (2005), pp. 108–114. DOI: 10.1002/prs.10073.

[41] E. Vanem, P. Antão, I. Østvik, and F. D. C. de Comas. "Analysing the risk of LNG carrier operations". In: *Reliability Engineering & System Safety* 93.9 (2008), pp. 1328–1344. DOI: 10.1016/j.ress.2007.07.007.

[42] D.-Y. Peng and D. B. Robinson. "A new two-constant equation of state". In: *Industrial & Engineering Chemistry Fundamentals* 15.1 (1976), pp. 59–64. DOI: 10.1021/i160057a011.

[43] R. C. Reid and B. L. Beegle. "Critical point criteria in Legendre transform notation". In: *AIChE Journal* 23.5 (1977), pp. 726–732. DOI: 10.1002/aic.690230515.

[44] J. W. Gibbs. "On the equilibrium of heterogeneous substances". In: *American Journal of Science* 16.96 (1878), pp. 441–458. DOI: 10.2475/ajs.s3-16.96.441.

[45] M. L. Michelsen and J. M. Mollerup. *Thermodynamic models: Fundamentals and computational aspects*. second. Holte, Denmark: Tie-Line Publictions, 2007. ISBN: 8798996134.

[46] Ø. Wilhelmsen, A. Aasen, G. Skaugen, P. Aursand, A. Austegard, E. Aursand, M. Gjennestad, H. Lund, G. Linga, and M. Hammer. "Thermodynamic Modeling with Equations of State: Present Challenges with Established Methods". In: *Industrial & Engineering Chemistry Research* 56.13 (2017), pp. 3503–3515. DOI: 10.1021/acs.iecr.7b00317.

[47] P. Aursand, M. Gjennestad, E. Aursand, M. Hammer, and Ø. Wilhelmsen. "The spinodal of single- and multi-component fluids and its role in the development of modern equations of state". In: *Fluid Phase Equilibria* 436 (2017), pp. 98–112. DOI: 10.1016/j.fluid.2016.12.018.

[48] V. K. Dhir. "Boiling heat transfer". In: *Annual review of fluid mechanics* 30.1 (1998), pp. 365–401. DOI: 10.1146/annurev.fluid.30.1.365.

[49] S. Nukiyama. "The maximum and minimum values of the heat Q transmitted from metal to boiling water under atmospheric pressure". In: *Journal of Japan Society of Mechanical Engineers* 37 (1934), pp. 367–374.

[50] T. Ytrehus. "Molecular-flow effects in evaporation and condensation at interfaces". In: *Multiphase Science and Technology* 9.3 (1997), pp. 205–327. DOI: 10.1615/MultScienTechn.v9.i3.10.

[51] H. Hertz. "Ueber die Verdunstung der Flüssigkeiten, insbesondere des Quecksilbers, im luftleeren Raume". In: *Annalen der Physik* 253.10 (1882), pp. 177–193. DOI: 10.1002/andp.18822531002.

[52] M. Knudsen. "Die maximale verdampfungsgeschwindigkeit des quecksilbers". In: *Annalen der Physik* 352.13 (1915), pp. 697–708. DOI: 10.1002/andp.19153521306.

[53] R. W. Schrage. *A theoretical study of interphase mass transfer*. New York: Columbia University Press, 1953.

[54] M.N. Kogan. "Kinetic theory in aerothermodynamics". In: *Progress in Aerospace Sciences* 29.4 (1992), pp. 271–354. DOI: 10.1016/0376-0421(92)90007-5.

[55] A. Frezzotti and P. Barbante. "Kinetic theory aspects of non-equilibrium liquid-vapor flows". In: *Mechanical Engineering Reviews* 4.2 (2017), pp. 16–00540. DOI: 10.1299/mer.16-00540.

[56] A.J. Patton and G.S. Springer. "A kinetic theory description of liquid vapor phase change". In: *Proc. 6th International Symposium of Rarefied Gas Dynamics*. Vol. 2. 1969, pp. 1497–1501.

[57] P.N. Shankar and F. E. Marble. "Kinetic theory of transient condensation and evaporation at a plane surface". In: *The physics of fluids* 14.3 (1971), pp. 510–516. DOI: 10.1063/1.1693464.

[58] Y.-P. Pao. "Application of kinetic theory to the problem of evaporation and condensation". In: *The Physics of Fluids* 14.2 (1971), pp. 306–312. DOI: 10.1063/1.1693429.

[59] Y.-P. Pao. "Temperature and density jumps in the kinetic theory of gases and vapors". In: *The Physics of Fluids* 14.7 (1971), pp. 1340–1346. DOI: 10.1063/1.1693612.

[60] M.N. Kogan and N.K. Makashev. "Role of the Knudsen layer in the theory of heterogeneous reactions and in flows with surface reactions". In: *Fluid Dynamics* 6.6 (1971), pp. 913–920. DOI: 10.1007/BF01019794.

[61] Y. Sone and Y. Onishi. "Kinetic theory of evaporation and condensation–Hydrodynamic equation and slip boundary condition". In: *Journal of the Physical Society of Japan* 44.6 (1978), pp. 1981–1994. DOI: 10.1143/JPSJ.44.1981.

[62] T. Ytrehus. "Theory and experiments on gas kinetics in evaporation". In: *Rarefied Gas Dynamics* 2 (1977), pp. 1197–1212. DOI: 10.2514/5.9781600865251.1197.1212.

[63] C. Cercignani. *The Boltzmann Equation and Its Applications*. Berlin: Springer, 1988. ISBN: 9781461210399.

[64] A. F. Mills. *Heat and Mass Transfer*. Boca Raton: CRC Press, 1995. ISBN: 9780256114430.

[65] M. D. Arthur and C. Cercignani. "Non-existence of a steady rarefied supersonic flow in a half-space". In: *Zeitschrift für angewandte Mathematik und Physik ZAMP* 31.5 (1980), pp. 634–645. DOI: 10.1007/BF01596163.

[66] S. Cheng, J. B. Lechman, S. J. Plimpton, and G. S. Grest. "Evaporation of Lennard-Jones fluids". In: *The Journal of chemical physics* 134.22 (2011), p. 224704. DOI: 10.1063/1.3595260.

[67] T. Tsuruta and G. Nagayama. "Molecular dynamics studies on the condensation coefficient of water". In: *The Journal of Physical Chemistry B* 108.5 (2004), pp. 1736–1743. DOI: 10.1021/jp035885q.

[68] B.-Y. Cao, J.-F. Xie, and S. S. Sazhin. "Molecular dynamics study on evaporation and condensation of n-dodecane at liquid–vapor phase equilibria". In: *The Journal of chemical physics* 134.16 (2011), p. 164309. DOI: 10.1063/1.3579457.

[69] J.-F. Xie, S. S. Sazhin, and B.-Y. Cao. "Molecular dynamics study of the processes in the vicinity of the n-dodecane vapour/liquid interface". In: *Physics of Fluids* 23.11 (2011), p. 112104. DOI: 10.1063/1.3662004.

[70] T. Ishiyama, S. Fujikawa, T. Kurz, and W. Lauterborn. "Nonequilibrium kinetic boundary condition at the vapor-liquid interface of argon". In: *Physical Review E* 88.4 (2013), p. 042406. DOI: 10.1103/PhysRevE.88.042406.

[71] E. K. Iskrenova and S. S. Patnaik. "Molecular dynamics study of octane condensation coefficient at room temperature". In: *International Journal of Heat and Mass Transfer* 115 (2017), pp. 474–481. DOI: j.ijheatmasstransfer.2017.07.064.

[72] Z. Liang, T. Biben, and P. Keblinski. "Molecular simulation of steady-state evaporation and condensation: Validity of the Schrage relationships". In: *International Journal of Heat and Mass Transfer* 114 (2017), pp. 105–114. DOI: j.ijheatmasstransfer.2017.06.025.

[73] A. Oron, S. H. Davis, and S. G. Bankoff. "Long-scale evolution of thin liquid films". In: *Reviews of modern physics* 69.3 (1997), pp. 931–980. DOI: 10.1103/RevModPhys.69.931.

[74] J. P. Burelbach, S. G. Bankoff, and S. H. Davis. "Nonlinear stability of evaporating/condensing liquid films". In: *Journal of Fluid Mechanics* 195 (1988), pp. 463–494. DOI: 10.1017/S0022112088002484.

[75] T. G. Myers. "Thin films with high surface tension". In: *SIAM Review* 40.3 (1998), pp. 441–462. DOI: 10.1137/S003614459529284X.

[76] R. V. Craster and O. K. Matar. "Dynamics and stability of thin liquid films". In: *Reviews of modern physics* 81.3 (2009), pp. 1131–1198. DOI: 10.1103/RevModPhys.81.1131.

[77] C. H. Panzarella, S. H. Davis, and S. G. Bankoff. "Nonlinear dynamics in horizontal film boiling". In: *Journal of Fluid Mechanics* 402 (2000), pp. 163–194. DOI: 10.1017/S0022112099006801.

[78] S. H. Davis. "Thermocapillary instabilities". In: *Annual Review of Fluid Mechanics* 19.1 (1987), pp. 403–435. DOI: 10.1146/annurev.fl.19.010187.002155.

[79] N. Zuber. "Hydrodynamic aspects of boiling heat transfer". PhD thesis. Univ. of California, Los Angeles, CA (USA), June 1959.

[80] P. J. Berenson. "Film-boiling heat transfer from a horizontal surface". In: *Journal of Heat Transfer* 83.3 (1961), pp. 351–356. DOI: 10.1115/1.3682280.

[81] P. Spiegler, J. Hopenfeld, M. Silberberg, C. F. Bumpus, and A. Norman. "Onset of stable film boiling and the foam limit". In: *International Journal of Heat and Mass Transfer* 6.11 (1963), pp. 987–989. DOI: 10.1016/0017-9310(63)90053-X.

[82] S.-C. Yao and R. E. Henry. "An investigation of the minimum film boiling temperature on horizontal surfaces". In: *Journal of Heat Transfer* 100.2 (1978), pp. 260–267. DOI: 10.1115/1.3450793.

[83] J. D. Bernardin and I. Mudawar. "The Leidenfrost point: experimental study and assessment of existing models". In: *Journal of Heat Transfer* 121.4 (1999), pp. 894–903. DOI: 10.1115/1.2826080.

[84] P. K. Kundu, I. M. Cohen, and D. R. Dowling. *Fluid Mechanics*. 5th. Cambridge: Academic Press, 2007. ISBN: 9780123821003.

[85] J.A. Moriarty, L.W. Schwartz, and E.O. Tuck. "Unsteady spreading of thin liquid films with small surface tension". In: *Physics of Fluids A: Fluid Dynamics* 3.5 (1991), pp. 733–742. DOI: 10.1063/1.858006.

[86] E. Aursand and S. H. Davis. "Inclined film boiling: Film stability and heat transfer". In: *International Journal of Multiphase Flow* 111 (2019), pp. 175–187. DOI: 10.1016/j.ijmultiphaseflow.2018.11.017.

[87] V. Y. Shkadov. "Wave flow regimes of a thin layer of viscous fluid subject to gravity". In: *Fluid Dynamics* 2.1 (1967), pp. 29–34. DOI: 10.1007/BF01024797.

[88] V. Y. Shkadov. "Wave-flow theory for a thin viscous liquid layer". In: *Fluid Dynamics* 3.2 (1968), pp. 12–15. DOI: 10.1007/BF01013543.

[89] S. V Alekseenko, V. E. Nakoryakov, and B. G. Pokusaev. "Wave formation on vertical falling liquid films". In: *International journal of multiphase flow* 11.5 (1985), pp. 607–627. DOI: 10.1016/0301-9322(85)90082-5.

[90] T. Prokopiou, M. Cheng, and H.-C. Chang. "Long waves on inclined films at high Reynolds number". In: *Journal of fluid mechanics* 222 (1991), pp. 665–691. DOI: 10.1017/S002211209100126X.

[91] J.-J. Lee and C. C. Mei. "Stationary waves on an inclined sheet of viscous fluid at high Reynolds and moderate Weber numbers". In: *Journal of Fluid Mechanics* 307 (1996), pp. 191–229. DOI: 10.1017/S0022112096000092.

[92] C. Ruyer-Quil and P. Manneville. "Modeling film flows down inclined planes". In: *The European Physical Journal B-Condensed Matter and Complex Systems* 6.2 (1998), pp. 277–292. DOI: 10.1007/s100510050550.

[93] C. Ruyer-Quil and P. Manneville. "Improved modeling of flows down inclined planes". In: *The European Physical Journal B-Condensed Matter and Complex Systems* 15.2 (2000), pp. 357–369. DOI: 10.1007/s100510051137.

[94] C. Ruyer-Quil and P. Manneville. "Further accuracy and convergence results on the modeling of flows down inclined planes by weighted-residual approximations". In: *Physics of Fluids* 14.1 (2002), pp. 170–183. DOI: 10.1063/1.1426103.

[95] M. Bestehorn, Q. Han, and A. Oron. "Nonlinear pattern formation in thin liquid films under external vibrations". In: *Physical Review E* 88.2 (2013), p. 023025. DOI: 10.1103/PhysRevE.88.023025.

[96] M. Bestehorn. "Laterally extended thin liquid films with inertia under external vibrations". In: *Physics of Fluids* 25.11 (2013), p. 114106. DOI: 10.1063/1.4830255.

[97] E. Aursand, S. H. Davis, and T. Ytrehus. "Thermocapillary instability as a mechanism for film boiling collapse". In: *Journal of Fluid Mechanics* 852 (2018), pp. 283–312. DOI: 10.1017/jfm.2018.545.

[98] P. J. Linstrom and W. G. Mallard, eds. *NIST Chemistry WebBook, NIST Standard Reference Database Number 69*. National Institute of Standards and Technology, Gaithersburg MD, 20899, 2017. DOI: 10.18434/T4D303.

[99] A. Sakurai, M. Shiotsu, and K. Hata. "Effects of system pressure on minimum film boiling temperature for various liquids". In: *Experimental Thermal and Fluid Science* 3.4 (1990), pp. 450–457. DOI: 10.1016/0894-1777(90)90043-7.

[100] B. S. Gottfried and K. J. Bell. "Film boiling of spheroidal droplets. Leidenfrost phenomenon". In: *Industrial & Engineering Chemistry Fundamentals* 5.4 (1966), pp. 561–568. DOI: 10.1021/i160020a023.

[101] Y. M. Qiao and S. Chandra. "Experiments on adding a surfactant to water drops boiling on a hot surface". In: *Proceedings of the Royal Society of London A: Mathematical, Physical and Engineering Sciences*. Vol. 453. 1959. The Royal Society. 1997, pp. 673–689. DOI: 10.1098/rspa.1997.0038.

[102] K. J. Baumeister and F. F. Simon. "Leidenfrost temperature– Its correlation for liquid metals, cryogens, hydrocarbons, and water". In: *(American Society of Mechanical Engineers, 1973.) ASME, Transactions, Series C- Journal of Heat Transfer,* 95 (1973), pp. 166–173. DOI: 10.1115/1.3450019.

[103] N. Nagai and S. Nishio. "Leidenfrost temperature on an extremely smooth surface". In: *Experimental thermal and fluid science* 12.3 (1996), pp. 373–379. DOI: 10.1016/0894-1777(95)00129-8.

[104] J. A. Valencia-Chavez. "The effect of composition on the boiling rates of liquefied natural gas for confined spills on water". PhD thesis. Massachusetts Institute of Technology, Feb. 1978.

[105] V. Vesovic. "The influence of ice formation on vaporization of LNG on water surfaces". In: *Journal of hazardous materials* 140.3 (2007), pp. 518–526. DOI: j.jhazmat.2006.10.039.

[106] H. Merte. *Incipient and steady boiling of liquid nitrogen and liquid hydrogen under reduced gravity*. Tech. rep. NAS-8-20228. NASA/University of Michigan, 1970.

[107] J. C. Y. Koh. "Analysis of Film Boiling on Vertical Surfaces". In: *Journal of Heat Transfer* 84.1 (1962), pp. 55–62. DOI: 10.1115/1.3684293.

[108] L. E. Brown and C. P. Colver. "Nucleate and film boiling heat transfer to liquefied natural gas." In: *Advances in Cryogenic Engineering* 13 (1968), pp. 647–654.

[109] E. Aursand and M. Hammer. "Predicting triggering and consequence of delayed LNG RPT". In: *Journal of Loss Prevention in the Process Industries* 55 (2018), pp. 124–133. DOI: 10.1016/j.jlp.2018.06.001.

[110] E. Aursand. "Inclination dependence of planar film boiling stability". In: *International Journal of Multiphase Flow* 106 (2018), pp. 243–253. DOI: 10.1016/j.ijmultiphaseflow.2018.05.010.

[111] E. Aursand and T. Ytrehus. "Comparison of kinetic theory evaporation models for liquid thin-films". Submitted to *International Journal of Multiphase Flow* in 2018.

Part II

Research articles

Paper A

Thermocapillary instability as a mechanism for film boiling collapse

Eskil Aursand, Stephen H. Davis, Tor Ytrehus

Published in *Journal of Fluid Mechanics*.
(2018) Vol. 852, pp. 283–312
https://doi.org/10.1017/jfm.2018.545

J. Fluid Mech. (2018), *vol.* 852, *pp.* 283–312.
doi:10.1017/jfm.2018.545

Thermocapillary instability as a mechanism for film boiling collapse

Eskil Aursand[1,2,†], Stephen H. Davis[2] and Tor Ytrehus[1]

[1]Department of Energy and Process Engineering, Norwegian University of Science and Technology (NTNU), Kolbjørn Hejes v. 1B, Trondheim N-7491, Norway

[2]Department of Engineering Sciences and Applied Mathematics, McCormick School of Engineering and Applied Science, Northwestern University, 2145 Sheridan Road, Evanston, IL 60208, USA

(Received 2 February 2018; revised 20 May 2018; accepted 3 July 2018)

We construct a model to investigate the interfacial stability of film boiling, and discover that instability of very thin vapour films and subsequent large interface superheating is only possible if thermocapillary instabilities are present. The model concerns horizontal saturated film boiling, and includes novel features such as non-equilibrium evaporation based on kinetic theory, thermocapillary and vapour thrust stresses and van der Waals interactions. From linear stability analysis applied to this model, we are led to suggest that vapour film collapse depends on a balance between thermocapillary instabilities and vapour thrust stabilization. This yields a purely theoretical prediction of the Leidenfrost temperature. Given that the evaporation coefficient is in the range 0.7–1.0, this model is consistent with the average Leidenfrost temperature of every fluid for which data could be found. With an evaporation coefficient of 0.85, the model can predict the Leidenfrost point within 10 % error for every fluid, including cryogens and liquid metals where existing models and correlations fail.

Key words: lubrication theory, thermocapillarity, thin films

1. Introduction

When a liquid is poured on top of a solid surface whose temperature is significantly above the liquid's saturation temperature, the liquid will start to boil. If we plot the resulting heat flux as a function of surface temperature, we obtain the well-known boiling curve (Dhir 1998), which is illustrated in figure 1. At very high surface temperatures, we get the phenomenon of film boiling, where direct liquid–solid contact is prevented by a continuous sub-millimetre vapour film. This drastically reduces heat transfer compared to the conventional nucleate boiling regime.

Of particular importance here is the Leidenfrost point (ΔT_L), also called the minimum film boiling temperature, which is the limiting ΔT below which film boiling turns unstable. When passing this point from the right, it is called film boiling collapse. Predicting the location of the Leidenfrost point is important for a

† Email address for correspondence: eskil.aursand@ntnu.no

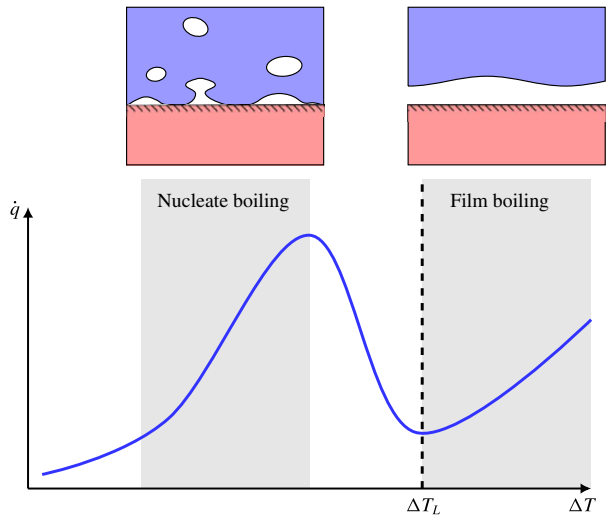

FIGURE 1. (Colour online) An illustration of the boiling curve: a plot of boiling heat flux ($\dot{q}$) against the difference between surface temperature and liquid saturation temperature (ΔT). At moderate surface temperatures, conventional nucleate boiling occurs, and heat flux is an increasing function of ΔT. However, at large enough ΔT, heat flux drops as a transition into the film boiling regime occur. The lowest ΔT in the film boiling regime is called the Leidenfrost point, ΔT_L.

variety of industrial concerns such as high heat flux cooling applications (e.g. nuclear reactors (Theofanous *et al.* 1997)) and high performance electronics (Agostini *et al.* 2007), where it is crucial to avoid the film boiling regime in order to keep the heat flux large. Also, film boiling collapse is often believed to be the triggering cause of vapour explosions (rapid phase transition) in nuclear fuel–coolant interactions (Fletcher 1995; Berthoud 2000) and liquefied natural gas (LNG) spill incidents (Luketa-Hanlin 2006; Cleaver, Johnson & Ho 2007). The supposed mechanism behind such vapour explosions is liquid superheating, i.e. the heating of a liquid above its saturation temperature. As we will show, significant superheating at the liquid–vapour interface is only possible if the vapour film becomes very thin, and this is only possible if the uniformly growing solution becomes unstable. Certainly, knowing the value of ΔT_L can be very useful in a variety of applications.

What is known about the Leidenfrost temperature for a given fluid? A lower bound is obviously the saturation temperature. For an upper bound, an empirically supported and physically reasonable value is the liquid spinodal, the temperature beyond which it is thermodynamically impossible for a liquid to be superheated. However, this is quite a large range. For example, water at standard pressure has a saturation temperature of 373 K, while the spinodal can be calculated to be 550 K to 600 K. Measurements of the Leidenfrost point for pools and large droplets of water commonly fall around 460 K (see table 1), but the relative position along the saturation–spinodal interval varies from fluid to fluid.

There have been a large variety of efforts to pinpoint the Leidenfrost point for any given fluid. Some are based on simplified fluid mechanical considerations, such as the efforts of Zuber (1959) and Berenson (1961). Others estimate it by the supposed

Fluid	T_s (K)	γ (N m^{-1} K^{-1})	Avg. T_L (K)	Std. T_L (K)	N_L
Water	373.15	0.000192	462.78	19.39	12
Nitrogen	77.36	0.000229	100.00	4.31	7
Freon113	320.74	0.000110	378.03	10.40	5
Freon11	296.92	0.000128	346.50	8.38	4
Acetone	329.30	0.000112	409.40	4.15	4
Methane	111.70	0.000250	163.33	12.47	3
Mercury	629.80	0.000220	862.67	62.10	3
Ethanol	351.50	0.000089	429.10	9.97	3
Pentane	309.21	0.000108	367.00	N/A	1
Cyclohexane	353.89	0.000114	438.15	N/A	1
Benzene	353.30	0.000124	448.15	N/A	1

TABLE 1. Fluids for which experimental data on the Leidenfrost temperature could be found. Also shown are the saturation temperature T_s and the surface tension temperature sensitivity γ, found from the NIST database (Linstrom & Mallard 2017; Dean 1998). The fourth and fifth columns show the average and standard deviation of the Leidenfrost temperature at atmospheric pressure, based on N_L data points from the literature. The Leidenfrost temperature data points were found in Berenson (1961), Gottfried & Bell (1966), Baumeister & Simon (1973), Valencia-Chavez (1978), Yao & Henry (1978), Sakurai, Shiotsu & Hata (1990), Nagai & Nishio (1996), Qiao & Chandra (1997), Bernardin & Mudawar (1999), Vesovic (2007).

upper bounds of the spinodal (Spiegler *et al.* 1963) or the superheat limit from nucleation theory (Yao & Henry 1978). However, as concluded by Bernardin & Mudawar (1999) and in the present work, none of the older models appear to predict in a satisfactory manner the Leidenfrost point for a wide variety of fluids. Also, the ones that are reasonably accurate for conventional fluids are semi-empirical, which provides less physical insight and is dubious for extrapolation to unconventional fluids. Overall, it appears that the underlying mechanism behind film boiling collapse has eluded discovery.

In the present work, we attempt to arrive at a prediction of the Leidenfrost point from the hypothesis that the mechanism behind vapour film collapse is a fluid dynamical instability. The approach is to describe vapour film dynamics through the well-studied long-wave (lubrication) approximation of thin film flow. This approach generally leads to a single scalar highly nonlinear equation for the film-thickness function, and has been thoroughly reviewed by Oron, Davis & Bankoff (1997), Myers (1998) and Craster & Matar (2009) for the case of liquid films. However, the present model considers a thin vapour film beneath a liquid bulk and will differ from these well-established models in several ways.

The present work is heavily inspired by two previous works, which both consider thin film flow with phase transition: the model for evaporating liquid films by Burelbach, Bankoff & Davis (1988), and the model for film boiling by Panzarella, Davis & Bankoff (2000). However, while the former includes the thermocapillary effect (Davis 1987), liquid films give qualitatively different dynamics than vapour films. On the other hand, while the latter does consider a vapour film, it does not include the thermocapillary effect. The present model is the first to include van der Waals, thermocapillary, vapour thrust and non-equilibrium evaporation effects in the context of film boiling. As will be shown later, the thermocapillary effect will turn

out to be crucial, and including it in film boiling is dependent on two model novelties being present:

(i) *Non-equilibrium evaporation:* in the quasi-equilibrium limit, the interface temperature is locked at the saturation temperature, and no thermocapillary effect is possible. Therefore, it is essential to use a non-equilibrium model, which includes an evaporation-rate-dependent departure from saturation temperature at the interface.

(ii) *Non-trivial liquid dynamics:* while the liquid velocity far away from the vapour film is assumed to be zero, when there is a non-zero velocity in the vapour the liquid close by will be pulled along to a small degree. However, as we shall show, approximating this by assuming a completely stationary liquid will decouple the model from the thermocapillary effect. It is crucial then to account for the small but non-zero liquid velocity.

The procedure to arrive at the present Leidenfrost model is as follows. In § 2 we set up a flow model for the vapour film, including a van der Waals disjoining pressure, a (linearized) non-equilibrium evaporation model and interface stress conditions that include both vapour thrust (normal stress) and thermocapillary effects (tangential stress). We then apply the long-wave approximation while modelling the effect of liquid pressure and drag to arrive at a single scalar highly nonlinear partial differential equation (PDE) for the dimensionless film thickness.

In § 3 we apply linear stability analysis to the PDE, and arrive at a stability condition for uniform base states. This condition depends on the scale of initial film thickness. We pose the hypothesis that film boiling collapse occurs when the film is unstable for any choice of film-thickness scale, and follow that to its logical conclusion, which turns out to be a theoretical prediction for the Leidenfrost point. This expression suggests that the mechanism for film boiling collapse is that the thermocapillary instability becomes stronger than vapour thrust stabilization. This is a claim that to our knowledge has not been stated previously.

In § 4 we compare with experimental Leidenfrost measurements for 11 different fluids and find decent predictive capabilities for all of them. As we then show in § 5, the most common existing models/correlations are unable to perform as well, especially for the more unusual fluids such as cryogens and liquid metals.

We go on in § 6 to discuss the benefits of this new model, as well as the problem of the unknown evaporation coefficient from kinetic theory. We summarize in § 7, and suggest how the validity of the hypothesis could be proved (or disproved) by further experiments.

2. Model

We consider the case of two-dimensional saturated film boiling on a horizontal solid plane, as illustrated in figure 2. The spatial coordinates x and z run parallel and perpendicular to the plane, respectively. The purpose of the analysis is to predict the dynamics of the film-thickness function, $z = h(x, t)$, where t is the time.

2.1. *Governing equations of vapour flow*

The vapour has velocity components u and w, in the x and z directions, respectively. Viscosity (μ_v), density (ρ_v), thermal conductivity (k_v) and heat capacity ($c_{p,v}$) are all assumed constant. The governing equations for the vapour flow are the standard

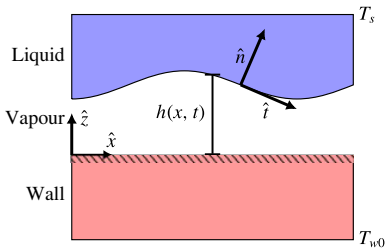

FIGURE 2. (Colour online) Illustration of the physical situation to be modelled. On one side is a liquid whose bulk is held at its saturation temperature. On the other side is a solid slab whose bulk is held at a considerably higher temperature. T_{w0} and T_s are the only given temperatures in this case, and the remaining temperature profile comes from a solution to the problem. The overall temperature difference is ΔT, and if it is large enough, it will lead to film boiling, i.e. a continuous thin vapour film between the two bulk phases. The general purpose of this model is to predict the dynamics of the liquid–vapour interface, located at $z = h(x, t)$.

continuity, momentum and energy equations for incompressible flow (Kundu, Cohen & Dowling 2007),

$$u_x + w_z = 0, \tag{2.1}$$

$$\rho_v(u_t + uu_x + wu_z) = -p_x + \mu_v(u_{xx} + u_{zz}) - \phi_x, \tag{2.2}$$

$$\rho_v(w_t + uw_x + ww_z) = -p_z + \mu_v(w_{xx} + w_{zz}) - \phi_z, \tag{2.3}$$

$$\rho_v c_{p,v}(T_t + uT_x + wT_z) = k_v(T_{xx} + T_{zz}), \tag{2.4}$$

where variable subscripts imply differentiation. Here p is the pressure and ϕ is the body-force potential. The only difference from standard flow equations so far is that ϕ includes not only the gravity contribution, but also a film-thickness-dependent addition that represents van der Waals interactions between the liquid surface and the solid surface. This is called a disjoining pressure (Oron *et al.* 1997), and gives a total potential of the form

$$\phi = \phi_0 + \rho_v g b z + \frac{\tilde{A}}{6\pi h^3}. \tag{2.5}$$

Here g is the gravitational acceleration, and $\tilde{A}$ is the effective Hamaker constant from van der Waals interaction theory. The constant $b = \pm 1$ is $+1$ for the liquid-above-solid configuration and -1 for the solid-above-liquid configuration. The constant ϕ_0 is an arbitrary reference potential. The van der Waals interaction will only become significant on the sub-micrometre scale of film thickness. A derivation of the last term in (2.5) for the case of thin liquid films can be found in the work of Ruckenstein & Jain (1974), and here we assume that a term of the same form is valid for thin vapour films. Generally, the interaction may be either attractive ($\tilde{A} > 0$) or repulsive ($\tilde{A} < 0$).

2.2. *Evaporation model*

Due to the high temperature of the solid, evaporation occurs at the liquid–vapour interface, giving an evaporation heat flux j. The only given temperatures are the

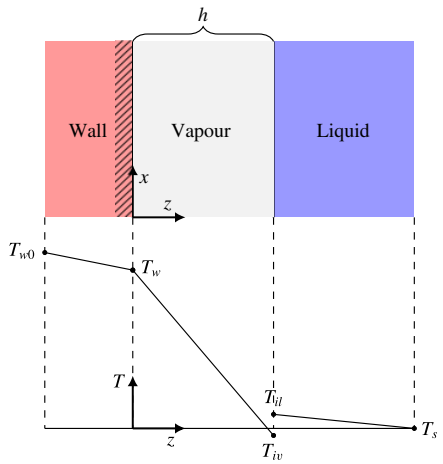

FIGURE 3. (Colour online) Illustration of the local temperature profile in film boiling, on x-scales much shorter than the wavelength seen in figure 2, so that the interface appears flat.

controlled temperature in the solid bulk, T_{w0}, and the saturation temperature known from thermodynamics, T_s. The wall surface temperature, T_w, will generally be a bit lower than T_{w0} due to the finite thermal conductivity of the solid. Still, the temperature will be continuous at the wall. The situation at the liquid–vapour interface is more complicated. Classically, in the quasi-equilibrium limit, the interface temperature is assumed to be continuous and equal to T_s. However, generally there is a temperature discontinuity at the interface, and neither side is necessarily equal to T_s. However, they will both approach T_s in the limit of weak evaporation. This situation is illustrated in figure 3.

We label the vapour-side and liquid-side interface temperatures as T_{iv} and T_{il}, respectively. When evaporating, we always have that $T_{il} > T_s$ and $T_{il} > T_{iv}$. The interface vapour temperature T_{iv} may either be below T_s (supersaturated) or above T_s (superheated), depending on conditions (Ytrehus 1997). For moderate evaporation rates, we may neglect the effect of the discontinuity and consider a single interface temperature, $T_i = T_{il} \approx T_{iv}$, which is superheated ($T_i > T_s$). In these cases we may linearize the relationship between evaporation mass flux and T_i of the form

$$T_i - T_s = \tilde{K} j, \tag{2.6}$$

as used by Burelbach *et al.* (1988). The interfacial thermal resistance can be estimated from kinetic gas theory and typically has the form

$$\tilde{K} = \frac{\sqrt{2\pi R_s} T_s^{3/2}}{f(\alpha_e)\rho_{v,s} L}, \tag{2.7}$$

where R_s is the specific gas constant, L is the latent heat of evaporation, $\rho_{v,s}$ is the vapour density at the saturation temperature and α_e is the evaporation coefficient. The function $f(\alpha_e)$ depends on the specific model. In the moderate-evaporation limit of the classical Hertz–Knudsen model, (Hertz 1882; Knudsen 1915), we get

$$f(\alpha_e) = \alpha_e, \tag{2.8}$$

which is what was used by Burelbach *et al.* (1988). A more recent refinement of this model is the Schrage formula, whose moderate-evaporation limit yields (Mills 1995)

$$f(\alpha_e) = \frac{\alpha_e}{1 - \frac{1}{2}\alpha_e}. \tag{2.9}$$

Some more advanced evaporation models do exist (Ytrehus 1997), but quantitatively they reduce to something very similar to the Schrage formula for low-to-moderate evaporation rates.

Usually these models are stated in terms of density differences, not temperature differences like in the constitutive equation used here. Matching the form (2.6) may be achieved by applying the ideal gas law, linearizing the saturation line by the Clausius–Clapeyron relation and assuming that the differences between T_{il}, T_{iv} and T_s are small.

The evaporation coefficient α_e is the subject of much uncertainty, debate and active research to this date. It is typically assumed equal to the related condensation coefficient (Ytrehus 1997; Cheng *et al.* 2011). This unknown coefficient is introduced through a boundary condition in kinetic theory, and cannot be determined from within kinetic theory itself. It represents the probability of an incoming vapour molecule sticking to the liquid, as opposed to reflecting back, and is thus by definition in the range of zero to one. The exact nature of this coefficient appears to be far from settled. Water is the only somewhat well-studied fluid, and even there the experiments show a large scatter from 0.1 to 1.0, as seen in e.g. Tsuruta & Nagayama (2004, Table 1). Besides experiments, a common way of estimating the coefficient is molecular dynamics simulations (MD). These methods show somewhat more consistent results, and generally give values quite close to unity. Overall, MD simulations from the last decade seem to generally agree on the following trends (Tsuruta & Nagayama 2004; Cao, Xie & Sazhin 2011; Cheng *et al.* 2011; Xie, Sazhin & Cao 2011; Ishiyama *et al.* 2013; Iskrenova & Patnaik 2017; Liang, Biben & Keblinski 2017):

(i) For a given fluid, the evaporation/condensation coefficient decreases as liquid temperature is increased.

(ii) As long as the liquid temperature is less than 0.7 times T_c (critical temperature), we can expect $\alpha_e \in (0.7, 1.0)$ for a considerable variety of fluids.

In the cases considered here the liquid surface temperatures are very close to the saturation temperatures, and every liquid considered here has $T_s < 0.7T_c$. Thus we may expect that $\alpha_e \in (0.7, 1.0)$.

2.3. *Surface tension model*

In order to capture the thermocapillary effect, it is essential to include the temperature dependence of surface tension (σ). We follow Davis (1987) and model the variation as a linearization around its value at the saturation temperature, σ_0,

$$\sigma(T) = \sigma_0 - \gamma(T - T_s). \tag{2.10}$$

Thus, the factor γ is

$$\gamma = -\frac{\partial \sigma}{\partial T}. \tag{2.11}$$

For most liquids, γ is positive and often around 0.0002 N m^{-1} K^{-1}. As we shall demonstrate, γ will play a crucial role in the prediction of vapour film collapse.

2.4. *Boundary conditions*

2.4.1. *Solid wall*

The solid wall at $z = 0$ is an impermeable no-slip surface. Also, as with any interface, there must be a continuity of energy flux. We represent the heat transfer inside the solid with a heat transfer coefficient α_w. Since this is a solid, α_w could of course be found from the thermal conductivity and a thermal boundary layer thickness, but for simplicity we keep the factor α_w. Given the above, the wall surface boundary conditions are

$$u|_{z=0} = w|_{z=0} = 0, \tag{2.12}$$

$$\alpha_w(T_{w0} - T_w) = -k_v T_z|_{z=0}. \tag{2.13}$$

2.4.2. *Liquid–vapour interface*

The liquid–vapour interface is also no-slip, in the sense that the tangential velocity is continuous. In contrast to the solid surface, fluid may pass into this interface at a rate governed by the evaporation mass flux. The relation between the flow velocity at the interface, the velocity of the interface itself, and the evaporation rate is given by the kinematic boundary condition. Additionally, we must have continuity of stress and energy flux across the interface. Given the above, the interface boundary conditions are

$$(\boldsymbol{v} - \boldsymbol{v}_l) \cdot \hat{\boldsymbol{t}}|_{z=h} = 0, \tag{2.14}$$

$$\rho_v \frac{(h_t + uh_x - w)|_{z=h}}{\sqrt{1 + h_x^2}} = j, \tag{2.15}$$

$$[j(\boldsymbol{v}_{l,e} - \boldsymbol{v}_e) \cdot \hat{\boldsymbol{n}} - ([\boldsymbol{T} - \boldsymbol{T}_l] \cdot \hat{\boldsymbol{n}}) \cdot \hat{\boldsymbol{n}}]_{z=h} = -\kappa\sigma, \tag{2.16}$$

$$([\boldsymbol{T} - \boldsymbol{T}_l]_{z=h} \cdot \hat{\boldsymbol{n}}) \cdot \hat{\boldsymbol{t}} = \nabla\sigma|_{z=h} \cdot \hat{\boldsymbol{t}}, \tag{2.17}$$

$$-k_v \nabla T \cdot \hat{\boldsymbol{n}}|_{z=h} - \alpha_l(T_i - T_s) = jL. \tag{2.18}$$

Here the vectors $\boldsymbol{v} = [u, w]$, $\hat{\boldsymbol{n}}$ and $\hat{\boldsymbol{t}}$ are the velocity, interface unit normal and interface unit tangent, respectively. The latter two are defined as shown in figure 2. The symbol κ is the interface curvature. The symbol $\boldsymbol{T}$ is the incompressible Newtonian flow stress tensor, j is the evaporation mass flux, and L is the fluid's latent heat of evaporation. The efficiency of heat transfer from the interface to the liquid bulk is represented by a heat transfer coefficient α_l. Overall, the subscript l indicates the corresponding property on the liquid side.

2.5. *Comparison with some previous models*

The inclusion of a disjoining-pressure term in § 2.1 is identical to the treatment in Burelbach *et al.* (1988), though here presumably with a different value for the Hamaker constant due to the nature of the thin film. Similarly, the constitutive equation for evaporation in § 2.2 is similar, though here with a generalization allowing for different factors $f(\alpha_e)$. The model of Burelbach *et al.* (1988) only uses the older Hertz–Knudsen model (2.8). The linearized surface tension model in § 2.3 is quite standard.

The differences to previous works become more nuanced when it comes to the boundary conditions in § 2.4. At the solid surface, the flow boundary conditions (2.12) are standard. However, an energy flux balance like (2.13) is not included in Burelbach *et al.* (1988), which simply assumes a constant given wall surface temperature.

The interface boundary conditions (2.14)–(2.18) are essentially the same as the ones initially presented in Burelbach *et al.* (1988, equations (2.6)–(2.12)), besides some subtle sign changes due to the liquid–vapour role reversal. However, in Burelbach *et al.* (1988), the full boundary conditions are considerably simplified due to the negligible density, viscosity and conductivity of the bulk vapour phase outside the film. This cannot be done here as the outside bulk is liquid, and thus, the boundary conditions must remain in their complex form.

Some of the commonalities missing from Burelbach *et al.* (1988) are present in Panzarella *et al.* (2000). The latter considers a vapour film and does allow the solid surface temperature to vary. However, they include neither vapour thrust, thermocapillary nor van der Waals effects. In fact, they take the infinite liquid viscosity limit, which leads to setting the vapour interface velocity to zero. As we shall show, this limit has an important qualitative consequence, as it causes the model to decouple from the thermocapillary effect.

2.6. *Scales and dimensionless numbers*

We introduce a length scale h_0 for z and h in order to define the dimensionless equivalents Z and H. Similarly, we introduce a length scale x_0 for x in order to define the dimensionless distance X. The scales h_0 and x_0 are not arbitrary, and must be set similar to the typical film-thickness and interface disturbance wavelength, in order to ensure $\partial/\partial X \sim \partial/\partial Z \sim O(1)$ in the dimensionless equations. Here we choose $x_0 = \lambda/(2\pi)$, where λ is the wavelength of the disturbance. The ratio between the two scales is defined as

$$\epsilon = \frac{h_0}{x_0} = 2\pi\frac{h_0}{\lambda}. \tag{2.19}$$

We shall later take the long-wave approximation, which formally is the limit of small ϵ, i.e. $\lambda \gg h_0$. We use a velocity scale u_0 to define the dimensionless tangential velocity, $U = u/u_0$. Similarly we define the dimensionless perpendicular velocity $W = w/w_0$, where continuity implies that $w_0 = \epsilon u_0$. The dimensionless time τ is defined by the time scale x_0/u_0. We scale the temperature according to its position on the scale between T_{w0} and T_s,

$$\theta = \frac{T - T_s}{\Delta T}, \tag{2.20}$$

where $\Delta T = T_{w0} - T_s$. We scale the remaining variables as

$$p = \frac{\mu_v u_0}{\epsilon h_0}P, \quad \phi = \frac{\mu_v u_0}{\epsilon h_0}\Phi, \quad j = \frac{k_v \Delta T}{h_0 L}J, \quad \sigma = \sigma_0 \Sigma, \tag{2.21a–d}$$

where P, Φ, J and Σ are the dimensionless pressure, body-force potential, evaporation mass flux and surface tension, respectively. We define the following dimensionless numbers:

$$\left.\begin{gathered} Re = \frac{\rho_v u_0 h_0}{\mu_v}, \quad Pr = \frac{\mu_v c_{p,v}}{k_v}, \quad \Psi = \frac{\mu_v}{\mu_l}, \quad D = \frac{\rho_v}{\rho_l}, \quad E = \frac{k_v \Delta T}{\rho_v u_0 h_0 L}, \\ K = \frac{\tilde{K} k_v}{h_0 L}, \quad Ca = \frac{\mu_v u_0}{\sigma_0}, \quad M = \frac{\Delta T \gamma}{\mu_v u_0}, \quad A = \frac{\tilde{A}}{6\pi\mu_v u_0 h_0^2}, \\ G_v = \frac{\rho_v g h_0^2}{\mu_v u_0}, \quad G_l = \frac{\rho_l g h_0^2}{\mu_v u_0}, \quad G = \frac{\Delta\rho g h_0^2}{\mu_v u_0}, \quad Bi_w = \frac{\alpha_w h_0}{k_v}, \quad Bi_l = \frac{\alpha_l h_0}{k_v}. \end{gathered}\right\} \tag{2.22}$$

2.7. *Long-wave approximation*

2.7.1. *Approximate equations*

We introduce the scales and dimensionless numbers of § 2.6 and make the assumptions of long waves and small Reynolds number, while retaining surface tension effects to leading order,

$$\epsilon \ll 1, \quad \epsilon Re \ll 1, \quad D \ll 1, \quad Pr \sim O(1), \quad \epsilon^3 Ca^{-1} \sim O(1), \quad \epsilon M \sim O(1). \tag{2.23a–f}$$

We also want to retain the vapour thrust, van der Waals and gravitational effects to leading order, so we keep the terms ϵReE^2J^2, $\epsilon A/H^3$ and ϵG_v. Given this, the governing equations of the vapour flow, equations (2.1)–(2.3) and (2.5) become

$$U_X + W_Z = 0, \tag{2.24}$$

$$(P + \Phi)_X = U_{ZZ}, \tag{2.25}$$

$$(P + \Phi)_Z = 0, \tag{2.26}$$

$$\Phi = \Phi_0 + \epsilon b G_v Z + \frac{\epsilon A}{H^3}, \tag{2.27}$$

respectively. The boundary conditions of the vapour flow (2.12), (2.14), (2.15), (2.16) and (2.17) become

$$[U]_{Z=0} = [W]_{Z=0} = 0, \tag{2.28}$$

$$[U - U_l]_{Z=H} = 0, \tag{2.29}$$

$$\frac{E}{\epsilon} J = [H_\tau + UH_X - W]_{Z=H}, \tag{2.30}$$

$$[P - P_l]_{Z=H} + \epsilon ReE^2J^2 = -H_{XX}\epsilon^3 Ca^{-1}, \tag{2.31}$$

$$[U_Z - \Psi^{-1} U_{l,Z}]_{Z=H} = -\epsilon M(\theta_i)_X, \tag{2.32}$$

respectively. Similarly, the energy equation (2.4) becomes

$$\theta_{ZZ} = 0, \tag{2.33}$$

and the temperature boundary conditions (2.6), (2.13) and (2.18) become

$$KJ = \theta_i, \tag{2.34}$$

$$-\theta_Z|_{Z=0} = Bi_w(1 - \theta_w), \tag{2.35}$$

$$J = -\theta_Z|_{Z=H} - Bi_l\theta_i, \tag{2.36}$$

respectively. The van der Waals effect is included in (2.27) ($\sim A$), the vapour thrust effect is included in (2.31) ($\sim ReE^2$), and the thermocapillary effect is included in (2.32) ($\sim M$). These long-wave approximation equations have many similarities to the ones presented in Burelbach *et al.* (1988, equations (5.5)–(5.10)). However, there are significant differences. Besides some sign changes, these differences all relate to the fact that the bulk phase outside the thin film is different. In Burelbach *et al.* (1988), the normal-stress condition (here (2.31)) does not include a term for the outside pressure as it could be conveniently set constant and equal to zero. In the tangential-stress condition (here (2.32)), the bulk phase shear rate was set to zero, as the interface could be treated as a free surface. Neither simplification is possible in the present work, as the liquid and vapour have switched places. The equations for the temperature profile are also somewhat more complicated in the present work, since the wall surface temperature is allowed to vary (giving (2.35)) and since the bulk phase conductivity cannot be neglected (giving the final term of (2.36)). Overall, the main difference is that with this problem we cannot make a purely 'one-sided' model like in Burelbach *et al.* (1988).

2.7.2. *Solution to temperature equations*

We note how (2.33)–(2.36) for the temperature profile have no explicit time dependence, only implicitly through the variables $J(X, \tau)$ and $H(X, \tau)$. Since J is determined directly from the temperature profile through (2.34), the instantaneous value of H determines the current temperature profile θ as well as the evaporation mass flux J. The solution is

$$J(H) = \frac{1}{K + (Bi_w^{-1} + H)C}, \tag{2.37}$$

$$\theta_i(H) = \frac{K}{K + (Bi_w^{-1} + H)C}, \tag{2.38}$$

$$\theta_w(H) = \frac{K + HC}{K + (Bi_w^{-1} + H)C}, \tag{2.39}$$

where we have defined the new constant

$$C = 1 + C'. \tag{2.40}$$

Here $C' = Bi_l K = \alpha_l \tilde{K}/L$ and represents the effect of heat lost into the liquid bulk. Interestingly, C' is independent of h_0, even though the interface temperature θ_i is not. It is instructive to look at a few special cases of this solution. In the quasi-equilibrium limit ($K \to 0$), we get

$$J(K \to 0) = \frac{1}{Bi_w^{-1} + H}, \tag{2.41}$$

$$\theta_i(K \to 0) = 0, \tag{2.42}$$

$$\theta_w(K \to 0) = \frac{H}{Bi_w^{-1} + H}. \tag{2.43}$$

As expected, the interface temperature is locked to T_s. The evaporation rate is somewhat limited by the finite conductivity of the solid. If $H \to 0$, J does not diverge, due to the finite solid heat transfer efficiency. In the limit of a perfectly conducting solid ($Bi_w \to \infty$) we get

$$J(Bi_w \to \infty) = \frac{1}{K + HC}, \tag{2.44}$$

$$\theta_i(Bi_w \to \infty) = \frac{K}{K + HC}, \tag{2.45}$$

$$\theta_w(Bi_w \to \infty) = 1. \tag{2.46}$$

As expected, the wall surface temperature is locked to the bulk temperature, T_{w0}. The evaporation rate is somewhat limited by the non-equilibrium effect ($K \neq 0$) and liquid conduction ($C > 1$). If $H \to 0$, J does not diverge, due to the interface thermal resistance ($K \neq 0$). Generally, if $H \to 0$, we get

$$J(H \to 0) = \frac{1}{K + Bi_w^{-1} C}, \tag{2.47}$$

$$\theta_i(H \to 0) = \theta_w(H = 0) = \frac{K}{K + Bi_w^{-1} C}, \tag{2.48}$$

i.e. the evaporation rate stays finite and the interface/surface temperature approaches an intermediate value between T_s and T_{w0}. However, note that in the $H \to 0$ limit, it is likely that the linearized relation in (2.6) for moderate evaporation rates becomes inaccurate.

We proceed by using the general solution in (2.37)–(2.39) in order to include both the non-equilibrium effect and the potential effects of heat transfer on both sides of the vapour film. Note that the non-equilibrium ($K \neq 0$) effect is absolutely necessary for capturing the thermocapillary effect. If $K = 0$, θ_i becomes a constant, and the thermocapillary term in the tangential-stress condition (2.32) disappears.

2.7.3. *Velocity profile*

We define the reduced dimensionless pressure as $\bar{P} = P + \Phi$. From (2.26) we know that $\bar{P}$ is constant across the film, and thus, we may choose to evaluate it at $Z = H$ in (2.25), so that it reduces to

$$U_{ZZ} = \bar{P}(X, H)_X. \tag{2.49}$$

If we combine (2.31) and (2.27), we find that the gradient of reduced pressure is

$$\bar{P}(X, H)_X = P_l(X, H)_X + \epsilon b G_v H_X - 2\epsilon Re E^2 J J_X - \epsilon^3 Ca^{-1} H_{XXX} - 3\epsilon A \frac{H_X}{H^4}. \tag{2.50}$$

The right-hand side of (2.49) is independent of Z, and thus we may integrate the equation twice and use the no-slip wall boundary condition (2.28) to get the velocity profile

$$U = \tfrac{1}{2}\bar{P}_X(Z^2 - 2HZ) + U_Z|_{Z=H} Z, \tag{2.51}$$

$$= \tfrac{1}{2}\bar{P}_X(Z^2 - HZ) + U|_{Z=H} \frac{Z}{H}, \tag{2.52}$$

expressed in two different ways depending on whether one wants to use the interface shear rate or the interface velocity to define the $Z = H$ boundary. From this, we find the total flow rate to be

$$\int_0^H U \, \mathrm{d}Z = -\tfrac{1}{3} H^3 \bar{P}_X + \tfrac{1}{2} H^2 U_Z|_{Z=H}, \tag{2.53}$$

$$= -\tfrac{1}{12} H^3 \bar{P}_X + \tfrac{1}{2} H U|_{Z=H}. \tag{2.54}$$

The two extremes of behaviour can be found by either setting the liquid velocity to zero at the boundary (corresponding to infinite liquid viscosity) or setting the liquid shear rate to zero at the boundary (treating the interface like a free surface). Thus, regardless of the specific liquid properties, we know that the flow rate must be within the range

$$\int_0^H U \, \mathrm{d}Z = \begin{cases} -\frac{1}{12} H^3 \bar{P}_X, & U|_{Z=H} = 0, \\ -\frac{1}{3} H^3 \bar{P}_X - \frac{1}{2} H^2 \epsilon M \theta_{i,X}, & U_{l,Z}|_{Z=H} = 0, \end{cases} \tag{2.55}$$

where we in the latter case have used the tangential-stress condition (2.32) to find the vapour shear rate. Generally, the interface velocity $U_i = U|_{Z=H} = U_l|_{Z=H}$ is

$$U_i = -\tfrac{1}{2} H^2 \bar{P}_X + \Psi^{-1} H U_{l,Z}|_{Z=H} - \epsilon M H \theta_{i,X}, \tag{2.56}$$

and if we evaluate (2.51) at $Z=H$, we get the following constraint on the boundary:

$$[U - HU_Z]_{Z=H} = -\tfrac{1}{2}H^2\bar{P}_X. \tag{2.57}$$

Note that if we take the zero interface-velocity limit, the flow rate is fully determined by the first case of (2.55). Then there is no way to involve the tangential-stress condition (2.32), and therefore, any coupling to the thermocapillary effect is lost. Thus, the choice of velocity boundary condition made by Panzarella *et al.* (2000) is not an option here.

2.7.4. *Liquid dynamics*

So far we have made no assumptions regarding the liquid flow outside the vapour film. However, in order to find the final vapour velocity profile we require a liquid pressure (as seen in (2.50)) and information regarding the liquid–vapour boundary (as seen in (2.51) and (2.52)).

First, we assume that the liquid pressure is purely hydrostatic,

$$P_l = -\epsilon b G_l Z, \tag{2.58}$$

similar to Panzarella *et al.* (2000). Note that the liquid layer is much thicker than the vapour layer, so the former does not have any disjoining-pressure contribution.

Second, we need to make an assumption regarding the liquid flow in order to find the interface velocity. The liquid is assumed to be stationary far away in the bulk, but close to the interface it will be pulled along with the vapour. From the perspective of the vapour film, the liquid slows down the vapour flow due to viscous drag. Generally, we expect the liquid velocity profile to monotonically decay from U_i at $Z=H$ to zero at $Z=\infty$. Regardless of the details of the liquid flow, we know that the interface velocity U_i must be between the following two hypothetical extreme cases:

(i) Minimum interface velocity: $U_i^{min}=0$ (interface acts like a wall).
(ii) Maximum interface velocity: $U_i = U_i^{max}$ (interface acts like a free surface).

The second case corresponds to the case of zero liquid shear, i.e. when the liquid does not resist the vapour flow at all. If we set $U_{l,Z}|_{Z=H}=0$ in (2.56) we find that

$$U_i^{max} = -\tfrac{1}{2}H^2\bar{P}_X - \epsilon MH\theta_{i,X}. \tag{2.59}$$

We then interpolate between the two known extreme cases by introducing the interpolation parameter $\eta \in [0, 1]$,

$$\begin{aligned} U_i &= \eta U_i^{max} + (1-\eta)U_i^{min} \\ &= \eta\left(-\tfrac{1}{2}H^2\bar{P}_X - \epsilon MH\theta_{i,X}\right), \end{aligned} \tag{2.60}$$

which satisfies the constraint (2.57) for any value of η. While the value of η is unknown for now, we make the crucial assumption that it is independent of position X, and thus only depends on constant fluid properties. Specifically, we expect η to increase monotonically with the viscosity ratio Ψ, with the limits

$$\lim_{\Psi\to 0}[\eta(\Psi)] = 0, \qquad \lim_{\Psi\to\infty}[\eta(\Psi)] = 1 \tag{2.61a,b}$$

since the two extreme cases correspond to the theoretical limits $\Psi \to 0$ and $\Psi \to \infty$, respectively. Since the driving force for flow is the vapour film pressure gradient and the almost stationary liquid just passively applies drag to this flow, we expect the average vapour velocity to be significantly larger than the interface velocity. This means that we can expect η to be much closer to zero than one.

More detailed information on the value of η requires more bold assumptions regarding the liquid velocity profile. One such assumption is shown in appendix A, which leads to the convenient approximation

$$\eta = \frac{1}{1+\Psi^{-1}} = \Psi + O(\Psi^2). \tag{2.62}$$

For common values of Ψ this means that η is in the range of 0.025–0.050. Note that while this is quite close to zero, taking the actual $\eta \to 0$ approximation is not an option as it would eliminate the thermocapillary effect.

No matter the specific model used to find a value for η, we may insert (2.60) into (2.54) and find the mass flow rate to be

$$\int_0^H U \,\mathrm{d}Z = -\frac{1}{12}(1+3\eta)H^3\bar{P}_X - \frac{1}{2}\eta\epsilon M H^2\theta_{i,X}, \tag{2.63}$$

which as intended matches (2.55) in the limiting cases of $\eta = 0$ and $\eta = 1$. The following derivation of a film thickness PDE, and the stability analysis thereof, is performed with a general unknown η.

The problems addressed in this section represent a central modelling complication compared to the related works of Burelbach *et al.* (1988) and Panzarella *et al.* (2000). The former was able to ignore all bulk phase dynamics because it considered a liquid film with a free surface ($\eta = 1$). The latter made stationary liquid ($\eta = 0$) approximation, which eliminates the thermocapillary effect. Here it is necessary to have an actual intermediate value for the interface velocity in order to arrive at a one-sided model. The assumptions made for the effect of liquid shear in this section are admittedly somewhat bold. Ultimately their validity rests on the success of the resulting model for the Leidenfrost point.

2.7.5. *Film-thickness PDE*

If we integrate the continuity equation (2.24) across the film from $Z=0$ to $Z=H(\tau)$, and apply the Leibniz integral rule, the kinematic boundary condition (2.30) and the wall boundary condition (2.28), we get the basic mass-conservation PDE

$$H_\tau + \left(\int_0^H U \,\mathrm{d}Z\right)_X = \frac{E}{\epsilon}J, \tag{2.64}$$

with a flux term and a source term. We find the reduced pressure gradient by inserting (2.37) and (2.58) into (2.50):

$$\bar{P}(X,H)_X = -\epsilon b G H_X + \frac{2\epsilon ReE^2C}{[K+(Bi_w^{-1}+H)C]^3}H_X - \epsilon^3 Ca^{-1}H_{XXX} - 3\epsilon A\frac{H_X}{H^4}. \tag{2.65}$$

We can then insert $\bar{P}_X$ into (2.63) while using (2.38) for θ_i, in order to yield the flow rate. When we insert this flow rate into (2.64) and use (2.37) for J in the source term, we get the final PDE for the film thickness H:

$$H_{\bar{\tau}} + \underbrace{\frac{b\xi G}{12E}\epsilon^2[H^3H_X]_X}_{\textit{gravity}} - \underbrace{\frac{\xi ReEC}{6}\epsilon^2[F^3(H)H_X]_X}_{\textit{vapour thrust}} + \underbrace{\frac{\xi}{12CaE}\epsilon^4[H^3H_{XXX}]_X}_{\textit{capillary}}$$
$$+ \underbrace{\frac{\xi A}{4E}\epsilon^2\left[\frac{H_X}{H}\right]_X}_{\textit{vdW}} + \underbrace{\frac{\tilde{M}KC}{2E}\epsilon^2[F^2(H)H_X]_X}_{\textit{thermocapillary}} = \underbrace{\frac{F(H)}{H}}_{\textit{evaporation}}. \tag{2.66}$$

Here we have changed to the evaporative time scale,

$$\tilde{t}_0 = \frac{h_0}{(j_0/\rho_v)} = \frac{\rho_v h_0^2 L}{k_v \Delta T}, \tag{2.67}$$

with the corresponding dimensionless time $\tilde{\tau}$, and we have defined the shorthands

$$\xi = 1 + 3\eta, \tag{2.68}$$

$$\tilde{M} = \eta M, \tag{2.69}$$

$$F(H) = \frac{H}{C(H + Bi_w^{-1}) + K}. \tag{2.70}$$

The function $F(H)$ will in most cases stay close to unity, since $K \ll 1$, $Bi_w^{-1} \ll 1$ and $C \approx 1$. The constants C, G/E, ReE, CaE, A/E and $\tilde{M}K/E$, as well as the function F, are all independent of the unknown scale u_0, and thus (2.66) is also independent of it.

3. Linear stability analysis

We now seek to examine the linear stability of a uniform film according to (2.66). This means finding under which conditions small perturbations of uniform solutions will grow, and under which conditions the uniform solutions will remain stable. In § 3.1 we find the form of the uniform basic solution and we examine its stability in § 3.2. Finally, in § 3.4, we propose how these results may be used to predict vapour film collapse.

3.1. *Basic solution*

We consider a spatially uniform time-dependent base solution to (2.66), $\bar{H}(\tilde{\tau})$. We define the scale h_0 as the initial film thickness so that $\bar{H}(0) = 1$. The analytical solution is

$$\bar{H}(\tilde{\tau}) = \frac{\sqrt{2C\tilde{\tau} + (Bi_w^{-1}C + K + C)^2} - (Bi_w^{-1}C + K)}{C}. \tag{3.1}$$

The initial growth rate of this basic solution is reduced by every non-ideal effect, $K > 0$, $Bi_w^{-1} > 0$ and $C > 1$. If all these effects are negligible, we get the upper-bound ideal solution $\bar{H} = \sqrt{1 + 2\tilde{\tau}}$. In any case, we see that the basic solution will grow monotonically, and thus, any vapour film collapse must be initiated by instabilities of this uniform solution.

3.2. *Linear stability of basic solution*

We now propose a solution which is a sum of the base solution and a spatially periodic perturbation with a small time-dependent amplitude,

$$H(X, \tilde{\tau}) = \bar{H}(\tilde{\tau}) + \hat{H}(\tilde{\tau}) \exp\left(\mathrm{i}\frac{k}{\epsilon}X\right). \tag{3.2}$$

Here k/ϵ is the dimensionless wavenumber on the scale x_0, and thus k is the dimensionless wavenumber on the scale h_0. If we insert (3.2) into (2.66) and reduce

to first order in the perturbation, we get the following ordinary differential equation for the perturbation amplitude,

$$\frac{\partial}{\partial\tilde{\tau}}\hat{H} = \frac{\xi Gb\bar{H}^3k^2}{12E} + \frac{\xi Ak^2}{4E\bar{H}} + \frac{C\bar{F}^2K\tilde{M}k^2}{2E} - \frac{\xi C\bar{F}^3E\mathrm{Re}k^2}{6} - \frac{\xi\bar{H}^3k^4}{12E\mathrm{Ca}} - \frac{C\bar{F}^2}{\bar{H}^2}. \tag{3.3}$$

The recurring factor $\bar{F}$, which appears in every term directly related to the temperature profile, is simply $F(H)$ from (2.70) with $\bar{H}$ substituted for H. The last k-independent term in (3.3) will only have an algebraic contribution to the exponential instability for the same reasons as the ones stated by Burelbach *et al.* (1988), and may thus be disregarded in the following analysis. All the remaining terms are $O(k^2)$ except the capillary term, which is $O(k^4)$. The latter will simply provide a cutoff in k and stabilize the shorter wavelengths. We may then consider the stability of long waves by only comparing the $O(k^2)$ terms.

If we have initial stability, the film will grow according to (3.1). If it later turns unstable after growing somewhat, we might re-scale h_0 and reset the time parameter, and consider it a new stability problem from $\bar{H}=1$. Thus we simply consider initial stability at $\tilde{\tau}=0$, and investigate the terms' dependence on film thickness h_0. Stability of long waves may then be analysed by considering the sign of

$$S = \underbrace{\frac{\xi Gb}{12E}}_{\textit{gravity}} + \underbrace{\frac{CF_0^2K\tilde{M}}{2E}}_{\textit{thermocap.}} - \underbrace{\frac{\xi CF_0^3E\mathrm{Re}}{6}}_{\textit{vapour thrust}} + \underbrace{\frac{\xi A}{4E}}_{\textit{vdW}}, \tag{3.4}$$

where F_0 is $\bar{F}$ evaluated at $\bar{H}=1$. Here $S>0$ indicates a growing perturbation (instability). We can make the following observations about the terms in (3.4):

(i) *Gravity:* this term is destabilizing (if $b>0$).
(ii) *Thermocapillary:* this term is destabilizing, which is also the case for evaporating liquid films (Burelbach *et al.* 1988).
(iii) *Vapour thrust:* this term is stabilizing, in contrast to its destabilizing influence in evaporating liquid films (Burelbach *et al.* 1988).
(iv) *Van der Waals:* this term is destabilizing (if $A>0$).

The main qualitative difference compared to the stability analysis of evaporating liquid films lies in the vapour thrust term, which here is found to be stabilizing. In the analysis of Burelbach *et al.* (1988), every $O(k^2)$ term is found to have a destabilizing influence, which means that an evaporating liquid film is always unstable if sufficiently large wavelengths are allowed. Film boiling appears to be different in that it has a stabilizing $O(k^2)$ term, which means that the stability of long waves depend on specific conditions. This is the key to the vapour film collapse prediction in the following section.

3.3. *Influence of non-ideal effects*

We now briefly investigate the influence on stability by the following non-ideal effects:

(i) Non-equilibrium evaporation: $K\neq 0$.
(ii) Heat transfer to liquid bulk: $C\neq 1$.
(iii) Imperfect wall temperature control: $Bi_w^{-1}\neq 0$.

Among the terms in (3.4), only the thermocapillary and vapour thrust terms are influenced by these effects. Besides the thermocapillary factor $K\tilde{M}$, all dependencies on these non-idealities are collected into the factor

$$F_0 = \frac{1}{(1 + C')(1 + Bi_w^{-1}) + K}. \tag{3.5}$$

Out of the three factors, K and Bi_w^{-1} are dependent on film-thickness scale. They both decrease towards zero as h_0 increases ($\sim h_0^{-1}$). Generally we will have $K \lll 1$ and $Bi_w^{-1} \ll 1$ when $h_0 > 1$ μm. The third factor C' is actually independent of h_0, but as explained in appendix B it can be expected to be very close to zero. In other words, the energy transferred into the liquid bulk is negligible compared to the energy spent on evaporation, no matter the film thickness.

Overall, this means that for moderate to large film thicknesses ($h_0 > 1$ μm) the influence of these non-ideal effects are negligible, and we have $F_0 \approx 1$. For very thin films, $F_0 < 1$. For such films, the reduction in F_0 reduces the vapour thrust term ($\sim F_0^3$) more than it reduces the thermocapillary term ($\sim F_0^2$), which means that the non-ideal effects have a destabilizing influence, if any.

3.4. *Predicting vapour film collapse*

In (3.4) we have three destabilizing terms (assuming $b > 0$ and $A > 0$) working against the sole stabilizing vapour thrust term. Their typical dependencies on film-thickness scale are illustrated in figure 4. We note the following features:

(i) For large h_0, the destabilizing influence of gravity will dominate.
(ii) For $h_0 < 100$ nm, the destabilizing influence of van der Waals forces will dominate
(iii) For intermediate h_0, there is a remarkably even struggle between the destabilizing influence of the thermocapillary effect and the stabilizing influence of the vapour thrust effect.

We see that the vapour film is always predicted to be unstable at very small or very large thickness scales due to the van der Waals and gravity terms, respectively. However, at the intermediate thickness scales the vapour thrust and thermocapillary terms are of similar magnitude but approximately two orders of magnitude larger than the other two. This means that the thermocapillary effect is the only destabilizing effect that is capable of cancelling out the stabilizing vapour thrust in the intermediate thickness range. While the gravity and van der Waals (vdW) terms also work against vapour thrust, their effect is negligible in comparison. In summary, the model suggests the following:

(i) The very small and very large thickness scales are always unstable.
(ii) The intermediate thickness scale can only be unstable if the thermocapillary term overpowers the vapour thrust term.

We may combine these two observations with the following hypothesis:

(i) *Hypothesis*: observed vapour film collapse (Leidenfrost transition) occurs when there is instability on every thickness scale.

The hypothesis implies that a necessary condition for film boiling collapse is that all three regions indicated in figure 4 are unstable. As stated above, the very small and very large scales are always unstable. This leaves the intermediate scales, which

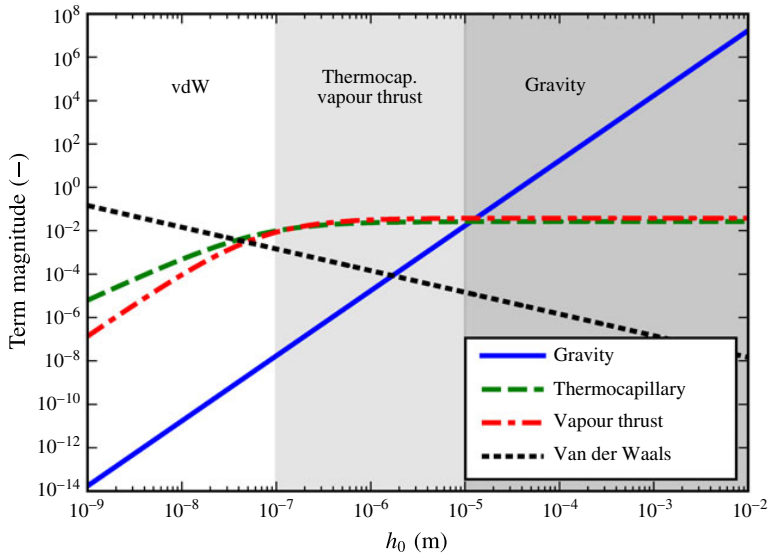

FIGURE 4. (Colour online) Sample values for the terms in (3.4) in the case of water film boiling with $\Delta T = 225$ K (above the Leidenfrost point), as a function of film-thickness scale h_0. The different shaded parts have labels indicating the dominant influence(s) in the given region.

are dominated by the thermocapillary and vapour thrust terms. To be even more specific, film boiling collapse would require instability in the $h_0 > 1$ μm part of the intermediate region. On these scales F_0 approaches unity, as discussed in § 3.3.

In summary, the above hypothesis together with the behaviour of the terms in (3.4) implies that a theoretical predictor for the Leidenfrost point may be found from the balance between the thermocapillary and vapour thrust terms in the $F_0 \to 1$ limit. Based on this we find the following h_0-independent criterion for vapour film collapse:

$$\frac{K\tilde{M}}{2E} > \frac{\xi E \mathrm{Re}}{6}. \tag{3.6}$$

The above condition depends on fluid properties as well as the superheat ΔT. We interpret the ΔT that satisfies (3.6) as an equality as the Leidenfrost point, ΔT_L. This is the superheat below which film boiling collapse is observed.

Note that the vapour density and conductivity contained in K, E, and Re are supposed to be evaluated at the average film temperature, $T_f = T_s + \Delta T/2$, which is initially unknown. We seek an explicit expression for ΔT_L that depends on known saturation properties only. When we insert expressions for the dimensionless constants in (3.6), we get

$$\frac{\Delta T_L}{T_s} = \left(\frac{3\eta}{1+3\eta}\right) \frac{\sqrt{2\pi R_s T_s}}{f(\alpha_e) k_{v,s}} \gamma \left[\frac{\rho_v}{\rho_{v,s}} \frac{k_{v,s}}{k_v}\right]. \tag{3.7}$$

The left-hand side is a convenient dimensionless quantity which we call the ‘relative Leidenfrost temperature’. We see that (3.7) is an implicit equation for the relative Leidenfrost temperature, since the square bracket also depends on it. For ideal gases

at constant pressure we know that $\rho_v \sim 1/T$ and $k_v \sim \sqrt{T}$, and thus, we may collect all ΔT_L dependence on the left-hand side, giving

$$\left(1+\frac{1}{2}\frac{\Delta T_L}{T_s}\right)^{3/2}\frac{\Delta T_L}{T_s}=\left(\frac{3\eta}{1+3\eta}\right)\left(\frac{\sqrt{2\pi}}{f(\alpha_e)}\right)\left(\frac{\sqrt{R_sT_s}}{k_{v,s}}\right)\gamma\equiv\Theta. \tag{3.8}$$

Here the right-hand side, labelled Θ for short, may be evaluated solely from known saturation properties. Its value is usually considerably less than unity. For small $\Delta T_L/T_s$, we may make (3.8) explicit, as

$$\frac{\Delta T_L}{T_s}\approx\frac{2}{3}[\sqrt{1+3\Theta}-1]. \tag{3.9}$$

It turns out that the third parenthesis in Θ is essentially fluid independent because we generally have that $k_v \sim \sqrt{R_sT}$, as known from ideal kinetic theory. When we define the (almost constant) variable

$$c_k=\frac{\sqrt{RT}}{k_v}, \tag{3.10}$$

the expression for Θ becomes

$$\Theta\approx\left(\frac{3\eta}{1+3\eta}\right)\left(\frac{c_k\sqrt{2\pi}}{f(\alpha_e)}\right)\gamma. \tag{3.11}$$

If we apply the expression (2.62) for $\eta(\Psi)$, we find that $3\eta/(1+3\eta)=3/(4+\Psi^{-1})$, which gives

$$\Theta\approx\left(\frac{3}{4+\Psi^{-1}}\right)\left(\frac{c_k\sqrt{2\pi}}{f(\alpha_e)}\right)\gamma. \tag{3.12}$$

Equation (3.9) with (3.12) constitute the final and relatively simple practical result which may be used to predict the relative Leidenfrost temperature. Given that fluids generally have the same values for Ψ, c_k and α_e, this model predicts that the relative Leidenfrost temperature depends almost solely on γ and that this relationship is approximately linear.

4. Experimental validation

We now seek to evaluate the predictive power of the present model by comparing it to experimental observations of ΔT_L. From now on, when we refer to the 'present model', we mean (3.9) with (3.12) while using the constant values

$$\overline{c_k}=14\,000\ \mathrm{K\ m\ N^{-1}}, \tag{4.1}$$

$$\overline{\Psi}=1/30, \tag{4.2}$$

which are simply rounded-off averages from the fluids studies here. Constant values for these parameters are used since c_k and Ψ are very similar for most fluids, compared to the variations in γ. Making this choice significantly simplifies the

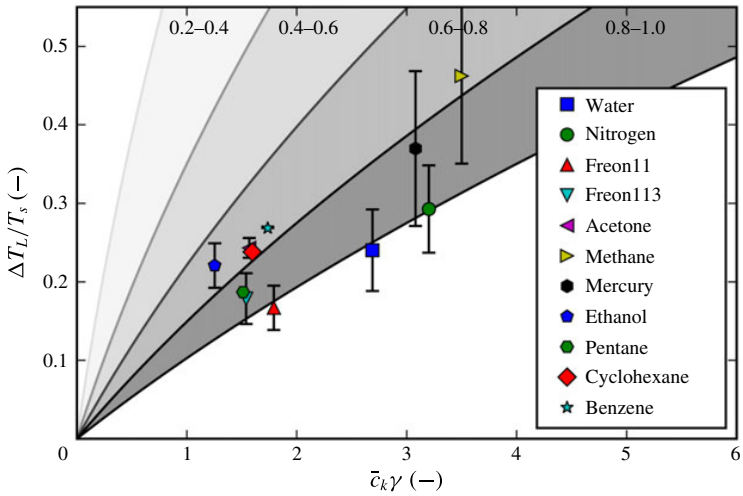

FIGURE 5. (Colour online) Comparison of the present model with the experimental data shown in table 1. The shaded regions indicate model predictions for different ranges of α_e. Error bars indicate the standard deviation of the different data points found in the literature. The lack of an error bar indicates that only a single data point could be found.

application of the model, and serves to illustrate the point that the model mostly depends on two parameters only: γ and $\alpha_e \in [0, 1]$. We look up γ directly from surface tension data, and use the Schrage form of the kinetic theory evaporation models, equation (2.9).

For each fluid, we look for a single experimentally measured property: the Leidenfrost temperature (T_L) found at atmospheric pressure. This number is then made dimensionless by considering its relative distance from the saturation temperature T_s, thus matching the left-hand side of (3.9). The data are shown in table 1.

We compare the model with the experimental data in figure 5, where model predictions are shown for the various possible ranges of the evaporation coefficient α_e. The figure shows that all data points are at least consistent with the model, in the sense that none of them would imply the impossible value $\alpha_e > 1$. The data points all fall within the predictions corresponding to $\alpha_e \in (0.7, 1.0)$, but the unknown nature of the evaporation coefficient prevents any accurate confirmation of the dependence on γ. The implications of figure 5 are further discussed in § 6.1.

5. Comparison with previous Leidenfrost point models

We now seek to evaluate the predictive capabilities of the present model compared to some existing models and correlations for the Leidenfrost point. The models considered here are either based on semi-empirical fluid mechanical considerations or based on the hypothesis that the Leidenfrost point corresponds to the superheat limit. The latter comes in two different versions, depending on how the superheat limit is represented.

5.1. *Simplified fluid mechanical models*

A semi-empirical model for the Leidenfrost point was developed by Berenson (1961, equation (40)), who developed a model for the film boiling heat transfer coefficient

based on classical Rayleigh–Taylor stability analysis and conservation equations in a simplified geometry. When he combined this with the minimum heat flux model by Zuber (1959), which also employs simplified fluid mechanical considerations, this resulted in an expression for ΔT_L,

$$\frac{\Delta T_L}{T_s} = 0.127 \frac{\rho_v L}{k_v T_s} \left(\frac{g \Delta \rho}{\rho_l + \rho_v} \right)^{2/3} \left(\frac{\sigma_0}{g \Delta \rho} \right)^{1/2} \left(\frac{\mu_v}{g \Delta \rho} \right)^{1/3}. \tag{5.1}$$

Note that (5.1) is semi-empirical. The exponents are theoretically derived, but the pre-factor 0.127 stems from an experimental fit to film boiling data.

5.2. *Leidenfrost point from superheat limit*

A different class of models is based on the simple hypothesis that the Leidenfrost point corresponds to the liquid superheat limit, also called the homogeneous nucleation temperature. The superheat limit is commonly estimated in two different ways. The first method is by calculating the spinodal temperature from an equation of state. The spinodal is the theoretical absolute maximum superheat temperature, where the vapour nucleation barrier goes to zero. However, homogeneous nucleation will usually proceed spontaneously before the barrier reaches zero, and the temperature where this happens may be approximated by classical nucleation theory (CNT). This is the second method. Both methods are purely theoretical and do not have any fitted empirical parameters. See Aursand *et al.* (2017) for further discussion on nucleation theory and the spinodal.

Superheat limit from spinodal. Using the spinodal to estimate the Leidenfrost point was first suggested by Spiegler *et al.* (1963). They used the van der Waals equation of state to analytically relate the spinodal (T_{sp}) to the critical temperature, $T_{sp} = (27/32)T_c$. This implies that the relative Leidenfrost temperature is simply

$$\frac{\Delta T_L}{T_s} = \frac{27}{32} \frac{T_c}{T_s} - 1. \tag{5.2}$$

Superheat limit from nucleation theory. Alternatively, one may use classical nucleation theory to predict the vapour nucleation rate at a given degree of liquid superheating. In combination with high accuracy equations of state, using this to predict the experimental superheat limit has been found to be quite accurate (Aursand *et al.* 2017). Going one step further and using this to represent the Leidenfrost point is less established but has been suggested by authors such as Yao & Henry (1978) and Sakurai *et al.* (1990). In classical nucleation theory (Aursand *et al.* 2017) the nucleation rate Λ (s−1 m^{-3}) is expressed as an Arrhenius rate law,

$$\Lambda = \Lambda_0 \exp\left(-\frac{\Delta G}{k_B T} \right), \tag{5.3}$$

with the activation energy being

$$\Delta G = \frac{16 \pi \sigma^3(T)}{3(p_s(T) - p)^2}, \tag{5.4}$$

and the rate at zero activation barrier being

$$\Lambda_0 = \frac{\rho_l}{m^{3/2}}\sqrt{\frac{2\sigma}{\pi}}. \tag{5.5}$$

Here, m is the mass of a single molecule and p_s is the thermodynamic saturation pressure. The specific expression for Λ_0 may vary a little between authors, but this has a negligible effect on the final result for the superheat limit.

The expression in (5.3) simply gives the nucleation rate as a function of fluid properties and temperature. In order to find the superheat limit, one must define a critical nucleation rate $\Lambda_c < \Lambda_0$, which corresponds to sudden macroscopic phase change. It turns out that due to the rapid growth of the exponential in (5.3), the result is quite insensitive to the specific choice of Λ_c. Here, we use the value of $\Lambda_c = 1 \times 10^{12}$ s^{-1} m^{-3}, as seen in previous works (Bernardin & Mudawar 1999; Aursand *et al.* 2017). Thus, in order to predict the superheat limit, we simply have to solve the implicit equation

$$\Lambda(T) = \Lambda_c \tag{5.6}$$

for T. Note that it is absolutely essential to include the temperature dependence of σ in (5.4), as it is one of the major sources of temperature dependence in ΔG. In order to obtain a model of comparable simplicity and avoid having to iteratively solve for the saturation line using an equation of state, we use the Clausius–Clapeyron relation to estimate the saturation pressure as

$$p_s(T) = p \exp\left[\frac{L}{R_s}\left(\frac{1}{T_s(p)} - \frac{1}{T}\right)\right]. \tag{5.7}$$

5.3. *Performance comparison*

We now seek to compare the predictive performance of the present model with the three alternative models presented in § 5.1 (Berenson model) and § 5.2 (Spiegler model and CNT model). Since α_e can generally be anywhere in the range of (0, 1), well-defined prediction by the present model requires the choice of a specific value. Here, we choose $\alpha_e = 0.85$, which is the centre point of the expected range identified in § 2.2. The fluid properties necessary to evaluate the other models were mainly found from the NIST database (Linstrom & Mallard 2017; Dean 1998). Missing mercury properties were found in Skapski (1948), Epstein & Powers (1953), Vinogradov (1981) and Huber, Laesecke & Friend (2006).

The evaluation of predictive performance is shown in figure 6, where we see that only the present model can accurately predict the relative Leidenfrost point within an error of 10 % for every fluid. This is further discussed in § 6.2.

6. Discussion

6.1. *Model validity and predictive power*

The present model for the Leidenfrost point depends on the somewhat unknown evaporation coefficient α_e, which is generally unknown but always lies within the range (0, 1). The model predicts that $\Delta T_L \to \infty$ when $\alpha_e \to 0$, and thus, generally the model merely provides a lower bound on ΔT_L given by the $\alpha_e = 1$ result. In terms of figure 5, this means that any data point above the bottom line ($\alpha_e = 1$) is consistent

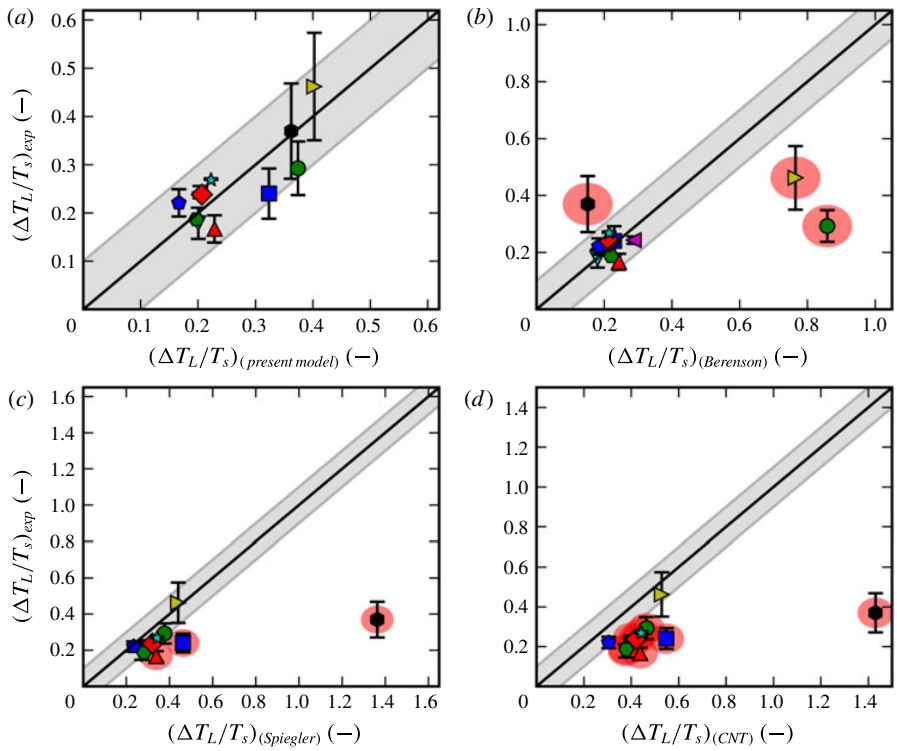

FIGURE 6. (Colour online) Comparison of model predictions with experimental data for the relative Leidenfrost point for (*a*) the present model (with $\alpha_e = 0.85$), (*b*) the Berenson model (5.1), (*c*) the Spiegler model (5.2) and (*d*) the CNT model (5.6). See figure 5 for data point legend. Grey bands show the range of a $\pm 10\,\%$ error in prediction of T_L, relative to T_s. Data points that fall outside this band are marked with red circles.

with the model. As discussed in § 2.2, molecular dynamics simulations indicate that α_e should be within the range 0.7–1.0. This is consistent with every data point seen in figure 5. Note that data points falling above the bottom line in figure 5 may also be explained by imperfect wall temperature control ($Bi_w^{-1} > 0$). On the other hand, if any data points were to fall significantly below the bottom line, that would count as evidence against the model. In this sense, the model is still falsifiable.

Qualitatively, the present model predicts that to a good approximation $\Delta T_L/T_s$ only depends on γ and α_e. Whereas all the data found are quantitatively consistent with the model, the γ dependence is not satisfactorily tested since all the fluids with available Leidenfrost data have γ-values within the same order of magnitude. Given this limited range of γ, we see in figure 5 that any good confirmation of the γ dependence is muddled by uncertainty in α_e. However, just as important as the prediction of γ-dependence is the predicted independence on very variable fluid properties such as T_s, σ_0 or L. While the fluids studied here have very variable values of these three parameters (even different orders of magnitude), they have values of $\Delta T_L/T_s$ within the same order of magnitude. This is correctly predicted by the present model.

Despite the fact that every data point is consistent with the model, the relatively uncertain nature of the evaporation coefficient may pose a problem for the predictive

power of the model. Without any additional information on α_e for a specific fluid, we have little choice but to assume a value. Thankfully, as we saw in figure 6(*a*), choosing the centre of the expected interval ($\alpha_e = 0.85$) yields a correct prediction for every data point within 10 % error. Additionally, the prediction of a lower bound on ΔT_L appears to be without flaw, as seen in figure 5.

Finally, an interesting observation can be made by looking at the effect of uncertainty in α_e on the predicted Leidenfrost temperature. The review in § 2.2 implies that the uncertainty in α_e is of the order of 10 %. Around the presumed average point $\alpha_e = 0.85$, a change of $\pm 10\,\%$ in α_e implies a change of approximately $\mp 20\,\%$ in the quantity $\Delta T_L / T_s$, as we may also see from the width of the shaded bands in figure 5. As an approximate general rule, this means that the uncertainty in absolute T_L (K) due to α_e is about 5 % of the fluid's saturation temperature. For the fluids where we have a sufficient number of data points to know the underlying variance with decent confidence, this 5 % rule corresponds remarkably well with the experimental standard deviation numbers in table 1. For water the model predicts an uncertainty of 18.7 K while the data have a standard deviation of 19.4 K. For nitrogen the model predicts an uncertainty of 3.87 K while the data have a standard deviation of 4.31 K. This may suggest that the reason for the relatively large variability in T_L measurements is that α_e varies between experiments, not because of any flaws in the Leidenfrost measurements. The fact that the present model can seemingly predict this variation gives it some additional credibility.

Overall, there are compelling pieces of evidence for the hypothesis that the thermocapillary instability is the governing effect behind film boiling collapse. However, there is insufficient available data to be certain.

6.2. *Benefits over existing models/correlations*

As shown in § 5 and especially in figure 6, the quantitative predictive power for the Leidenfrost point seems to be stronger in the present model compared to the three alternative models considered here. While the alternative models work reasonably well for conventional fluids, they are vastly erroneous for some of the more unusual fluids. Specifically, the Berenson model underpredicts the value for mercury and vastly overpredicts the value for the cryogens nitrogen and methane. The superheat limit based models moderately overpredict the conventional fluids and vastly overpredict the value for mercury. These problems are likely due to these fluids having unconventional values for saturation temperature and/or surface tension. Among the previous models, the semi-empirical Berenson model appears to quantitatively perform the best for conventional fluids, as seen in figure 6(*b*). However, the data do not appear to correlate in the suggested way. The model simply cuts through the group of data points from conventional fluids, while completely missing the fluids such as mercury and the cryogens, which were likely not part of the original parameter fitting.

Overall, we may claim that the present model for the Leidenfrost point has the following benefits:

(i) *Simplicity:* there is no need to know a large variety of fluid properties in order to make a prediction. Only a measured value for γ and an assumption regarding α_e is needed.

(ii) *Accuracy:* given only the value of γ, the present model is able to predict ΔT_L within an error of 10 % for every fluid considered here, including the cryogen and the liquid metal.

(iii) *Insight:* the model is purely theoretical, i.e. it involves no empirical parameters fitted to film boiling experiments. Such models are not only expected to have greater predictive capabilities, but are also more likely to provide insight into the physical mechanisms behind film boiling collapse. Specifically, the present model suggests that the mechanism of collapse is that the thermocapillary instability overpowers vapour thrust stabilization. To our knowledge, this has not been suggested before.

6.3. *Prediction in the absence of thermocapillary effect*

Note that this model's prediction of the Leidenfrost point is completely dependent on two complicating effects: non-equilibrium evaporation model and non-trivial liquid shear rate. Making either the approximation of quasi-equilibrium or zero liquid velocity would eliminate the thermocapillary effect from the model.

We may ask what the model would predict for the relative Leidenfrost temperature if the thermocapillary effect is absent, such as in the quasi-equilibrium limit ($K \to 0$). First of all, as discussed and made explicit in (3.4), this will completely remove the thermocapillary effect. If we go back to figure 4 and make the same kind of arguments as before, we see that film boiling collapse would necessitate that the gravity term is stronger than the vapour thrust in the intermediate region. This requirement leads to the criterion

$$\frac{G}{12E} > \frac{E\mathrm{Re}}{6(1+Bi_w^{-1})^3}, \tag{6.1}$$

which leads to the following prediction for the relative Leidenfrost point:

$$\frac{\Delta T_L}{T_s} = \sqrt{\frac{\rho_v \Delta\rho g}{2}}\frac{L}{k_v T_s}[(1+Bi_w^{-1})h_0]^{3/2}. \tag{6.2}$$

Qualitatively, equation (6.2) predicts that the relative Leidenfrost temperature is dependent on both T_s and L. As mentioned previously, this is not supported by the data. Note that (6.2) is dependent on the film-thickness scale h_0. If we make the assumption that we only need gravity to overpower vapour thrust down to the 1 μm scale before van der Waals forces take over, we still find that $\Delta T_L/T_s \approx 0.02$ for H_2O and $\Delta T_L/T_s \approx 0.05$ for N_2, both of which are approximately an order of magnitude below the experimental values in figure 5. Thus, the quasi-equilibrium limit of this model appears useless for predicting vapour film collapse.

6.4. *Modifying the Leidenfrost point*

It has been reported by authors such as Qiao & Chandra (1997) that adding surfactant (reducing σ_0) reduces the Leidenfrost temperature, i.e. it makes film boiling more stable. Without considering the thermocapillary instability, this seems counter-intuitive, since reducing surface tension would be expected to have a destabilizing effect, if any.

The present model can explain this qualitative effect. Since surface tension must reach zero at the fluid's critical point, if we can assume that γ is close to temperature independent it must be given by

$$\gamma \approx \frac{\sigma_0}{T_c - T_s}, \tag{6.3}$$

where T_c is the critical temperature of the fluid and σ_0 is the surface tension at the saturation temperature. Note that (6.3) does not imply that fluids with large surface tension necessarily will have a large γ. Water and especially mercury have large surface tensions but still quite ordinary γ values. Given this the present model

provides a new explanation for this observation: reducing σ_0 for a given fluid will reduce γ through (6.3) and thus weaken the thermocapillary instability relative to the vapour thrust.

A commonly suggested method of modifying the Leidenfrost point is through the solid surface topography, such as addition of micro- or nanostructures (Auliano *et al.* 2017). This cannot be predicted by this model in its present form, as a flat and smooth solid surface has been assumed from the beginning.

7. Conclusions

In summary:

(i) We presented governing equations for vapour flow in film boiling. Of particular importance and novelty was the use of a non-equilibrium evaporation model based on kinetic theory, which allowed for the inclusion of thermocapillary effects along the evaporating liquid–vapour interface.

(ii) We used the long-wave approximation and simplified liquid dynamics to derive a single highly nonlinear scalar PDE for the film thickness function: (2.66).

(iii) We applied linear stability analysis to the above mentioned PDE and identified four terms which govern the long-wave stability of a uniform vapour film: (3.4). Analysis of their dependence on film-thickness scale revealed that the question of stability at the intermediate (micrometre) scale is primarily a struggle between destabilizing thermocapillary effects and stabilizing vapour thrust. The scales above and below are always unstable.

(iv) We posed the hypothesis that film boiling collapse occurs when the film is unstable for any film-thickness scale. According to the present stability analysis, this would necessitate that thermocapillary instabilities overpower vapour thrust.

(v) Based on the above hypothesis we derived a relatively simple model for the Leidenfrost temperature, equations (3.9) with (3.12), which mainly depends on γ, the temperature dependence of surface tension.

(vi) We gathered experimental data for 11 different fluids and showed how the model is consistent with the average Leidenfrost temperature for every one of them given that the evaporation coefficient is in the range 0.7–1.0. As mentioned in § 2.2, this range for α_e is consistent with recent evaporation/condensation studies using molecular dynamics simulations.

(vii) We showed how the assumption of evaporation coefficient equal to 0.85 can successfully predict the Leidenfrost point for each of the fluids within 10 % error, a feat that commonly cited models/correlations could not perform.

The present model is a completely theoretical prediction and involves no empirical parameters fitted to film boiling experiments. This allows us to draw conclusions regarding the underlying phenomena. We have found compelling but preliminary evidence to support the following statements:

(i) *The governing mechanism behind film boiling collapse (Leidenfrost transition) may be the thermocapillary instability at the liquid–vapour interface.* The thermocapillary instability at an evaporating interface is closely connected to non-equilibrium evaporation effects.

(ii) The relative Leidenfrost point, $\Delta T_L/T_s$, depends almost linearly on γ, the temperature dependence of surface tension.

(iii) The relative Leidenfrost point also depends on the evaporation coefficient α_e from kinetic theory. Its value is generally unknown but the range 0.7–1.0 gives consistency with all the data. The maximum value of 1.0 gives a reliable lower bound, and the central value 0.85 gives overall good prediction.

Additional research is needed to further validate or disprove these conclusions. Efforts should be made to identify fluids with uncommon (high or low) values of γ and then measure their Leidenfrost point. While any data points in the shaded regions of figure 5 is consistent with the model, any new points below would count as evidence against it. Finally, it would be very helpful to resolve some of the uncertainty regarding the evaporation coefficient, as it would sharpen the prediction of the model and put it to a stronger test. This could be resolved with a combination of theory and experiments.

Acknowledgements

E.A. was supported by the Research Council of Norway [244076/O80] and The Gas Technology Centre (NTNU–SINTEF) through the funding programme MAROFF. His research visit at Northwestern University was supported by the US-Norway Fulbright Foundation. Additional thanks to Bernhard Müller, Svend Tollak Munkejord and Morten Hammer for discussions and feedback.

Appendix A. Liquid velocity profile and the value of η

In § 2.7.4 the issue of the unknown liquid velocity profile was handled by interpolating the interface velocity between the two calculable theoretical extremes: the case of zero interface velocity, and the case of zero liquid shear. The specific point on the interpolation was set by the unknown parameter $\eta \in [0, 1]$.

In this section we explore what a specific assumption regarding the liquid velocity profile implies for the value of η. We follow the method proposed in Aursand (2018), and assume a liquid velocity profile of the form

$$U_l \sim \frac{1}{Z}. \tag{A 1}$$

While (A 1) is arguably quite *ad hoc*, it has the desirable property of monotonically and smoothly decreasing to zero value (and zero derivatives) as $Z \to \infty$. If we now combine the velocity profiles (2.52) and (A 1) with the boundary conditions (2.29) and (2.32), we may solve explicitly for the vapour velocity profile,

$$U = \frac{1}{2}\bar{P}_X \left(Z^2 - \frac{2 + \Psi^{-1}}{1 + \Psi^{-1}} HZ \right) - \frac{1}{1 + \Psi^{-1}} \epsilon M (\theta_i)_X Z, \tag{A 2}$$

and the interface velocity,

$$U_i = \frac{1}{1 + \Psi^{-1}} \left(-\frac{1}{2} H^2 \bar{P}_X - \epsilon M H (\theta_i)_X \right). \tag{A 3}$$

If we compare (A 3) with its generic version (2.60), we see that

$$\eta = \frac{1}{1 + \Psi^{-1}} = \Psi + O(\Psi^2). \tag{A 4}$$

Appendix B. Liquid heat transfer

In § 2.7.2, the shorthand $C = 1 + C'$ was introduced to express the solution to the energy equation, with the small deviation from unity being

$$C' \equiv Bi_l K = \frac{\tilde{K} \alpha_l}{L}. \tag{B 1}$$

Note that while Bi_l and K individually are dependent on h_0, C is not. Since Bi_l does not appear outside of C in the model, all influence of liquid heat transfer in the dimensionless equations turns out to be independent of film-thickness scale.

The present model assumes that the liquid bulk is held at the saturation temperature. To be more precise, one could state that the temperature is regulated to T_s a constant distance $z = \Delta z_l \gg h_0$ from the solid wall. The heat transfer coefficient in the liquid, α_l, may then be expressed as a conductive contribution multiplied by a Nusselt number (Nu) to account for possible convective enhancement,

$$\alpha_l = Nu \frac{k_l}{\Delta z}. \tag{B 2}$$

If we use water as an example,

$$\tilde{K} \approx 0.14 \text{ K m}^2 \text{ s kg}^{-1}, \tag{B 3}$$

$$L \approx 2 \times 10^6 \text{ J kg}^{-1}, \tag{B 4}$$

$$k_l \approx 0.7 \text{ W m}^{-1} \text{ K}^{-1}, \tag{B 5}$$

and assume that the liquid temperature control happens on the scale of $\Delta z \sim 1$ cm, the small parameter becomes

$$C' = Nu \frac{\tilde{K} k_l}{L \Delta z} \approx Nu \times 10^{-6}. \tag{B 6}$$

Due to the small velocities and temperature differences in the liquid, we may likely assume that the convective enhancement is laminar and weak, i.e. $Nu \sim O(1)$. Thus, we get $C' \lll 1$, and we may assume

$$C \approx 1 \tag{B 7}$$

for the remaining analysis.

This means that the energy transferred from the interface to the liquid bulk is negligible compared to the energy spent on evaporation, no matter the film thickness h_0. This can be explained by the fact that the interface temperature is only slightly different from the saturation temperature ($\theta_i \sim K$). While the interface temperature increases if the film becomes thinner, so does the evaporation rate, so the former remains negligible.

Note that if one considers subcooled film boiling instead, i.e. a bulk liquid temperature considerably below saturation, the liquid heat transfer is no longer negligible.

REFERENCES

AGOSTINI, B., FABBRI, M., PARK, J. E., WOJTAN, L., THOME, J. R. & MICHEL, B. 2007 State of the art of high heat flux cooling technologies. *Heat Transfer Engng* **28** (4), 258–281.

AULIANO, M., FERNANDINO, M., ZHANG, P. & DORAO, C. A. 2017 The Leidenfrost phenomenon on sub-micron tapered pillars. In *ASME 2017 15th International Conference on Nanochannels, Microchannels, and Minichannels*, pp. V001T08A003–V001T08A003. American Society of Mechanical Engineers.

AURSAND, E. 2018 Inclination dependence of planar film boiling stability. *Intl J. Multiphase Flow* doi:10.1016/j.ijmultiphaseflow.2018.05.010.

AURSAND, P., GJENNESTAD, M., AURSAND, E., HAMMER, M. & WILHELMSEN, Ø. 2017 The spinodal of single- and multi-component fluids and its role in the development of modern equations of state. *Fluid Phase Equilib.* **436**, 98–112.

BAUMEISTER, K. J. & SIMON, F. F. 1973 Leidenfrost temperature: its correlation for liquid metals, cryogens, hydrocarbons, and water. *Trans. ASME J. Heat Transfer* **95**, 166–173.

BERENSON, P. J. 1961 Film-boiling heat transfer from a horizontal surface. *Trans. ASME J. Heat Transfer* **83** (3), 351–356.

BERNARDIN, J. D. & MUDAWAR, I. 1999 The Leidenfrost point: experimental study and assessment of existing models. *Trans. ASME J. Heat Transfer* **121** (4), 894–903.

BERTHOUD, G. 2000 Vapor explosions. *Annu. Rev. Fluid Mech.* **32** (1), 573–611.

BURELBACH, J. P., BANKOFF, S. G. & DAVIS, S. H. 1988 Nonlinear stability of evaporating/ condensing liquid films. *J. Fluid Mech.* **195**, 463–494.

CAO, B.-Y., XIE, J.-F. & SAZHIN, S. S. 2011 Molecular dynamics study on evaporation and condensation of n-dodecane at liquid–vapor phase equilibria. *J. Chem. Phys.* **134** (16), 164309.

CHENG, S., LECHMAN, J. B., PLIMPTON, S. J. & GREST, G. S. 2011 Evaporation of Lennard-Jones fluids. *J. Chem. Phys.* **134** (22), 224704.

CLEAVER, P., JOHNSON, M. & HO, B. 2007 A summary of some experimental data on LNG safety. *J. Hazard. Mater.* **140** (3), 429–438.

CRASTER, R. V. & MATAR, O. K. 2009 Dynamics and stability of thin liquid films. *Rev. Mod. Phys.* **81** (3), 1131–1198.

DAVIS, S. H. 1987 Thermocapillary instabilities. *Annu. Rev. Fluid Mech.* **19** (1), 403–435.

DEAN, J. A. 1998 *Lange's Handbook of Chemistry*, 15th edn. McGraw-Hill.

DHIR, V. K. 1998 Boiling heat transfer. *Annu. Rev. Fluid Mech.* **30** (1), 365–401.

EPSTEIN, L. F. & POWERS, M. D. 1953 Liquid metals. Part I. The viscosity of mercury vapor and the potential function for mercury. *J. Phys. Chem.* **57** (3), 336–341.

FLETCHER, D. F. 1995 Steam explosion triggering: a review of theoretical and experimental investigations. *Nucl. Engng Des.* **155**, 27–36.

GOTTFRIED, B. S. & BELL, K. J. 1966 Film boiling of spheroidal droplets: Leidenfrost phenomenon. *Ind. Engng Chem. Fundam.* **5** (4), 561–568.

HERTZ, H. 1882 Ueber die Verdunstung der Flüssigkeiten, insbesondere des Quecksilbers, im luftleeren Raume. *Ann. Phys.* **253** (10), 177–193.

HUBER, M. L., LAESECKE, A. & FRIEND, D. G. 2006 Correlation for the vapor pressure of mercury. *Ind. Engng Chem. Res.* **45** (21), 7351–7361.

ISHIYAMA, T., FUJIKAWA, S., KURZ, T. & LAUTERBORN, W. 2013 Nonequilibrium kinetic boundary condition at the vapor–liquid interface of argon. *Phys. Rev.* E **88** (4), 042406.

ISKRENOVA, E. K. & PATNAIK, S. S. 2017 Molecular dynamics study of octane condensation coefficient at room temperature. *Intl J. Heat Mass Transfer* **115**, 474–481.

KNUDSEN, M. 1915 Die maximale Verdampfungsgeschwindigkeit des Quecksilbers. *Ann. Phys.* **352** (13), 697–708.

KUNDU, P. K., COHEN, I. M. & DOWLING, D. R. 2007 *Fluid Mechanics*, 5th edn. Academic.

LIANG, Z., BIBEN, T. & KEBLINSKI, P. 2017 Molecular simulation of steady-state evaporation and condensation: validity of the Schrage relationships. *Intl J. Heat Mass Transfer* **114**, 105–114.

LINSTROM, P. J. & MALLARD, W. G. (Eds) 2017 *NIST Chemistry WebBook, NIST Standard Reference Database Number 69*. National Institute of Standards and Technology.

LUKETA-HANLIN, A. 2006 A review of large-scale LNG spills: experiments and modeling. *J. Hazard. Mater.* **132**, 119–140.

MILLS, A. F. 1995 *Heat and Mass Transfer*. CRC Press.

MYERS, T. G. 1998 Thin films with high surface tension. *SIAM Rev.* **40** (3), 441–462.

NAGAI, N. & NISHIO, S. 1996 Leidenfrost temperature on an extremely smooth surface. *Exp. Therm. Fluid Sci.* **12** (3), 373–379.

ORON, A., DAVIS, S. H. & BANKOFF, S. G. 1997 Long-scale evolution of thin liquid films. *Rev. Mod. Phys.* **69** (3), 931–980.

PANZARELLA, C. H., DAVIS, S. H. & BANKOFF, S. G. 2000 Nonlinear dynamics in horizontal film boiling. *J. Fluid Mech.* **402**, 163–194.

QIAO, Y. M. & CHANDRA, S. 1997 Experiments on adding a surfactant to water drops boiling on a hot surface. *Proc. R. Soc. Lond. A Math. Phys. Engng Sci.* **453**, 673–689.

RUCKENSTEIN, E. & JAIN, R. K. 1974 Spontaneous rupture of thin liquid films. *J. Chem. Soc. Faraday Trans.* **70**, 132–147.

SAKURAI, A., SHIOTSU, M. & HATA, K. 1990 Effects of system pressure on minimum film boiling temperature for various liquids. *Exp. Therm. Fluid Sci.* **3** (4), 450–457.

SKAPSKI, A. S. 1948 The temperature coefficient of the surface tension of liquid metals. *J. Chem. Phys.* **16** (4), 386–389.

SPIEGLER, P., HOPENFELD, J., SILBERBERG, M., BUMPUS, C. F. & NORMAN, A. 1963 Onset of stable film boiling and the foam limit. *Intl J. Heat Mass Transfer* **6** (11), 987–989.

THEOFANOUS, T. G., LIU, C., ADDITON, S., ANGELINI, S., KYMÄLÄINEN, O. & SALMASSI, T. 1997 In-vessel coolability and retention of a core melt. *Nucl. Engng Des.* **169** (1–3), 1–48.

TSURUTA, T. & NAGAYAMA, G. 2004 Molecular dynamics studies on the condensation coefficient of water. *J. Phys. Chem.* B **108** (5), 1736–1743.

VALENCIA-CHAVEZ, J. A. 1978 The effect of composition on the boiling rates of liquefied natural gas for confined spills on water. PhD thesis, Massachusetts Institute of Technology.

VESOVIC, V. 2007 The influence of ice formation on vaporization of LNG on water surfaces. *J. Hazard. Mater.* **140** (3), 518–526.

VINOGRADOV, Y. K. 1981 Thermal conductivity of mercury vapor. *J. Engng Phys. Thermophys.* **41** (2), 868–870.

XIE, J.-F., SAZHIN, S. S. & CAO, B.-Y. 2011 Molecular dynamics study of the processes in the vicinity of the n-dodecane vapour/liquid interface. *Phys. Fluids* **23** (11), 112104.

YAO, S.-C. & HENRY, R. E. 1978 An investigation of the minimum film boiling temperature on horizontal surfaces. *J. Heat Transfer* **100** (2), 260–267.

YTREHUS, T. 1997 Molecular-flow effects in evaporation and condensation at interfaces. *Multiphase Sci. Technol.* **9** (3), 205–327.

ZUBER, N. 1959 Hydrodynamic aspects of boiling heat transfer. PhD thesis, University of California, Los Angeles, CA.

Paper B

Inclination dependence of planar film boiling stability

Eskil Aursand

Published in *International Journal of Multiphase Flow*.
(2018) Vol. 106, pp. 243–253
https://doi.org/10.1016/j.ijmultiphaseflow.2018.05.010

International Journal of Multiphase Flow 106 (2018) 243–253

Contents lists available at ScienceDirect

International Journal of Multiphase Flow

journal homepage: www.elsevier.com/locate/ijmulflow

Inclination dependence of planar film boiling stability

Eskil Aursand

Department of Energy and Process Engineering, Norwegian University of Science and Technology (NTNU), Trondheim N-7491, Norway

ARTICLE INFO

Article history:
Received 16 October 2017
Revised 6 April 2018
Accepted 9 May 2018
Available online 11 May 2018

Keywords:
Film boiling
Liquid–vapor interface
Thin vapor film
Stability
Inclination angle
Kelvin–Helmholtz

ABSTRACT

Understanding the dynamics of film boiling is crucial for predicting its heat transfer properties. Besides the complete breakdown of film boiling (Leidenfrost point), the most prominent transition is the change from a steady state to an unstable and oscillating vapor film. Here we consider the stability of saturated planar non-horizontal film boiling, with particular attention given to its dependence on inclination angle. Based on the lubrication approximation and a quasi-equilibrium evaporation model, we derive a model for transient film boiling dynamics. We investigate the stability of its steady-state solution by locally applying potential flow linear stability analysis. We show how the behavior will be an inclination dependent mixture of Kelvin–Helmholtz and Rayleigh–Taylor type instabilities, and a relatively simple stability criterion is derived. We also show how the transient lubrication model is incapable of predicting the former kind of instability. The model's ability to predict the inclination dependence of stability limits is tested against an experimental data set from the literature, and we see that the model displays reasonable accuracy considering its lack of free empirical parameters.

1. Introduction

When a heated solid surface is submerged in a liquid with a considerably lower saturation temperature, a vapor phase will begin to nucleate at the surface of contact. The resulting relationship between the surface superheat and the heat flux is the *boiling curve* (Dhir, 1998), also called the Nukiyama curve, named after the person who first characterized it in the 1930s (Nukiyama, 1934). At moderate superheat, in the nucleate boiling regime, the boiling curve exhibits the intuitive behavior of increasing heat flux with increasing superheat. However, this will only continue up to the *critical heat flux* (CHF), which signals the transition from *nucleate boiling* to *film boiling*, and is seen as a counterintuitive decrease in heat flux with increasing surface temperature. The drop in heat flux is due to the formation of a continuous vapor film between the solid and the liquid, which has an insulating effect on the heat transfer. In some practical situations film boiling is desirable, and in some it is not. In either case it is of interest to predict the dynamics of the vapor film, and under which conditions it may become unstable. Instabilities indicate a change in heat transfer properties, and may also precede vapor film collapse (Leidenfrost point) (Dhir, 1998).

Predicting the overall heat transfer efficiency of film boiling is important for various industrial concerns. This includes the relatively common case of quenching hot solid surfaces with water (Dhir, 1998), but also the more exotic case of cryogens boiling when spreading on top of water (Hissong, 2007). The stability limits and breakdown of film boiling are also important, as they are believed to be the triggering mechanism for vapor explosions (rapid phase transition) in nuclear fuel-coolant interactions (Fletcher, 1995; Berthoud, 2000) and liquefied natural gas (LNG) (Luketa-Hanlin, 2006; Cleaver et al., 2007).

The problem to be solved in this work is illustrated in Fig. 1. This is a case of two-dimensional saturated natural convection film boiling on a heated solid plate. Since the model assumes a state of film boiling, it is only applicable at surface temperatures above the value at the fluid's CHF. At the same time, it is assumed that the surface temperature is low enough that radiation heat transfer may be neglected. As shown by Jouhara and Axcell (2009), this is valid for quite a wide range of surface temperatures.

The objective is to predict the spatiotemporal behavior of the liquid–vapor interface, mathematically represented by the film thickness function $h(x, t)$. The plate is submerged at a given angle α, and particular attention is given to how the dynamics change depending on this inclination. Under common conditions the formed vapor film is very thin, of the order of 100 µm (Dhir, 1998; Jouhara and Axcell, 2002). Since this is likely to be much thinner than the tangential length scale, thin-film flow theory is applicable for the analysis of the vapor film dynamics. A common way of approaching thin-film flow is by use of the *lubrication approximation* (Kundu et al., 2007, Sec. 8.3), which exploits the large difference in length scales in order to simplify the Navier–Stokes

E-mail address: eskil.aursand@ntnu.no

https://doi.org/10.1016/j.ijmultiphaseflow.2018.05.010
0301-9322/

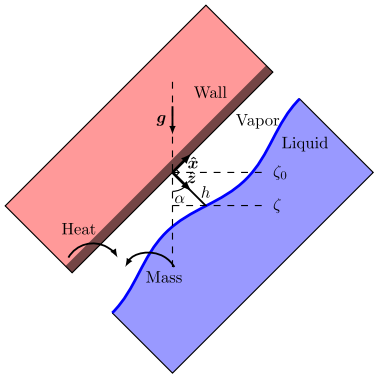

Fig. 1. Illustration of the planar film boiling problem. A wall at angle α supplies heat to a boiling liquid, which feeds vapor into the vapor film in between. Buoyancy then drives vapor flow along the wall.

equations. When combined with the mass-conservation principle, this will reduce the full set of governing equations and boundary conditions to a single highly nonlinear scalar PDE (Myers, 1998).

The dynamics of thin liquid films on solid surfaces, including analysis by the lubrication approximation, has been extensively reviewed in the past by Oron et al. (1997), Myers (1998) and Craster and Matar (2009). Considerable analysis has been done specifically on horizontal evaporating or condensing liquid films, e.g. by Burelbach et al. (1988). The case of an evaporating liquid film falling down an inclined plane has been treated by authors such as Joo et al. (1991). The case of film boiling is different, as the thin film consists of vapor, not liquid. Some work has been done on analyzing film boiling dynamics with thin-film models, such as in Panzarella et al. (2000), Kim et al. (2015) and Kim and Kim (2016). However, these were for the purely horizontal case, with no net tangential flow or significant shear forces. In terms of stability analysis, horizontal film boiling has uniform but time-dependent base states. The vertical and inclined cases are different, as they have steady but non-uniform base states. Such steady solutions have been studied since the work of Bromley (1950) in the 50s, and have since been elaborated by many authors, such as Koh (1962), Bui and Dhir (1985), Kolev (1998) and Jouhara and Axcell (2009). While they show some variations due to different assumptions regarding liquid dynamics outside the film, most have the same general form of $h \sim x^{1/4}$, with x being the distance along the solid surface. There are few works on film boiling considering the effect of inclination away from the vertical. Examples are Nishio and Chandratilleke (1991) and Kim and Suh (2013).

The purpose of the present study is to investigate the limits of stability of the steady solutions found in non-horizontal film boiling. Particular attention is given to the interplay of Kelvin–Helmholtz and Rayleigh–Taylor instability mechanisms, and how this depends on inclination angle. The goal is to achieve this analysis with a relatively simple model, in order to gain insight and practically useful expressions. While Kim and Suh (2013) consider the inclination dependence of film boiling stability, the actual onset of instability in their model is given by the *critical Reynolds number*, an empirical parameter that is fitted to the experiments. The present work avoids any free empirical parameters, and thus offers ab initio predictions on stability.

In Section 2 we derive a transient model for inclined planar saturated film boiling based on the lubrication approximation. The result is a fourth-order highly nonlinear parabolic PDE for the vapor film thickness. We show that the equation has an analytical approximate steady-state solution, with a corresponding expression for the average tangential vapor velocity.

In Section 3 we show how scales based on these steady solutions can give a useful dimensionless formulation of the model based on a few dimensionless numbers. We highlight how the values of these numbers depend on position and orientation. In Section 4 we find under which conditions the previously found steady-state solutions will turn unstable, and which wavelengths will be prominent once that occurs. This is done in two different ways. First, this is done by performing linear stability analysis of the PDE from the lubrication approximation, and then by locally applying potential flow stability analysis to the steady-state solution from the lubrication model. Both lead to their own stability criteria, with some similarities and some differences. As will be shown, the former method lacks predictive capabilities for a prominent stability mechanism. We go on to analyze why.

In Section 5 we leave the dimensionless world for a while in order to show practical results for a specific case involving water film boiling over a range of superheat degrees. In Section 6 we compare predictions from the stability analysis with certain experimental measurements by Kim and Suh (2013). Finally, the important messages of the present study are summed up in Section 7.

2. Lubrication approximation model

We aim to model the behavior of the film thickness function $h(x, t)$, in the setup illustrated in Fig. 1. In order to do this, we make the following assumptions:

- We assume that the thickness of the film is much smaller than its length scale. This allows the application of the lubrication approximation.
- We assume that the thermo-physical properties of the vapor, such as density and viscosity, can be treated as constant.
- We assume that the evaporation rate is small enough that it is in quasi-equilibrium, thus locking the interface temperature to the saturation temperature. This has the secondary effect of also neglecting any thermo-capillary effects, since the interface temperature will be constant.
- We neglect any effect the liquid dynamics may have on pressure, i.e. the interface pressure on the liquid side is given by the hydrostatic pressure.
- The pressure jump across the liquid–vapor interface is given by surface tension alone, i.e. we are neglecting the vapor thrust effect.
- We neglect any van der Waals contributions to the film pressure (disjoining pressure).

2.1. Mass flow rate from lubrication approximation

In the case of thin-film flow of an incompressible fluid, we may apply the classical lubrication approximation (Kundu et al., 2007, Sec. 8.3). This assumption uses the large difference in the film's tangential and perpendicular length scales to neglect the inertial and time-differential terms in the Navier–Stokes equations. The momentum equations reduce to

$$\frac{\partial p}{\partial x} = \rho_{\mathrm{v}} g_x + \mu_{\mathrm{v}} \frac{\partial^2 u}{\partial z^2}, \tag{1}$$

and

$$\frac{\partial p}{\partial z} = \rho_{\mathrm{v}} g_z. \tag{2}$$

Here p is the pressure, u is the x-directed velocity, μ_{v} is the vapor viscosity, ρ_{v} is the vapor density, and g_x, g_z are the gravitational acceleration projected along the x and z-directions, respectively.

According to the definition of the inclination angle α in Fig. 1, we have that

$$g_x = -g\sin\alpha, \tag{3}$$

$$g_z = g\cos\alpha, \tag{4}$$

where g is the gravitational acceleration. Under the assumption that $\partial p/\partial x$ is independent of z, which will be justified in Section 2.2, we find from Eq. (1) that the second derivative of u with respect to z is constant at a given x, and can be written as

$$\frac{\partial^2 u}{\partial z^2} = -\frac{1}{\mu_\mathrm{v}} D(x), \tag{5}$$

where we have defined the driving force $D(x)$,

$$D(x) \equiv \rho_\mathrm{v} g_x - \frac{\partial p}{\partial x}. \tag{6}$$

The expression in Eq. (5) implies a parabolic velocity profile with a given curvature. In order to find this profile we need two additional pieces of information, and these are the boundary conditions at the solid wall ($z = 0$) and at the liquid-vapor interface ($z = h$). At the solid wall, the no-slip condition simply implies that $u = 0$. At the liquid–vapor interface, we assume continuity of tangential velocity and shear stress. Here we will make no specific assumptions about the interface tangential velocity, but rather investigate the two extreme possibilities: These are the assumption of zero velocity ($u = 0$), and the assumption of zero shear stress at the interface ($\partial u/\partial z = 0$). In either case, this leads to the same kind of expression for the mass flow rate along the film,

$$M(x) = W\frac{\rho_\mathrm{v} h^3}{\beta\mu_\mathrm{v}} D(x), \tag{7}$$

where W is the depth of the film in the symmetry direction, and the difference from the two assumptions enter through the factor β, with values

$$\beta = \begin{cases} 12 & \text{Maximum shear stress.} \\ 3 & \text{Zero shear stress.} \end{cases} \tag{8}$$

When $\beta = 12$, the tangential interface velocity is zero. When $\beta = 3$, the tangential interface velocity is 3/2 times the average vapor velocity. In reality, the value of β would be somewhere in between, but we see that in any case the order of magnitude of $M(x)$ stays the same. A discussion on estimating the actual value of β from the viscosity ratio can be found in Appendix A.

2.2. Pressure model

In order to use the expression Eq. (7), we will need a model for the driving force Eq. (6), and thus the pressure gradient $\partial p/\partial x$ in the film. With the boundary condition $p(z = h) = p_{\mathrm{v,i}}$, the solution to Eq. (2) is

$$p = p_{\mathrm{v,i}} - \rho_\mathrm{v} g_z (h - z), \tag{9}$$

where $p_{\mathrm{v,\,i}}$ is the pressure at the vapor side of the liquid-vapor interface. Since neither $p_{\mathrm{v,\,i}}$ nor h are functions of z, we see that $\partial p/\partial x$ will be independent of z, as assumed earlier. The pressure jump at the interface is given by the surface tension contribution,

$$p_{\mathrm{l,i}} - p_{\mathrm{v,i}} = \sigma\kappa, \tag{10}$$

where $p_{\mathrm{l,\,i}}$ is the interface pressure on the liquid side, σ is the surface tension, and κ is the interface curvature. The curvature can be calculated from the film thickness function by

$$\kappa = \frac{\frac{\partial^2 h}{\partial x^2}}{\left(1 + \left(\frac{\partial h}{\partial x}\right)^2\right)^{3/2}} \approx \frac{\partial^2 h}{\partial x^2}, \tag{11}$$

where the final approximation can be used for long waves where $\partial h/\partial x \ll 1$, which will be applicable here. The liquid pressure at the interface is given by the hydrostatic contribution corresponding to the vertical position of the interface,

$$p_{\mathrm{l,i}} = p_0 - \rho_\mathrm{l} g\zeta, \tag{12}$$

where p_0 is a reference pressure, ρ_l is the liquid density, and $\zeta = \zeta_0 - h\cos(\alpha)$ is the vertical position of the interface (see Fig. 1). The latter depends on x as

$$\frac{\partial \zeta}{\partial x} = \sin(\alpha) - \cos(\alpha)\frac{\partial h}{\partial x}. \tag{13}$$

If we combine Eqs. (9), (10), (12), (13), we find that

$$\frac{\partial p}{\partial x} = -\rho_\mathrm{l} g\sin(\alpha) + \Delta\rho g\cos(\alpha)\frac{\partial h}{\partial x} - \sigma\frac{\partial \kappa}{\partial x}, \tag{14}$$

where $\Delta\rho \equiv \rho_\mathrm{l} - \rho_\mathrm{v}$. The driving force is thus given by

$$D(x) = \Delta\rho g\left[a + b\frac{\partial h}{\partial x}\right] + \sigma\frac{\partial \kappa}{\partial x}, \tag{15}$$

where we have defined the short-hands

$$a = \sin\alpha, \tag{16}$$

$$b = -\cos\alpha. \tag{17}$$

Note that in this pressure model both the vapor thrust and van der Waals terms have been neglected, for the same reasons as those presented by Panzarella et al. (2000).

2.3. Heat transfer and evaporation

The evaporation is driven by a heat flux across the vapor film, caused by a temperature difference between the wall and the liquid-vapor interface. When considerable evaporation or condensation occurs across a liquid–vapor interface, the liquid interface temperature T_i is not actually exactly at the thermodynamic saturation temperature T_sat of the fluid. For moderate evaporation rates, we may linearize this effect through the following constitutive equation,

$$T_\mathrm{i} - T_\mathrm{sat} = Kj, \tag{18}$$

where j is the evaporation mass flux, and K is the non-equilibrium coefficient whose value can be estimated from kinetic gas theory (Burelbach et al., 1988; Oron et al., 1997; Panzarella et al., 2000). For strong evaporation there may also be a slight temperature discontinuity at the liquid-vapor interface. In this work we take the quasi-equilibrium limit, which implies a temperature that is continuous, and equal to the saturation temperature at the interface, i.e. $T_\mathrm{i} = T_\mathrm{sat}$. In fact, we state that the entire bulk of the liquid is at the temperature T_sat, i.e. we have so-called *saturated film boiling*. This has the consequence that all the heat conducted into the interface from the vapor side is spent on evaporation. Accounting for any further heating of the liquid above T_sat would require a non-equilibrium model.

With the lubrication approximation, the energy equation in the vapor film reduces to

$$\frac{\partial^2 T}{\partial z^2} = 0, \tag{19}$$

i.e. the temperature profile is linear. This means that in this approximation, the heat flux conducted into the liquid–vapor interface is equal to the heat flux conducted from the wall to the vapor. In reality, some energy must be spent heating the newly added vapor from T_sat to the temperature in the vapor film, the so-called *sensible heat* effect, but this is negligible when the lubrication approximation applies. If one wanted to account for this, it may be

achieved by slightly adjusting the effective latent heat of evaporation, and therefore it will not affect the qualitative conclusions of this work.

Since the liquid is assumed to be uniformly at its saturated state, all heat reaching the liquid–vapor interface will be spent on evaporation. This energy balance can be expressed as

$$\dot{q}|_{z=h} = Lj \tag{20}$$

where $\dot{q}$ is the heat flux and L is the latent heat of evaporation. Since we stay in the regime of negligible radiation heat, the heat flux reaching the liquid–vapor interface is given by Fourier's law alone, which states that

$$\dot{q}|_{z=h} = k_v \frac{\partial T}{\partial z}\bigg|_{z=h} = k_v \frac{\Delta T}{h}, \tag{21}$$

where the last equality follows from Eq. (19). Here, k_v is the vapor thermal conductivity and ΔT is the difference between wall temperature and saturation temperature (wall superheat). If we combine Eqs. (20) and (21), we may write the mass flux as a function of film thickness,

$$j = \frac{Q}{h}, \tag{22}$$

where we have defined the constant

$$Q = \frac{k_v \Delta T}{L}. \tag{23}$$

2.4. Mass conservation

We now consider mass conservation in a control volume of vapor film from x_L to x_R, i.e. of length $\Delta x = x_R - x_L$. The conservation principle implies that the rate of change of mass contained in this volume of vapor film must be equal to the net mass flow rate into it. With a constant density, this becomes

$$W\rho_v \frac{\partial}{\partial t}\int_{x_L}^{x_R} h(x)\mathrm{d}x + M(x_R) - M(x_L) = W\int_{x_L}^{x_R} j(x)\mathrm{d}x \tag{24}$$

Given the mass flow rate of Eq. (7) and an evaporation mass flux model of the form Eq. (22), Eq. (24) becomes

$$\frac{\partial}{\partial t}\int_{x_L}^{x_R} h(x)\mathrm{d}x + \frac{h^3(x_R)}{\beta\mu_v}D(x_R) - \frac{h^3(x_L)}{\beta\mu_v}D(x_L) = \frac{Q}{\rho_v}\int_{x_L}^{x_R}\frac{1}{h(x)}\mathrm{d}x \tag{25}$$

In the limits $\Delta x \to 0$ and $h \gg \Delta x$, Eq. (25) reduces to the PDE

$$\frac{\partial h}{\partial t} + \frac{1}{\beta\mu_v}\frac{\partial}{\partial x}\left[h^3\left(\Delta\rho g\left(a + b\frac{\partial h}{\partial x}\right) + \sigma\frac{\partial \kappa}{\partial x}\right)\right] = \frac{Q}{\rho_v h}, \tag{26}$$

which is the governing equation for the film thickness $h(x, t)$ in this set of approximations.

2.5. Approximate steady-state solution

We seek a steady-state solution to this problem, $\bar{h}(x)$, and assume that such a solution will be so slowly varying in space that the surface tension contribution to the mass flow rate is negligible. The full equation Eq. (25) then reduces to

$$\left(\bar{h}^3\left[a + b\frac{\partial \bar{h}}{\partial x}\right]\right)_R - \left(\bar{h}^3\left[a + b\frac{\partial \bar{h}}{\partial x}\right]\right)_L = \frac{\beta\mu_v Q}{\rho_v\Delta\rho g}\int_{x_L}^{x_R}\frac{1}{\bar{h}(x)}\mathrm{d}x. \tag{27}$$

It turns out that an exact analytical solution to Eq. (27) can be found, and it is

$$\bar{h}(x) = \left(\frac{4\beta}{3}\frac{\mu_v Q}{\rho_v\Delta\rho g a}\right)^{1/4} x^{1/4}. \tag{28}$$

Curiously, the solution Eq. (28) is independent of b. This is possible because solutions in the form $\bar{h} \sim x^{1/4}$ has the property that $\bar{h}^3\partial\bar{h}/\partial x$ is constant, and thus the contribution of the b-term to the flux gradient is zero.

A steady-state solution with the properties $\bar{h} \sim x^{1/4}$ and $\bar{h} \sim a^{-1/4}$ has been presented before by authors such as Nishio and Chandratilleke (1991) and Kim and Suh (2013). However, Eq. (28) includes the factor β, which in a simple way shows the effects of the possible range of assumptions that could be made for the liquid flow. What is typically not discussed in relation to this solution is its inconsistency with the lubrication approximation in the $h(x) \to 0$ limit. Physically, we would expect the mass flow rate $M(x)$ to approach zero, but with the expression in Eq. (15), $h^3D(x)$ and thus $M(x)$ incorrectly approaches a finite value, giving infinite velocity. Fortunately this error is small for small aspect ratios and/or inclinations close to vertical.

If we accept the film thickness function given by Eq. (28), we may calculate the average vapor velocity at position x by considering total mass conservation,

$$\begin{aligned}\bar{u}(x) &= \frac{Q}{\rho_v\bar{h}(x)}\int_0^x \frac{1}{\bar{h}(x')}\mathrm{d}x' \\ &= \frac{\Delta\rho g a}{\beta\mu_v}\bar{h}^2(x) \\ &= \sqrt{\frac{4}{3\beta}\frac{\Delta\rho g Q a}{\mu_v\rho_v}}\sqrt{x}.\end{aligned} \tag{29}$$

The above shows the dependence of $\bar{u}$ on both position x and the position-dependent film thickness $\bar{h}$. Both are useful forms. The vapor velocity will increase in proportion to $\sqrt{x}$, and as we will see, eventually the velocities will be large enough for Kelvin–Helmholtz instabilities to be important.

3. Scales and dimensionless numbers

3.1. Scales of film boiling dynamics

A planar film boiling case is given by fluid properties, an inclination angle α, a superheat ΔT, and a plate length x_0. We define the scales of a given case by the steady-state solution Eq. (28) at $x = x_0$. In order to highlight the effects of inclination, we use the corresponding vertical ($a = 1$) case as a reference. Thus the length scale, used for both x and z, is

$$h_0 = \left(\frac{4\beta}{3}\frac{\mu_v Q}{\rho_v\Delta\rho g}x_0\right)^{1/4} = a^{1/4}\bar{h}(x_0). \tag{30}$$

We use the average vapor velocity as the velocity scale,

$$u_0 = \frac{\Delta\rho g}{\beta\mu_v}h_0^2 = \sqrt{\frac{4}{3\beta}\frac{\Delta\rho g Q}{\mu_v\rho_v}x_0} = \frac{\bar{u}(x_0)}{\sqrt{a}}. \tag{31}$$

This enables us to define a time scale,

$$t_0 = \frac{h_0}{u_0} = \frac{\beta\mu_v}{\Delta\rho g h_0} = \left(\frac{3\beta^3\mu_v^3\rho_v}{4Qx_0(\Delta\rho g)^3}\right)^{1/4}. \tag{32}$$

3.2. Dimensionless numbers

The dimensionless numbers used in this work, and their common definitions, are shown in Table 1. If we insert the film thickness Eq. (28) and the velocity Eq. (29) into the general definitions

Table 1
Summary of dimensionless numbers used in this work, and their common definitions.

Name	Definition	Description
Bond number	$\mathrm{Bo} = \frac{\Delta\rho g h^2}{\sigma}$	Buoyant vs capillary forces.
Reynolds number	$\mathrm{Re} = \frac{\rho_v u h}{\mu_v}$	Inertial vs viscous forces.
Weber number	$\mathrm{We} = \frac{\rho_v u^2 h}{\sigma}$	Inertial vs capillary forces.
Aspect ratio	$\epsilon = \frac{h}{x_0}$	Film thickness vs film length.

in Table 1, we get the film-boiling specific expressions,

$$\mathrm{Bo} = \frac{\Delta\rho g h^2}{\sigma} = \frac{1}{\sigma}\sqrt{\frac{4\beta\Delta\rho g\mu_v Q}{3\rho_v a}}x_0, \tag{33}$$

$$\mathrm{Re} = \frac{\rho_v\Delta\rho g a h^3}{\beta\mu_v^2} = \left(\frac{64\rho_v\Delta\rho g Q^3 a}{27\beta\mu_v^5}x_0^3\right)^{1/4}, \tag{34}$$

$$\mathrm{We} = \frac{\rho_v(\Delta\rho g)^2 a^2 h^5}{\beta^2\sigma\mu_v^2} = \frac{1}{\sigma}\left(\frac{1024(\Delta\rho g)^3 Q^5 a^3 x_0^5}{243\beta^3\rho_v\mu_v^3}\right)^{1/4}, \tag{35}$$

$$\epsilon = \frac{h}{x_0} = \left(\frac{4\beta\mu_v Q}{3\rho_v\Delta\rho g a x_0^3}\right)^{1/4}. \tag{36}$$

We see that in the film boiling case, we have the relation

$$\mathrm{We} = \frac{a\mathrm{ReBo}}{\beta}, \tag{37}$$

since the buoyant and viscous forces become directly related in the lubrication approximation. When referring to the reference (vertical) case, we add a subscript 0 to the dimensionless numbers. The angular dependence of these numbers are

$$\mathrm{Bo} = a^{-1/2}\mathrm{Bo}_0, \tag{38}$$

$$\mathrm{Re} = a^{1/4}\mathrm{Re}_0, \tag{39}$$

$$\mathrm{We} = a^{3/4}\mathrm{We}_0, \tag{40}$$

$$\epsilon = a^{-1/4}\epsilon_0. \tag{41}$$

In some cases it is useful to substitute the full plate length x_0 for the film thickness h in the definition of the Bond number. We label this Bo_X, and it is defined as

$$\mathrm{Bo}_X = \frac{\Delta\rho g x_0^2}{\sigma}. \tag{42}$$

An overview of typical values for these scales and dimensionless numbers is shown in Table 2.

4. Linear stability analysis

We now wish to investigate the conditions where the steady-state solution Eq. (28) is stable with respect to small perturbations. This is done by two different approaches:

- In Section 4.1, we apply linear stability analysis to the dimensionless version of the PDE from the lubrication approximation, Eq. (26).
- In Section 4.2, we use the classical result from potential flow stability analysis for the shear flow of two immiscible fluids in a gravitational field. We then use the steady-state solution from the lubrication approximation to insert expressions for the vapor film thickness and the velocities on either side of the interface.

As will be shown, the two approaches give consistent results in some respects, but will also have significant qualitative differences.

Table 2
Overview of possible values for scales and dimensionless numbers, here for boiling water with case parameters $\Delta T = 100$–200 K and $X_0 = 0.5$–10 cm. These ranges of ΔT and X_0 yield a range of values for each scale and dimensionless number, based on expressions found in Section 3. The max/min limits of these ranges are shown in this table.

	Min	Max	Unit	Eq.
h_0	120	300	μm	(30)
u_0	0.94	6.0	ms^{-1}	(31)
t_0	0.048	0.12	ms	(32)
Bo_0	0.0021	0.013	–	(33)
Re_0	5.3	84	–	(34)
We_0	0.0010	0.10	–	(35)
ϵ_0	0.0024	0.027	–	(36)
Bo_X	4.0	1600	–	(42)

4.1. Lubrication approximation

4.1.1. Dispersion relation

If we use the length and time scales defined in Section 3.1, as well as the approximate expression for curvature in Eq. (11), the PDE in Eq. (26) can be written in dimensionless form as

$$\frac{\partial H}{\partial\tau} + \frac{\partial}{\partial X}\left[H^3\left(a + b\frac{\partial H}{\partial X} + c\frac{\partial^3 H}{\partial X^3}\right)\right] = \frac{3\epsilon_0}{4}\frac{1}{H}, \tag{43}$$

where H, τ and X are the dimensionless film thickness, time and position, respectively, and we have defined $c = 1/\mathrm{Bo}_0$. Eq. (43) can be classified as a fourth-order nonlinear parabolic equation with a source term. Such thin-film equations with inclination have been studied previously by e.g. Myers (1998), but commonly in the context of falling liquid films, not buoyant vapor films. The specific form in Eq. (43) may be solved numerically by semi-implicit methods, as demonstrated by Aursand (2017).

The steady-state solution Eq. (28) takes on an especially simple dimensionless form,

$$\bar{H}(X) = \left(\frac{\epsilon_0 X}{a}\right)^{1/4}. \tag{44}$$

This is thus a steady-state solution of Eq. (43) for $c = 0$. We see that for a vertical plate, $\bar{H}(1/\epsilon_0) = 1$, as was intended by the scaling. We now investigate the stability of a steady solution $\bar{H}(X)$ by considering solutions to Eq. (43) that are equal to the steady solution with a small added transient perturbation, $H(X,\tau) = \bar{H}(X) + \eta(X,\tau)$. The perturbation can be written as $\eta(x,t) = Af(X,\tau)$, where A is a small number giving the magnitude of the perturbation, and $f(X,\tau)$ is the shape of the perturbation. If we insert this into Eq. (43), use Eq. (44) for $\bar{H}(x)$ and its derivatives, and assume that $\bar{H}(x) \sim \mathcal{O}(1)$, we obtain the following PDE for the perturbation $\eta(X,\tau)$,

$$\begin{aligned}\frac{\partial\eta}{\partial\tau} + c\bar{H}^3\frac{\partial^4\eta}{\partial X^4} + \frac{3c\epsilon_0}{4\bar{H}a}\frac{\partial^3\eta}{\partial X^3} + b\bar{H}^3\frac{\partial^2\eta}{\partial X^2} \\ + \left(3a\bar{H}^2 + \frac{3b\epsilon_0}{2\bar{H}a}\right)\frac{\partial\eta}{\partial X} + \frac{9\epsilon_0}{4\bar{H}^2}\eta \\ = \mathcal{O}\left(A^2\right) + \mathcal{O}\left(\epsilon_0^2\right),\end{aligned} \tag{45}$$

We may then investigate the initial evolution of a plane wave disturbance $f(x,t) = \exp[i(kX - \omega\tau)]$, where k is the wavenumber and ω is the complex angular frequency. If we insert this form for η into the PDE Eq. (45), and discard the higher order terms in A and ϵ_0, we get the following dispersion relation,

$$\omega = 3a\bar{H}^2 k + \frac{3b\epsilon_0}{2\bar{H}a}k - \frac{3c\epsilon_0}{4\bar{H}a}k^3 + i\left[\bar{H}^3 k^2\left(b - ck^2\right) - \frac{9\epsilon_0}{4\bar{H}^2}\right]. \tag{46}$$

4.1.2. Stability

The disturbance is unstable if the imaginary part of ω is positive. We see that in this model, the only source of instability is

the b-term (Rayleigh-Taylor type buoyant effect), and this will be present only if $b > 0$. When $b > 0$, we have unconditional stabilization due to surface tension for all wavenumbers above the maximum value $k_{\max}^2 = b\mathrm{Bo}_0$. Additionally, there is the evaporation term (ϵ_0-term) which stabilizes all wavenumbers equally. However, its effect is most noticeable for small k, where surface tension has little effect. Thus, for positive b there is a potential for instabilities, but surface tension stabilizes short wavelengths, and evaporation stabilizes long wavelengths.

We see from Eq. (46) that the largest potential for instability is where $\bar{H}$ is largest, i.e. where $\bar{H} = a^{-1/4}$. In order to investigate total stability, we look at the stability at this point. For $b > 0$, there is instability between the critical wavenumbers,

$$k_{\mathrm{crit}}^2 = \frac{1}{2c}\left(b \pm \sqrt{b^2 - 9c\epsilon_0 a^{5/4}}\right). \tag{47}$$

However, for a given case with plate length x_0, not all wavenumbers are available for excitation. If we decide that wavelengths larger than x_0 are not allowed, we get a minimum allowable dimensionless wavenumber of $k_{\min} = 2\pi\epsilon_0$. A sufficient and necessary criterion for stability is that $k_{\min} > k_{\mathrm{crit}}$, which can be stated as

$$4\pi^2 > b\mathrm{Bo}_X \frac{1}{2}\left(1 + \sqrt{1 - \frac{9a^{5/4}}{\epsilon_0 \mathrm{Bo}_X b^2}}\right). \tag{48}$$

The above criterion is quite unwieldy, but we may also state simpler sufficient (but not necessary) criteria for stability. These are

$$b\mathrm{Bo}_X < 4\pi^2, \tag{49}$$

$$\frac{b^2}{a^{5/4}} < \frac{9}{\epsilon_0 \mathrm{Bo}_X}. \tag{50}$$

Either one of these is sufficient for stability. Eq. (49) is satisfied when all allowable wavelengths are stabilized by surface tension. Eq. (50) is satisfied when the evaporation effect is sufficient to stabilize all wavelengths until the end of the plate. Note that Eq. (48) is satisfied for all $b \leq 0$ regardless of other conditions, and thus the vertical case and all liquid-below-vapor orientations are predicted to be stable.

The most dangerous (fastest growing) wavenumber can be found as the value of k giving the largest imaginary value in Eq. (46),

$$k_{\mathrm{d}}^2 = \frac{1}{2} b\mathrm{Bo}_0, \tag{51}$$

which in the horizontal ($b = 1$) limit agrees with the common Rayleigh–Taylor instability result from lubrication theory (Kim et al., 2015).

4.2. Potential flow

4.2.1. General thin-film flow

We now disregard evaporation for a moment, and consider the case of a thin vapor film of constant thickness h, with a solid wall on one side, and an infinite liquid on the other side. The vapor and the liquid both have a given base state velocity, u_{v} and u_{l}, respectively. If we apply potential flow linear stability analysis (Drazin and Reid, 2004) to the liquid–vapor interface in this model case, the dispersion relation for a small harmonic disturbance ($\sim \exp(i[\tilde{k}x - \tilde{\omega}t])$) becomes

$$\tilde{\omega} = \frac{\tilde{k}\left(\rho_{\mathrm{l}} u_{\mathrm{l}} + \rho_{\mathrm{v}}' u_{\mathrm{v}}\right)}{\rho_{\mathrm{l}} + \rho_{\mathrm{v}}'} \pm \left(\frac{\tilde{k}^3\sigma}{(\rho_{\mathrm{l}} + \rho_{\mathrm{v}}')} + \frac{\tilde{k} g_z \Delta\rho}{(\rho_{\mathrm{l}} + \rho_{\mathrm{v}}')} - \frac{\tilde{k}^2 \rho_{\mathrm{l}} \rho_{\mathrm{v}}' (u_{\mathrm{v}} - u_{\mathrm{l}})^2}{(\rho_{\mathrm{l}} + \rho_{\mathrm{v}}')^2}\right)^{\frac{1}{2}}. \tag{52}$$

where $\tilde{\omega}$ is the dimensional complex angular frequency, $\tilde{k}$ is the dimensional wavenumber, and we have introduced the following shorthand for the effective vapor density due to the thin-film effect,

$$\rho_{\mathrm{v}}' = \frac{\rho_{\mathrm{v}}}{\tanh(\tilde{k}h)}. \tag{53}$$

We may state Eq. (52) in dimensionless form by choosing a length scale h_0 and a velocity scale u_0. The result is in the form

$$\omega = \omega_{\mathrm{R}} \pm \omega_{\mathrm{I}}, \tag{54}$$

where ω_{R} is always real, while ω_{I} is imaginary in the case of instabilities. The latter turns out to be

$$\omega_{\mathrm{I}} = \left(\frac{\sigma}{h_0 u_0^2 \rho_{\mathrm{l}}\left(1 + \frac{\rho_{\mathrm{v}}'}{\rho_{\mathrm{l}}}\right)}\right)^{\frac{1}{2}} \left(k^3 - b\mathrm{Bo}_0 k - \left(\frac{u_{\mathrm{v}}}{u_0}\right)^2 \left(1 - \frac{u_{\mathrm{l}}}{u_{\mathrm{v}}}\right)^2 \frac{\rho_{\mathrm{v}}'}{\rho_{\mathrm{v}}} \frac{\mathrm{We}_0 k^2}{1 + \frac{\rho_{\mathrm{v}}'}{\rho_{\mathrm{l}}}}\right)^{\frac{1}{2}}, \tag{55}$$

Here ω and k are the dimensionless angular frequency and wavenumber, respectively, according to the length scale h_0 and the time scale h_0/u_0. We have introduced Bo_0 and We_0 according to their definitions in Table 1 using h_0 and u_0. We allow the actual film thickness to be different from the scale h_0, and the deviation is given by the dimensionless film thickness H, such that $\tilde{k}h = kH$. Under the assumption that the waves are long but not extremely long,

$$\frac{\rho_{\mathrm{v}}}{\rho_{\mathrm{l}}} \ll kH \ll 1, \tag{56}$$

an assumption that will be checked for self consistency later, we may perform the simplifications $\tanh(kH) \approx kH$ and $1 + \rho_{\mathrm{v}}'/\rho_{\mathrm{l}} \approx 1$ and thus simplify Eq. (55) to

$$\omega_{\mathrm{I}} = \left(\frac{\sigma}{h_0 u_0^2 \rho_{\mathrm{l}}}\right)^{\frac{1}{2}} \left(k^3 - b\mathrm{Bo}_0 k - \left(\frac{u_{\mathrm{v}}}{u_0}\right)^2 \left(1 - \frac{u_{\mathrm{l}}}{u_{\mathrm{v}}}\right)^2 \frac{\mathrm{We}_0 k}{H}\right)^{\frac{1}{2}}. \tag{57}$$

4.2.2. With steady-state film boiling solution

The result in Eq. (57) has so far not included anything specific to film boiling, but is simply an expression which, besides thermophysical properties, requires three inputs in order to consider stability: A film thickness H, a characteristic vapor velocity u_{v}, and a characteristic liquid velocity u_{l}. We will now use the results from the steady-state lubrication analysis of film boiling to get values for these quantities. First, the dimensionless film thickness is given by Eq. (44), $\bar{H}(X) = (\epsilon_0 X/a)^{1/4}$. Second, we set the characteristic vapor velocity to be the average velocity in the film, $u_{\mathrm{v}} = \bar{u}$, according to Eq. (29). We can then see from Eqs. (29) and (31) that at position X the ratio between average velocity and the velocity scale is

$$\frac{u_{\mathrm{v}}(X)}{u_0} = \sqrt{a\epsilon_0 X}. \tag{58}$$

Third, if we assume the characteristic liquid velocity to be about half of the interface velocity, we can use the result in Eq. (A.7) from Appendix A to state that

$$\frac{u_{\mathrm{l}}}{u_{\mathrm{v}}} = 1 - \frac{\beta}{12}. \tag{59}$$

If we insert all this into Eq. (57), we get

$$\omega_{\mathrm{I}} = \left(\frac{\sigma}{h_0 u_0^2 \rho_{\mathrm{l}}}\right)^{\frac{1}{2}} \left(k^3 - b\mathrm{Bo}_0 k - (\epsilon_0 X)^{\frac{3}{4}} a^{\frac{5}{4}} \left(\frac{\beta}{12}\right)^2 \mathrm{We}_0 k\right)^{\frac{1}{2}}. \tag{60}$$

Since Eq. (54) involves $\pm\omega_{\mathrm{I}}$, an imaginary ω_{I} will always enable an exponentially growing disturbance (instability). It will be imaginary if the contents of the last square root in Eq. (60) is negative. We see that there are two terms that contribute towards instability: A term with the Bond number Bo_0 which represents the Rayleigh–Taylor (RT) instability, and a term with the Weber number We_0 which represents the Kelvin–Helmholtz (KH) instability. We see that the RT term is equal at all positions, while the KH term increases as $X^{3/4}$ since the vapor velocity is larger further out in the film. Thus we have the highest potential for instability close to the end of the plate.

4.2.3. Limits of stability

We may now look at the conditions required for the film boiling to stay stable across a plate of a given physical length x_0. If the contents of the final square root in Eq. (60) is positive, we have stability. As mentioned, the highest potential for instability is at the end of the plate, where $\epsilon_0 X = 1$, so we will look for the conditions where this position will be stable. We can immediately see that the film will be stable with respect to very high k. Thus there may exist some critical wavenumber k_{crit} below which there may be instabilities. We find this as

$$k_{\mathrm{crit}}^2 = \mathrm{Bo}_0\left(b + a^{5/4}\Phi_{\mathrm{KH}}\right), \tag{61}$$

where we have used the vertical special case of Eq. (37), $\mathrm{We}_0 = \mathrm{Re}_0\mathrm{Bo}_0/\beta$, and defined the quantity

$$\Phi_{\mathrm{KH}} = \frac{\beta \mathrm{Re}_0}{144} \tag{62}$$

as the angle-independent relative importance of the KH instability. Given the typical ranges for Re_0 in Table 2, and given that $\beta \approx 10$, we see that $\Phi_{\mathrm{KH}} \in (0.35, 5.625)$. Since $\Phi_{\mathrm{KH}} \sim \mathcal{O}(1)$, we see that the KH instability will dominate close to the vertical configuration, and that the RT instability will dominate close to the horizontal configuration.

While all wavenumbers $k < k_{\mathrm{crit}}$ can go unstable, not all the corresponding wavelengths can fit on the plate. If we again state that we only allow wavelengths shorter than the plate itself, we get a minimum allowable wavenumber of $k_{\mathrm{min}} = 2\pi\epsilon_0$. If $k_{\mathrm{min}} > k_{\mathrm{crit}}$ we can expect total stability, which leads to the stability condition

$$\frac{\mathrm{Bo}_X}{4\pi^2}\left(b + a^{5/4}\Phi_{\mathrm{KH}}\right) < 1. \tag{63}$$

In Eq. (63), all dependence on surface tension is contained in Bo_X. However, if the contents of the parenthesis is negative, we will have stability regardless of how weak the surface tension is. This may occur in the $\alpha < \pi/2$ region, if the KH instability is sufficiently balanced by a stabilizing RT effect. The limiting angle of this region, α_{min}, is given by

$$\frac{\cos(\alpha_{\mathrm{min}})}{\sin^{5/4}(\alpha_{\mathrm{min}})} = \Phi_{\mathrm{KH}}. \tag{64}$$

A decent approximation is then $\alpha_{\mathrm{min}} \approx \arctan(\Phi_{\mathrm{KH}}^{-1})$. Due to surface tension, the actual onset of instabilities will happen at some critical angle larger than α_{min}, where Eq. (63) is no longer satisfied. However the left hand side of Eq. (63) is not always monotonous with respect to angle α. If $\mathrm{Bo}_X < 4\pi^2$, i.e. if the plate length is of the order of the capillary length (or shorter), there is a potential for a return to stability as the angle starts to approach $\alpha \to \pi$. However, for any reasonable set of parameters this can only happen very close to $\alpha = \pi$, where the usage of the steady-state lubrication solutions becomes dubious anyway, so we will limit ourselves to looking for the first critical angle, α_{crit}, the smallest angle where Eq. (63) is satisfied as an equality.

In Fig. 2, we have numerically solved for α_{crit} in $(\mathrm{Bo}_X, \mathrm{Re}_0)$ space, while indicating typical parameter combinations occurring in the case of water film boiling. We see that at a given value of Bo_X, increasing Re_0 (e.g. by increasing ΔT) will cause instabilities to arise at smaller angles. It appears quite common that the critical angle will be far into the liquid-below-vapor region (blue regions in Fig. 2). In fact, for larger plate lengths instabilities can appear at $\alpha < 45°$ and lower, due to the high vapor velocities obtained. In the blue regions, the RT mechanism is stabilizing, so these instabilities are purely due to the KH mechanism.

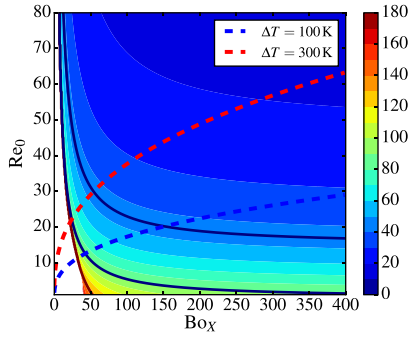

Fig. 2. A contour map of α_{crit} (the solution of Eq. (63) as an equality) in degrees across $(\mathrm{Bo}_X, \mathrm{Re}_0)$ space, with $\beta = 10.67$. The white area is the region of global stability. The solid black lines mark specially the angles 45°, 90° and 135°. The dashed lines indicate the domain expected in water film boiling in the region $\Delta T \in (100\ \mathrm{K}, 300\ \mathrm{K})$. Moving to the right along the dashed lines indicate an increased plate length X_0. (For interpretation of the references to colour in this figure legend, the reader is referred to the web version of this article.)

4.2.4. Characteristic wavelengths

If we start out with a stable case, and slowly change a parameter to increase k_{crit} towards k_{min}, the instability that appears first will then obviously be $k \approx k_{\mathrm{min}}$, i.e. with the largest allowable wavelength. As we go further into the unstable region, the fastest growing allowable wavelength will keep being $k \approx k_{\mathrm{min}}$, until reaching the most dangerous wavenumber, k_{d}. Once k_{d} is within the range of allowed wavenumbers, it will be the dominant instability. See Fig. 3 for an illustration.

As before, the expression for k_{d} can be found as the value of k that gives the largest magnitude to ω_{I}, now found from Eq. (60). This turns out to be

$$k_{\mathrm{d}}^2 = \frac{1}{3}\mathrm{Bo}_0\left(b + a^{5/4}\Phi_{\mathrm{KH}}\right) = \frac{1}{3}k_{\mathrm{crit}}^2, \tag{65}$$

i.e the most dangerous wavelength is about 1.7 times the critical wavelength. We may show that the squared most dangerous wavelength ($\lambda_{\mathrm{d}} = 2\pi/k_{\mathrm{d}}$) becomes akin to a weighted harmonic (non-normalized) mean based on two other squared wavelengths, so that

$$\lambda_{\mathrm{d}}^2 = \left(b\frac{1}{\lambda_{\mathrm{RT}}^2} + a^{5/4}\frac{1}{\lambda_{\mathrm{KH}}^2}\right)^{-1}, \tag{66}$$

where λ_{RT} is the dimensionless Rayleigh–Taylor wavelength approached at the liquid-above-vapor horizontal configuration,

$$\lambda_{\mathrm{RT}} = 2\pi\sqrt{\frac{3}{\mathrm{Bo}_0}}, \quad \tilde{\lambda}_{\mathrm{RT}} = 2\pi\sqrt{\frac{3\sigma}{\Delta\rho g}}, \tag{67}$$

and λ_{KH} is the dimensionless Kelvin–Helmholtz wavelength approached at the vertical configuration,

$$\lambda_{\mathrm{KH}} = 2\pi\sqrt{\frac{3}{\frac{\beta^2}{144}\mathrm{We}_0}}, \quad \tilde{\lambda}_{\mathrm{KH}} = 2\pi\sqrt{\frac{3h_0\sigma}{\rho_{\mathrm{v}}\left(\frac{\beta}{12}u_0\right)^2}}, \tag{68}$$

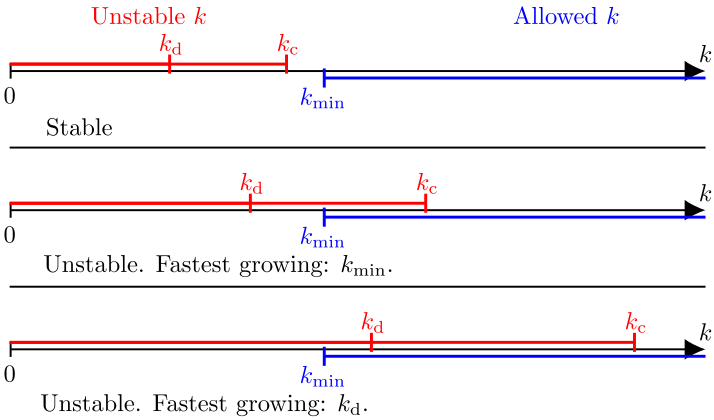

Fig. 3. Illustration of the three different states of (in)stability. Top: There is no overlap between unstable wavenumbers and allowed wavenumbers, so the case is stable. Middle: There is overlap between unstable wavenumbers and allowed wavenumbers, so the case is unstable. The wavenumber k_d is still not allowed, so the dominant instability will be k_{min}. Bottom: There is overlap between unstable wavenumbers and allowed wavenumbers, so the case is unstable. The wavenumber k_d will be the dominant instability.

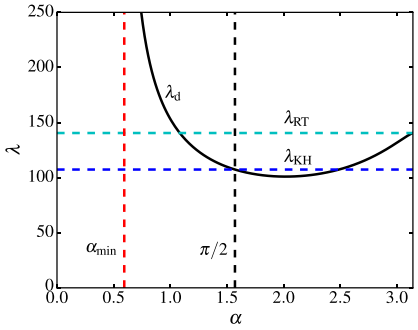

Fig. 4. A plot of the fastest growing wavelength according to Eq. (66), with $\mathrm{Bo}_0 = 0.006$ and $\mathrm{We}_0 = 0.013$ (reasonable values for water film boiling), and thus $\mathrm{Re}_0 \approx 23$. Also shown are the limiting wavelengths λ_{RT} and λ_{KH}, according to Eqs. (67), (68), respectively. The RT wavelength is 30% larger, as predicted by the Reynolds number and Eq. (69).

with inclination-dependent weights $b = -\cos(\alpha)$ and $a^{5/4} = \sin^{5/4}(\alpha)$. The symbols $\tilde{\lambda}$ in Eqs. (67), (68) indicate the corresponding dimensional wavelengths. These are consistent with the classical results from potential flow stability analysis. The ratio between the two wavelengths is

$$\frac{\lambda_{RT}}{\lambda_{KH}} = \sqrt{\Phi_{KH}}. \tag{69}$$

Since $\Phi_{KH} \sim \mathcal{O}(1)$, the wavelengths will mostly be of the same order of magnitude. Either could be somewhat larger than the other, and the point of equality is around $\mathrm{Re}_0 \approx 14$. Since Eq. (66) has the form of a harmonic mean, if the wavelengths are very different, the smaller one will dominate the value of λ_d at most angles.

We consider the behavior of λ_d in Fig. 4. It is seen that it approaches λ_{KH} and λ_{RT} at the vertical and horizontal (liquid-above-vapor) configurations, respectively. We also see that there is absolute stability in the region $\alpha < \alpha_{min}$.

We are now able to make a statement about the range of wavelengths to be expected in a case when going through the possible orientations. The maximum wavelength appearing will be approximately equal to the plate length. The minimum wavelength appearing will be approximately equal to the minimum value of λ_d. Since Eq. (66) is not normalized average, it is possible that the minimum wavelength is less than $\min(\lambda_{RT}, \lambda_{KH})$, as seen in Fig. 4. In the $a^{5/4} \approx a$ approximation we may solve for this minimum. We find that in the case where one of $(\lambda_{RT}, \lambda_{KH})$ is considerably smaller than the other, the minimum wavelength is very close to the smallest of the two. The difference between the minimum wavelength and $\min(\lambda_{RT}, \lambda_{KH})$ is largest when the latter two are equal, and in this case the minimum wavelength is about 84% of $\min(\lambda_{RT}, \lambda_{KH})$. In summary, we have

$$\max(\lambda) \approx 1/\epsilon_0$$

$$\min(\lambda) \approx \begin{cases} \lambda_{RT} + \mathcal{O}\left(\Phi_{KH}^2\right), & \lambda_{RT} < \lambda_{KH} \\ \lambda_{KH} + \mathcal{O}\left((1/\Phi_{KH})^2\right), & \lambda_{RT} > \lambda_{KH} \\ 2^{-1/4}\lambda_{RT}, & \lambda_{RT} \approx \lambda_{KH} \end{cases} \tag{70}$$

We should now check that the resulting wavelengths satisfy the assumptions of Eq. (56). In terms of wavelength, this can be stated as $2\pi \ll \lambda \ll 2\pi\,\rho_l/\rho_v$. Since $2\pi\,\rho_l/\rho_v \approx 10^4$, $\max(\lambda)$ is definitely well below the upper limit. Given the typical range of values indicated in Table 2, we get value ranges of $\lambda_{RT} \in (100, 200)$ and $\lambda_{KH} \in (40, 400)$. This means that $\min(\lambda)$ is well above the lower limit of 2π.

4.3. Discussion

It is clear from the analysis in Section 4.2 that Kelvin–Helmholtz type instabilities are significant in the cases concerned, so much that the critical angle of instability will usually be less than 90° (liquid-below-vapor). At the same time, the stability analysis based on the lubrication approximation PDE, Section 4.1 predicts unconditional stability in the vertical and all liquid-below-vapor cases, as its only source of instability is the Rayleigh–Taylor mechanism.

Why does the lubrication approximation fail at capturing the dominant type of instability in cases close to the vertical? The KH instability is an inertial effect, and such effects have been neglected in the lubrication approximation. Formally, terms with both ϵ^2 and $\epsilon\mathrm{Re}$ have been neglected from the Navier–Stokes equation. However, if we have intermediate Re in the range of 10–100, as is the case here, $\epsilon\mathrm{Re}$ may not be so small, and inertial effects may be significant. Remarkably, $\epsilon\mathrm{Re}$ from the steady-state solution in

Eq. (28) is independent of both plate length and inclination, and can simply be stated as

$$\epsilon \mathrm{Re} = \frac{4}{3}\frac{Q}{\mu_v}. \tag{71}$$

Thus ϵRe depends only on ΔT and fluid properties. For boiling water with $\Delta T < 200$ K, $\epsilon \mathrm{Re} \approx 0.25$, which is still small, but far from negligible. We must have ΔT as low as 80 K to obtain $\epsilon \mathrm{Re} < 0.1$.

Note how the stability criterion Eq. (63) agrees with the sufficient criterion Eq. (49) from the lubrication PDE in the small Re limit. The additional criterion Eq. (50) is not accounted for in the potential flow analysis, since it stems from the source term in the lubrication PDE, and represents stabilization of very thin films through the evaporation effect. In reality, this effect may not be able to stabilize the inertial KH instabilities that are missing from the lubrication model. Here we consider cases with intermediate Re, as shown in Table 2, and thus we must prefer the stability analysis of Section 4.2.

It is worth pointing out an inconsistency between the origins of the parameter β and how it appears in the potential flow analysis. The attentive reader may notice that the KH term, whose origin is shear, remains nonzero even in the $\beta = 3$ case which represents the case of zero interface shear in the lubrication model. The crucial point here is that only two things are carried over from the lubrication model: The film thickness and the average vapor velocity, both as a function of β. The proper interpretation of β in the context of the potential flow stability analysis is that it shows the effect of the range of possible vapor velocities. However, it does not reflect the actual assumptions behind β in the lubrication model. Instead, the shear in the potential flow stability analysis stems from the given vapor velocity profile and the simplified liquid velocity profile derived in Appendix A. This could in principle be replaced with a more sophisticated model that is consistent with the assumptions behind β in the $\beta \to 3$ limit. However, this was not deemed necessary since the value in real film boiling cases is expected to be much closer to the $\beta \to 12$ limit, in which case the interpretation of β is consistent.

It is interesting to see how the stability criterion Eq. (63) is affected by other factors, at a given plate length and orientation. First of all, it is clear that increased surface tension stabilizes both mechanisms through Bo_X, as expected. For a given surface tension, the KH mechanism's strength is proportional to Re_0. This is given by Eq. (34), showing the dependency $\sim Q^{3/4}$. Thus a smaller superheat ΔT will decrease the Reynolds number, through decreasing both h_0 and u_0. This creates somewhat of a paradox, as we predict a very thin but very stable vapor film as $\Delta T \to 0$ in the vertical case, while from reality it is known that film boiling must break down at some finite ΔT (vapor film collapse at the Leidenfrost point (Dhir, 1998)). This can possibly be resolved by introducing additional mechanisms of instability that become pronounced at very small film thicknesses, such as van der Waals and thermocapillary effects.

Finally, it should be recognized that the final stability criterion Eq. (63) is obtained through potential flow stability analysis applied to a steady state derived under the assumption that viscous forces dominate. Therefore the results herein must mainly be interpreted qualitatively, or quantitatively as a rough approximation.

5. Example case

In order to illuminate the results, we consider the example of water film boiling at atmospheric pressure. Additional case parameters to vary are then the superheat ΔT and the plate length X_0. We vary these in the region 100–250 K and 1–5 cm, respectively. This gives steady-state film thickness scales of $h_0 \approx$ 130–250 µm.

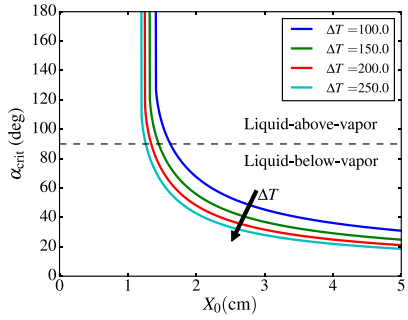

Fig. 5. Critical inclination angle for loss of stability plotted against plate length, according to Eq. (63), for various degrees of superheat.

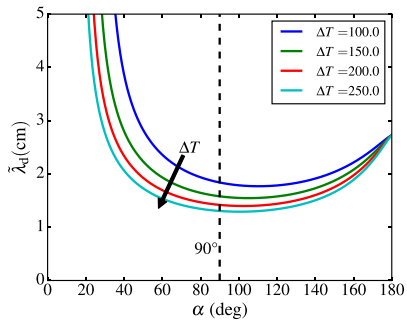

Fig. 6. Dimensional fastest growing wavelength, $\tilde{\lambda}_d = h_0 \lambda_d$ according to Eq. (66), plotted against inclination angle, for various degrees of superheat. The plate length is $X_0 = 5$ cm.

We may again investigate α_{crit}, the first angle where the inequality Eq. (63) is broken and instabilities arise. The results are shown in Fig. 5. We see that the possibility of $\pi/2 < \alpha_{\mathrm{crit}} < \pi$ is very rare: Either instabilities arise while still in the liquid-below-vapor configuration, or they never arise at all (global stability). This means that in most cases, the initial instabilities arising when rotating the plate will be caused purely by KH instabilities, not RT instabilities. We also see that the sensitivity due to degree of superheat is quite small.

We may also choose a specific plate length, in this case $X_0 = 5$ cm, and investigate how the dimensional fastest growing wavelength $\tilde{\lambda}_d$ depends on the inclination angle. Here we get Reynolds numbers in the range $\mathrm{Re}_0 \in (40, 60)$, and thus $\Phi_{\mathrm{KH}} \in (3, 5)$. This means that the KH effect will dominate at most orientations, and also that λ_{KH} (found at $\alpha = 90^\circ$) is less than λ_{RT} (found at $\alpha = 180^\circ$), as shown in Fig. 6. We again observe a relatively weak dependence on superheat, with all cases giving wavelengths in the range 1–5 cm. We see that when $\alpha \to \pi$ we approach a single RT wavelength, as $\tilde{\lambda}_{\mathrm{RT}}$ only depends on the (assumed constant) fluid thermo-physical properties.

6. Experimental comparison

Unfortunately there are few experimental works studying the influence of inclination on film boiling stability. However, one such study was published by Kim and Suh (2013), which included indirect approximate measurements of the maximum stable film thickness for water film boiling. The principle behind the measurements is as follows: A planar film boiling experiment is performed with a

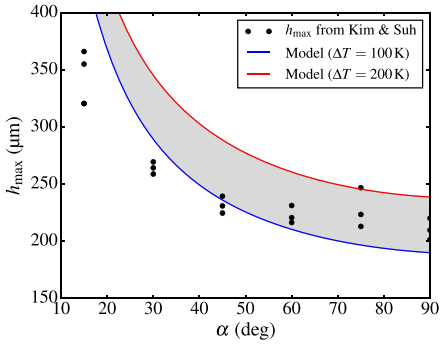

Fig. 7. A comparison of the angular dependence of h_{max} from Kim and Suh (2013) with predictions using the present model. The gray band shows the range of predictions for the same range of ΔT values as the experiments.

plate much longer than the characteristic wavelengths of instability. They then assume that the film grows according to the smooth steady-state solution until its limit of stability. The film then collapses, and begins growing again from a very small thickness, thus forming a repeating pattern. Given the approximations that the collapse happens very rapidly, and resets the film to a thickness of practically zero, steady solutions of the form $\sim x^{1/4}$ will give the property that

$$\mathrm{HTC} \approx \frac{4k_v}{3h_{max}}, \tag{72}$$

where HTC is the average heat transfer coefficient over the long plate, and h_{max} is the peak film thickness right before the reset. The authors measured HTC, thus providing indirect measurement for h_{max}. This was performed with a range of α and ΔT values.

From the present model, we may attempt to predict h_{max} by searching for the first point where k_d becomes an allowable wavenumber, i.e. numerically solve

$$k_d(x_0) = k_{min}(x_0) \tag{73}$$

for x_0, while using Eq. (65) for k_d. This is similar to what was done by Kolev (1998), except that due to the vertical orientation, purely Kelvin–Helmholtz wavelengths were considered. Once the solution has been found, Eq. (28) can be used as a predictor for h_{max}. The vapor properties should in each case be set according to the average film temperature. A comparison with the experimental values for h_{max} is shown in Fig. 7 as a function of inclination angle α. The experiments were run with ΔT in the region 100–200 K. However, this parameter was not strictly controlled and has only a small effect on h_{max}, so these points were simply grouped together at their α values. The model predictions were calculated for the edges of this ΔT range, and plotted as a band of possible values.

The comparison in Fig. 7 is quite close and qualitatively similar. It can never be expected to be a perfect prediction, for two reasons. First, the measurement of h_{max} is indirect, and the conversion from the actual measured quantity, HTC, is dependent on approximations and assumptions. Second, what is being measured is not a property of a small (linear) wave disturbance, but rather an averaged property of a fully developed instability. Thus the stability analysis in the present work can only be expected to be an approximate predictor. In that respect, it appears successful.

Note that the prediction has zero fitted or empirical parameters, as the value of β is calculated from fluid properties through Eq. (A.6) in Appendix A. In contrast, the model in Kim and Suh (2013) is dependent on fitting two parameters to the experiments. Note also how the stability analysis of the lubrication PDE in Section 4.1 predicts unconditional stability throughout the entire range of $\alpha \in [0, \pi/2]$ in Fig. 7, and thus the corresponding predicted h_{max} would be infinite. We therefore see that including Kelvin–Helmholtz effects is crucial.

7. Conclusions

From the model analyses and examples in this work, we may draw the following conclusions:

- In planar vertical or inclined film boiling, parallel velocities can become large enough to make Kelvin-Helmholtz type instabilities important.
- The transient model Eq. (43) based on the lubrication approximation is not capable of predicting these Kelvin-Helmholtz type instabilities, only Rayleigh-Taylor type instabilities. It will thus incorrectly predict absolute stability in e.g. the vertical case.
- When applying classical potential flow stability analysis to the steady-state solution of the lubrication model, both types of instabilities can be predicted.
- We identified an angle α_{min}, given by Eq. (64), below which there will be stability regardless of surface tension. This angle depends on the vertical case Reynolds number Re_0.
- The full stability criterion, including surface tension stabilization, is given by Eq. (63). This allows the numerical calculation of α_{crit}, the angle of instability onset. We saw from Fig. 2 that in most cases, instabilities arise before reaching the vertical configuration, i.e. in the liquid-below-vapor configurations. In these cases, instabilities are purely due to Kelvin–Helmholtz effects.
- Once well into the unstable region, the characteristic wavelength of the instabilities will be an inclination-dependent harmonic mean like combination of the Rayleigh–Taylor and Kelvin–Helmholtz wavelengths, as given by Eq. (66). Due to the way vapor velocity and film thickness develop in film boiling, the two wavelength contributions turn out to be quite similar, as shown in Eq. (69). The range of wavelengths possible when passing through all orientations is summed up in Eq. (70).
- From the practical case of water film boiling in Section 5, we saw that the critical angle and characteristic wavelengths are only weakly dependent on the degree of superheat. Depending on plate length, most cases will either be globally stable, or have $\alpha_{crit} < 45°$, with only a small intermediate region. The case had Kelvin–Helmholtz wavelengths in the range of 1–2 cm, depending on superheat, while the Rayleigh–Taylor wavelengths were 2.7 cm.
- We saw that the model is reasonably able to predict how the limit of stability depends on inclination, based on experimental data from the literature.

The second point does not mean that the standard lubrication approximation is useless for describing film boiling in general. However, it does mean that it is likely incapable of correctly describing transient dynamics of inclined or vertical film boiling. Using the lubrication approximation to predict dynamics in horizontal film boiling, such as in Panzarella et al. (2000) and Kim et al. (2015) is still valid, as these cases do not have significant shear/inertial forces.

While the stability criterion derived herein may be somewhat successful at predicting the onset of instabilities, it is not sufficient for simulating the full nonlinear behavior of the vapor film as the instabilities grow. Doing this would require a PDE such as Eq. (43), but as we have shown, this model cannot predict the onset of the Kelvin–Helmholtz type instabilities. In further work, if one still wants to avoid solving the full set of governing equations and boundary conditions, the thin-film model derivation of Section 2 may have to be mended to include inertial terms to leading order. This may be possible through Karman–Pohlhausen

methods (Dávalos-Orozco et al., 1997), as demonstrated for a vertically falling liquid film by Alekseenko et al. (1985). Also, if one also wants to predict vapor film collapse at lower superheat values, it may be necessary to include additional instability mechanisms such as van der Waals forces and thermo-capillary effects (Burelbach et al., 1988; Oron et al., 1997). Including the latter would necessitate using a non-equilibrium evaporation model, to allow for tangential interface temperature gradients.

Acknowledgments

This publication is based on results from the research project *Predicting the risk of rapid phase-transition events in LNG spills (Predict-RPT)*, performed under the MAROFF program. The authors acknowledge the Research Council of Norway (244076/O80) for support. Special thanks to Tor Ytrehus, Bernhard Müller, Svend Tollak Munkejord, and Morten Hammer for fruitful discussions and feedback.

Appendix A. Liquid velocity profile

In Section 2.1, we avoided having to calculate the liquid flow outside of the vapor film by introducing the factor β, which has the values 3 or 12 in the two possible extreme cases. The former comes from assuming that the liquid applies no shear stress on the vapor (free surface), while the latter comes from assuming a zero tangential liquid velocity. The actual value of β, and thus the actual mass flow rate from Eq. (7), must be somewhere in between. In this section we attempt to approximate this value from the viscosity ratio of the liquid–vapor pair. First we make the assumption of a reciprocal liquid velocity profile

$$u_{\mathrm{l}}(z) = \frac{C}{z}, \tag{A.1}$$

where C is some constant to be found. This is arguably ad-hoc, but retains the desired property of both u_{l} and $\partial u_{\mathrm{l}}/\partial z$ going to zero as $z \to \infty$. The boundary conditions at the liquid–vapor interface give the vapor velocity profile

$$u(z) = \frac{Dh^2}{2\mu_{\mathrm{v}}}\left[\left(\frac{\Psi+2}{\Psi+1}\right)\frac{z}{h} - \left(\frac{z}{h}\right)^2\right], \tag{A.2}$$

and the liquid velocity profile

$$u_{\mathrm{l}}(z) = \frac{Dh^2}{2\mu_{\mathrm{v}}}\frac{1}{(\Psi+1)}\frac{h}{z}, \tag{A.3}$$

where we have defined the viscosity ratio

$$\Psi = \frac{\mu_{\mathrm{l}}}{\mu_{\mathrm{v}}}. \tag{A.4}$$

The average vapor velocity is then

$$\bar{u} = \frac{Dh^2}{12\mu_{\mathrm{v}}}\frac{\Psi+4}{\Psi+1}, \tag{A.5}$$

which may be compared with the average velocity implied by Eq. (7) to give the relation

$$\beta = 12\frac{\Psi+1}{\Psi+4}. \tag{A.6}$$

We see that the limit $\Psi \to \infty$ corresponds to $\beta = 12$, and that the limit $\Psi \to 0$ corresponds to $\beta = 3$. The viscosity ratio Ψ at saturation for either water or cryogens is typically in the range 20–30. For values that large, Eq. (A.6) is not very sensitive to Ψ, and this range of Ψ gives the narrow range of $\beta = 10.75 \pm 0.25$. We see that this is quite close to the assumption of zero interface velocity ($\beta = 12$). Specifically for boiling water, the value is $\beta = 10.67$.

The value of β (or Ψ) decides the ratio between the interface velocity and the average vapor velocity, and this can be found as

$$\frac{u_{\mathrm{i}}}{\bar{u}} = \frac{6}{\Psi+4} = \frac{1}{6}(12-\beta). \tag{A.7}$$

Note that the rightmost expression in Eq. (A.7) (in terms of β) does not actually require the assumption of a particular velocity profile, as long as we can assume that $u_{\mathrm{i}}/\bar{u}$ should be a linear function of β between the well defined extremes $\beta = 3$ and $\beta = 12$.

References

Alekseenko, S.V., Nakoryakov, V.E., Pokusaev, B.G., 1985. Wave formation on vertical falling liquid films. Int. J. Multiphase Flow 11 (5), 607–627. doi:10.1016/0301-9322(85)90082-5.

Aursand, E., 2017. Modelling planar film boiling of arbitrary inclination with the lubrication approximation. In: Skallerud, B., Andersson, H.I. (Eds.), Proceedings of the 9. National Conference on Computational Mechanics MekIT'17. CIMNE http://hdl.handle.net/11250/2479443.

Berthoud, G., 2000. Vapor explosions. Annu. Rev. Fluid Mech. 32 (1), 573–611. doi:10.1146/annurev.fluid.32.1.573.

Bromley, L.A., 1950. Heat transfer in stable film boiling. Chem. Eng. Prog. 46, 221–227.

Bui, T.D., Dhir, V.K., 1985. Film boiling heat transfer on an isothermal vertical surface. ASME J. Heat Transfer 107 (4), 764–771. doi:10.1115/1.3247502.

Burelbach, J.P., Bankoff, S.G., Davis, S.H., 1988. Nonlinear stability of evaporating/condensing liquid films. J. Fluid Mech. 195, 463–494. doi:10.1017/S0022112088002484.

Cleaver, P., Johnson, M., Ho, B., 2007. A summary of some experimental data on LNG safety. J. Hazard. Mater. 140 (3), 429–438. doi:10.1016/j.jhazmat.2006.10.047.

Craster, R.V., Matar, O.K., 2009. Dynamics and stability of thin liquid films. Rev. Mod. Phys 81 (3), 1131–1198. doi:10.1103/RevModPhys.81.1131.

Dávalos-Orozco, L.A., Davis, S.H., Bankoff, S.G., 1997. Nonlinear instability of a fluid layer flowing down a vertical wallunder imposed time-periodic perturbations. Phys. Rev. E 55 (1), 374–380. doi:10.1103/PhysRevE.55.374.

Dhir, V.K., 1998. Boiling heat transfer. Annu. Rev. Fluid Mech. 30 (1), 365–401. doi:10.1146/annurev.fluid.30.1.365.

Drazin, P.G., Reid, W.H., 2004. Hydrodynamic Stability, 2nd Cambridge University Press, Cambridge. ISBN 9780631525417

Fletcher, D.F., 1995. Steam explosion triggering: a review of theoretical and experimental investigations. Nucl. Eng. Des. 155, 27–36. doi:10.1016/0029-5493(94)00865-V.

Hissong, D.W., 2007. Keys to modeling LNG spills on water. J. Hazard. Mater. 140 (3), 465–477. doi:10.1016/j.jhazmat.2006.10.040.

Joo, S.W., Davis, S.H., Bankoff, S.G., 1991. Long-wave instabilities of heated falling films: two-dimensional theory of uniform layers. J. Fluid Mech. 230, 117–146. doi:10.1017/S0022112091000733.

Jouhara, H., Axcell, B.P., 2009. Film boiling heat transfer and vapour film collapse on spheres, cylinders and plane surfaces. Nucl. Eng. Des. 239 (10), 1885–1900. doi:10.1016/j.nucengdes.2009.04.008.

Jouhara, H.I., Axcell, B.P., 2002. Forced convection film boiling on spherical and plane geometries. Chem. Eng. Res. Des. 80 (3), 284–289. doi:10.1205/026387602753582060.

Kim, B.J., Kim, K.D., 2016. Rayleigh-taylor instability of viscous fluids with phase change. Phys. Rev. E 93 (4), 043123. doi:10.1103/PhysRevE.93.043123.

Kim, B.J., Lee, J.H., Kim, K.D., 2015. Rayleigh–Taylor instability for thin viscous gas films: application to critical heat flux and minimum film boiling. Int. J. Heat Mass Transfer 80, 150–158. doi:10.1016/j.ijheatmasstransfer.2014.08.084.

Kim, C.S., Suh, K.Y., 2013. Angular dependency on film boiling heat transfer from relatively long inclined flat plates. J. Heat Transfer 135 (12), 121502. doi:10.1115/1.4024583.

Koh, J.C.Y., 1962. Analysis of film boiling on vertical surfaces. J. Heat Transfer 84 (1), 55–62. doi:10.1115/1.3684293.

Kolev, N.I., 1998. Film boiling on vertical plates and spheres. Exp. Therm. Fluid Sci. 18 (2), 97–115. doi:10.1016/S0894-1777(98)10021-3.

Kundu, P.K., Cohen, I.M., Dowling, D.R., 2007. Fluid Mechanics, 5th Academic Press, Cambridge. ISBN 9780123821003.

Luketa-Hanlin, A., 2006. A review of large-scale LNG spills: experiments and modeling. J. Hazard. Mater. 132, 119–140. doi:10.1016/j.jhazmat.2005.10.008.

Myers, T.G., 1998. Thin films with high surface tension. SIAM Rev. 40 (3), 441–462. doi:10.1137/S003614459529284X.

Nishio, S., Chandratilleke, G.R., 1991. Natural-convection film-boiling heat transfer: saturated film boiling with long vapor film. JSME Int.J. Ser. 2 Fluids Eng.Heat TransferPowerCombust.Thermophys.Prop. 34 (2), 202–211. doi:10.1299/jsmeb1988.34.2_202.

Nukiyama, S., 1934. The maximum and minimum values of the heat Q transmitted from metal to boiling water under atmospheric pressure. J. Jpn. Soc. Mech. Eng. 37, 367–374.

Oron, A., Davis, S.H., Bankoff, S.G., 1997. Long-scale evolution of thin liquid films. Rev. Mod. Phys. 69 (3), 931–980. doi:10.1103/RevModPhys.69.931.

Panzarella, C.H., Davis, S.H., Bankoff, S.G., 2000. Nonlinear dynamics in horizontal film boiling. J. Fluid Mech. 402, 163–194. doi:10.1017/S0022112099006801.

Paper C

Inclined film boiling: Film stability and heat transfer

Eskil Aursand, Stephen H. Davis

Published in *International Journal of Multiphase Flow*.
(2019) Vol. 111, pp. 175–187
https://doi.org/10.1016/j.ijmultiphaseflow.2018.11.017

International Journal of Multiphase Flow 111 (2019) 175–187

Contents lists available at ScienceDirect

International Journal of Multiphase Flow

journal homepage: www.elsevier.com/locate/ijmulflow

Inclined film boiling: Film stability and heat transfer

Eskil Aursand [a,b,*], Stephen H. Davis [b]

[a] Department of Energy and Process Engineering, Norwegian University of Science and Technology (NTNU), Kolbjørn Hejes v. 1B, Trondheim N-7491, Norway
[b] Department of Engineering Sciences and Applied Mathematics, McCormick School of Engineering and Applied Science, Northwestern University, 2145 Sheridan Road, Evanston, IL, 60208, United States

ARTICLE INFO

Article history:
Received 6 August 2018
Revised 24 October 2018
Accepted 28 November 2018
Available online 29 November 2018

Keywords:
Film boiling
Vapor thin-film
Inertial instabilities
Heat transfer
Inclination angle

ABSTRACT

An inertially modified long-wave model is used to analyze the stability of inclined saturated film boiling. By performing quasi-parallel linear stability analysis on this model and combining the result with a heat-transfer model, an explicit expression for the heat-transfer coefficient is obtained. The results appear to fit all relevant data for film-boiling heat-transfer coefficient within an error of 15%.

1. Introduction

When a liquid is put in contact with a solid surface that is ΔT degrees hotter than the liquid's saturation temperature there is a resulting boiling heat flux q. The plot of q vs. ΔT is called the *boiling curve*, which was first characterized by Nukiyama (1934). At superheat values (ΔT) beyond the conventional nucleate boiling regime, one finds the *film-boiling* regime (Dhir, 1998). This is characterized by a relatively low heat flux due to the formation of a continuous vapor film between the surface and the liquid, which leads to two issues of practical concern: The limits of the film-boiling regime (Leidenfrost point) and the heat transfer in the film-boiling regime. The present work is concerned with the latter, in the context of saturated natural-convection non-horizontal film boiling.

The heat transfer coefficient (HTC) of vertical/inclined film boiling was first studied by Bromley (1950), and the resulting model has come to be known as the *laminar smooth interface* (LSI) model. The model was later expanded to include liquid drag effects by authors such as Koh (1962) and Kaneyasu and Takehiro (1966), creating the *two-layer models*. These LSI models are based on a steady-state balance between vapor buoyancy and surface/interface drag, while neglecting inertial effects and assuming that evaporation is purely due to conductive heat transfer. The result is that the vapor-film thickness grows as $h(x) \sim x^{1/4}$, where x is the distance along the solid surface starting from the leading edge. Since the heat transfer occurs mainly by conduction across the film, this implies that the local heat flux decreases as $q(x) \sim x^{-1/4}$ and it follows that the average HTC of a plate of length ℓ would be

$$\overline{\mathcal{H}}(\ell) = \frac{4k_v}{3\ h(\ell)} \sim \ell^{-1/4}, \tag{1}$$

with k_v being the vapor conductivity. However, further research showed that this is only true for very short plates/rods (about $\ell < 1$cm). For longer surfaces it has been established that the time-averaged heat flux has practically no dependence on distance from the leading edge. Consequently, the average HTC is independent of total surface length ℓ and severely underpredicted by the smooth interface model (Hsu and Westwater, 1958; Suryanarayana and Merte, 1972; Bui and Dhir, 1985; Nishio and Chandratilleke, 1991; Nishio and Ohtake, 1993; Vijaykumar and Dhir, 1992). It is evident that the liquid–vapor interface profile is unsteady and far from smooth, with waves/crests running in the direction dictated by buoyancy.

These discoveries seemed to imply that the LSI solution has a limit to its stability, in the sense that it may only grow to a certain critical thickness before collapsing and thus yielding an average film thickness smaller than one would expect. This led to the proposal of *laminar vapor-film unit* (LVFU) type models by authors such as Bui and Dhir (1985) and Nishio and Chandratilleke (1991). These models assume that the LSI solution only grows across a certain critical length scale λ_c before collapsing to a near-zero film thickness and giving way to the next identical unit. While these crests will in reality move along the surface, the time-averaged

* Corresponding author.
E-mail address: eskil.aursand@ntnu.no (E. Aursand).

https://doi.org/10.1016/j.ijmultiphaseflow.2018.11.017
0301-9322/

HTC will be close to the corresponding stationary profile. Given these assumptions, the measured time/space averaged HTC for a long plate ($\ell \gg \lambda_c$) would be

$$\mathcal{H} = \overline{\mathcal{H}}(\lambda_c), \tag{2}$$

with $\overline{\mathcal{H}}$ given by the LSI solution Eq. (1). Since λ_c is not dependent on the total plate length, this would explain the apparent non-dependence on ℓ in the case of long plates. Thus, in the context of the LVFU model the main challenge is to determine the length scale λ_c, which is essentially an issue of hydrodynamic stability. There have typically been two approaches to determining λ_c in the literature:

- Semi-empirical models: Derive the model based on LSI-type solutions with the critical Reynolds number as an empirical parameter, and fit it to a series of experiments. Make further predictions by assuming that the critical Reynolds number is constant under different conditions (e.g. Kim and Suh, 2013).
- Hybrid models: Apply classical potential-flow stability analysis to investigate the stability of the interface implied by the LSI solution (e.g. Bui and Dhir, 1985; Nishio and Chandratilleke, 1991; Kolev, 1998; Aursand, 2018). Such an analysis generally includes a mixture of Kelvin–Helmholtz and Rayleigh–Taylor effects, depending on plate inclination.

Both of these methods have some issues: The former uses empirical fitting and thus does not provide any insight into why the vapor-film breaks down at a certain Reynolds number. The latter combines potential-flow (irrotational) analysis with a base state from the lubrication approximation that is far from irrotational. Despite this, both methods demonstrate clearly that inertial (Reynolds-number dependent) instabilities are central to the problem. The present work suggests a third method which is able to predict the dominant instabilities of inclined film-boiling based on a set of partial differential equations related to the long-wave approximation methods for thin-film flow. In this way, both the base state and the stability analysis stem from the same formalism, and this avoids the inconsistent addition of potential-flow theory.

The use of long-wave approximation methods to describe the transient dynamics of thin liquid films has a long history, as reviewed by Oron et al. (1997), Myers (1998) and Craster and Matar (2009). Similar use for thin vapor films is somewhat less developed, but the method has been applied to horizontal film boiling by authors such as Panzarella et al. (2000) and Aursand et al. (2018).

The long-wave (lubrication) approximation relies on a film aspect-ratio ϵ, which is essentially the ratio between film thickness and disturbance wavelength. Terms of order $\mathcal{O}(\epsilon^2)$ and $\mathcal{O}(\epsilon\mathrm{Re})$ are then neglected, which vastly simplifies the Navier–Stokes equation. Simple integration of the continuity equation across the film then allows for the derivation of a highly-nonlinear equation for the film thickness. Crucially, this method does not merely require that ϵ is small but also that the Reynolds number (Re) is small enough. This is easily valid for horizontal film boiling, but as shown in Aursand (2018), applying this method to vertical film boiling fails to predict the all-important inertial instability. This is because the strong buoyancy greatly increases the Reynolds number in the vapor film, and the ϵRe-terms are no longer negligible.

In Section 2 the standard long-wave method is extended by only neglecting terms $\mathcal{O}(\epsilon^2)$ while retaining the inertial terms $\mathcal{O}(\epsilon\mathrm{Re})$. The resulting governing equations and boundary conditions are similar to the ones formulated in Burelbach et al. (1988) and Joo et al. (1991) for horizontal/falling liquid films and more recently in Aursand et al. (2018) for horizontal vapor films, except there are additional $\mathcal{O}(\epsilon\mathrm{Re})$ inertial terms. These additional terms significantly complicate the momentum equation, and the problem may no longer be reduced to a single equation for the film thickness. Following the Karman-Pohlhausen type integral boundary-layer methods of Alekseenko et al. (1985) and Prokopiou et al. (1991), the momentum equation is integrated across the film while assuming a parabolic velocity profile. As discussed in the reviews Oron et al. (1997, Section 6B) and Chang (1994), this inevitably leads to a complicated system of coupled partial differential equations (PDE) in two variables: The film thickness and the vapor flow rate.

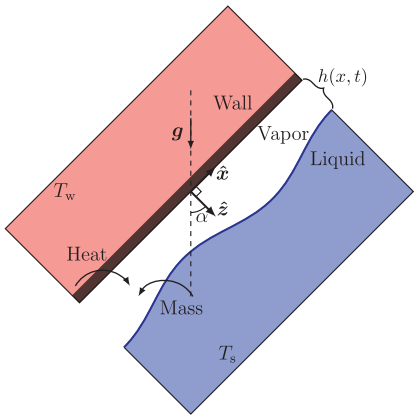

Fig. 1. Illustration of the planar film-boiling problem. A wall at angle α supplies heat to a boiling liquid, which feeds vapor into the vapor film between. Buoyancy then drives vapor flow along the wall. The goal is to predict the dynamics of the film thickness function $h(x, t)$.

In Section 3 quasi-parallel linear stability analysis is applied to the model in order to find a complex dispersion relation for harmonic disturbances. This allows the determination of a stability condition for given case-parameters and film thickness. Specifically it allows the determination of the critical Reynolds number for the onset of inertial instabilities and the wavelength of the resulting waves. Predicting the critical Reynolds number within the long-wave formalism is one of the significant novelties of the present work, as it previously has had to be empirically estimated in works such as Kim and Suh (2013). In Section 4 the estimated disturbance wavelength λ_c is combined with the LVFU heat-transfer model in Eq. (2) to make a prediction for the long-plate heat-transfer coefficient. This prediction is subsequently compared with experimental data in Section 5. Finally, the validity and implications of the findings herein are discussed in Section 6, before the conclusions are summarized in Section 7.

2. Model

2.1. Problem description

The physical problem to be considered is that of inclined planar saturated film-boiling, as illustrated in Fig. 1. The problem involves a large heated solid surface submerged in a liquid at an angle α. A local coordinate system (x, z) is aligned with the solid surface, and the liquid–vapor interface is located at $z = h(x, t)$, with t being time. The goal is to predict the dynamics of the film-thickness function $h(x, t)$, and under what conditions the time-independent solutions are stable.

A case is defined by the (assumed constant) fluid properties, the plate angle α and the characteristic temperature difference $\Delta T = T_w - T_s$, where T_w is a given solid surface temperature and T_s is the

Table 1
Overview of dimensionless variables in the governing equations. By default variables describe the vapor, and a subscript "l" indicates the corresponding liquid variable outside the vapor film.

Variable	Description	Scaling	
X	Parallel coordinate	$X = x/x_0$	
Z	Perpendicular coordinate	$Z = z/h_0$	
τ	Time	$\tau = t/t_0$	$t_0 = x_0/u_0$
$H(X,\tau)$	Film thickness	$H = h/h_0$	
$U(X,Z,\tau)$	Velocity (X-component)	$U = u/u_0$	
$W(X,Z,\tau)$	Velocity (Z-component)	$W = w/w_0$	$w_0 = \epsilon u_0$
$P(X,Z,\tau)$	Pressure	$P = p/p_0$	$p_0 = \mu_v u_0/(\epsilon h_0)$
$\Phi(X,Z,\tau)$	Body-force potential	$\Phi = \phi/p_0$	
$\theta(X,Z,\tau)$	Temperature	$\theta = (T - T_s)/\Delta T$	
$J(X,\tau)$	Evaporation mass flux	$J = j/j_0$	$j_0 = k_v \Delta T/(h_0 L)$
$\theta_i(X,\tau)$	Interface temperature	$\theta_i = (T_i - T_s)/\Delta T$	

fluid's saturation temperature. The liquid bulk ($z \gg h$) is assumed to be held at the liquid's saturation temperature T_s.

2.2. Long-wave approximation with inertia

2.2.1. Governing equations and boundary conditions

The derivation and non-dimensionalization of the governing equations is covered in Appendix A, and only the core principles behind the derivation will be summarized below. The derivation is a generalization of the one in Aursand et al. (2018) for non-horizontal configurations, which in turn was inspired by the work of Burelbach et al. (1988) for evaporating liquid films. The dimensionless variables describing the system are summarized in Table 1.

The expansion parameter in the long-wave approximation is the aspect-ratio of the disturbances,

$$\epsilon = \frac{h_0}{x_0} \ll 1, \tag{3}$$

where h_0 is the typical film thickness and $x_0 = \lambda/(2\pi)$ is the longitudinal scale given from the disturbance wavelength λ. According to the long-wave approach, x_0 is used as the scale for x, and h_0 is used as the scale for z and h. The velocity scale is set to

$$u_0 = \frac{g h_0^2 \Delta\rho}{12\mu_v}, \tag{4}$$

as explained in Appendix B. The tangential velocity u is scaled with u_0. Continuity then implies that the normal velocity w should be scaled by $w_0 = \epsilon u_0$. With this choice of u_0 the relevant dimensionless parameters more generally defined in A.3 may be written as

$$\mathrm{Re} = \frac{\rho_v \Delta\rho g h_0^3}{12\mu_v^2} \text{ (Reynolds number)},$$

$$E = \frac{12\mu_v k_v \Delta T}{\rho_v \Delta\rho g \hat{L} h_0^3} \text{ (Evaporation number)},$$

$$\mathrm{Ca} = \frac{\Delta\rho g h_0^2}{12\sigma_0} \text{ (Capillary number)},$$

$$K = \frac{\tilde{K} k_v}{h_0 \hat{L}} \text{ (Disequilibrium number)},$$

$$M = \frac{12\gamma\Delta T}{\Delta\rho g h_0^2} \text{ (Marangoni number)},$$

$$S = \frac{k_v \Delta T}{\mu_v \hat{L}} \text{ (Vapor-thrust number)},$$

$$\mathrm{Pr} = \frac{\mu_v c_{p,v}}{k_v} \text{ (Vapor Prandtl number)},$$

$$\Psi = \mu_v/\mu_l \text{ (Viscosity ratio)},$$

$$G_v = \frac{12\rho_v}{\Delta\rho} \text{ (Vapor gravity number)},$$

$$G_l = \frac{12\rho_l}{\Delta\rho} \text{ (Liquid gravity number)},$$

$$G = G_l - G_v = 12 \text{ (Gravity number)}. \tag{5}$$

Here, ρ_v is the vapor density, ρ_l is the liquid density, $\Delta\rho = \rho_l - \rho_v$, g is the gravitational acceleration, μ_v is the vapor viscosity, μ_l is the liquid viscosity, $c_{p,v}$ is the vapor heat capacity, k_v is the vapor thermal conductivity, $\hat{L}$ is the effective latent heat of vaporization, $\tilde{K}$ is a constant from the kinetic theory evaporation model, σ_0 is the surface tension at saturation, and γ is the temperature sensitivity of surface tension. The effective latent-heat is used to account for the *sensible-heat effect*. It modifies the conventional latent heat (L) according to $\hat{L} = L + c_{p,v}\Delta T/2$, as used in Bui and Dhir (1985). This only has a significant effect for large superheats ($\Delta T > T_s$).

Given these dimensionless numbers and the scaling described in Appendix A, the governing equations may be written as

$$U_X + W_Z = 0, \tag{6}$$

$$\epsilon \mathrm{Re}(U_\tau + UU_X + WU_Z) = -(P + \Phi)_X + U_{ZZ}, \tag{7}$$

$$(P + \Phi)_Z = 0, \tag{8}$$

$$\epsilon \mathrm{Re}\,\mathrm{Pr}\,(\theta_\tau + U\theta_X + W\theta_Z) = \theta_{ZZ}, \tag{9}$$

where Eq. (6) is the continuity equation, Eqs. (7) and (8) are the momentum equations, and Eq. (9) is the energy equation. Note that a subscript of either X, Z or τ implies differentiation with respect to that variable. The body-force potential is given by

$$\Phi = \Phi_0 + G_v(aX + \epsilon bZ), \tag{10}$$

where we, as opposed to the more general formulation in Appendix A.1, have neglected the van der Waals interaction term. Here, the parameters a and b are simply shorthands for the inclination effects, $a = \sin(\alpha)$ and $b = -\cos(\alpha)$, respectively. Additionally, the kinetic-theory evaporation model relates the evaporation rate to the interface superheat,

$$KJ = \theta_i. \tag{11}$$

The parameter K indicates the relative importance of non-equilibrium evaporation effects, with the limit $K \to 0$ representing the quasi-equilibrium approximation (interface at saturation). The boundary conditions at the wall are simply no-slip and a given temperature

$$[U]_{Z=0} = [W]_{Z=0} = 0, \tag{12}$$

$$[\theta]_{Z=0} = 1. \tag{13}$$

At the liquid–vapor interface, the standard boundary conditions are

$$[U - U_l]_{Z=H} = 0, \tag{14}$$

$$\epsilon[H_\tau + UH_X - W]_{Z=H} = EJ, \tag{15}$$

$$[P - P_l]_{Z=H} = -\epsilon ESJ^2 - \epsilon^3 \mathrm{Ca}^{-1} H_{XX}, \tag{16}$$

$$\left[U_Z - \Psi^{-1} U_{l,Z}\right]_{Z=H} = -\epsilon M[\theta_i]_X, \tag{17}$$

$$-[\theta_Z]_{Z=H} = J \tag{18}$$

where Eq. (14) is the no-slip condition, Eq. (15) is the kinetic boundary condition (with evaporation), Eq. (16) is the normal stress balance, Eq. (17) is the tangential stress balance, and Eq. (18) is the energy balance. Compared to the more general formulation in Appendix A.1, we have neglected the heat transfer between interface and liquid bulk. As shown in Aursand et al. (2018), its effect is very small regardless of film thickness.

In the $\epsilon\mathrm{Re} \to 0$ and horizontal limits, the above equations are equivalent to the work in Burelbach et al. (1988) for evaporating liquid thin films, given the necessary adjustments due to the liquid–vapor role reversal. However, due to the fact that the outside bulk phase is now dense compared to the thin film, some additional assumptions are required to still arrive at a closed one-sided model which avoids having to solve a separate set of PDEs for the liquid dynamics:

- Liquid pressure closure: Assume that the liquid pressure at a given position may be approximated by the hydrostatic pressure corresponding to that position. This provides the unknown $[P_\mathrm{l}]_{Z=H}$ in Eq. (16):

$$[P_\mathrm{l}]_{Z=H} = -G_\mathrm{l}(aX + \epsilon bH), \tag{19}$$

- Liquid shear closure: The tangential stress balance Eq. (17) can not initially be used due to the unknown liquid shear $U_{\mathrm{l},Z}$ at the interface. However, this term vanishes in the hypothetical free-surface case ($\Psi \to \infty$), and this yields a solvable problem. Since it is known that this case should represent the maximum possible interface velocity due to the absence of liquid drag, one may make the assumption that the actual interface velocity $[U]_{Z=H}$ is some fraction of this hypothetical maximum value. By introducing the constant factor $\eta \in [0, 1]$, which should only depend on fluid properties, the liquid shear closure may formally be expressed as

$$[U]_{Z=H} = \eta\Big(\lim_{\Psi\to\infty}[U]_{Z=H}\Big). \tag{20}$$

The above two assumptions are essentially the same as those made for the case of horizontal film-boiling in Aursand et al. (2018). For consistency, η must have the property that

$$\eta \to \begin{cases} 1 & \Psi \to \infty \quad \text{(Maximum interface velocity.)} \\ 0 & \Psi \to 0 \quad \text{(Zero interface velocity.)} \end{cases} \tag{21}$$

In practice, the problem in the free-surface case is solved first, and then Eq. (20) is used to include the effects of liquid drag on the vapor film. As shown in Appendix C, earlier models indicate that η may be estimated from

$$\eta = \frac{3}{16}\Big(\frac{\rho_\mathrm{v}\mu_\mathrm{v}}{\rho_\mathrm{l}\mu_\mathrm{l}}\Big)^{1/4}, \tag{22}$$

which means that η will typically be in the range of 0.01–0.05.

2.2.2. General considerations

The following relations derived from the equations in the previous section are valid in both the low-Re and the high-Re cases. First, note that the *reduced pressure*, defined as $\bar{P} = P + \Phi$, is independent of Z according to Eq. (8). This means that for a given X it may be evaluated at any Z, and by choosing to evaluate it at $Z = H$, one finds that

$$\bar{P}_X(X) = -\underbrace{G(a + \epsilon bH_X)}_{\text{gravity}} - \underbrace{\epsilon^3\mathrm{Ca}^{-1}H_{XXX}}_{\text{capillary}} - \underbrace{\epsilon ES(J^2)_X}_{\text{vapor thrust}}, \tag{23}$$

which is needed for the right-hand side of Eq. (7). This expression captures not only the conventional gravity and capillary (surface tension) contributions, but also vapor thrust effect due to strong evaporation. Second, one may integrate Eq. (6) across the film while applying Leibniz's integral rule and the boundary conditions Eqs. (12) and (15) to find the general mass-conservation PDE,

$$H_\tau + \Big(\int_0^H U\mathrm{d}Z\Big)_X = \frac{E}{\epsilon}J. \tag{24}$$

Eq. (24) is the sought-after PDE for the film thickness $H(X, \tau)$. However, it requires two additional pieces: The velocity profile U and the evaporation rate J, both as functions of H. If it may be assumed that $\epsilon\mathrm{Re} \ll 1$, it is relatively simple to proceed, and one retains a single PDE for H, as shown in Section 2.3. If not, it will couple to a second PDE for the mass-flow rate, as shown in Section 2.4

2.3. The $\epsilon Re \ll 1$ approximation

2.3.1. PDE For film thickness

In the classical lubrication theory, it is assumed that Re is so small that terms $\mathcal{O}(\epsilon\mathrm{Re})$ may be neglected, which leads to the X-momentum and energy Eqs. (7) and (9) being vastly simplified. Since $\bar{P}$ is independent of Z, the velocity profile may be found by integrating Eq. (7) twice and applying the velocity boundary conditions,

$$U = \frac{1}{2}\bar{P}_X\big(Z^2 - (1+\eta)HZ\big) - \epsilon\eta KMJ_XZ. \tag{25}$$

The corresponding mass flow rate is

$$\int_0^H U\mathrm{d}Z = -\frac{\xi}{12}\bar{P}_XH^3 - \frac{1}{2}\epsilon\eta KMJ_XH^2, \tag{26}$$

with the shorthand $\xi = 1 + 3\eta$. Similarly, in this approximation the temperature profile

$$\theta = 1 - \frac{1-\theta_\mathrm{i}}{H}Z \tag{27}$$

satisfies Eq. (9) and the temperature boundary conditions. When combined with the energy balance Eq. (18) and the evaporation model Eq. (11), this leads to the evaporation rate being

$$J = \frac{1}{H+K}. \tag{28}$$

By inserting Eqs. (23), (26) and (28) into Eq. (24), one obtains a nonlinear PDE for $H(X, \tau)$,

$$\begin{aligned} &\epsilon H_\tau + \frac{\xi G}{12}\epsilon\big[H^3(a + \epsilon bH_X)\big]_X \\ &\quad - \frac{\xi ES}{6}\epsilon^2\bigg[\Big(\frac{H}{H+K}\Big)^3H_X\bigg]_X + \frac{\xi}{12\mathrm{Ca}}\epsilon^4\big[H^3H_{XXX}\big]_X \\ &\quad + \frac{1}{2}\epsilon^2\eta KM\bigg[\Big(\frac{H}{H+K}\Big)^2H_X\bigg]_X = E\frac{1}{H+K}. \end{aligned} \tag{29}$$

Eq. (29) is a generalization of Aursand et al. (2018, Eq. 2.66) from horizontal film boiling to arbitrary orientation. However, as will be shown, this equation does not capture the essential inertial instabilities arising in non-horizontal film boiling.

2.3.2. Approximate steady-state solution

The steady state is expected to have a very smooth interface, which would imply a very small ϵ. If one keeps only first order ϵ-terms from Eq. (29), set the time-derivative to zero, and assume that the film has grown so thick that $K \ll H$, the following ODE is found for the steady-state solution $\bar{H}(X)$,

$$\epsilon\bar{H}_X = \frac{4E}{\xi Ga}\frac{1}{\bar{H}^3}. \tag{30}$$

With the assumption that $H = 0$ at the leading edge $X = 0$, Eq. (30) may be integrated to find the explicit expression

$$\bar{H}(X) = \Big(\frac{16E}{\epsilon\xi Ga}X\Big)^{1/4}. \tag{31}$$

The corresponding dimensional form is

$$\bar{h}(x) = \left(\frac{16 \mu_v k_v \Delta T}{\xi a \rho_v \Delta \rho g \hat{L}} x \right)^{1/4}, \tag{32}$$

which reveals that this is the common LSI-type solution introduced in Section 1. This solution will be used to approximate the actual steady state in the following stability analysis.

Let the film thickness scale h_0 be given by the steady solution Eq. (32) in the vertical case. The Reynolds number as given by Eq. (5) then grows as $\mathrm{Re} \sim x^{3/4}$, and thus, it will eventually grow too large for the $\epsilon \mathrm{Re} \ll 1$ approximation. However, a longer distance from the leading edge will also accommodate longer disturbance waves, i.e. a smaller ϵ. If the longest disturbance wavelength that fits is equal to x, the distance from the leading edge, the smallest allowed ϵ is $\bar{\epsilon} = h_0(x)/x$. The product of this and Re is surprisingly simple,

$$\bar{\epsilon} \mathrm{Re} = \frac{4}{3} \frac{k_v \Delta T}{\xi \mu_v \hat{L}} = \frac{4}{3} \frac{S}{\xi} \sim \mathcal{O}\left(10^{-1}\right). \tag{33}$$

Since $\epsilon > \bar{\epsilon}$, this is actually a lower bound for $\epsilon \mathrm{Re}$, and thus, one must conclude that no allowed disturbance to the steady state may actually satisfy $\epsilon \mathrm{Re} \ll 1$.

The above does not imply that $\epsilon \mathrm{Re} \ll 1$ is invalid in the commonly studied case of horizontal film-boiling since the velocity scale in Eq. (4) is not appropriate in such cases. However, for the purposes of non-horizontal film-boiling, the inertial $\epsilon \mathrm{Re}$ terms must be retained. The next section shows how.

2.4. $\epsilon Re \sim \mathcal{O}(1)$

2.4.1. Averaged momentum equation

If one integrates the X-momentum equation, Eq. (7), across the layer while applying the continuity equation, Eq. (6), the wall boundary condition, Eq. (12), and the kinetic boundary condition, Eq. (15), the result is

$$\epsilon \mathrm{Re} \left(\left[\int_0^H U \mathrm{d}Z \right]_\tau + \left[\int_0^H U^2 \mathrm{d}Z \right]_X - \frac{E}{\epsilon} [U]_{Z=H} J \right) = -\overline{P}_X H + [U_Z]_{Z=H} - [U_Z]_{Z=0}. \tag{34}$$

This result is similar to the one on liquid films by Alekseenko et al. (1985, Eq. 15), except that Eq. (34) is complicated by the inclusion of evaporation, interface drag (not a free surface), and a driving force $\overline{P}_X$ that includes vapor thrust and vdW forces in addition to gravity and surface tension.

The left-hand side of Eq. (34) constitutes the inertia correction, and this would be zero in the conventional lubrication approximation. In order to evaluate the integrals in Eq. (34) and obtain a PDE for scalar quantities, it is necessary to model the velocity profile $U(Z)$. This is done in the next section.

2.4.2. Assumed velocity profile

In Section 2.3 it was shown how the low-Re case leads to a parabolic velocity profile Eq. (25) that is zero at the wall and small but non-zero at the interface. It is now assumed that the general velocity-profile has the same shape, and this will be used to compute the inertial corrections at higher Re. Such a generic profile may be written as

$$U(X,Z) = \hat{U}(X) \left[(1 + s(X)) \frac{Z}{H} - \left(\frac{Z}{H} \right)^2 \right], \tag{35}$$

where the overall flow-speed is given by the function $\hat{U}(X)$, and the relative speed at the interface is given by the function $s(X) \ll 1$. The boundary conditions Eqs. (17) and (20) provide a solution for s in terms of η and the thermocapillary effect,

$$s(X) = \eta \left(1 - \epsilon K M \frac{H J_X}{\hat{U}} \right) \tag{36}$$

where the evaporation model Eq. (11) has been used to represent the interface temperature in terms of J. By then defining a flow rate function Q,

$$Q = \frac{\xi}{6} H \hat{U}, \tag{37}$$

and some short-hand functions of η,

$$\xi = 1 + 3\eta, \tag{38}$$

$$\zeta = \frac{10\eta^2 + 5\eta + 1}{\xi^2} = 1 - \eta + \mathcal{O}\left(\eta^2\right), \tag{39}$$

$$\chi = \frac{\xi + \eta}{\xi} = 1 + \eta + \mathcal{O}\left(\eta^2\right), \tag{40}$$

the integrals needed in Eq. (34) may be calculated as

$$\int_0^H U \mathrm{d}Z = Q - \frac{1}{2} \epsilon \eta K M H^2 J_X, \tag{41}$$

$$\int_0^H U^2 \mathrm{d}Z = \frac{6}{5} \zeta \frac{Q^2}{H} - \chi K \epsilon \eta M H Q J_X + \frac{1}{3} (K \epsilon \eta M)^2 H^3 (J_X)^2, \tag{42}$$

and the right-hand side friction term as

$$[U_Z]_{Z=H} - [U_Z]_{Z=0} = -\frac{12}{\xi} \frac{Q}{H^2}. \tag{43}$$

The vapor film dynamics are now described by two functions in $1+1$ dimensions: $H(X, \tau)$ for the film thickness and $Q(X, \tau)$ for the volumetric flow rate. As will be shown in the next section, the integrated continuity-equation Eq. (24) and the integrated momentum-equation Eq. (34) provide two coupled PDEs for these functions.

2.4.3. Coupled PDEs governing film behavior

It is assumed that the most important inertial corrections happen through the momentum equation, not the energy equation. This means that Eq. (28) is also used as a model for the evaporation mass flux J in the general case. The thermocapillary effect scales with the overall strength of evaporation and thus, the film thickness. Its relative strength is indicated by the film-thickness independent constant $\hat{M}$, defined as

$$\hat{M} = \frac{KM}{E} = \frac{\rho_v \gamma \tilde{K}}{\mu_v}. \tag{44}$$

Then, it is assumed that

$$E \ll 1, \quad K \ll 1, \tag{45}$$

so that terms $\mathcal{O}\left(E^2\right)$, $\mathcal{O}\left(K^2\right)$ and $\mathcal{O}(EK)$ may be neglected. This greatly simplifies governing equations and will be justified in the next section. One may now insert Eqs. (28) and (41) into the integrated continuity-equation Eq. (24) to yield the first PDE,

$$\underbrace{\epsilon H_\tau + \epsilon Q_X}_{\text{mass advection}} + \underbrace{\frac{1}{2} \eta E \hat{M} \epsilon^2 H_{XX}}_{\text{thermocapillary}} = \underbrace{E \frac{1}{H}}_{\text{evap.}}. \tag{46}$$

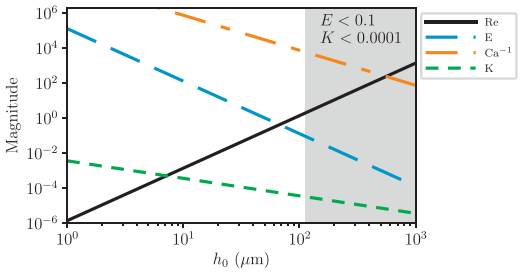

Fig. 2. Magnitude of h_0-dependent dimensionless numbers. This example is made from water boiling at $\Delta T = 200$K. The shading marks the region of model validity, i.e. where h_0 is such that both E and K are small.

Similarly, one may combine Eqs. (28), (36), (41) and (42) with the integrated momentum-equation Eq. (34) to yield the second PDE,

$$\epsilon \mathrm{Re}\Big(\underbrace{Q_\tau + \frac{6\zeta}{5}\left[\frac{Q^2}{H}\right]_X}_{\text{advection}} + \underbrace{\eta E \hat{M}\left[\frac{1}{2}\epsilon H_{X\tau} + \chi\epsilon\left[\frac{Q}{H}H_X\right]_X\right]}_{\text{thermocapillary}} - \underbrace{\frac{E}{\epsilon}\frac{6\eta}{\xi}\frac{Q}{H^2}}_{\text{mom. injection}} \Big) = \underbrace{-\overline{P}_X H}_{\text{friction balance}} - \underbrace{\frac{12}{\xi}\frac{Q}{H^2}}_{} . \tag{47}$$

with Eq. (23) reduced to

$$\overline{P}_X = \underbrace{-G(a + b\epsilon H_X)}_{\text{gravity}} + \underbrace{2SE\epsilon\frac{H_X}{H^3}}_{\text{vapor thrust}} \underbrace{-\mathrm{Ca}^{-1}\epsilon^3 H_{XXX}}_{\text{capillary}} \tag{48}$$

The inertia correction is the left-hand side of Eq. (47). Note also how all non-equilibrium evaporation effects (K-terms) are negligible under the approximation Eq. (45), except for their part in the thermocapillary effect, which is collected into the parameter $\hat{M}$.

Eqs. (46) and (47) with Eq. (48) constitute the main result of this section, and the following content concerns the conditions under which they allow for a stable steady-state solution.

2.5. Magnitudes of dimensionless constants

According to Eqs. (46) to (48), the dynamics of the unknown variables H and Q at a given inclination are governed by the following dimensionless numbers:

- Re: Strength of inertial effects.
- E: Strength of evaporation effects.
- Ca^{-1}: Strength of surface tension.
- $\hat{M}$: Strength of thermocapillary effect relative to evaporation effects.
- S: Strength of vapor thrust effect relative to evaporation effects.
- η: Fraction of actual interface velocity to the hypothetical maximum.

The latter three ($\hat{M}$, S and η) are only dependent on fluid properties and ΔT, and will in most cases be

$$\hat{M} \sim \mathcal{O}(1), \qquad S \sim \mathcal{O}\big(10^{-1}\big), \qquad \eta \sim \mathcal{O}\big(10^{-2}\big), \tag{49}$$

Whereas the governing equations depend on G as well, one sees from Eq. (5) that with the chosen velocity scale it is simply constant and equal to 12. The first four dimensionless numbers in the list are dependent on film-thickness scale h_0. Fig. 2 shows these four parameters, as well as K, as functions of h_0. It indicates that the present approximation, Eq. (45), can be expected to be valid in the region where $h_0 > 100\,\mu$m. The following stability analysis will apply to this regime (shaded in Fig. 2).

3. Quasi-parallel stability analysis

3.1. Base state

The task now is to examine under which conditions stable steady-state solutions to the governing Eqs. (46) and (47) exist. This *base state* is denoted by functions $\bar{H}(X)$ and $\bar{Q}(X)$ corresponding to H and Q, respectively. While these functions are generally not known analytically, when explicit expressions are required they will be approximated by the low-Re solution in Eq. (31). Under the same approximation, the momentum equation tells us that the base state flow rate $\bar{Q}$ is

$$\bar{Q} = \frac{\xi Ga}{12}\bar{H}^3. \tag{50}$$

The stability analysis that will follow is applied locally at a specific position X_0, and at that point the base state is used to define the film thickness scale h_0. In order to have an orientation-independent scale, it is defined such that $\bar{H}(X_0) = 1$ in the vertical configuration, and thus, Eq. (31) implies that

$$\bar{H}(X_0) = a^{-1/4}. \tag{51}$$

3.2. Quasi-parallel perturbation analysis

The disturbances $\hat{H}$ and $\hat{Q}$ are defined by

$$H(X,\tau) = \bar{H}(X) + c\hat{H}(X,\tau), \tag{52}$$

$$Q(X,\tau) = \bar{Q}(X) + c\hat{Q}(X,\tau), \tag{53}$$

and this combined solution is inserted into the nonlinear governing Eqs. (46) and (47). By approximating to first order in the perturbation magnitude, $\mathcal{O}(c^1)$, and subtracting the zeroth order (steady state) equations, one arrives at a set of two linear and homogeneous PDEs for the perturbations $\hat{H}$ and $\hat{Q}$. However, a complication arises due to the fact that the coefficients of these linear PDEs depend on $\bar{H}(X)$, $\bar{Q}(X)$, and their derivatives. This means that the coefficients are X-dependent, and standard normal-mode analysis would not apply for the X-dimension.

This situation may be remedied (in approximation) by applying quasi-parallel analysis. This entails assuming that the base state $\bar{H}(X)$ is locally constant for the purposes of the stability analysis. This procedure yields PDEs for the perturbations $\hat{H}$ and $\hat{Q}$ that formally have constant coefficients, though the value of these coefficients will depend on the film thickness at which stability is examined. The quasi-constant film thickness at the location under consideration is denoted as H_0, and due to the choice of scaling, it depends on orientation according to $H_0 = a^{-1/4}$. Note that since H_0 is defined as such, the effect of position X on the stability analysis enters through changes in the film thickness scale h_0, which in turn affect the dimensionless parameters shown in Fig. 2.

Since the equations for the perturbations now are linear, homogeneous, and with constant coefficients, an arbitrary disturbance may be represented by a linear combination of normal-modes such as the following,

$$\hat{H} = \tilde{H}\exp\left(i\frac{kX - \omega\tau}{\epsilon}\right), \qquad \hat{Q} = \tilde{Q}\exp\left(i\frac{kX - \omega\tau}{\epsilon}\right). \tag{54}$$

The division by ϵ in the exponent simply means that the dimensionless wavenumber k and frequency ω are defined according to the spatial and temporal scales h_0 and h_0/u_0, respectively. The long-wave approximation then implies that k must be small. The

following task is to examine temporal stability, which means considering the real wavenumber k as an input and observing the effect on the resulting complex frequency ω. A positive imaginary part of ω implies an exponentially growing instability.

3.3. General solution

When performing the above described quasi-parallel stability analysis on the governing Eqs. (46) and (47), the result is a quadratic equation for $\omega(k)$,

$$c_2\omega^2 + c_1\omega + c_0 = 0 \tag{55}$$

with complex coefficients

$$c_2 = \mathrm{Re}, \tag{56}$$

$$c_1 = \frac{12i}{H_0^2\xi} + \mathrm{Re}\left(\frac{iE}{H_0^2}\left[1 - \frac{6\eta}{\xi}\right] - \frac{GaH_0^2\xi\zeta}{5}k\right), \tag{57}$$

$$\begin{aligned} c_0 = {} & H_0Gbk^2 - 3iGak - \frac{H_0}{\mathrm{Ca}}k^4 \\ & + \frac{12E}{\xi}\left(\frac{\hat{M}\eta}{2H_0^2}k^2 - \frac{\xi S}{6H_0^2}k^2 - \frac{1}{H_0^4}\right) \\ & + \mathrm{Re}\left(\frac{H_0^4\zeta G^2a^2\xi^2}{120}k^2 + iEGH_0^2\hat{M}a\eta\xi\left[\frac{\zeta}{10} - \frac{\chi}{12}\right]k^3\right. \\ & \left. - \frac{iEGa\xi\zeta}{5}k\right). \end{aligned} \tag{58}$$

While Eq. (55) may be solved directly, the resulting expression does not allow for easy inspection of qualitative effects. Its general behavior must be revealed by repeated numerical solutions.

3.4. Low reynolds number limit

In the limit of negligible inertial effect ($\mathrm{Re} \to 0$), just like in the classical lubrication approximation, Eq. (55) is simplified to a first-order equation that may be solved explicitly for the complex frequency, here labeled as ω_0. The imaginary part turns out to be

$$\begin{aligned} \mathcal{I}(\omega_0) = {} & -\underbrace{\frac{H_0^3\xi}{12\mathrm{Ca}}k^4}_{\text{capillary}} - \underbrace{\frac{\xi ES}{6}k^2}_{\text{Vapor thrust}} + \underbrace{\frac{\eta E\hat{M}}{2}k^2}_{\text{Thermocap.}} \\ & + \underbrace{\frac{Gb\xi H_0^3}{12}k^2}_{\text{Gravity}} - \underbrace{\frac{E}{H_0^2}}_{\text{Evap.}}. \end{aligned} \tag{59}$$

This result, while missing the essential inertial effect, is still useful. From Eq. (59) it is clear that the system is stable at $k \to \infty$ by capillarity and as $k \to 0$ by evaporation. At intermediate wavenumbers, stability is a matter of balance between the k^2 terms: a stabilizing vapor thrust, a destabilizing thermocapillary effect, and a gravitational (Rayleigh–Taylor) effect, whose sign depends on inclination.

An important note about Eq. (59) is that in the vertical case the only destabilizing influence is thermocapillarity, which is unable to explain the instabilities seen in experiments on vertical plates. The missing piece is the inertial (Kelvin–Helmholtz) instabilities, and these are captured when using the full coefficients in Section 3.3.

3.5. Limits of stability: critical reynolds number

The goal is to evaluate stability as a function of film-thickness scale h_0. As found in Section 3.2, the stability analysis depends on a number of dimensionless parameters, some of which are h_0-dependent:

$$\mathrm{Re} \propto h_0^3, \quad E \propto h_0^{-3}, \quad \mathrm{Ca} \propto h_0^2. \tag{60}$$

It is convenient to isolate the h_0-dependence into a single parameter. Here, this is achieved by choosing Re as that parameter and letting E and Ca be functions of Re through some h_0-independent relations. These relations are

$$E(\mathrm{Re}) = \frac{S}{\mathrm{Re}}, \qquad \mathrm{Ca}(\mathrm{Re}) = \frac{\mathrm{Re}^{2/3}}{B}, \tag{61}$$

where the h_0-independent parameters S and B are defined by Eq. (5) and

$$B = \mathrm{Ca}^{-1}\mathrm{Re}^{2/3} = 12\sigma_0\left(\frac{\rho_v^2}{144\Delta\rho g\mu_v^4}\right)^{1/3} \sim \mathcal{O}\left(10^4\right), \tag{62}$$

respectively. This has the convenient effect that for a given case (fluid, ΔT and inclination) stability may be evaluated as a function of the Reynolds number alone.

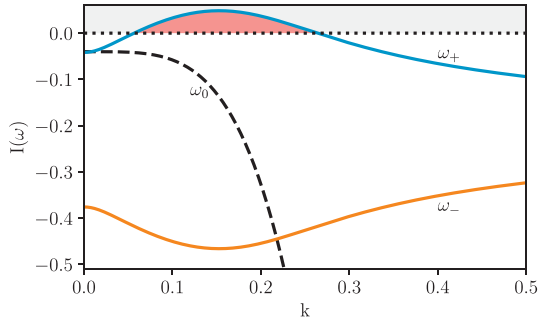

Fig. 3. Imaginary part of typical solutions of Eq. (55) (ω_+, ω_-) and Eq. (59) (ω_0) as functions of dimensionless wavenumber k, for the vertical case ($\alpha = \pi/2$). Red shading marks the region where $\mathcal{I}(\omega) > 0$, i.e. predicted instabilities. This example is made based on $\mathrm{Re} = 25$, $S = 1$, $\hat{M} = 1$, $B = 15,000$ and $\eta = 0.025$.

Since the dispersion relation Eq. (55) is a quadratic equation, it will generally yield two values of ω for every given value of k; call these ω_+ and ω_-. The typical shapes of these two branches in the vertical case are shown in Fig. 3. It is generally the case that the ω_- branch has no potential for instability, and from now on, the interesting branch ω_+ will simply be labeled as ω. Fig. 3 reveals that while the system is stable at both wavenumber extremes, there is a potential for instability at intermediate wavenumbers. that is almost completely due to inertial (Kelvin–Helmholtz type) instabilities. Note also how the low-Re model (ω_0) fails at predicting this instability.

A plot like Fig. 3 can be made for a range of Re values, and this allows the construction of neutral-curve plots, such as in Fig. 4. The neutral curve also indicates the critical Reynolds number and wavenumber, formally defined by:

Definition. The critical Reynolds number ($\mathrm{Re_c}$) is the smallest Reynolds number (Re) for which $\mathcal{I}(\omega(k)) = 0$ for some value of k. The corresponding value of k is the critical wavenumber (k_c).

These two properties, $\mathrm{Re_c}$ and k_c, are the most important results from the stability analysis. Their values depend on S, B, $\hat{M}$, α and η, though in practice it is found that the thermocapillary effect ($\hat{M}$-terms) is too weak to matter in the regime where the present approximation ($E \ll 1$) applies. In contrast, the parameters $S \propto \Delta T$ and $B \propto \sigma_0$ both have appreciable effects and may vary much between cases. Their typical ranges for real cases are $S \in (0.1, 1.0)$ and $B \in (5000, 30,000)$. Throughout this range it is found that the

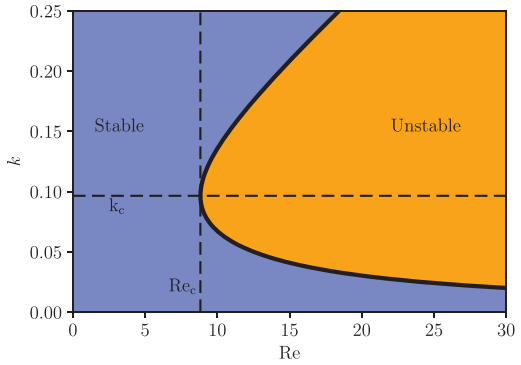

Fig. 4. Example of a neutral curve in (Re, k) space. This plot was generated with parameters corresponding to vertical water film boiling at $\Delta T = 200$ K. The dashed vertical line shows the critical Reynolds number, and the dashed horizontal line shows the corresponding critical wavenumber.

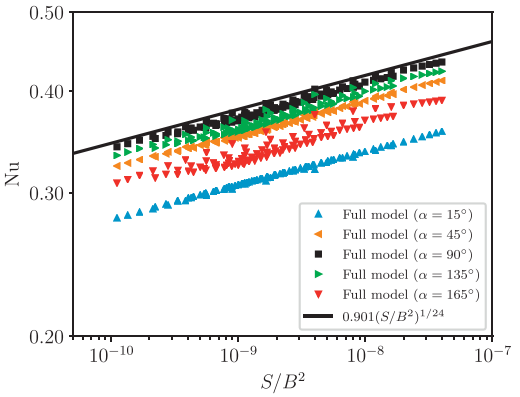

Fig. 5. Calculation of the Nusselt number according to Eq. (70) throughout the range $S \in (0.1, 1.0)$, $B \in (5000, 30, 000)$, plotted as a function of S/B^2. This is repeated for a number of different inclination angles α. Also shown is the vertical approximation according to Eq. (71).

critical wavenumber k_c, and thus ϵ, is approximately 0.1 or less. This justifies the neglection of terms ϵ^2 in the long-wave approximation.

Generally, it is necessary to solve iteratively for Re_c and k_c in each case. However, in the vertical case it was discovered through inspection of numerous numerical solutions that the results may be captured to good approximation by the relations

$$\mathrm{Re}_{c\perp} \approx \frac{3}{2}(SB)^{1/4}, \tag{63}$$

$$k_{c\perp} \approx \frac{3}{2}\left(\frac{S}{B}\right)^{1/4}, \tag{64}$$

where the subscript $\perp$ implies vertical configuration. Given the typical ranges of S and B, Eqs. (63) and (64) imply that $\mathrm{Re}_{c\perp} \in (5, 20)$ and $k_{c\perp} \in (0.05, 0.2)$. For non-vertical configurations the results are too complicated to be captured in simple power-laws.

The base state Eq. (32) has a monotonically growing film thickness and thus a monotonically growing Reynolds number, which eventually crosses the critical value Re_c. The resulting disturbance is predicted to have the dimensionless wavenumber k_c, and the corresponding dimensional wavelength is

$$\lambda_c = \frac{2\pi}{k_c} h_0(\mathrm{Re}_c) = \frac{2\pi}{k_c}\left(\frac{12\mu_v^2}{\rho_v \Delta\rho g}\mathrm{Re}_c\right)^{1/3} = \frac{2\pi\,\mathrm{Re}_c^{1/3}}{k_c}\lambda_0, \tag{65}$$

with the definition

$$\lambda_0 = \left(\frac{12\mu_v^2}{\rho_v \Delta\rho g}\right)^{1/3}. \tag{66}$$

The fluid-dependent length scale λ_0 is usually in the range of $10 - 100\,\mu m$. In the vertical case, one may insert Eqs. (63) and (64) into Eq. (70) to find the expression

$$\lambda_{c\perp} = 2\pi\left(\frac{2}{3}\right)^{2/3} \underbrace{\left(\frac{B^2}{S}\right)^{1/6}}_{\sim\mathcal{O}(10)} \lambda_0, \tag{67}$$

i.e. the critical wavelength will be about 100 times longer than λ_0.

4. Predicting the long-plate heat-transfer coefficient

Now that a model for the loss of stability has been found, this may be combined with the laminar vapor-film unit (LVFU) model to predict the heat-transfer coefficient (HTC). Given the LVFU model, Eq. (2), the HTC may be found as

$$\mathcal{H} = \frac{4k_v}{3\bar{h}(\lambda_c)} = \mathcal{H}_0 \mathrm{Nu}, \tag{68}$$

with the function $\bar{h}(x)$ according to Eq. (32). The last equality shows how this may be split into a reference HTC ($\mathcal{H}_0$) and a Nusselt number (Nu). The reference HTC is commonly defined simply as the conductivity divided by some known thickness. However, the present case presents the problem that there is no obvious ab initio known length scale. The only emergent easily calculable length scale so far is λ_0, so here we choose to define $\mathcal{H}_0$ as the conductive heat transfer across a uniform vapor film of thickness $\bar{h}(\lambda_0)$,

$$\mathcal{H}_0 = \frac{k_v}{\bar{h}(\lambda_0)} = k_v\left(\frac{\xi a \rho_v \Delta\rho g \hat{L}}{16\mu_v k_v \Delta T \lambda_0}\right)^{1/4}. \tag{69}$$

This definition has the advantage of letting $\mathcal{H}_0$ be calculable from known case/fluid properties alone, and thus independent of the specific solution of the stability problem. Of course, there are many possible definitions with this property, but this one allows for $\mathrm{Nu} \sim \mathcal{O}(1)$. Given the choice of Eq. (69), the Nusselt number is

$$\mathrm{Nu} = \frac{\mathcal{H}}{\mathcal{H}_0} = \frac{4}{3}\left(\frac{\lambda_0}{\lambda_c}\right)^{1/4} = \frac{4}{3}\left(\frac{k_c}{2\pi\,\mathrm{Re}_c^{1/3}}\right)^{1/4}. \tag{70}$$

Here, Eq. (65) has been used for the critical wavelength. In the general case, one must solve numerically for Re_c and k_c using Eq. (55) and insert the result into Eq. (70). However, as shown earlier, in the vertical case one may use the fitted power laws Eqs. (63) and (64), and this gives

$$\mathrm{Nu}_\perp = \underbrace{\frac{4}{3}\left(\frac{3}{2}\right)^{1/6}\left(\frac{1}{2\pi}\right)^{1/4}}_{=0.9010\ldots} \underbrace{\left(\frac{S}{B^2}\right)^{1/24}}_{\sim 0.4-0.5}. \tag{71}$$

This reveals a very weak dependence on S and B, making the Nusselt number nearly constant/universal. The Nusselt number has been calculated from Eq. (70) for many combinations of S and B and plotted against the single parameter S/B^2 in Fig. 5. This plot illustrates how Eq. (71) is a good approximation to the full calculation in the vertical case. It also reveals that Nu follows the

$(S/B^2)^{1/24}$ dependency in non-vertical inclinations as well. However, its reduction when deviating from the vertical configuration is asymmetric. The reason for the asymmetry is that the gravitational (Rayleigh–Taylor) effect is a stabilizing influence on one side and a destabilizing influence on the other.

The inclination dependence of Re_c and k_c from solving the full model is too complicated to be well estimated by simple power laws such as Eqs. (63) and (64), and thus, an accurate expression like Eq. (71) could not be derived for the general case. However, numerical computations of the resulting Nusselt number with the use of Eq. (70) for a wide variety of S and B showed that on the liquid-below-vapor side the Nusselt number may to a decent approximation be given by

$$\mathrm{Nu} \approx a^{1/6}\mathrm{Nu}_{\perp}, \qquad (\text{for } \alpha \leq \pi/2). \tag{72}$$

Note that for the total HTC this $a^{1/6}$ dependence combines with the $a^{1/4}$ dependence of $\mathcal{H}_0$ in Eq. (69), giving a total inclination dependence of $a^{5/12}$.

5. Experimental validation

The predictions for the HTC described in Section 4 may now be tested against experimental data. Relevant experiments are long-plate film-boiling heat-transfer measurements with a liquid bulk that is stationary and saturated. Note that when making predictions using the model it is crucial to evaluate the vapor properties μ_v, ρ_v, k_v and $c_{p,\,v}$ at some average *film-temperature*, not simply at T_s. In the present work, the common choice of $T_s + \Delta T/2$ is made for the film temperature. The liquid properties are simply evaluated at the saturation temperature.

Series of HTC measurements on vertical plates under different values of ΔT for a variety of fluids were found in the works of Bui and Dhir (1985); Okkonen et al. (1996); Vijaykumar and Dhir (1992); Nishio and Chandratilleke (1991); Hsu and Westwater (1958); Nishio and Chandratilleke (1989); Liaw and Dhir (1986). Given an orientation and a specific fluid, the only remaining variable is the surface superheat ΔT. The HTC data are plotted against relative superheat ($\Delta T/T_s$) in Fig. 6. For each fluid, three model curves are shown. They all use Eq. (68) but with different methods for finding Nu: The result from numerically solving for Re_c and k_c and inserting these into Eq. (70), the result from using the simplified model for vertical Nusselt number in Eq. (71), and the result from using a constant $\mathrm{Nu} = 0.4$. It is revealed that the full model predicts virtually all the data within a 15% HTC uncertainty and that the simplification in Eq. (71) gives almost identical results.

By dividing the measured HTC by the corresponding $\mathcal{H}_0$, one may also find the Nusselt numbers of the data. In Fig. 7 these are compared to the dependence on S/B^2 implied by Eq. (71). This confirms that the Nusselt number is nearly constant/universal and that the weak variations are according to $(S/B^2)^{1/24}$ is as predicted.

A series of HTC measurements with water on a plate of varying inclinations was provided by Kim and Suh (2013). The inclination-dependence of the HTC is compared with the predictions of the present model in Fig. 8. Both the full model (numerical solution), and the approximation implied by the combined angular dependence of Eqs. (69) and (72), are shown. As expected, the two are practically identical in the $\alpha \leq \pi/2$ region, but the approximation does not capture the asymmetry in Nu and thus, fails slightly in the $\alpha > \pi/2$ region. For comparison, the $a^{1/4}$ dependence of the LSI-type model ($\mathcal{H}_0$) is also shown. It is seen that this is considerably less successful in predicting the observed angular dependence.

The implications of these comparisons with experimental data will be further discussed in the next section.

6. Discussion

6.1. Inertial instabilities and the critical Reynolds number

It should now be clear that the classical lubrication approximation with the assumption of $\epsilon\mathrm{Re} \ll 1$ is insufficient for predicting the loss of stability in vertical/inclined film boiling, and by extension, that it is insufficient for predicting the heat transfer coefficient. As shown in Section 2.3.2, the approximation is not self-consistent. Additionally, as seen in Section 3.4, the approximation yields a dispersion relation that has no significant mechanism for instability in the vertical case, which would incorrectly predict a vapor film that remains smooth indefinitely. Note that this does not discredit the $\epsilon\mathrm{Re} \ll 1$ approximations made in works such as Panzarella et al. (2000); Aursand et al. (2018), since those are concerned with horizontal film-boiling with no strong buoyancy-induced net vapor-flow.

By retaining the inertial terms and using an integral method, it is possible to derive a valid long-wave model. Linear stability analysis of said model results in a dispersion relation, Eq. (55), that reveals neutral curves such as Fig. 4 and by extension predicted values for the critical Reynolds number and wavenumber. Characterizing film boiling stability through a critical Reynolds number has been suggested before by authors such as Kim and Suh (2013), though they fitted a value to a combination of HTC and velocity measurements, as opposed to theoretically predicting it. As seen in Fig. 4, in the present work a value of $\mathrm{Re}_c \approx 10$ is predicted for water. This theoretical prediction is consistent with the experimental findings of Kim and Suh (2013).

As shown in Section 3.5, for the vertical case the predicted critical Reynolds number and wavenumber for any case may to a good approximation be represented by simple power laws with weak dependencies on the parameters S and B. The only result of the stability analysis that carries over into the HTC model is the dimensional wavelength of the resulting disturbances, called the critical wavelength λ_c. Since Re grows very fast as the film thickness grows ($\sim h_0^3$), λ_c depends only weakly on the critical Reynolds number, as seen in Eq. (65) ($\sim \mathrm{Re}_c^{1/3}$). As seen in Eq. (67), the overall result for the vertical case is that this wavelength is only weakly dependent on S and B and that it is accurately predicted by the fluid-dependent wavelength λ_0 multiplied with a relatively constant (≈ 100) factor.

6.2. Validity of the model and its approximations

While inertial terms were retained, the present long-wave approximation still assumes that the $\mathcal{O}(\epsilon^2)$ terms could be neglected, and it is necessary for self-consistency that the predicted instabilities from the model have wavelengths that satisfy this assumption. According to the definitions in Section 3.2, the condition of $\epsilon \ll 1$ is equivalent to $k \ll 1$. As seen from Fig. 4 and Eq. (64), the first occurring instability generally has $k \sim 0.1$ in the vertical cases, and for other orientations k is smaller. Thus, the $\mathcal{O}(\epsilon^2)$ terms may safely be neglected compared to the $\mathcal{O}(1)$ terms.

Additionally, in order to simplify the model, it was assumed in Section 2.4.3 that $E \ll 1$. Since the value of E becomes smaller as the vapor film grows thicker, self-consistency would require that the predicted onset of instabilities occurs after E becomes small. The value of E along the growing base state is $E(x) = S/\mathrm{Re}(x)$. Since $S \sim 0.1$ and $\mathrm{Re}_c \sim 10$, one can expect that $E \sim 0.01$ by the time instabilities occur, which is certainly small enough to make the approximation reasonable.

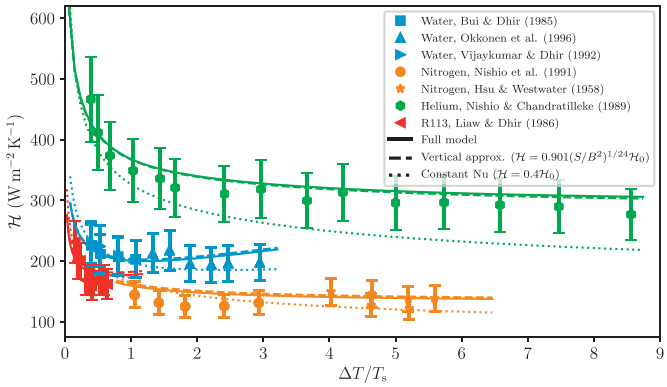

Fig. 6. Experimentally measured vertical-plate heat-transfer coefficients plotted against relative surface superheat, with error bars representing a 15% uncertainty. The corresponding model predictions are shown as three lines for each fluid, corresponding to three different models/values for the Nusselt number.

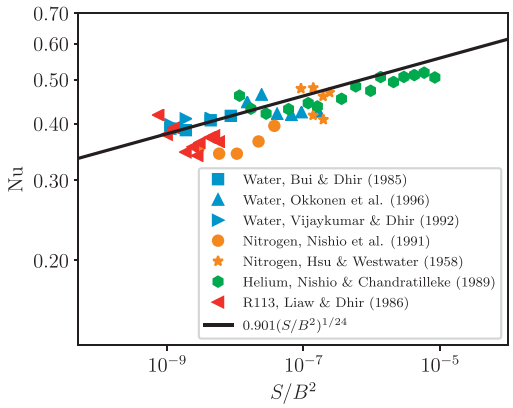

Fig. 7. The Nusselt numbers $\mathrm{Nu} = \mathcal{H}/\mathcal{H}_0$ corresponding to the data points in Fig. 6, plotted against S/B^2. The solid line shows the prediction by Eq. (71).

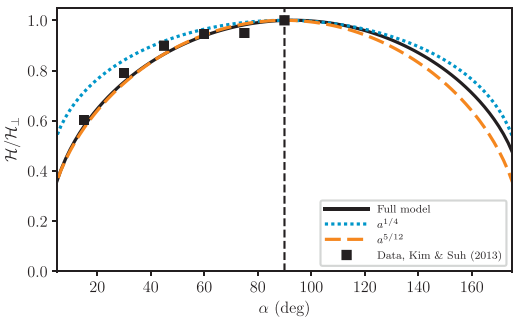

Fig. 8. Experimentally measured heat transfer coefficients for water with $\Delta T = 150$K at varying inclination angles, relative to the value in the vertical orientation. The solid line shows the prediction of the present model. The dashed line shows the approximation resulting from Eq. (72) ($a^{5/12}$). The dotted line shows the angular dependence of the Bromley-type models ($a^{1/4}$).

6.3. Heat-transfer coefficient

In order to predict the heat-transfer coefficient, the premise of the LVFU model was accepted at face value, and the only result needed from the model herein was the critical wavelength λ_c in Eq. (65) inserted into Eq. (2). The result was the general expression, Eq. (68), where the critical wavelength's dependence on λ_0 carried over into the reference HTC ($\mathcal{H}_0$), while the relatively weak dependence on S/B^2 carried over into the corresponding Nusselt number.

As seen in Fig. 6, the present model appears to work very well for vertical film boiling. It is interesting to note how most of the variation in the HTC between different fluids and ΔT values is accounted for by $\mathcal{H}_0$ alone. Such a constant-Nu model, seen in the dotted line in Fig. 6, seems quite sufficient for small to moderate superheat ($\Delta T/T_s < 1$). This means that the wavelength λ_0 combined with the LVFU model is a good predictor for the HTC and that variations in the Nusselt number, as defined here, only accounts for a moderate adjustment. This is confirmed experimentally in Fig. 7 by the fact that every single measurement shows approximately the same Nusselt number,

$$\mathrm{Nu}_\perp \approx 0.4 \pm 0.1, \tag{73}$$

regardless of fluid and ΔT. For the little variation in Nu there is, Fig. 7 shows that the predicted weak power-law $(S/B^2)^{1/24}$ fits quite well.

The reason for the almost universal Nusselt number, $\mathrm{Nu} \approx 0.4$, seems to be due to the fact that the critical Reynolds number Re_c and the corresponding dimensionless wavenumber k_c vary little from case to case, as seen from the weak S and B power-laws in Eqs. (63) and (64). This leads to the critical wavelength in Eq. (67) having a weak dependence on S and B and essentially being just λ_0 times a slightly varying factor. Since the dependence on λ_0 is absorbed into the definition of $\mathcal{H}_0$, the Nusselt number is left to only account for a small adjustment.

For the vertical case, it is apparent from Fig. 6 that the difference between the full model and the approximation in Eq. (71) is virtually zero, so there is little reason to not use the latter. In the case of general inclination, one must either solve the full stability problem, or combine Eq. (71) with the approximation Eq. (72). As seen in Fig. 8, the two give practically identical results in the cases where $\alpha \lesssim \pi/2$. It is also apparent from Fig. 8 that the classical inclination dependence of $a^{1/4}$ from LSI-type models are less

accurate at predicting the observations. Overall there is too little data to draw strong conclusions regarding the inclination dependence. In the $\alpha > \pi/2$ configurations, there seems to be no data at all, and it is not even clear if LVFU-type models apply at all due to the possibility of bubble detachment.

7. Conclusions

From the present work the following may be concluded:

- Retaining the inertial (ϵRe) terms in the long-wave approximation is crucial for correctly predicting stability in non-horizontal film boiling.
- When applying an integral boundary layer method to the long-wave approximation with inertial terms, the result is the two coupled nonlinear partial differential equations in Eqs. (46) and (47).
- Linear stability analysis of this model indicates that the critical Reynolds number for the onset of the inertial instabilities is $\mathrm{Re}_c \approx 10$ and that the resulting waves are much longer than the film thickness.
- Before the critical Reynolds number is reached, the stabilizing evaporation effect seems to dominate. After it is reached, the film is so thick that vapor thrust, non-equilibrium and thermocapillary effects are negligible.
- For inclination angles $\alpha \leq \pi/2$, as defined in Fig. 1, the present model implies that the long-plate film-boiling heat-transfer coefficient may be quite accurately predicted by

$$\mathcal{H} = 0.901(\sin\alpha)^{5/12}\left(\frac{S}{B^2}\right)^{1/24}\left(\frac{\xi k_{\mathrm{v}}^3 \rho_{\mathrm{v}} \Delta\rho g \hat{L}}{16\mu_{\mathrm{v}}\Delta T \lambda_0}\right)^{1/4}, \tag{74}$$

with S and B given by Eqs. (5) and (62), and the vapor properties evaluated at the film-temperature. This model could predict all relevant heat transfer coefficient data within an error of 15%. The model is non-empirical, in the sense that the prefactor 0.9010 comes from expressions generated by numerical solutions of Re_c and k_c, and not from experimental data.

The full nonlinear model Eqs. (46) and (47), and the subsequent results derived thereof, are all made under the assumption of $E \ll 1$, which implies that the vapor film thickness $\bar{h}(x)$ has grown to be at least 100 µm and is quite parallel to the solid wall. As possible further work, it would be interesting to explore the properties of vapor film stability in the regime where $E \approx 1$. This could involve either solving the full nonlinear model numerically, or performing some nonparallel stability analysis akin to Saric and Nayfeh (1975).

Acknowledgements

E. Aursand was supported by the Research Council of Norway [244076/O80] and The Gas Technology Centre (NTNU–SINTEF) through the funding program MAROFF. His research visit at Northwestern University was supported by the U.S.-Norway Fulbright Foundation. Thanks to Bernhard Müller, Tor Ytrehus, Svend Tollak Munkejord, and Morten Hammer for discussions and feedback. Finally, thanks to Hunter Beck for language assistance.

Appendix A. Derivation of dimensionless equations

The following derivation is similar to the one in Aursand et al. (2018) for horizontal film boiling, but generalized for any orientation. Readers are directed there for more detailed comments on the model assumptions that do not relate to the generalization.

A1. Governing equations

The two-dimensional vapor flow in Fig. 1 is characterized by a velocity field $\boldsymbol{v} = u\hat{\boldsymbol{x}} + w\hat{\boldsymbol{z}}$, a temperature field T, and a pressure field p. The governing equations are the standard continuity equation, x and z momentum equations, and the energy equation (Kundu et al., 2007),

$$u_x + w_z = 0, \tag{A.1}$$

$$\rho_{\mathrm{v}}(u_t + uu_x + wu_z) = -p_x + \mu_{\mathrm{v}}(u_{xx} + u_{zz}) - \phi_x, \tag{A.2}$$

$$\rho_{\mathrm{v}}(w_t + uw_x + ww_z) = -p_z + \mu_{\mathrm{v}}(w_{xx} + w_{zz}) - \phi_z, \tag{A.3}$$

$$\rho_{\mathrm{v}} c_{\mathrm{p,v}}(T_t + uT_x + wT_z) = k_{\mathrm{v}}(T_{xx} + T_{zz}), \tag{A.4}$$

where subscripts t, x and z imply differentiation. The body-force potential ϕ,

$$\phi = \phi_0 + \rho_{\mathrm{v}} g(ax + bz) + \frac{\tilde{A}}{6\pi h^3(x)}, \tag{A.5}$$

includes not only the gravitational potential, but also a *disjoining pressure* term (Oron et al., 1997) that represents the van der Waals interaction. Here ϕ_0 is a constant reference potential, g is the gravitational acceleration, $\tilde{A}$ is the Hamaker constant. The quantities a and b are the inclination dependent shorthands $a = \sin(\alpha)$ and $b = -\cos(\alpha)$.

A2. Boundary conditions

At the solid wall we have zero velocity and a given temperature T_{w},

$$[\boldsymbol{v}]_{z=0} = 0, \tag{A.6}$$

$$[T]_{z=0} = T_{\mathrm{w}}. \tag{A.7}$$

At the liquid–vapor interface $z = h(x,t)$ the boundary conditions are continuity of tangential velocity, the kinematic boundary condition (with evaporation), the normal stress balance, the tangential stress balance, and the energy balance. In this order, these may be formally written as

$$\left[(\boldsymbol{v} - \boldsymbol{v}_{\mathrm{l}}) \cdot \hat{\boldsymbol{t}}\right]_{z=h} = 0, \tag{A.8}$$

$$\rho_{\mathrm{v}}\left[(\boldsymbol{v}_{\mathrm{i}} - \boldsymbol{v}) \cdot \hat{\boldsymbol{n}}\right]_{z=h} = j \tag{A.9}$$

$$\left[j(\boldsymbol{v}_{\mathrm{l}} - \boldsymbol{v}) \cdot \hat{\boldsymbol{n}} - \left([\mathcal{T} - \mathcal{T}_{\mathrm{l}}] \cdot \hat{\boldsymbol{n}}\right) \cdot \hat{\boldsymbol{n}}\right]_{z=h} = -\kappa\sigma \tag{A.10}$$

$$\left[\left((\mathcal{T} - \mathcal{T}_{\mathrm{l}}) \cdot \hat{\boldsymbol{n}}\right) \cdot \hat{\boldsymbol{t}} - \nabla\sigma \cdot \hat{\boldsymbol{t}}\right]_{z=h} = 0 \tag{A.11}$$

$$-k_{\mathrm{v}}\left[\nabla T \cdot \hat{\boldsymbol{n}}\right]_{z=h} = \mathcal{H}_{\mathrm{l}}(T_{\mathrm{i}} - T_{\mathrm{s}}) + j\hat{L}. \tag{A.12}$$

Here a subscript "l" indicates the corresponding property on the liquid side of the interface. The symbol $\mathcal{T}$ is the Newtonian flow viscous stress tensor, j is the evaporation mass flux, and $\hat{L}$ is the effective latent heat of vaporization (modified for the sensible heat effect according to Bui and Dhir (1985)). The interface has unit vectors $\hat{\boldsymbol{n}}$ and $\hat{\boldsymbol{t}}$ defined according to Fig. 1, a velocity given by $\boldsymbol{v}_{\mathrm{i}}$, and a temperature $T_{\mathrm{i}} = T(x, z = h)$ which during evaporation is slightly higher than the saturation (and liquid bulk) temperature T_{s}. The

heat transfer coefficient between the interface and the liquid bulk is $\mathcal{H}_\mathrm{l}$. The surface tension of the interface, σ, depends on the interface temperature. This dependence is approximated as a linearization around a value σ_0 at T_s (Davis, 1987),

$$\sigma(T) = \sigma_0 - \gamma[T - T_\mathrm{s}]. \tag{A.13}$$

As discussed in Aursand et al. (2018) the evaporation mass flux may be modelled according to kinetic theory,

$$T_\mathrm{i} - T_\mathrm{s} = \tilde{K} j, \tag{A.14}$$

with

$$\tilde{K} = \left(\frac{1 - \frac{1}{2}\alpha_\mathrm{e}}{\alpha_\mathrm{e}}\right)\frac{\sqrt{2\pi R_\mathrm{s}} T_\mathrm{s}^{3/2}}{\rho_\mathrm{v} L}, \tag{A.15}$$

where α_e is the evaporation coefficient with an assumed value of 0.85.

Finally, in order to avoid having to compute the detailed dynamics of the bulk liquid outside the vapor film, some additional simplifying assumptions are made. First, it is assumed that the liquid pressure is given by hydrostatics alone, so that the liquid pressure p_l outside the interface is

$$[p_\mathrm{l}]_{z=h} = -\rho_\mathrm{l} g(ax + bh). \tag{A.16}$$

Second, it is assumed that the tangential interface velocity must be somewhere between zero and the hypothetical maximum (free surface, $\mu_\mathrm{l} \to 0$),

$$\left[\boldsymbol{v}\cdot\hat{\boldsymbol{t}}\right]_{z=h} = \eta\left(\lim_{\mu_\mathrm{l}\to 0}\left[\boldsymbol{v}\cdot\hat{\boldsymbol{t}}\right]_{z=h}\right) \tag{A.17}$$

with the fluid-dependent constant $\eta \in (0, 1)$ specifying the position within this range.

A3. Scales and dimensionless numbers

As commonly done in the long-wave approximation, a film thickness scale h_0 is used to define dimensionless equivalents $Z = z/h_0$ and $H = h/h_0$. The dimensionless parallel distance is scaled according to the wavelength λ of the vapor film disturbances, $X = x/x_0$ with $x_0 = \lambda/(2\pi)$. The aspect ratio central to this approximation is simply the ratio between these two scales, $\epsilon = h_0/x_0$. For the velocity components a scale u_0 is used to define dimensionless equivalents $U = u/u_0$ and $W = w/w_0$, where continuity implies that $w_0 = \epsilon u_0$. Time is scaled according to $t_0 = x_0/u_0$, which is used to define the dimensionless time τ. The dimensionless pressure P and potential Φ are defined using the pressure scale implied by viscous pressure-drop in a channel, $p_0 = \mu_\mathrm{v} u_0/(\epsilon h_0)$. The evaporation rate $J = j/j_0$ is scaled with $j_0 = k_\mathrm{v}\Delta T/(h_0 L)$, where $\Delta T = T_\mathrm{w} - T_\mathrm{s}$. Finally, the dimensionless temperature is $\theta = (T - T_\mathrm{s})/\Delta T$.

Without any further knowledge about the velocity scale u_0, the dimensionless numbers listed in Section 2.2.1 may now generally be written as

$$\mathrm{Re} = \frac{\rho_\mathrm{v} u_0 h_0}{\mu_\mathrm{v}} \text{ (Reynolds number)},$$

$$E = \frac{k_\mathrm{v}\Delta T}{\rho_\mathrm{v} u_0 h_0 L} \text{ (Evaporation number)},$$

$$\mathrm{Ca} = \frac{\mu_\mathrm{v} u_0}{\sigma_0} \text{ (Capillary number)},$$

$$K = \frac{\tilde{K} k_\mathrm{v}}{h_0 \hat{L}} \text{ (Disequilibrium number)},$$

$$M = \frac{\Delta T \gamma}{\mu_\mathrm{v} u_0} \text{ (Marangoni number)},$$

$$S = \frac{k_\mathrm{v}\Delta T}{\mu_\mathrm{v}\hat{L}} \text{ (Vapor-thrust number)},$$

$$\mathrm{Pr} = \frac{\mu_\mathrm{v} c_{\mathrm{p,v}}}{k_\mathrm{v}} \text{ (Vapor Prandtl number)},$$

$$\Psi = \mu_\mathrm{v}/\mu_\mathrm{l} \text{ (Viscosity ratio)},$$

$$G_\mathrm{v} = \frac{\rho_\mathrm{v} g h_0^2}{\mu_\mathrm{v} u_0} \text{ (Vapor gravity number)},$$

$$G_\mathrm{l} = \frac{\rho_\mathrm{l} g h_0^2}{\mu_\mathrm{v} u_0} \text{ (Liquid gravity number)},$$

$$G = \frac{\Delta\rho g h_0^2}{\mu_\mathrm{v} u_0} \text{ (Gravity number)}. \tag{A.18}$$

The dimensionless governing equations and boundary conditions listed in Section 2.2.1 result from combining the governing equations of Appendix A.1 and the boundary conditions of Appendix A.2 with the dimensionless scalings and numbers herein. In this process, the effects of van der Waals interactions in Eq. (A.5) and liquid heat transfer in Eq. (A.12) are neglected.

Appendix B. Base state velocity profile

According to total mass conservation, a steady state solution must have the same rate of vapor flowing out at x as the amount of vapor is supplied through evaporation along the entire length of $0 \to x$. This means that the average vapor velocity corresponding to the simplified steady state in Eq. (32) may be written as a function of the growing film thickness,

$$\begin{aligned}\langle\bar{u}\rangle &= \frac{1}{\rho_\mathrm{v}\bar{h}}\int_0^{x'}\frac{k_\mathrm{v}\Delta T}{\hat{L}\bar{h}(x)}\mathrm{d}x', \\ &= \frac{a\xi\,\Delta\rho g\bar{h}^2}{12\mu_\mathrm{v}}.\end{aligned} \tag{B.1}$$

The special case of Eq. (B.1) with $a = 0$ and $\xi = 1$ is what inspired the choice of velocity scale u_0 in Eq. (4). With this scaling the dimensionless velocity profile of the base state is

$$\bar{U} = \frac{Ga}{2}\left[(1+\eta)\bar{H}Z - Z^2\right], \tag{B.2}$$

which means that the interface velocity and maximum velocity are

$$\bar{U}_\mathrm{i} = \frac{Ga}{2}\eta\bar{H}^2, \qquad \bar{U}_\mathrm{max} = \frac{Ga}{2}\left[\frac{1}{4}(1+\eta)^2\right]\bar{H}^2, \tag{B.3}$$

respectively.

Appendix C. The value of η

As seen from Eq. (B.3), information on the velocity profile in film boiling may give insight into what the value of η should be. From the theoretical calculations by Koh (1962) on the velocity profile in smooth steady solutions one can see that

$$\frac{U_\mathrm{i}}{U_\mathrm{max}} \approx \frac{3}{4}\left(\frac{\rho_\mathrm{v}\mu_\mathrm{v}}{\rho_\mathrm{l}\mu_\mathrm{l}}\right)^{1/4}. \tag{C.1}$$

Since Eq. (B.3) implies that

$$\frac{\bar{U}_\mathrm{i}}{\bar{U}_\mathrm{max}} = 4\frac{\eta}{(1+\eta)^2} \approx 4\eta, \tag{C.2}$$

the value of η may then be approximated by

$$\eta \approx \frac{1}{4}\frac{U_\mathrm{max}}{U_\mathrm{i}} \approx \frac{3}{16}\left(\frac{\rho_\mathrm{v}\mu_\mathrm{v}}{\rho_\mathrm{l}\mu_\mathrm{l}}\right)^{1/4}. \tag{C.3}$$

References

Alekseenko, S.V., Nakoryakov, V.E., Pokusaev, B.G., 1985. Wave formation on vertical falling liquid films. Int. J. Multiphase Flow 11 (5), 607–627. doi:10.1016/0301-9322(85)90082-5.

Aursand, E., 2018. Inclination dependence of planar film boiling stability. Int. J. Multiphase Flow 106, 243–253. doi:10.1016/j.ijmultiphaseflow.2018.05.010.

Aursand, E., Davis, S.H., Ytrehus, T., 2018. Thermocapillary instability as a mechanism for film boiling collapse. J. Fluid Mech. 852, 283–312. doi:10.1017/jfm.2018.545.

Bromley, L.A., 1950. Heat transfer in stable film boiling. Chem. Eng. Prog. 46, 221–227.

Bui, T.D., Dhir, V.K., 1985. Film boiling heat transfer on an isothermal vertical surface. ASME J. Heat Transf. 107 (4), 764–771. doi:10.1115/1.3247502.

Burelbach, J.P., Bankoff, S.G., Davis, S.H., 1988. Nonlinear stability of evaporating/condensing liquid films. J. Fluid Mech. 195, 463–494. doi:10.1017/S0022112088002484.

Chang, H., 1994. Wave evolution on a falling film. Annu. Rev. Fluid Mech. 26 (1), 103–136. doi:10.1146/annurev.fl.26.010194.000535.

Craster, R.V., Matar, O.K., 2009. Dynamics and stability of thin liquid films. Rev. Mod. Phys. 81 (3), 1131–1198. doi:10.1103/RevModPhys.81.1131.

Davis, S.H., 1987. Thermocapillary instabilities. Annu. Rev. Fluid Mech. 19 (1), 403–435. doi:10.1146/annurev.fl.19.010187.002155.

Dhir, V.K., 1998. Boiling heat transfer. Annu. Rev. Fluid Mech. 30 (1), 365–401. doi:10.1146/annurev.fluid.30.1.365.

Hsu, Y.Y., Westwater, J.W., 1958. Film boiling from vertical tubes. AIChE J. 4 (1), 58–62. doi:10.1002/aic.690040112.

Joo, S.W., Davis, S.H., Bankoff, S.G., 1991. Long-wave instabilities of heated falling films: two-dimensional theory of uniform layers. J. Fluid Mech. 230, 117–146. doi:10.1017/S0022112091000733.

Kaneyasu, N., Takehiro, I., 1966. Two-phase boundary-layer treatment of free-convection film boiling. Int. J. Heat Mass Transf. 9 (2), 103–115. doi:10.1016/0017-9310(66)90125-6.

Kim, C.S., Suh, K.Y., 2013. Angular dependency on film boiling heat transfer from relatively long inclined flat plates. J. Heat Transf. 135 (12), 121502. doi:10.1115/1.4024583.

Koh, J.C.Y., 1962. Analysis of film boiling on vertical surfaces. J. Heat Transf. 84 (1), 55–62. doi:10.1115/1.3684293.

Kolev, N.I., 1998. Film boiling on vertical plates and spheres. Exp. Therm. Fluid Sci. 18 (2), 97–115. doi:10.1016/S0894-1777(98)10021-3.

Kundu, P.K., Cohen, I.M., Dowling, D.R., 2007. Fluid mechanics. Academic Press, Cambridge, 5th edition. ISBN 9780123821003.

Liaw, S.P., Dhir, V.K., 1986. Effect of surface wettability on transition boiling heat transfer from a vertical surface. In: Proceedings of the 8th international heat transfer conference, 4, pp. 2031–2036.

Myers, T.G., 1998. Thin films with high surface tension. SIAM Rev. 40 (3), 441–462. doi:10.1137/S003614459529284X.

Nishio, S., Chandratilleke, G.R., 1989. Steady-state pool boiling heat transfer to saturated liquid helium at atmospheric pressure. JSME Int. J. Ser. 2 32 (4), 639–645. doi:10.1299/jsmeb1988.32.4_639.

Nishio, S., Chandratilleke, G.R., 1991. Natural-convection film-boiling heat transfer: saturated film boiling with long vapor film. JSME Int. J. Ser. 2 34 (2), 202–211. doi:10.1299/jsmeb1988.34.2_202.

Nishio, S., Ohtake, H., 1993. Vapor-film-unit model and heat transfer correlation for natural-convection film boiling with wave motion under subcooled conditions. Int. J. Heat Mass Transf. 36 (10), 2541–2552. doi:10.1016/S0017-9310(05)80192-9.

Nukiyama, S., 1934. The maximum and minimum values of the heat Q transmitted from metal to boiling water under atmospheric pressure. J. Jpn. Soc. Mech. Eng. 37, 367–374.

Okkonen, T., Wennerstroem, H., Hedberg, S., Blomstrand, J., Sehgal, B.R., Frid, W., 1996. Film boiling on a long vertical surface under high heat flux and water subcooling conditions. AIChE Symp. Ser. 92, 294–303. American Institute of Chemical Engineers

Oron, A., Davis, S.H., Bankoff, S.G., 1997. Long-scale evolution of thin liquid films. Rev. Mod. Phys. 69 (3), 931–980. doi:10.1103/RevModPhys.69.931.

Panzarella, C.H., Davis, S.H., Bankoff, S.G., 2000. Nonlinear dynamics in horizontal film boiling. J. Fluid Mech. 402, 163–194. doi:10.1017/S0022112099006801.

Prokopiou, T., Cheng, M., Chang, H.C., 1991. Long waves on inclined films at high reynolds number. J. Fluid Mech. 222, 665–691. doi:10.1017/S002211209100126X.

Saric, W.S., Nayfeh, A.H., 1975. Nonparallel stability of boundary-layer flows. Phys. Fluids 18 (8), 945–950. doi:10.1063/1.861266.

Suryanarayana, N.V., Merte, H., 1972. Film boiling on vertical surfaces. J. Heat Transf. 94 (4), 377–384. doi:10.1115/1.3449955.

Vijaykumar, R., Dhir, V.K., 1992. An experimental study of subcooled film boiling on a vertical surface–thermal aspects. J. Heat Transf. 114 (1), 169–178. doi:10.1115/1.2911243.

Paper D

Predicting triggering and consequence of delayed LNG RPT

Eskil Aursand, Morten Hammer

Published in *Journal of Loss Prevention in the Process Industries*.
(2018) Vol. 55, pp. 124–133
https://doi.org/10.1016/j.jlp.2018.06.001

Journal of Loss Prevention in the Process Industries 55 (2018) 124–133

Contents lists available at ScienceDirect

Journal of Loss Prevention in the Process Industries

journal homepage: www.elsevier.com/locate/jlp

Predicting triggering and consequence of delayed LNG RPT

Eskil Aursand[a,*], Morten Hammer[b]

[a] Department of Energy and Process Engineering, Norwegian University of Science and Technology (NTNU), Trondheim N-7491, Norway
[b] SINTEF Energy Research, Sem Sælands vei 11, Trondheim NO-7034, Norway

ARTICLE INFO

Keywords:
LNG
Rapid phase transition
Film boiling
Superheating
Thermodynamics

ABSTRACT

We develop a model for delayed rapid phase transition (RPT) in LNG spills based on thermodynamics and nucleation theory which includes predictions of both triggering and vapor explosion consequence. We discover that the model predictions can be accurately characterized by two independent parameters alone: The initial fraction of methane and the molar mass of the remaining non-methane part. Based on this we develop correlations for risk assessment which may be used without access to the underlying advanced algorithms, and we give practical advice for risk mitigation. The model is consistent with an often reported empirical triggering criterion for cryogen RPT. We show that spilled LNG must typically boil down to about 10–20% of the original amount before RPT may occur, and after triggering one may expect energy yields of 10–20 g TNT per kg of triggered LNG. Explosive pressures in the range 20–60 bar can be expected.

1. Introduction

Natural gas is a common fossil fuel mainly consisting of methane (CH_4) and with progressively smaller amounts of the heavier alkanes ethane (C_2H_6), propane (C_3H_8), butane (C_4H_{10}), etc. Some nitrogen may also be present. For the purposes of ship transport it is commonly cooled to form liquefied natural gas (LNG), a cryogen at about − 162°C. This is the hazardous material considered in this work.

In the LNG safety literature of the last couple of decades, the phenomenon called rapid phase transition (RPT) (Reid, 1983) is typically listed among the main concerns. This can range from giving it significant attention (Luketa-Hanlin, 2006; Shaw et al., 2005; Pitblado and Woodward, 2011; Cleaver et al., 2007), to little more than noting it as a concern (Alderman, 2005; Hightower et al., 2005; Havens and Spicer, 2007; Raj and Bowdoin, 2010; Forte and Ruf, 2017). The present work concerns the risk of RPT when LNG is spilled onto water, which is a possibility in maritime LNG operations, either during production, transportation, or usage. In such a spill, LNG will spread in a pool on the water surface while gradually boiling off, often without incident. However, in some cases it is observed to suddenly, and seemingly at random, explosively vaporize in large quantities at once. This is an RPT event, whose peak pressures and released mechanical energy can be large enough to displace and damage heavy equipment (Luketa-Hanlin, 2006; Pitblado and Woodward, 2011; Forte and Ruf, 2017) and could theoretically cause secondary structural damage and cascading containment failure (Havens and Spicer, 2007). Note that this is not an explosion in the common sense of the word, i.e. it does not involve combustion or other chemical reactions. It is what is sometimes called a vapor explosion or a physical explosion.

LNG has been transported in carriers at sea for roughly 50 years and is commonly stated to have an excellent safety record (Alderman, 2005; Forte and Ruf, 2017). However, there are still good reasons to address the issue of RPT risk: First, there is a record of actual unintended (though small scale) RPT-related incidents in the industry (Nédelka et al., 2003). Second, small accidents or near-accidents are not necessarily in the public record, so the risks may be higher than they appear to be. Third, the offshore activities of the LNG industry are growing more diverse. The use of LNG as a marine fuel is projected to increase significantly, which will lead to more small-scale bunkering operations. The industry is also moving towards increased use of floating facilities for production, storage, offloading and regasification (FPSO/FSRU) in order to make remote gas fields economically feasible (see emerging FLNG vessels). These developments introduce additional scenarios for LNG leakage, as well as potentially more severe consequences due to the addition of passengers, workers and more sensitive equipment. Such operations may not necessarily inherit the good safety record of the established LNG carrier operations. Overall, in the interest of preserving the excellent safety record of the industry, no significant theoretical risk should remain poorly understood.

Several research programs have been dedicated partly or fully to the subject of LNG RPT in the last few decades. The results and lessons from these projects have been thoroughly reviewed in the past (Cleaver et al., 1998; Nédelka et al., 2003; Luketa-Hanlin, 2006; Koopman and Ermak, 2007; Melhem et al., 2006). In parallel to this research, the RPT

* Corresponding author.
E-mail address: eskil.aursand@ntnu.no (E. Aursand).

https://doi.org/10.1016/j.jlp.2018.06.001
Received 16 March 2018; Received in revised form 12 May 2018; Accepted 5 June 2018

phenomenon has also received considerable attention in the context of fuel–coolant interactions in the nuclear power industry (Fletcher and Theofanous, 1994; Berthoud, 2000), which shares many of the same features. Overall, due to the small spatial scales (film boiling), small temporal scales (rapid nucleation) and poor reproducibility, exact quantification of LNG RPT risk and consequence has so far been elusive.

Models for RPT usually fall into one of two categories: Triggering prediction or consequence prediction. The former is concerned with then "if, when and where" of RPT, while the latter is concerned with the resulting energy yield and pressure peaks given that RPT does occur. LNG RPT triggering prediction have mostly been in the form of empirically based relationships between water temperature and thermodynamic properties of the LNG such as the superheat limit (Reid, 1983). Some more sophisticated methods have appeared in recent years (Melhem et al., 2006), based on gradual compositional change, but the details of the triggering criteria are not always clear. RPT consequence prediction is somewhat more mature. Thermodynamic methods to estimate the explosive yield of vapor explosions first appeared in the 1960s, in the context of nuclear fuel–coolant interactions. This is commonly referred to as the Hicks and Menzies (1965) method (Cleaver et al., 1998; Berthoud, 2000), and uses an idealized thermodynamic path of equilibration and isentropic expansion. While these methods may be applied directly to immediate RPT, that is not the case for delayed RPT due to the unknown LNG composition at the time of triggering.

Overall, the practical assessment of risk and consequence from a given LNG spill seems to still be unsettled, mostly due to the lack of reliable triggering prediction. A report made for the US Federal Energy Regulatory Commission in 2004 concluded that there was no satisfactory theoretical method for practical risk assessment of RPT in the case of LNG carriers (ABS Consulting, 2004). Still, a quite clear qualitative consensus has emerged in the literature regarding the mechanisms behind the RPT process:

1. Initially, after LNG spills on water, film boiling occurs. Since the heat transfer rate is limited, all the heat is spent on evaporation and the LNG stays in its quasi-equilibrium state while boiling (at the bubble point).
2. For some reason, film boiling collapse occurs, which suddenly increases the heat transfer rate by orders of magnitude. We call this the *triggering event*.
3. The sudden and large increase in heat transfer rate causes the liquid to superheat and then rapidly evaporate.
4. Since the vapor takes over 200 times as much space as the liquid, and the evaporation is so rapid, the event seems explosive in nature.

There is an established distinction in the literature between *early RPT* and *delayed RPT* in large scale LNG spills (Hightower et al., 2004; Luketa-Hanlin, 2006; Koopman and Ermak, 2007; Bubbico and Salzano, 2009). Early RPT triggers at the chaotic spill point at any time during the spill, while delayed RPT occurs in the outer parts of the spreading pool after considerable time has passed.

In the present work we concern ourselves with delayed RPT, whose probability appears to depend strongly on the composition of the LNG. While it has been shown that RPT will not occur with pure methane (Enger et al., 1973; Porteous and Reid, 1976), they may occur with low-methane mixtures or with high-methane LNG mixtures who have had time to lose significant methane through boil-off (Luketa-Hanlin, 2006; Koopman and Ermak, 2007; Cleaver et al., 2007, 1998). In fact, it has been shown that usually a methane molar fraction below about 40% is necessary to make LNG-like mixtures experience RPT (Enger et al., 1973). This is much lower than the typical initial fraction of 90%, thus explaining the boil-off time necessary for delayed RPT. As we will show, the composition is important because it changes important parameters such as the Leidenfrost point (minimum temperature of film boiling) and the liquid superheat limit.

The focus of this work is to predict the risk and consequence of delayed RPT when spilling LNG on water. Underpinning this model are the following common hypotheses or assumptions regarding its mechanisms:

- The RPT event occurs if and only if the LNG is superheated to its superheat limit.
- Considerable superheating is only possible after film boiling collapse because it enables direct LNG–water contact.
- Film boiling collapse occurs due to the LNG's Leidenfrost temperature reaching the water temperature.
- The Leidenfrost temperature for saturated liquid-liquid film boiling depends only on the composition of the boiling fluid.

While it may be worth questioning these assumptions, that is outside the scope of this work. In this work, we take them at face value and follow them to their conclusions through the use of thermodynamic modelling and nucleation theory. Specifically, the assumptions lead to the following RPT triggering criterion,

$$T_{\mathrm{SHL}} < T_{\mathrm{w}} < T_{\mathrm{leid}}, \tag{1}$$

where T_{w} is the water temperature, T_{SHL} is the LNG superheat limit, and T_{leid} is the LNG Leidenfrost temperature. Here, we consider T_{w} to be constant and equal to the freezing temperature of water, since the water is cooled by the LNG but rarely forms ice (Luketa-Hanlin, 2006). The variables are T_{SHL} and T_{leid}, which both increase as methane is removed from the mixture during boil-off. The right hand side inequality in Eq. (1) expresses that film boiling collapse is necessary to superheat the LNG. The left hand side in equality in Eq. (1) expresses that the water must be hot enough to heat the LNG to the superheat limit.

Note that the distinction between delayed and early RPT lies in the last two assumptions listed above. In the present work *delayed* RPTs are defined as RPTs that are triggered due to purely thermodynamic changes leading to Eq. (1) being satisfied. Given this, delayed RPTs may occur in a completely undisturbed LNG pool on top of water. Any RPT events that occur before Eq. (1) is satisfied, such as due to external flow disturbances, are by the present definition *early* RPTs.

The theorized delayed RPT triggering event is illustrated in Fig. 1, which shows how we effectively move to the left along the boiling curve as methane boils off from the LNG mixture, eventually passing from

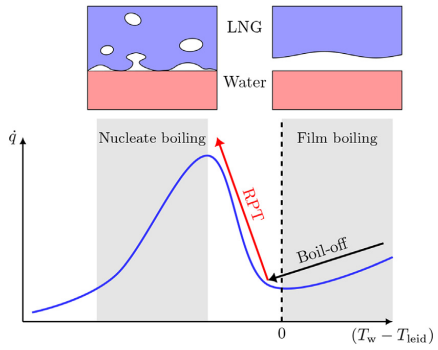

Fig. 1. An illustration of the boiling curve, here as a plot of boiling heat flux ($\dot{q}$) against the difference between water temperature T_{w} and LNG Leidenfrost temperature T_{leid}. When T_{w} approaches T_{leid}, heat flux drops as we transition into the film boiling regime. When methane-rich LNG spills onto water, we initially have that $T_{\mathrm{w}} \gg T_{\mathrm{leid}}$. However, as the arrows show, when methane is removed from the mixture through boil-off T_{leid} is increased, which effectively moves us towards the left along the curve. Eventually the Leidenfrost point is crossed, film boiling breaks down, and RPT is triggered due to a sudden large increase in heat flux.

film boiling to nucleate boiling. Note that the vertical axis in Fig. 1 is logarithmic, so the peak heat flux is actually several orders of magnitude larger than the heat flux at the Leidenfrost point.

Rather than presenting a radically new idea or theory for the RPT mechanism, the novelty of the present work lies in the following:

- The unification and refinement of leading theories for delayed LNG RPT, including both triggering and consequence models, into a single quantitative model. This model inherently takes into account the fact that the composition at the time of triggering is significantly different from the initial LNG compositon. The model also includes proper equation of state (EoS) thermodynamic modelling of mixtures, as opposed to the more common mole fraction average or ideal gas approaches.
- The use of this model to illustrate mechanisms behind triggering and expansion and to reveal a dependence on two independent parameters: The initial methane fraction, and the molar mass of the non-methane part.
- The mapping of simulation results throughout the entire relevant parameter space for LNG spills.
- The reduction of hundreds of simulation results into easy-to-use correlations that may be used for risk assessment without requiring access to advanced thermodynamic algorithms.

The most recent seemingly similar work is that of Benintendi and Rega (2014). The methods applied there are different in several ways, such as the use of correlations and mole fraction averaging instead of an EoS with mixture parameters. Their scope is also different, since they mostly consider the rapid fragmentation and evaporation of LNG droplets impacting the water and not long-term compositional change due to boil-off. Thus, their work mostly concerns early RPT, not delayed RPT as in the present work.

The present model is constructed as follows: In sec. 2 we describe how the thermodynamic properties of the LNG mixture are modelled by the use of an equation of state (EoS). The thermodynamic model is the basis of both the RPT triggering prediction and the RPT consequence models, which are described in Sec. 3 and Sec. 4, respectively.

It is revealed that in this model both triggering and consequence is dependent on only two independent parameters. We show the general effect of changing them (Sec. 5) and how this knowledge may be used in practical assessment and mitigation of risk (Sec. 6). In Sec. 7 we illustrate the application of the model for an example case. In Sec. 8 we make sure that the model predictions are consistent with the sparse experimental data available before giving an overview of conclusions in Sec. 9.

2. Thermodynamics of multi-component fluids

2.1. Fundamental concepts

Thermodynamics properties were calculated by an *equation of state* (EoS), which is an equation relating the three state variables pressure, temperature and density for a homogeneous fluid phase. If the fluid is a mixture, such as LNG, the EoS has parameters that are composition dependent. For certain regions of parameter space, it turns out that the most stable (equilibrium) state is not a single phase but rather a state where the mass is split between one low density phase (vapor) and one high density phase (liquid). When working with a mixture, the two phases generally have different molar compositions. While all the information regarding these two-phase equilibrium states are technically contained within the EoS, finding these states requires a set of advanced multi-phase equilibrium algorithms (Michelsen and Mollerup, 2007; Wilhelmsen et al., 2017).

Given an EoS and an implementation of multi-phase equilibrium algorithms, it is possible to predict the equilibrium state of LNG given temperature (T), pressure (p) and an overall molar composition (). This

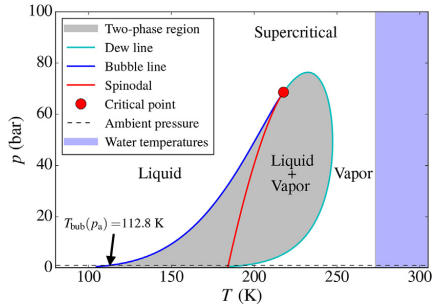

Fig. 2. Phase diagram and spinodal of a typical natural gas composition, as predicted by the PR EoS. We especially identify the ambient pressure bubble point temperature, at about 113 K. For reference, on the right we also indicate the range of temperatures for liquid water.

yields a phase diagram, such as the one shown in Fig. 2. Note the following features:

- Two-phase region (gray shaded): Here the equilibrium state consists of two phases: A liquid phase and a vapor phase, generally of different compositions.
- Bubble line: Boundary between liquid region and two-phase region.
- Dew line: Boundary between vapor region and two-phase region.
- Critical point: Point where liquid and vapor properties merge.
- Spinodal: Maximum temperature where a superheated meta-stable liquid may theoretically exist. Sometimes called the *thermodynamic superheat limit.*

The topic of the spinodal requires some additional comments. While the gray shaded region in Fig. 2 indicates that the equilibrium state is two-phase, it is still possible to temporarily have a meta-stable purely liquid state in parts of this region. The spinodal marks the temperature limit beyond which it is impossible for this meta-stable liquid to exist.

2.2. Representing LNG

The LNG mixture was modelled as a mixture of the first four alkanes,

$$\boldsymbol{z} = [z_1, z_2, z_3, z_4], \tag{2}$$

where each number represents the molar fraction of methane (C1), ethane (C2), propane (C3), and n-butane (C4), respectively. The basic properties of these components are shown in Table 1. Any small amount of N_2 would not change the overall conclusions, since it would evaporate very quickly. Note that is the given overall composition, and that in the two-phase region the liquid and vapor would generally have different compositions.

Table 1
Basic properties of the alkanes considered in this work: Critical temperature (T_{crit}) and molar mass (M). Data from the NIST database (Linstrom and Mallard, 2017).

Name		T_{crit}	M
		(K)	(kg mol^{-1})
Methane	("C1", (CH_4))	191	0.01604
Ethane	("C2", C_2H_6)	305	0.03007
Propane	("C3", C_3H_8)	370	0.04410
n-Butane	("C4", C_4H_{10})	425	0.05812

2.3. Choice of EoS

The ISO Standard (ISO 20765-2/3) EoS for natural gas mixtures is the GERG-2008 (Kunz and Wagner, 2012) EoS, a highly accurate model applicable across a wide parameter space. However, it is a so-called multiparameter EoS (Span, 2010), which are very computationally demanding and comes with robustness challenges in relation to two-phase equilibrium algorithms, as discussed by Wilhelmsen et al. (2017). A faster and more robust alternative is a cubic equation of state, such as the Soave–Redlich–Kwong (SRK) (Soave, 1972) or Peng–Robinson (PR) (Peng and Robinson, 1976) equations. The cubic equations are quite good at predicting the two-phase region and the phase compositions therein but are known to have significant errors for the speed of sound and liquid densities at high pressures (Kunz and Wagner, 2012, Sec. 2.1.2). What mattered most in the present study was the location of the bubble line, critical point, and the ambient pressure spinodal. Due to this, the calculations were performed with the PR EoS.

3. RPT triggering model

The stated triggering criterion in Eq. (1) was central to predicting delayed RPT. As mentioned, T_w was considered constant (273.15 K), while T_{SHL} and T_{leid} were considered -dependent variables. For typical LNG compositions triggering is initially prevented because $T_{leid} < T_w$ (film boiling). However, as methane boils off from the mixture T_{leid} will increases until eventual film boiling collapse, which will cause sudden heating to the superheat limit if $T_w > T_{SHL}$. The key to prediction is thus to estimate the functions $T_{leid}(\boldsymbol{z})$ and $T_{SHL}(\boldsymbol{z})$ in order to find the composition ranges where triggering is possible.

3.1. Predicting the Leidenfrost temperature

As shown in Fig. 1, the Leidenfrost temperature T_{leid} is the surface temperature below which film boiling breaks down. A decent amount of experimental data for T_{leid} of pure fluids could be found in the literature, as summarized in Table 2. It has been suggested by authors such as Spiegler et al. (1963) that the Leidenfrost point can be estimated from

$$T_{leid} = \frac{27}{32} T_{crit}. \tag{3}$$

The data from Table 2 was compared with Eq. (3) in Fig. 3. The simple equation appeared to give an excellent prediction for methane, and generally a decent upper estimate for all the other fluids. Therefore, Eq. (3) was adopted as an estimate for the T_{leid} of LNG, using a computed critical point for any given mixture. Looking further into the mechanisms of film boiling collapse was deemed beyond the scope of this work.

Table 2
Overview of fluids where data could be found on the Leidenfrost point at ambient pressure. Here T_{leid} is the average of the N_{leid} data points found. Also shown is the ambient pressure saturation (boiling) temperature, and the critical temperature, as given by the NIST database (Linstrom and Mallard, 2017). The sources for Leidenfrost point data are Sakurai et al. (1990); Yao and Henry (1978); Gottfried and Bell (1966); Qiao and Chandra (1997); Bernardin and Mudawar (1999); Sakurai et al. (1990); Baumeister and Simon (1973); Nagai and Nishio (1996); Valencia-Chavez (1978); Vesovic (2007); Yao and Henry (1978); Berenson (1961).

Fluid	T_{sat}(K)	T_{leid}(K)	T_{crit}(K)	N_{leid}
Water	373.15	462.78	647.0	12
Nitrogen	77.36	100.00	126.2	7
Freon11	296.92	346.50	471.2	4
Freon113	320.74	378.03	482.9	5
Acetone	329.30	409.40	508.0	4
Methane	111.70	163.33	190.6	3
Ethanol	351.50	429.10	514.0	3
Pentane	309.21	367.00	469.8	1
Cyclohexane	353.89	438.15	554.0	1
Benzene	353.30	448.15	562.0	1

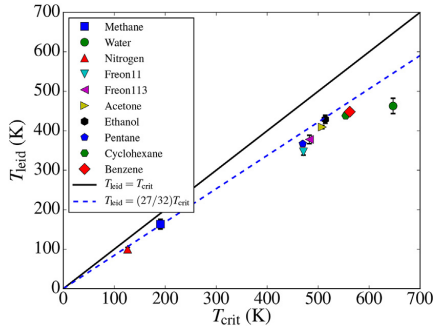

Fig. 3. The experimental pure fluid Leidenfrost temperatures from Table 2 plotted against critical temperature. Also shown (dashed line) is the simple Leidenfrost temperature model in Eq. (3). Error bars represent spread of data in the cases where more than one data point was found.

Note that evaluating Eq. (3) for mixtures is significantly more complicated than for pure fluids. The critical point must be solved for with the combination of an EoS and an iterative algorithm, as opposed to simply looking up the pure fluid T_{crit} in a table.

3.2. Predicting the liquid superheat limit

As mentioned in Sec. 2, it is possible to superheat a liquid to a meta stable state beyond the bubble line, and the liquid spinodal is the theoretical limit to this superheating. However, as discussed by Aursand et al. (2017), in practice spontaneous homogeneous nucleation happens before reaching the spinodal due to the always present thermal fluctuations. The magnitudes of both the nucleation barrier and the fluctuations are temperature dependent, and the threshold temperature where the fluctuations become very likely to overcome the barrier is called the *(kinetic) superheat limit* (SHL).

As shown in Aursand et al. (2017), the superheat limit for alkanes, both pure and mixture, may be accurately estimated through classical nucleation theory (CNT). The basic principle is to estimate the probability of thermal fluctuations creating tiny vapor nuclei beyond a critical size, and this is represented by a classical Arrhenius rate law,

$$J = J_0 \exp\left(-\frac{\Delta G}{k_B T}\right). \tag{4}$$

For pure fluids, the nucleation barrier is (Aursand et al., 2017)

$$\Delta G = \frac{16\pi\sigma^3(T)}{3(p_{sat}(T) - p)^2}, \tag{5}$$

and the rate at zero nucleation barrier is

$$J_0 = \frac{\rho_l}{m^{3/2}} \sqrt{\frac{2\sigma}{\pi}}. \tag{6}$$

Here, k_B is the Boltzmann constant, σ is the surface tension, p_{sat} is the saturation pressure at the given temperature, p is the actual pressure, ρ_l is the liquid density, and m is the mass of a single molecule. The expression for J_0 varies somewhat between sources, but this has a negligible effect on the predicted SHL.

The expression in Eq. (4) may only predict a nucleation rate. In order to find the SHL it was necessary to define a critical nucleation rate J_{crit} which corresponds to sudden macroscopic phase change. Due to the rapid growth of the exponential in Eq. (4), the result is quite insensitive to the specific choice of J_{crit}. In this work the value of $J_{crit} = 1{\cdot}10^{12}\mathrm{s}^{-1}\mathrm{m}^{-3}$

was used, similar to previous works (Bernardin and Mudawar, 1999; Aursand et al., 2017). Thus, in order to predict the superheat limit, it was necessary to solve the implicit equation

$$J(T) = J_{\text{crit}} \tag{7}$$

to yield T_{SHL}. However, due to the insensitivity to the values of J_0 and J_{crit}, the above could be simplified. Since $\ln(J_0/J_{\text{crit}})$ is almost constant (≈ 64), one is past the critical nucleation rate when $\Delta G < 64 k_{\text{B}} T$, and thus to a good approximation one could instead solve

$$\frac{(p_{\text{sat}}(T) - p)^2 k_{\text{B}} T}{\sigma^3(T)} = \frac{\pi}{12}, \tag{8}$$

for temperature. To solve Eq. (8) requires the surface tension function $\sigma(T)$ and an EoS to evaluate $p_{\text{sat}}(T)$. Note that it is critical to include the temperature dependence of σ.

The above theory was developed for pure fluids. For mixtures, the bubble line pressure was substituted for the saturation-line pressure, and the mixture surface tension was calculated as a mole fraction weighted average of the surface tension of the pure components. The surface tension functions for the pure components were found by interpolating tables from the NIST database (Linstrom and Mallard, 2017).

It is interesting to see how the predicted SHL generally follows the thermodynamics quantities. From solving Eq. (8) at atmospheric pressure throughout the possible composition range, it was found that

$$T_{\text{SHL}} \approx 0.95 T_{\text{spin}} \quad (p = 1 \text{ atm}), \tag{9}$$

regardless of composition. It was also found that the superheat limit loosely follows the critical temperature,

$$0.64 T_{\text{crit}} < T_{\text{SHL}} < 0.89 T_{\text{crit}} \quad (p = 1 \text{ atm}), \tag{10}$$

with the exact position within this interval depending on composition. Note from Eq. (1) that triggering is only possible if $T_{\text{SHL}} < T_{\text{leid}}$. When combining Eq. (3) with the average value from Eq. (10), it can be seen that typically $T_{\text{SHL}} \approx 0.9 T_{\text{leid}}$.

3.3. Detecting triggering during boil-off

The aim was to simulate the long-term thermodynamic effect of LNG film boiling on top of water. Having time as the progress parameter of the boil-off would require the estimation of heat transfer rate and pool thickness, which was beyond the scope of this work. In the present work, the progress parameter was chosen to be the decreasing methane amount during boil-off. Based on this one may look for the methane fractions where the triggering criterion Eq. (1) is satisfied.

The vapor leaving the LNG will not have the same composition as the liquid, since the lighter components are more volatile. To a good approximation one may assume that only CH_4 molecules escape into the vapor during boiling (Enger et al., 1973). Given an original composition $\boldsymbol{z}^{(0)}$ and a current methane fraction z_1, the current composition vector can be found from

$$z_i = z_i^{(0)} \frac{1 - z_1}{1 - z_1^{(0)}} \quad \forall \quad i > 1. \tag{11}$$

The above gives a linear increase in the fraction of the heavier alkanes as a function of the decreasing methane amount. This comes with a change in the thermodynamic properties of the LNG, generally shifting the two-phase region to higher temperatures, as shown in Fig. 4.

With the use of Eq. (11), all properties can be plotted as a function of methane fraction as shown in Fig. 5. Since both T_{leid} and T_{SHL} are now known as a function of z_1, the zone of z_1 values where the triggering criterion Eq. (1) is satisfied can be indicated (shaded red in Fig. 5). Note especially the highest methane fraction of this region, where $T_{\text{leid}} = T_{\text{w}}$, in this example about 0.4. This is denoted as z_{leid}, the *Leidenfrost fraction*. The corresponding composition vector is called the *Leidenfrost composition*.

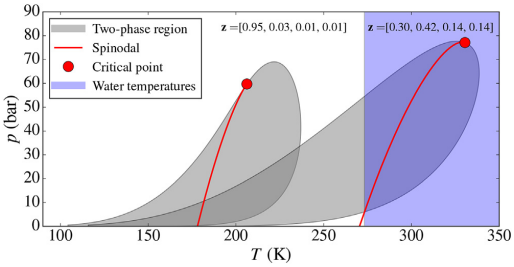

Fig. 4. Illustration of how the phase diagram changes as methane is removed from the LNG mixture, and eventually enters the region of water temperatures. Calculations were made with the PR EoS. See Eq. (2) for interpretation of the composition vector $\mathbf{z}$.

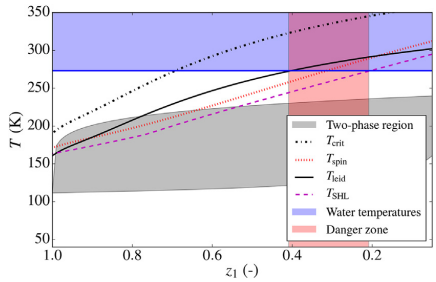

Fig. 5. Properties changing as methane is removed from the mixture, for the case of $\tilde{\boldsymbol{z}} = [0.5, 0.3, 0.2]$. The composition region shaded in red is where the RPT triggering criterion Eq. (1) is satisfied. The methane fraction when entering this region is called the *Leidenfrost fraction*, which in this case is $z_{\text{leid}} \approx 0.4$. Then, when $z_1 < 0.2$, the superheat limit is so high that RPT will not occur even though film boiling has collapsed. (For interpretation of the references to colour in this figure legend, the reader is referred to the Web version of this article.)

Note that a plot such as Fig. 5 does not depend on initial methane fraction $z_1^{(0)}$. Changing the initial methane fraction simply corresponds to changing the starting position on the same plot. The plot (and z_{leid}) does however depend on the composition of the non-methane part, which can be characterized by the *remainder composition*,

$$\tilde{\boldsymbol{z}} = \frac{1}{1 - z_1}[z_2, z_3, z_4], \tag{12}$$

which is constant during boil-off. While many results technically depend on every component in $\tilde{\boldsymbol{z}}$, it was found that many correlate strongly with a quantity $\eta(\tilde{\boldsymbol{z}})$, here called the *alkane factor*. The vector $\tilde{\boldsymbol{z}}$ maps to the scalar η by

$$\eta = \frac{[M_2, M_3, M_4] \cdot \tilde{\boldsymbol{z}}}{M_2}, \tag{13}$$

i.e. it is the molar mass of the non-methane part, relative to the molar mass of ethane. The value starts at $\eta = 1$ for C1 + C2 only, and increases as more of heavier alkanes C3 and C4 is added. Typical values for LNG mixtures are between 1.1 and 1.4.

It is now assumed that triggering occurs immediately once the criterion Eq. (1) is satisfied so that the methane fraction at that moment is z_{leid}. Formally, z_{leid} must be found by iteratively searching for the value of z_1 that solves $T_{\text{leid}} = T_{\text{w}}$ and for every step this would require the iterative calculation of the mixture critical point. Thankfully, it was found that z_{leid} correlated strongly with the alkane factor η, as seen in Fig. 6. The following fit was found,

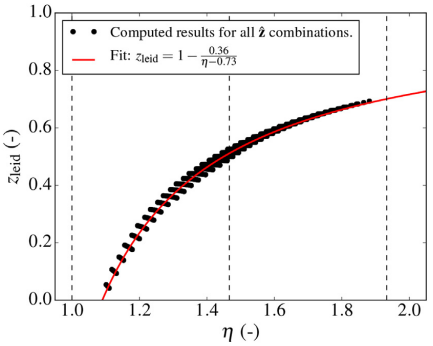

Fig. 6. Calculated values of the Leidenfrost fraction z_{leid} plotted against the alkane factor η. The solid red line shows a functional fit (Eq. (14)), which crosses zero at $\eta = 1.09$. The vertical dashed line show the η values corresponding to pure ethane, propane, and butane, from left to right. (For interpretation of the references to colour in this figure legend, the reader is referred to the Web version of this article.)

$$z_{\text{leid}} = 1 - \frac{0.36}{\eta - 0.73}, \tag{14}$$

which can be used for practical purposes.

Note the following features:

- Since η normally satisfies $\eta < 1.4$, z_{leid} is normally less than 0.5, i.e. the mixture needs to boil down to less than 50% methane in order to trigger RPT.
- If the initial mixture is close to being only methane and ethane ($\eta < 1.09$), it will never trigger. This is because the Leidenfrost temperature of the remainder composition is below the water temperature, so it doesn't matter if all the methane boils off.

While changing the initial methane fraction does not change the methane fraction needed for triggering (z_{leid}), it does change how much boil-off is necessary to reach it. The *reduction factor r* is defined as the moles of LNG remaining at triggering divided by the original moles of LNG spilled. It can be found from

$$r(z_1^{(0)}, z_{\text{leid}}) = \frac{1 - z_1^{(0)}}{1 - z_{\text{leid}}}, \quad (z_{\text{leid}} < z_1^{(0)} < 1.0), \tag{15}$$

where $z_1^{(0)}$ is the initial fraction of methane. By combining Eqs. (14) and (15), one may see that

$$r(z_1^{(0)}, \eta) = (1 - z_1^{(0)})\left(\frac{\eta - 0.73}{0.36}\right). \tag{16}$$

4. RPT consequence model

After triggering (film boiling collapse), heat flux increases dramatically due to the transition into the nucleate boiling regime (see Fig. 1). Since the evaporation process is unable to absorb the sudden heat flux increase, the liquid superheats. Superheating proceeds until the superheat limit T_{SHL}, which can be found by solving Eq. (8) at ambient pressure (p_a) and the Leidenfrost composition. Once at the superheat limit the fluid will have to find its equilibrium state. This state contains a significant amount of vapor, and thus it takes up a much larger volume at ambient pressure. Since the transition is very rapid, it will go through an intermediate high pressure state, which gives the event its explosive effect.

The RPT consequence model in the present work was based on the established basic principles of Hicks and Menzies (1965). However, no assumptions of ideal gas were made in the thermal equilibration nor the expansion process. Note also that the input composition to this model was based on the result of the RPT triggering model (Leidenfrost compositon), and not simply set to the initial LNG compositon. In the present work, akin to the Hicks & Menzies methodology, the triggering and explosion processes were approximated by the following series of steps (see Fig. 7):

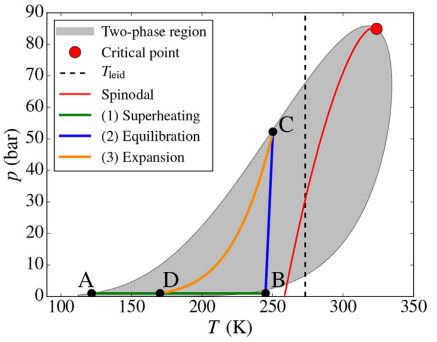

Fig. 7. The thermodynamic path of triggering and explosion for an example value of $\tilde{\mathbf{z}}$. The states are labelled A through D according to the list in Sec. 4.

- **A**(T_{bub}, p_a): The state at the moment of triggering (film boiling collapse). This is a liquid equilibrium state on the bubble line. After triggering the liquid temperature suddenly increases.
- **B**(T_{SHL}, p_a): The superheat limit. This is a liquid non-equilibrium (meta-stable) state, which will rapidly expand to its corresponding equilibrium.
- **C**(T^*, p^*): A liquid–vapor quasi-equilibrium state. This is the thermodynamic equilibrium state with the same volume and energy as the meta-stable state B, and can be found using two-phase equilibrium algorithms together with an EoS. This state is mostly liquid, but its pressure p^* is much higher than the ambient. It is usually quite close to the bubble line but slightly inside the two-phase region. This is an equilibrium state given the volume and energy from *B*. This is called a quasi-equilibrium state because it is not in thermal or mechanical equilibrium with the surroundings.
- **D**(T_{end}, p_a): The equilibrium state resulting from an isentropic expansion from state C to ambient pressure. This state is mostly vapor, and has more than a hundred times the volume of the other states.

The above process is similar to the one that was suggested by Melhem et al. (2006), except that they placed B at the spinodal (not superheat limit) and simply determined C as the point on the bubble line with the same temperature as B.

In the present work the explosive energy yield per mole of triggered liquid (E) was estimated as the expansion work of C → D, which could be found from the enthalpy difference between the two states. The pressure of state C was used to approximate the maximum explosion pressure p^*.

Both E and p^* are functions of the remainder composition only, since the process A → D occurs at the Leidenfrost composition, not the initial composition. Once again it turned out that these results correlated strongly with the alkane factor η, as shown in Figs. 8 and 9. Functions of η fitted to these results were

$$\frac{E}{1\ \text{kg mol}^{-1}} = 4.731\eta^3 - 24.65\eta^2 + 41.75\eta - 20.60, \tag{17}$$

and

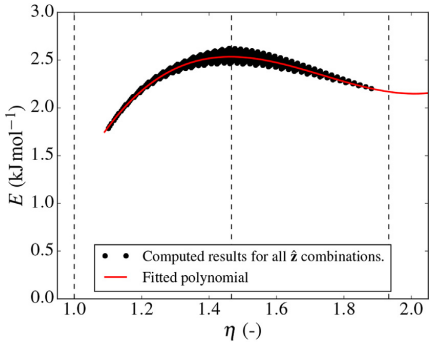

Fig. 8. Calculated values for RPT explosive yield according to the expansion step illustrated in Fig. 7, throughout the space of possible $\tilde{\boldsymbol{z}}$, plotted against η. Also shown is the polynomial fit in Eq. (17).

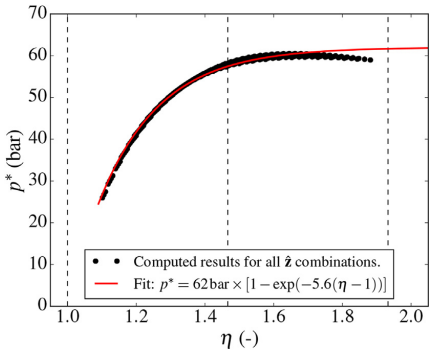

Fig. 9. Calculated values for maximum RPT explosive pressure according to the pressure of point C in Fig. 7, throughout the space of possible $\tilde{\boldsymbol{z}}$, plotted against η. Also shown is the fit in Eq. (18).

$$\frac{p^*}{62\ \text{bar}} = 1 - \mathrm{e}^{-5.6(\eta-1)}. \tag{18}$$

These correlations may be used in the range $\eta \in (1.0, 1.8)$, which is the range where most realistic cases were found to be in. The molar mass of the mixture during boil-off is a function of the changing methane fraction z_1 and the constant alkane factor η,

$$M = z_1 M_1 + \eta(1 - z_1)M_2. \tag{19}$$

The mixture molar mass at triggering (M_{leid}) is thus a function of η alone, since there $z_1 = z_{\text{leid}}(\eta)$. From the molar mass one may find the yield per mass,

$$E^{(\text{mass})}(\eta) = \frac{E}{M_{\text{leid}}}, \tag{20}$$

which is plotted in Fig. 10. Note how $E^{(\text{mass})}$ only depends on η, not the initial methane fraction.

The values in Fig. 10 and Eq. (17) are explosive yield per mole of LNG present at the time of triggering. It is also interesting to know the potential explosive yield for a given spilled amount of LNG. On a molar basis, this may simply be found by multiplying E with the reduction factor r. Per mass of spilled LNG it becomes

$$E_0^{(\text{mass})}(\eta, z_1^{(0)}) = \frac{rE}{M_0}, \tag{21}$$

where M_0 is the molar mass of the initial mixture, i.e. Eq. (19) evaluated

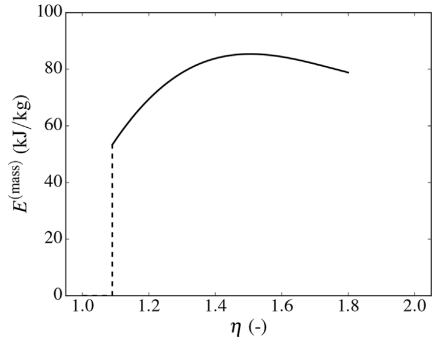

Fig. 10. The RPT explosive yield per mass of LNG at time of triggering based on Eq. (20) Below $\eta = 1.09$ the yield effectively drops to zero, since even the remaining mixture at zero methane does not have a high enough Leidenfrost temperature to trigger.

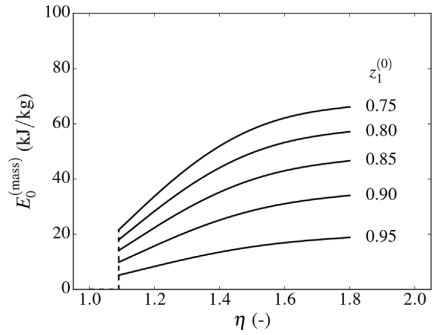

Fig. 11. The RPT explosive yield per mass of *initial* LNG based on Eq. (21). Below $\eta = 1.09$ the yield effectively drops to zero, since even the remaining mixture at zero methane does not have a high enough Leidenfrost temperature to trigger.

at $z_1 = z_1^{(0)}$. Note how $E_0^{(\text{mass})}$ depends on both η and $z_1^{(0)}$. Example results are shown in Fig. 11. Note that in contrast to Fig. 10, Fig. 11 shows that yield with respect to initial mass increases monotonously with η. This is due to the effect η has on the reduction factor r: Increasing η leads to earlier triggering so that more of the initial mass remains.

Note that the energy yield calculated here is from the combination of an isolated (B → C) and an isentropic (reversible) (C → D) process. Any other process will give irreversible loss of energy, so the present idealization will give an upper bound to the actual yield. It has been suggested that the actual yield is closer to 50% of this prediction (Melhem et al., 2006).

5. Discussion

5.1. RPT predictions

We have demonstrated how triggering and consequence of delayed LNG RPT may be affected by the following two independent properties of the initial LNG composition:

- **Alkane factor** (η): While the effects of the non-methane part are fully specified by the vector $\tilde{\boldsymbol{z}}$, we have shown that they can be accurately predicted through the corresponding scalar property η. This value represents how heavy the non-methane part of the LNG is, relative to the case of pure ethane.

- **Initial mole fraction of methane** ($z_1^{(0)}$): This value is found directly from the initial composition $\boldsymbol{z}^{(0)}$. Adding or removing methane does not affect η.

Overall, either reducing η or increasing $z_1^{(0)}$ will be beneficial to safety. Specifically, reducing η has the following effects:

- Reducing the explosive yield per initial mass ($E_0^{(\text{mass})}$), as shown in Fig. 11. This is mostly due to the reduction on the Leidenfrost fraction z_{leid} (Fig. 6), which in turn reduces the reduction factor r (Eq. (16)), i.e. there will be less total LNG remaining at the time of triggering. As seen in Fig. 10, the effect on the yield per *triggered* mass ($E^{(\text{mass})}$) is less clear-cut.
- Reducing the predicted maximum pressure of the RPT explosion (p^*), as shown in Fig. 9.

Increasing $z_1^{(0)}$ has the following effects:

- Reducing the explosive yield per initial mass, as shown in Fig. 11. This is mostly due to the effect of reducing the reduction factor r (Eq. (16)). It does not affect the yield per triggered mass ($E^{(\text{mass})}$).

5.2. Comments on early RPT

We may also ask what to expect of early RPT. While the triggering model in Sec. 3 is only for predicting delayed RPT, the consequence model in Sec. 4 still applies. The difference is that the calculation must be done on a mixture with much more methane than the Leidenfrost composition, since early RPT by definition occurs before that composition is reached. With a typical initial LNG composition as an extreme case, it was found that the maximum pressure is reduced to about 50% and that the yield (per triggered mass) is reduced to about 70%, compared to the corresponding delayed RPT event. This does not necessarily mean that the risk is less, since the total yield in a single early RPT event is not known. What is known is that the total potential explosive yield is actually higher, since there is 5–10 times more LNG available for early RPT due to the boil-off reduction factor.

5.3. Comments on model approximations

As with any model, the present one is an approximation and has certain weaknesses. A central approximation in the simulated boil-off is that we only allow methane to boil off, while the heavier alkanes stay in the liquid. This is a very good approximation as long as there is still significant methane amounts remaining in the liquid. An artifact of this approximation is that in the cases of $\eta < 1.09$ we predict that film boiling collapse will never happen, since the Leidenfrost temperature can never reach the water temperature. In reality significant ethane boil-off will commence once the methane is gone, and move the Leidenfrost temperature further up until eventual film boiling collapse. However, since we then know that the reduction factor will be very small ($r < 1 - z_1^{(0)}$), we consider the risk minimal when $\eta < 1.09$.

On the topic of film boiling collapse, the model is very much dependent on the assumption that the Leidenfrost point prediction in Eq. (3) is as accurate for mixtures as it is for pure fluids. However, without data on the Leidenfrost point of mixtures this cannot be confirmed.

Once film boiling collapses, superheat can commence, starting the transition from state A to state B (see Fig. 7). In this model, we assume that superheating proceeds until the superheat limit is reached, which is the point where homogeneous nucleation occurs due to thermal fluctuations, no matter how careful the heating is performed. However, in reality, external disturbances may cause phases transition to trigger before reaching this limit. In that case, we would expect both the yield and pressure to be lower, and in this sense the present model represents a worst-case estimate. Also, when finding the superheat limit it is necessary to evaluate some liquid properties outside the equilibrium region. Here we assume that the EoS reasonably extrapolates into the meta-stable region, despite mostly being fitted to equilibrium data.

6. Procedure for risk assessment and mitigation

We now present a procedure for practical risk assessment and mitigation which do not require access to advanced thermodynamic software and only uses the correlations developed in this work.

6.1. Predicting consequence

To estimate the worst-case RPT consequence of an LNG spill, perform the following procedure:

1. Find the initial mole fractions of alkanes, $\boldsymbol{z}^{(0)}$, and the molar mass of each component, M_i.
2. Calculate the following two parameters: The alkane factor η (through Eqs. (12) and (13)) and the initial methane fraction $z_1^{(0)}$ (first value in $\boldsymbol{z}^{(0)}$).
3. If $\eta > 1.09$:
   - Based on these two parameters, calculate reduction factor r (through Eq. (16)). This is the estimated fraction of initial LNG still present at the time of triggering.
   - Calculate the explosive yield per triggered LNG mass $E^{(\text{mass})}$ from Eq. (20) and Eq. (17).
   - Calculate the explosive yield per initial LNG mass $E_0^{(\text{mass})}$ from Eq. (21) and Eq. (17). If multiplied with total mass of spilled LNG, this represents the total potential explosive yield from RPT events, likely distributed between several blasts.
   - Calculate the maximum expected pressure from Eq. (18).

   If $\eta < 1.09$, risk is considered minimal.

6.2. Reducing consequence

Risk can generally be reduced by either reducing η or increasing $z_1^{(0)}$, while keeping the other constant. One can also do both simultaneously.

It may be tempting to achieve an increase in the initial methane fraction ($z_1^{(0)}$) by removing ethane. However, this can be counter-productive as it will increase η (and z_{leid}), and thus the maximum pressure p^*. Despite the increase in Leidenfrost fraction, the overall effect will still be to reduce the relative amount of remaining LNG at triggering (r), due to the increase in initial methane fraction.

According to this model, a more surefire way of reducing risk will be to reduce the amounts of the heavier hydrocarbons C3 and C4. This will ensure that both the pressure and energy yield of the vapor explosion is reduced. Only when these are down to very small fractions should one start removing C2 to further reduce risk.

7. Example

We now find the predictions of the model for a typical LNG composition. The quantitative results are shown in Table 3. Note that all the energy results are given in energy per amount of LNG. A single tank on an LNG carrier may hold around 20000-30000m^3 LNG, which is about $1{\cdot}10^7$ kg. When accounting for the boil-off before triggering, this is around $1{\cdot}10^5$ MJ of potential RPT vapor-explosion energy. Of course, this is unlikely to be released all in one explosion, but rather in multiple less powerful ones.

A different approach would be to assume that 1 L (10 cm cube) of LNG is triggered at once. The mass of 1 L of LNG right before triggering (bubble temperature at the Leidenfrost composition) is 0.651 kg, which when multiplied with $E^{(\text{mass})}$ gives a yield of 48 kJ, or about 11 g TNT equivalent.

Table 3
An overview of model results in a given example case.

Input:			
$\mathbf{z}^{(0)}$	[0.90, 0.06, 0.03, 0.01]	Initial composition	
Results:			
$\tilde{\mathbf{z}}$	[0.6, 0.3, 0.1]	Remainder composition	Eq. (12)
η	1.23	Alkane factor	Eq. (13)
z_{leid}	0.285	Leidenfrost fraction	Eq. (14)
r	0.14	Reduction factor	Eq. (16)
M_0	0.0181kg mol^{-1}	Initial molar mass	Eq. (19)
M_{leid}	0.0311kg mol^{-1}	Molar mass at triggering	Eq. (19)
$E^{(\text{mass})}$	73kJ kg^{-1}	Yield per triggered mass	Eq. (20)
$E_0^{(\text{mass})}$	17kJ kg^{-1}	Yield per initial mass	Eq. (21)
p^*	45 bar	Maximum pressure of vapor-explosion	Eq. (18)

8. Consistency with experiments

8.1. Triggering criteria

Empirical criteria for RPT to occur with cryogens have been presented in the literature. While this ultimately depends on chemical composition, the criteria are typically presented in terms of relations between surface temperature and composition-dependent temperature properties of the cryogen. A commonly cited empirically based criterion is (Porteous and Reid, 1976; Reid, 1983; Hightower et al., 2004; Luketa-Hanlin, 2006)

$$1.0 < \frac{T_{\text{w}}}{T_{\text{SHL}}} < 1.1. \tag{22}$$

The left hand side of our theoretical criterion Eq. (1) trivially agrees with the left hand side inequality of Eq. (22). Regarding the right hand side, if we combine Eq. (3) with the mid-point of the interval in Eq. (10) ($T_{\text{SHL}} \approx 0.77 T_{\text{crit}}$), we find that

$$T_{\text{leid}} \approx \frac{27}{32}\frac{T_{\text{SHL}}}{0.77} \approx 1.1 T_{\text{SHL}}. \tag{23}$$

Thus, the present model predicts the empirical observation in Eq. (22) and serves to explain its theoretical basis. The correspondence also serves as a validation of the present RPT triggering model.

On a more qualitative note, it has been reported that RPT will not occur when methane or ethane is spilled on water, but will occur if relatively small amounts of propane or butane are added (Enger et al., 1973; Porteous and Reid, 1976). This is correctly predicted by the present model, in which no RPT may occur when $\eta < 1.09$. Methane and ethane alone has $\eta = 1$, and the only way to increase η is to add heavier alkanes. For LNG-like mixtures, it has been shown that the methane fraction must be reduced to at least 40% for RPT to occur (Enger et al., 1973). This is consistent with the present model, which predicts $z_{\text{leid}} < 0.5$ for the typical range of $\eta \in (1.1, 1.4)$, as seen in Fig. 6. See also the example in Fig. 5, which predicts almost exactly 40%.

8.2. RPT consequence

Quantifying RPT energy yield and pressure from experiments has proven to be much more difficult than simply noting under which conditions RPT occurs. Still, some sporadic data does exist. Reported RPT underwater peak pressures 1 m from the triggering point have been reported to be 7 bar (Porteous and Reid, 1976), 15 bar (Enger et al., 1973) or "order of tens of bars" (Cleaver et al., 1998). As seen in Fig. 9 the model predicts 25–55 bar for the typical range of $\eta \in (1.1, 1.4)$, which is both in the correct order of magnitude and a reasonable upper bound. The fact that the pressure prediction is on the high side does not necessarily mean that it is incorrect, as it represents peak pressure at the source. The pressure is expected to decay rapidly with distance (Cleaver et al., 1998; Bubbico and Salzano, 2009), so the actual source pressure may be significantly higher.

It has been claimed that peak pressure is a poor predictor for RPT destructiveness (Jazayeri, 1977). It seems likely that RPT energy yield plays a more important role. This has to our knowledge not been directly measured but has been estimated from other measurements. The yield of single RPT events have been estimated to have TNT equivalents from a few grams all the way up to 6 kg (about 25 MJ) (Cleaver et al., 1998; ABS Consulting, 2004; Hightower et al., 2004; Melhem et al., 2006; Koopman and Ermak, 2007). Most authors do not specify whether a yield estimate is for an early or delayed RPT event. From the few instances where it is specified, there seems to be no clear trend regarding which kind of RPT has the highest yield, though the highest reported yield (6 kg) were from an early RPT. Delayed RPTs seem to have yields anywhere from a few grams to 3 kg. It is not known if this variability is due to a varying yield per mass, or a varying amount of mass participating in the event. As seen in Fig. 10, the present model predicts a yield of about 50–80kJ kg^{-1} for triggered LNG, which is about 10–20 g TNT equivalent per kg of LNG. Unfortunately, this cannot be compared directly to yields from actual RPT events because the amount of participating LNG in each single RPT event is unknown. Still, we may perform the following two consistency checks regarding the explosive yield:

- Use model to estimate total potential yield over multiple events: If we consider a limited LNG spill of 10 m^3 (about 5000 kg) with the composition of Table 3, we find from $E_0^{(\text{mass})}$ that this spill has a potential yield of about 85 MJ (20 kg TNT) after boiling off. This is certainly sufficient to provide multiple RPT events on the scale of kg TNT, as seen in experiments.
- Use model to estimate participating amount in single events: Experiments report that single delayed RPT events can have yields from a few grams to 3 kg TNT. According to the present model the yield is 10–20 g TNT per kg of LNG, which implies that such events would require the participation of LNG volumes anywhere from about 1L to 0.5m^3. The majority of events are in the lower end of this range, and such an amount surely seems reasonable given that events appear to occur in quite localized spots on the LNG pool.

While the above shows that the consequence model is reasonably consistent with observations, it is by no means a rigorous or conclusive validation. Such a thing would require additional experimental data, especially regarding the amount of LNG participating in single RPT events.

9. Conclusions

From established and reasonable assumptions a model for delayed LNG RPT based on thermodynamics and nucleation theory was developed. The model was then used to develop correlations which may be used without access to the underlying advanced algorithms. The model predicted the following general conclusions:

- Spilled LNG will typically boil down to about 10–20% of the original amount before triggering RPT. We found that the model is consistent with the often cited triggering criterion in Eq. (22).
- The RPT explosive yield per triggered LNG mass will generally be in the range 50–80kJ kg^{-1}, and this is quite independent of LNG parameters (Fig. 10). This yield is equivalent to 10–20 g TNT per kg LNG.
- Due to much of the LNG boiling off before triggering, the potential explosive yield per *spilled* mass will be in the range 5–60kJ kg^{-1}, but this is very dependent on LNG parameters (Fig. 11).
- The peak explosive pressure will generally be in the range of 20–60 bar, but this is very dependent on the alkane factor η (Fig. 9).
- Potential explosive yield and pressure may be reduced by decreasing

the alkane factor η. This is achieved by reducing the alkanes heavier than ethane from the LNG (e.g. propane and butane).

- Potential explosive yield may be reduced by increasing the initial fraction of methane in the mixture. This should preferably be achieved by first removing components heavier than ethane, so as to not increase η.

The model is wholly dependent on the following two critical assumptions: That RPT triggering only occurs when passing a well defined Leidenfrost point and that the model Eq. (3) for the Leidenfrost point is accurate for mixtures. Both of these should be investigated more closely through film boiling experiments with alkane mixtures.

A significant shortcoming of the present model is its inability to predict the energy yield of single vapor-explosions. Since it is based on thermodynamics alone, it can only provide yields per a given amount. Predicting the amount of LNG participating in single events will require a different kind of model, likely involving fluid dynamics. A small scale experiment able to measure both explosive yield and the participating LNG amount per event would be extremely useful, not just for validating such a future model, but also for properly validating the present model's predictions for yield per mass. In general, more quantitative data on the consequence of cryogen RPT is sorely needed. The current available data is quite sparse.

Acknowledgements

This publication is based on results from the research project “Predicting the risk of rapid phase-transition events in LNG spills (Predict-RPT)”, performed under the MAROFF program. The authors acknowledge the Research Council of Norway (244076/O80) for support.

References

ABS Consulting, 2004. Consequence Assessment Methods for Incidents Involving Releases from Liquefied Natural Gas Carriers. Tech. Rep. GEMS 1288209, Report for the Federal Energy Regulatory Commission. URL. http://www.ferc.gov/industries/gas/indus-act/lng/cons-model/cons-model.pdf.

Alderman, J.A., 2005. Introduction to LNG safety. Process Saf. Prog. 24 (3), 144–151.

Aursand, P., Gjennestad, M., Aursand, E., Hammer, M., Wilhelmsen, Ø., 2017. The spinodal of single- and multi-component fluids and its role in the development of modern equations of state. Fluid Phase Equil. 436, 98–112.

Baumeister, K.J., Simon, F.F., 1973. Leidenfrost temperature– its correlation for liquid metals, cryogens, hydrocarbons, and water. (American Society of Mechanical Engineers, 1973.). ASME, Transactions, Series C- Journal of Heat Transfer 95, 166–173.

Benintendi, R., Rega, S., 2014. A unified thermodynamic framework for lng rapid phase transition on water. Chem. Eng. Res. Des. 92 (12), 3055–3071.

Berenson, P.J., 1961. Film-boiling heat transfer from a horizontal surface. J. Heat Tran. 83 (3), 351–356.

Bernardin, J.D., Mudawar, I., 1999. The Leidenfrost point: experimental study and assessment of existing models. J. Heat Tran. 121 (4), 894–903.

Berthoud, G., 2000. Vapor explosions. Annu. Rev. Fluid Mech. 32 (1), 573–611.

Bubbico, R., Salzano, E., 2009. Acoustic analysis of blast waves produced by rapid phase transition of LNG released on water. Saf. Sci. 47 (4), 515–521.

Cleaver, P., Humphreys, C., Gabillard, M., Nédelka, D., Heiersted, R., Dahlsveen, J., 1998. Rapid phase transition of LNG. In: 12th International Conference on Liquefied Natural Gas, LNG12. Perth, Australia.

Cleaver, P., Johnson, M., Ho, B., 2007. A summary of some experimental data on LNG safety. J. Hazard Mater. 140 (3), 429–438.

Enger, T., Hartman, D.E., Seymour, E.V., 1973. Explosive Boiling of Liquefied Hydrocarbon/Water Systems. Springer US, Boston, MA, pp. 32–41.

Fletcher, D.F., Theofanous, T.G., 1994. Recent progress in the understanding of steam explosions. J. Loss Prev. Process. Ind. 7 (6), 457–462.

Forte, K., Ruf, D., 2017. Safety challenges of LNG offshore industry and introduction to risk management. In: ASME 2017 36th International Conference on Ocean, Offshore and Arctic Engineering. American Society of Mechanical Engineers, V03BT02A016–V03BT02A016.

Gottfried, B.S., Bell, K.J., 1966. Film boiling of spheroidal droplets. leidenfrost phenomenon. Ind. Eng. Chem. Fundam. 5 (4), 561–568.

Havens, J., Spicer, T., 2007. United States regulations for siting LNG terminals: problems and potential. J. Hazard Mater. 140 (3), 439–443.

Hicks, E.P., Menzies, D.C., 1965. Theoretical studies on the fast reactor maximum accident. In: Proceedings of Conference on Safety, Fuels and Core Design in Large Fast Power Reactors (ANL–7120), pp. 654–670.

Hightower, M., Gritzo, L., Luketa-Hanlin, A., Covan, J., Tieszen, S., Wellman, G., Irwin, M., Kaneshige, M., Melof, B., Morrow, C., Ragland, D., 2004. Guidance on Risk Analysis and Safety Implications of a Large Liquified Natural Gas (LNG) Spill over Water. Tech. Rep. Sandia Report SAND2004–6258. Sandia National Laboratories, Albuquerque, New Mexico URL. http://prod.sandia.gov/techlib/access-control.cgi/2004/046258.pdf.

Hightower, M., Gritzo, L., Luketa-Hanlin, A., 2005. Safety implications of a large lng tanker spill over water. Process Saf. Prog. 24 (3), 168–174.

Jazayeri, B., 1977. Impact Cryogenic Vapor Explosions. MIT Master’s thesis.

Koopman, R., Ermak, D., 2007. Lessons learned from LNG safety research. J. Hazard Mater. 140, 412–428.

Kunz, O., Wagner, W., 2012. The GERG-2008 wide-range equation of state for natural gases and other mixtures: an expansion of GERG-2004. J. Chem. Eng. Data 57 (11), 3032–3091.

Linstrom, P.J., Mallard, W.G. (Eds.), 2017. NIST Chemistry WebBook, NIST Standard Reference Database Number 69. National Institute of Standards and Technology, Gaithersburg MD, 20899 URL. http://webbook.nist.gov.

Luketa-Hanlin, A., 2006. A review of large-scale LNG spills: experiments and modeling. J. Hazard Mater. 132, 119–140.

Melhem, G., Saraf, S., Ozog, H., 2006. LNG Properties and Hazards, Understanding LNG Rapid Phase Transitions (RPT). An ioMosaic Corporation Whitepaper.

Michelsen, M.L., Mollerup, J.M., 2007. Thermodynamic Models: Fundamentals and Computational Aspects, second ed. Tie-Line Publictions, Holte, Denmark.

Nagai, N., Nishio, S., 1996. Leidenfrost temperature on an extremely smooth surface. Exp. Therm. Fluid Sci. 12 (3), 373–379.

Nédelka, D., Sauter, V., Goanvic, J., Ohba, R., 2003. Last developments in rapid phase transition knowledge and modeling techniques. In: Offshore Technology Conference.

Peng, D.-Y., Robinson, D.B., 1976. A new two-constant equation of state. Ind. Eng. Chem. Fundam. 15 (1), 59–64.

Pitblado, R.M., Woodward, J.L., 2011. Highlights of LNG risk technology. J. Loss Prev. Process. Ind. 24 (6), 827–836.

Porteous, W.M., Reid, R.C., 1976. Light hydrocarbon vapor explosions. Chem. Eng. Prog. 72, 83–89 5.

Qiao, Y.M., Chandra, S., 1997. Experiments on adding a surfactant to water drops boiling on a hot surface. In: Proceedings of the Royal Society of London a: Mathematical, Physical and Engineering Sciences, vol. 453. The Royal Society, pp. 673–689.

Raj, P.K., Bowdoin, L.A., 2010. Underwater LNG release: does a pool form on the water surface? What are the characteristics of the vapor released? J. Loss Prev. Process. Ind. 23 (6), 753–761.

Reid, R.C., 1983. Rapid phase transitions from liquid to vapor. In: Advances in Chemical Engineering, vol. 12. pp. 105–208.

Sakurai, A., Shiotsu, M., Hata, K., 1990. Effects of system pressure on minimum film boiling temperature for various liquids. Exp. Therm. Fluid Sci. 3 (4), 450–457.

Shaw, S., Baik, J., Pitblado, R., 2005. Consequences of underwater releases of lng. Process Saf. Prog. 24 (3), 175–180.

Soave, G., 1972. Equilibrium constants from a modified Redlich–Kwong equation of state. Chem. Eng. Sci. 27 (6), 1197–1203.

Span, R., 2010. Multiparameter Equations of State: an Accurate Source of Thermodynamic Property Data. Springer-Verlag, Berlin.

Spiegler, P., Hopenfeld, J., Silberberg, M., Bumpus, C.F., Norman, A., 1963. Onset of stable film boiling and the foam limit. Int. J. Heat Mass Tran. 6 (11), 987–989.

2Valencia-Chavez, J.A., 1978. The Effect of Composition on the Boiling Rates of Liquefied Natural Gas for Confined Spills on Water. Ph.D. thesis. Massachusetts Institute of Technology.

Vesovic, V., 2007. The influence of ice formation on vaporization of LNG on water surfaces. J. Hazard Mater. 140 (3), 518–526.

Wilhelmsen, Ø., Aasen, A., Skaugen, G., Aursand, P., Austegard, A., Aursand, E., Gjennestad, M., Lund, H., Linga, G., Hammer, M., 2017. Thermodynamic modeling with equations of state: present challenges with established methods. Ind. Eng. Chem. Res. 56 (13), 3503–3515.

Yao, S.-C., Henry, R.E., 1978. An investigation of the minimum film boiling temperature on horizontal surfaces. J. Heat Tran. 100 (2), 260–267.

Paper E

Comparison of kinetic theory evaporation models for liquid thin-films

Eskil Aursand, Tor Ytrehus

Submitted to *International Journal of Multiphase Flow*.

Paper F

The spinodal of single- and multi-component fluids and its role in the development of modern equations of state

Peder Aursand, Magnus Gjennestad, Eskil Aursand, Morten Hammer, Øivind Wilhelmsen

Published in *Fluid Phase Equilibria*.
(2017) Vol. 436, pp. 98–112
https://doi.org/10.1016/j.fluid.2016.12.018

Fluid Phase Equilibria 436 (2017) 98–112

Contents lists available at ScienceDirect

Fluid Phase Equilibria

journal homepage: www.elsevier.com/locate/fluid

The spinodal of single- and multi-component fluids and its role in the development of modern equations of state

Peder Aursand [a], Magnus Aa. Gjennestad [a], Eskil Aursand [a, b], Morten Hammer [a], Øivind Wilhelmsen [a, c, *]

[a] SINTEF Energy Research, Sem Sælands vei 11, NO-7034 Trondheim, Norway
[b] NTNU, Department of Energy and Process Engineering, Kolbjørn Hejes vei 1B, NO-7491 Trondheim, Norway
[c] NTNU, Department of Electrical Engineering and Renewable Energy, Gunnerus Gate 1, NO-7491 Trondheim, Norway

ARTICLE INFO

Article history:
Received 24 October 2016
Received in revised form
7 December 2016
Accepted 19 December 2016
Available online 26 December 2016

Keywords:
Thermodynamics
Equation of state
Spinodal
Nucleation
Phase stability
Superheat limit

ABSTRACT

The spinodal represents the limit of thermodynamic stability of a homogeneous fluid. In this work, we present a robust methodology to obtain the spinodal of multicomponent fluids described even with the most sophisticated equations of state (EoS) available. We elaborate how information about the spinodal and its uncertainty can contribute both in the development of modern EoS and to estimate their uncertainty in the metastable regions. Inequality constraints are presented that can be exploited in the fitting of modern EoS of single-component fluids to avoid inadmissible pseudo-stable states between the vapor and liquid spinodals. We find that even cubic EoS violate some of these constraints.

With the use of a selection of EoS representative of modern applications, we compare vapor and liquid spinodal curves, superheat and supersaturation limits from classic nucleation theory (CNT), and available experimental data for the superheat limit. Computations are performed with pure species found in natural gas, binary mixtures, as well as a multi-component natural gas mixture in order to demonstrate the scalability of the approach. We demonstrate that there are large inconsistencies in predicted spinodals from a wide range of EoS such as cubic EoS, extended corresponding state EoS, SAFT and multiparameter EoS. The overall standard deviation in the prediction of the spinodal temperatures were 1.4 K and 2.7 K for single- and multi-component liquid-spinodals and 6.3 K and 26.9 K for single- and multi-component vapor spinodals.

The relationship between the measurable limit of superheat, or supersaturation, and the theoretical concept of the spinodal is discussed. While nucleation rates from CNT can deviate orders of magnitude from experiments, we find that the limit of superheat from experiments agree within 1.0 K and 2.4 K with predictions from CNT for single- and multi-component fluids respectively. We demonstrate that a large part of the metastable domain of the phase diagram is currently unavailable to experiments, in particular for metastable vapor. Novel techniques, experimental or with computational simulations, should be developed to characterize the thermodynamic properties in these regions, and to identify the thermodynamic states that define the spinodal.

1. Introduction

Metastable fluids can be found everywhere and continue to attract attention [1]. Recent examples include the ongoing discussion on cavitation of water at large negative pressures [2–6], magma erupting from volcanoes [7] and violent vapor-explosions from liquids spills in contact with a substantially warmer substance [8–11]. It is challenging to measure the properties of highly metastable fluids. By their own labile nature, they transform into a more stable phase via nucleation, where the nucleation process is triggered by thermal fluctuations. These fluctuations occur naturally, even in perfectly homogeneous fluids at equilibrium [12].

Properties of metastable fluids are central in the description of many processes. An important example is nucleation, which is ubiquitous in a wide range of physical, chemical, and biological processes. In nucleation theory, the thermodynamic state of the

* Corresponding author. SINTEF Energy Research, Sem Sælands vei 11, NO-7034 Trondheim, Norway.
E-mail address: oivind.wilhelmsen@ntnu.no (Ø. Wilhelmsen).

http://dx.doi.org/10.1016/j.fluid.2016.12.018

critical embryo is within the metastable region of the fluid [12]. Even for the simple case of condensation of the noble gas argon, predictions of nucleation rates from classical nucleation theory (CNT) deviate more than 20 orders of magnitude from experiments. In contrast, we will here show that CNT predicts accurately the "limit of superheat" for many hydrocarbons, which represents the experimentally available limit of metastability of liquids. Some of the deviation between several theories [13,14] and experimental data is likely because of inaccuracies in current equations of state (EoS) in the metastable regions [13].

In the development of modern multiparameter EoS, for example for water [15], the thermodynamic properties of metastable fluid phases such as subcooled liquid (metastable with respect to solid-liquid) and superheated liquid (metastable with respect to the vapor-liquid) are included in the fitting procedure. The extrema for metastability are defined by the spinodal. At the spinodal, the homogeneous fluid becomes intrinsically unstable and the activation barrier for nucleation disappears. The unstable fluid will then spontaneously decompose into the more stable phases. From a thermodynamic point of view, much is known about the state of the fluid at the spinodal. For instance, for single-component fluids, several thermodynamic properties such as the bulk modulus and the inverse isobaric heat capacity equal zero. Therefore, information about the spinodal is valuable, both in the development of modern EoS and to estimate their uncertainty in the metastable regions. Moreover, a thermodynamically consistent behavior of the EoS in the unstable domain of the homogeneous fluid is a prerequisite for combining them with mass based density functional theory for studying interfacial phenomena [16].

A major challenge in the study of metastable fluids is that there are limitations to how close to the spinodal one can get in experiments with real fluids. No matter how careful an experiment has been carried out, thermal fluctuations that occur naturally in the fluid will trigger homogeneous nucleation before the spinodal has been reached, even though the metastable domain extends significantly further. Highly metastable states that are experimentally unavailable for bulk fluids can still be encountered in small cavities, or within the critical cluster or cavity during nucleation, and are thus of practical relevance. The experimentally attainable limit where a superheated liquid spontaneously transforms into vapor is known as the *limit of superheat* [1]. The most popular experimental technique for measuring the limit of superheat is the droplet explosion method, a technique dating back to the early work of Wakeshima and Takata [17] and Moore [18]. The droplet explosion method remains the most popular technique to date [8,11], and represents one of the techniques that can bring the liquid closest to the spinodal [19]. We shall in this work discuss how close to the spinodal it is possible to get experimentally, and how to get even closer.

From a theoretical perspective, we shall elaborate how information about the spinodal and its uncertainty can contribute both in the development of modern EoS and to estimate their uncertainty in the metastable regions. With the use of a selection of EoS with varying degree of complexity, we predict the spinodal curves for pure species and mixtures. The predicted spinodals are compared to both the limit of superheated liquid and supersaturated vapor from CNT and available experimental data. The present paper extends previous work on the topic spanning the last three decades [9,20–24]. Whereas previous studies have focused on cubic EoS, where obtaining the spinodal curve is straightforward, we present a general and robust approach based on thermodynamic stability analysis. This allows us to calculate and compare spinodals from a number of EoS with very different functional forms and levels of complexity. Moreover, while previous works have focused mostly on pure species, we calculate spinodals for hydrocarbon mixtures with up to five components. We show that the functional form of the EoS can have a significant influence on the predicted spinodal.

2. Theory

In this section, we present the theoretical foundation for the work. We start in Sec. 2.1 by describing the different types of EoS that will be used. In Sec. 2.2, we discuss how the spinodal can be characterized, before we in Sec. 2.3 explain how to estimate the experimental limit of stability for a homogeneous fluid with classical nucleation theory.

2.1. Equations of state

2.1.1. Cubic EoS (PR, SRK)

The simplest type of EoS that can still predict the spinodal are the cubic EoS. These can in general be represented as

$$P = \frac{RT}{v-b} - \frac{a\alpha(T)}{(v-bm_1)(v-bm_2)}. \tag{1}$$

Here, P is the pressure, T is the temperature, R the universal gas constant, v the molar volume, and a, α, and b are parameters of the EoS. The constants m_1 and m_2 characterize various two-parameter cubic EoS. For instance, for the van der Waals (VdW) EoS, $m_1 = m_2 = 0$, for the Soave–Redlich–Kwong (SRK) EoS [25], $m_1 = 1$ and $m_2 = 0$, and for the Peng–Robinson (PR) EoS [26], $m_1 = -1 + \sqrt{2}$ and $m_2 = -1 - \sqrt{2}$. All these EoS are two-parameter cubic EoS in the sense that they use the two parameters a and b. For fluids with several components, mixing rules are used to compute the parameters a and b, which then depend on the composition.

2.1.2. Extended corresponding state EoS (SPUNG)

An extension of the corresponding state (CSP) methodology was initiated by Leach, Rowlinson and Watson as elaborated in Ref. [27], by including so-called "shape factors" that take into account how the mixture in consideration differs from the reference fluid(s). For pure components, this extension has a basis in statistical mechanics. If cubic EoS are used to calculate the shape factors, one may combine the strength of cubic EoS observed in VLE calculations with improved prediction of bulk properties obtained from a very accurate reference EoS. This methodology has also been referred to as the SPUNG EoS, and has proven to be both computationally fast as well as accurate [28]. We refer to Chapter 4 in Ref. [29] for further details.

2.1.3. Statistical associating fluid theory (SAFT)

Statistical Associating Fluid Theory (SAFT) gives EoS that are founded on statistical mechanics [30]. The perhaps most commonly used formulation is PC-SAFT [31] that has, in general, substantially improved accuracy in comparison with cubic EoS. Since PC-SAFT is founded on statistical mechanics and accounts for sizes and shapes of molecules, it is also expected to be the EoS with the largest predictive ability of the EoS considered in this work, in particular for polar substances and associating substances.

2.1.4. Multiparameter equations of state (GERG-2008)

Multiparameter EoS are today the most accurate EoS for the regions where thermodynamic property data are available. The EoS are founded on a comprehensive analysis of experimental data and a diligent optimization procedure, with functional forms optimized for accuracy. They have been devised for single-component fluids [15,32–36] and mixtures [37]. For some of these EoS, the thermodynamic properties of metastable fluid phases such as

supersaturated vapor and superheated liquid have been included in the fitting procedure [15]. In this work, we will use the multiparameter EoS for natural gas called GERG-2008 [37]. It is defined in terms of a reduced Helmholtz energy function:

$$\alpha(\rho,T,\boldsymbol{x}) = \alpha^0(\rho,T,\boldsymbol{x}) + \sum_{i=1}^{N_c} x_i \alpha_i^{\mathrm{r}}(\rho,T) + \Delta\alpha^{\mathrm{r}}(\rho,T,\boldsymbol{x}), \tag{2}$$

where the superscripts 0 and r refer to the ideal gas and the residual contributions respectively, subscript i refers to species i, N_c is the number of components, ρ is the density and x_i is the mole fraction of component i. The last term on the right-hand-side, $\Delta\alpha^{\mathrm{r}}$ is the departure function that takes into account the deviation from ideal mixture.

2.2. Thermodynamic stability and the spinodal

The spinodal represents the limit of intrinsic stability of a single-phase fluid. The spinodal is a theoretical limit, since thermal fluctuations will lead to homogeneous nucleation long before the spinodal has been reached in experiments, as explained in Sec. 1.

2.2.1. Thermodynamic stability in terms of the eigenvalues of the Hessian matrices of the energy state functions

Classical thermodynamics states that at equilibrium, the entropy of an isolated system is at its maximum. By considering an isolated composite system consisting of a subsystem that interacts with a thermal, pressure or particle reservoir, this criterion can be reformulated in terms of minima of various energy state functions for the subsystem [38]. The identity of the energy state function depends on the surroundings of the subsystem, or alternatively which state variables that have been fixed. Some examples are:

$$\min\{U(S,V,\mathbf{N})\} \quad \text{at fixed } S,V \text{ and } \mathbf{N} \tag{3}$$

$$\min\{A(T,V,\mathbf{N})\} \quad \text{at fixed } T,V \text{ and } \mathbf{N} \tag{4}$$

$$\min\{H(S,P,\mathbf{N})\} \quad \text{at fixed } S,P \text{ and } \mathbf{N} \tag{5}$$

$$\min\{G(T,P,\mathbf{N})\} \quad \text{at fixed } T,P \text{ and } \mathbf{N} \tag{6}$$

where U is the internal energy, A is the Helmholtz energy, H is the enthalpy, G is the Gibbs energy, S is the entropy, V is the total volume, and $\mathbf{N}$ is the mole numbers, where boldface symbols are vectors. In addition, in a single-component system, $U^* = U - N\mu$ is the Legendre transform of the internal energy with respect to the mole number, where μ is the chemical potential. Even if U^* is not commonly used in engineering applications, we shall refer to it in subsequent discussions. The energy state functions A, U^* and H are Legendre transforms of the internal energy with respect to one variable, while G is a Legendre transform of the internal energy with respect to two variables.

The thermodynamic stability of a stationary homogeneous system can be examined by evaluating the change in internal energy when decomposing into two phases, denoted with subscripts α and β (the initial system has no subscript). Let us start with an isolated system where U is a minimum at equilibrium, meaning that $\mathrm{d}U = \mathrm{d}(U_\alpha + U_\beta) = 0$, i.e. the system is in a *stationary* state. This condition implies uniform intensive variables: T, P and μ_i, where subscript i refers to component i (see Chapters 5 and 6 in Ref. [38]). However, a *stationary* state can be a minimum, maximum or saddle point. For the energy state function to be a minimum, the lowest order of non-vanishing variation must be positive. In most cases, this is the second order variation:

$$\mathrm{d}^2U = \mathrm{d}^2U_\alpha + \mathrm{d}^2U_\beta = \mathrm{d}\mathbf{x}_\alpha^T \ \nabla\nabla U_\alpha \ \mathrm{d}\mathbf{x}_\alpha + \mathrm{d}\mathbf{x}_\beta^T \ \nabla\nabla U_\beta \ \mathrm{d}\mathbf{x}_\beta \geq 0, \tag{7}$$

where $\mathrm{d}\mathbf{x}^T = [\mathrm{d}S, \mathrm{d}V, \mathrm{d}N_1, \ldots, \mathrm{d}N_{N_c}]$ represents an arbitrary change in the state variables and $\nabla\nabla U$ is the Hessian matrix of the internal energy, i.e. the matrix containing the second order partial derivatives of U with respect to the variables in $\mathbf{x}$. Since the system is isolated, $\mathrm{d}\mathbf{x}_\alpha = -\mathrm{d}\mathbf{x}_\beta$ and since the α and the β phases have uniform intensive variables, Eq. (7) can be reformulated as [39]:

$$\mathrm{d}\mathbf{x}^T \ \nabla\nabla U \ \mathrm{d}\mathbf{x} \geq 0, \tag{8}$$

where we have omitted subscript α and a scaling factor of N/N_β. Equation (8) can be rewritten in terms of the eigenvalues of $\nabla\nabla U$, λ_j:

$$\sum_{j=1}^{N_c+2} c_j^2 \lambda_j \geq 0, \tag{9}$$

where $\mathrm{d}\mathbf{x} = \sum_j^{N_c+2} c_j e_j$ and $e_1, \ldots, e_{N_c+2}$ are the eigenvectors of the Hessian matrix. Here, we have expressed the vector $\mathrm{d}\mathbf{x}$ in terms of the eigenvector-space of the Hessian matrix and the parameters, c_j, which can take any value. Since c_j^2 is always positive for any real number, the criterion for thermodynamic stability of an isolated system expressed by Eq. (7) can be reformulated as:

$$\min\{\mathrm{eig}(\nabla\nabla U)\} \geq 0, \tag{10}$$

i.e., the Hessian matrix of U should be positive-semidefinite. Legendre transforming the internal energy gives other energy state functions, and equivalent thermodynamic stability criteria can be formulated for these by following a similar approach as elaborated above:

$$\min\{\mathrm{eig}(\nabla_{V,\mathbf{N}}\nabla_{V,\mathbf{N}} \ A(T,V,\mathbf{N}))\} \geq 0 \quad \text{at fixed } T,V \text{ and } \mathbf{N} \tag{11}$$

$$\min\{\mathrm{eig}(\nabla_{S,\mathbf{N}}\nabla_{S,\mathbf{N}} \ H(S,P,\mathbf{N}))\} \geq 0 \quad \text{at fixed } S,P \text{ and } \mathbf{N} \tag{12}$$

$$\min\{\mathrm{eig}(\nabla_{\mathbf{N}}\nabla_{\mathbf{N}} \ G(T,P,\mathbf{N}))\} \geq 0 \quad \text{at fixed } T,P \text{ and } \mathbf{N} \tag{13}$$

where the subscripts indicate which variables are included in the del-operator, i.e. only the extensive variables of the respective potentials are included. In fact, at equilibrium, the Legendre transformed energy state functions are concave functions of their intensive canonical variables, and they are only a minimum if these variables are fixed [38] (see Eqs. (3)–(6)). The spinodal can thus be identified by investigating the eigenvalues of the Hessian matrices above. The criteria above are completely general, however, the typical textbook treatment defines an alternative way of identifying the spinodal in terms of a set of thermodynamic quantities that become zero at the spinodal. Since this method can give further insight, we shall discuss it next.

2.2.2. Thermodynamic stability in terms of selected thermodynamic derivatives

In conventional textbook literature on thermodynamic stability analysis, the approach outlined by Beegle et al. is often referred to [40], where the inner product between the Hessian matrices and $\mathrm{d}\mathbf{x}$ is examined in more detail. In particular, they show that some thermodynamic quantities go to zero before any other properties at the spinodal. In their textbook on classical thermodynamics, Tester and Modell state that a necessary and sufficient condition for thermodynamic stability is that [39]:

$$\frac{\partial^2 U^{(N_c)}}{\partial x_{N_c+1}\partial x_{N_c+1}} > 0, \tag{14}$$

where the superscript in $U^{(k)}$ denotes that the internal energy has been Legendre transformed with respect to the number k, of the first variables in the vector $\mathbf{x}^T = [S, V, N_1, \ldots, N_{N_c}]$. Moreover, x_l defines index l of the vector $\mathbf{x}$. The spinodal is then defined in terms of the following equation:

$$\frac{\partial^2 U^{(N_c)}}{\partial x_{N_c+1}\partial x_{N_c+1}} = 0. \tag{15}$$

However, the order of the variables in $\mathbf{x}$ can be chosen arbitrarily. Therefore, Eq. (15) results in several thermodynamic identities that equal zero at the spinodal. For a single-component system, these are:

$$\frac{\partial^2 A}{\partial x_k^2} : -\left(\frac{\partial P}{\partial V}\right)_{T,N} = 0 \quad \text{and} \quad \left(\frac{\partial \mu}{\partial N}\right)_{T,V} = 0 \tag{16}$$

$$\frac{\partial^2 U^*}{\partial x_k^2} : \left(\frac{\partial T}{\partial S}\right)_{\mu,V} = 0 \quad \text{and} \quad -\left(\frac{\partial P}{\partial V}\right)_{\mu,S} = 0 \tag{17}$$

$$\frac{\partial^2 H}{\partial x_k^2} : \left(\frac{\partial \mu}{\partial N}\right)_{P,S} = 0 \quad \text{and} \quad \left(\frac{\partial T}{\partial S}\right)_{P,N} = 0 \tag{18}$$

where Eq. (16) contains the diagonal entries of $\nabla_{V,N}\nabla_{V,N}$ A, Eq. (17) of $\nabla_{S,V}\nabla_{S,V}$ U^* and Eq. (18) of $\nabla_{S,N}\nabla_{S,N}$ H. All of these equations are satisfied simultaneously at the spinodal, where they change from positive to negative. An interesting question we shall discuss in Sec. 3.1 is whether the left-hand-side of Eqs. (16)–(18) should remain negative between the vapor and liquid spinodals. Such information is useful in the development of modern EoS, because if one can argue that thermodynamic quantities such as those defined in Eqs. (16)–(18) should remain negative, they can be exploited as inequality constraints in the fitting of single-component EoS to avoid inadmissible pseudo-stable states between the vapor and liquid spinodals. Any of the thermodynamic quantities in Eqs. (16)–(18) can be used equivalently to locate the spinodal of a single-component fluid.

2.2.3. The numerical algorithm used to identify the spinodal in this work

The Hessian matrices of all the energy state functions are singular, i.e. one of their eigenvalues is always zero. The reason for this is that the energy state functions are Euler homogeneous functions of first degree with respect to their extensive variables, while the Hessian matrices contain derivatives of only intensive variables (see Theorem 4, Chapter 1 in Ref. [41]). In practice, the spinodal can be found by eliminating one row and one column of the Hessian matrix of an appropriate energy state function to construct the matrix Φ. In the stable domain, Φ is non-singular, and the smallest eigenvalue becomes 0 at the spinodal (see Theorem 6, Chapter 1 in Ref. [41]). In this work, we have used the following criterion to identify the spinodal:

$$\min\{\mathrm{eig}(\Phi)\} = 0 \quad \text{where} \quad \Phi = \nabla_{\mathbf{N}}\nabla_{\mathbf{N}} A(T, V, \mathbf{N}). \tag{19}$$

The use of the Helmholtz energy formulation has proven numerically robust when solving for critical points [42]. Applying the Hessian scaling suggested by Michelsen [43], the spinodal is found by solving for the temperature at a given specific volume. A second-order method that uses numerical differentials for the minimum eigenvalue, $\lambda_{\min}$ is used. The eigenvalue calculation of a symmetric matrix can be performed with high numerical efficiency. With a given initial point on the spinodal, the entire spinodal curve can easily be traversed with the use of uniform steps in $\ln(V)$. Extrapolation from a known spinodal point can be achieved by utilizing:

$$\mathrm{d}\lambda_{\min} = \left(\frac{\partial \lambda_{\min}}{\partial T}\right)_V \mathrm{d}T + \left(\frac{\partial \lambda_{\min}}{\partial V}\right)_T \mathrm{d}V = 0, \tag{20}$$

which provides a good initial value for the temperature at the next spinodal point.

2.3. The experimentally available limit of stability of a homogeneous fluid as predicted by classical nucleation theory (CNT)

When a liquid has been sufficiently superheated, the homogeneous nucleation rate becomes at some point so large that the liquid transforms into two phases in a much shorter time than the characteristic time of the experiment. This corresponds to the observed superheat limit, and nucleation theory can thus be used to predict this.

Nucleation is an activated process where an energy barrier must be overcome by thermal fluctuations. Accordingly, the nucleation rate J depends exponentially on the height of the nucleation barrier according to a standard Arrhenius rate law,

$$J = K\exp\left(-\frac{\Delta G^*}{k_B T}\right), \tag{21}$$

where ΔG^* is the nucleation barrier, k_B is Boltzmann's constant, and K is the kinetic prefactor. Equation (21) can be used both to describe the formation of bubbles and droplets; however, the expression for K and ΔG^* differ in the two cases. The nucleation barrier, ΔG^*, is:

$$\Delta G^* = \frac{4\pi\sigma r^{*2}}{3}, \tag{22}$$

where the radius of the critical cluster or cavity r^*, for bubble formation in a liquid [1], is

$$r^* = \frac{2\sigma}{P_{\mathrm{sat}}(T) - P_{\mathrm{l}}}, \tag{23}$$

or for droplet formation in a gas [1],

$$r^* = \frac{2\sigma}{\tilde{\rho}_{\mathrm{l}} k_B T \ln(P_{\mathrm{g}}/P_{\mathrm{sat}})}, \tag{24}$$

where $\tilde{\rho}_{\mathrm{l}}$ is the number density of the liquid phase. Further, the kinetic prefactors can be approximated by following a range of approaches. In this work, we have used the following expressions to calculate the kinetic prefactor for bubble formation in a liquid [1]:

$$K \approx \tilde{\rho}_{\mathrm{l}} \sqrt{\frac{2\sigma}{\pi m}}, \tag{25}$$

where $\tilde{\rho}_{\mathrm{l}}$ is the number density of the liquid phase and m is the mass of one molecule. For droplet formation in a gas, we have used [1]:

$$K \approx \frac{\tilde{\rho}_{\mathrm{g}}^2}{\tilde{\rho}_{\mathrm{l}}} \sqrt{\frac{2\sigma}{\pi m}}, \tag{26}$$

where $\tilde{\rho}_{\mathrm{g}}$ is the number density of the vapor-phase, i.e. Eqs. (25) and (26) differ by the factor $(\tilde{\rho}_{\mathrm{g}}/\tilde{\rho}_{\mathrm{l}})^2$. We have in this work provided only

the necessary formulas, and we refer to Refs. [1,44] for details and derivations. Once the nucleation barrier has been found and the kinetic prefactors have been estimated based on properties at saturation, the nucleation rate can be calculated by use of Eq. (21). However, to set a specific limit of superheat or supersaturation, one must decide on a *critical* nucleation rate that represents the observed sudden phase change. Experiments indicate values of J_{crit} in the range $10^2 - 10^6$ cm^{-3} s^{-1} [1]. Since the exact value of the critical nucleation rate has very little influence on the predicted limit of superheat (See Fig. 3.13 in Ref. [1]) we use $J_{\text{crit}} = 10^6$ cm^{-3} s^{-1} in this work.

Given a value for J_{crit}, we find the superheat/supersaturation temperature limits for a given pressure and composition by solving

$$J(T) = J_{\text{crit}}, \tag{27}$$

for T. In order to complete this model, thermodynamic properties are needed. The pressures and densities are supplied by an EoS, and in this work we have used the most accurate EoS for the components in natural gas, GERG2008 [37]. Pure component surface tensions were modeled by the corresponding state correlation recommended in Ref. [45] (see Chapter 12). The deviation between this correlation and experiments is below 5% for most fluids according to Tables 12–1 in Ref. [45]. The procedure for finding the limits of superheat/supersaturation is described above for pure components. We extend it to mixtures by replacing the saturation properties by the properties at the bubble line (superheat limit) or at the dew line (subcool limit) of the mixture. The molecule mass m is then replaced by the mole fraction averaged molecule mass. Also, we use the mole fraction weighted average of the pure component surface tensions.

3. Results

We shall in Secs. 3.1 and 3.2 discuss the vapor and liquid spinodals from a theoretical perspective and their relevance in the development of EoS. Next, we evaluate in Sec. 3.3 how much the spinodals predicted from various EoS differ, and the implications of this on prediction of properties in the metastable regions. Eventually, we discuss in Sec. 3.4 how close to the spinodal that current experiments can bring us. In the following, we will focus on hydrocarbons and their mixtures.

3.1. The spinodals and their relevance for developing EoS

Properties of metastable fluids have received much attention in recent literature, partly because such states are ubiquitous in nature, including in important processes such as nucleation of droplets or bubbles in condensation and evaporation processes. It is therefore important to develop EoS that give an accurate representation of the metastable regions of the fluid.

Fig. 1a shows the pressure as a function of the density for methane at $T = 175$ K, as predicted by the Peng–Robinson cubic EoS. The figure highlights five regimes, one regime with single-phase gas at low densities (green solid line), one regime with single-phase liquid at high densities (blue solid line), two regimes where the single-phase fluid is metastable (dashed lines) and one regime where it is unstable (dotted line). If the inequality, $(\partial P/\partial \rho) < 0$, is satisfied where ρ is the density (equivalent to Eq. (16)-left), the single-phase fluid is mechanically unstable and will spontaneously decompose into liquid and vapor.

The shape of the pressure, P plotted as a function of the density, ρ displayed in Fig. 1a with a local maximum followed by a local minimum is called a Maxwell loop. Many EoS have a single Maxwell loop, but some EoS have a second, artificial Maxwell loop in the two-phase region. One example is shown in Fig. 1b, where GERG2008 (blue solid line) exhibits a second loop. Since $(\partial P/\partial \rho) > 0$ (mechanically stable) and also other thermodynamic stability criteria are satisfied, the EoS predicts a pseudo-stable single-phase fluid within a region where experiments show a coexistence between vapor and liquid. For many fluids and conditions, the pseudo-stable phase has even a lower energy than the vapor-liquid coexistence [16]. The second Maxwell loop is an artifact of the functional form and parameters of the GERG2008 EoS, and is a general problem/challenge in the present development of multiparameter EoS.

Fig. 1b shows the behavior of several EoS in the metastable and unstable regions, and elucidates some important points:

- The exact location of the spinodals (the maxima and minima) varies much with the choice of EoS.
- The EoS have different behaviors between the spinodals; some EoS exhibit a thermodynamically consistent behavior (a single Maxwell loop), while other EoS do not.
- The behavior of the metastable regions depends much on the choice of EoS.

A goal should be to develop EoS that are accurate and thermodynamically consistent, also in the metastable and unstable regions of the phase diagram of the single-phase fluid. A future goal should be to develop EoS without inadmissible pseudo-stable states in the unstable domain of the single-phase fluid. This is of importance, both for combining them with mass based density functional theory and to develop thermodynamically consistent mixing rules with a physical interpretation as elaborated in detail in Ref. [16].

Fig. 1b shows that GERG2008 and PC-SAFT follow each other closely in the first part of the metastable regions. This is expected, as their Taylor-expansions of the pressure as a function of density about the saturation state are very similar, because they both reproduce well the thermodynamic properties at saturation from experiments. Therefore, accurate prediction of equilibrium properties at the saturation curve is a prerequisite for accurately predicting properties in the metastable regions. However, the figure also shows that GERG2008 and PC-SAFT predict very different pressures for the onset of the liquid-spinodal (the minima of the curves). Since equilibrium measurements at saturation can provide the right slope of, for instance P as a function of ρ into the metastable regions, the location of the spinodal would provide a reference for this extrapolation. Therefore, if it was possible to find the precise onset of the spinodal, either through experiments or computations, it would be possible to characterize the whole metastable region with good accuracy. Moreover, if the spinodal could be determined to some degree of uncertainty it would be possible, based on the known uncertainty of properties at coexistence, to make statements about how accurate extrapolations to the metastable regions from various EoS are. We shall discuss the current uncertainty in the prediction of the liquid and vapor spinodals in Sec. 3.3.

One of the more urgent challenges in the development of EoS is to remove the second artificial Maxwell loop in the two-phase region, an artifact characteristic for so-called multiparameter EoS (see Sec. 2.1.4). Multiparameter EoS are founded on a comprehensive analysis of experimental data and a diligent optimization procedure, with functional forms optimized for accuracy. By adding new terms to the Helmholtz energy functional of multiparameter EoS and with the use of additional constraints in the nonlinear fitting routine, Lemmon and Jacobsen managed to reduce the magnitude of the second Maxwell loop in the multiparameter EoS for the fluid R125 [46] from $\sim 10^6$ MPa to below $\sim 10^2$ MPa. In 2009, Lemmon et al. presented a multiparameter EoS for propane,

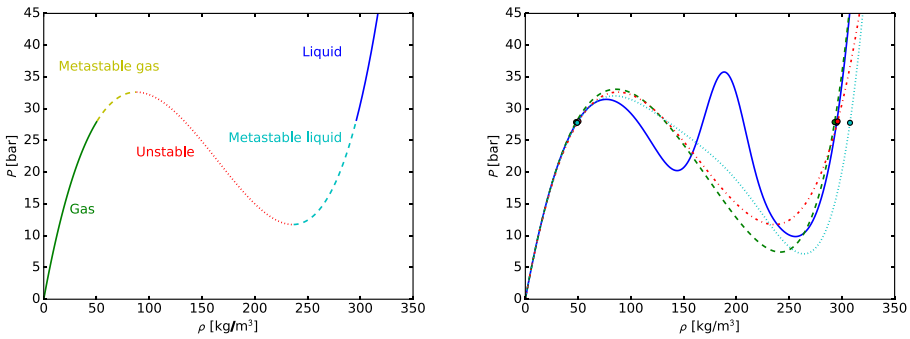

Fig. 1. Pure methane isotherms at 175 K. (a), the stable, metastable and unstable regions are illustrated by an isotherm as predicted by the PR EoS. (b), isotherms are drawn with different EoS: GERG2008 (solid blue), PC-SAFT (dashed green), PR (dash-dot red) and extended CSP (dotted cyan). The saturation points are indicated by circles. (For interpretation of the references to colour in this figure legend, the reader is referred to the web version of this article.)

where they reverted back to the functional form with Gaussian bell shaped terms [47]. With the use of the new fitting techniques and constraints from Ref. [46], they were able to reduce the magnitude of the artificial Maxwell loop. Recent multiparameter EoS are formulated with the functional form presented in Ref. [47]. Lemmon and Jacobsen implemented the constraint discussed by Elhassan et al. [48]:

$$a(\rho) - a_{\text{tang}}(\rho) \geq 0 \tag{28}$$

where a is the Helmholtz energy and subscript tang means the Helmholtz energy evaluated at the equilibrium tangent line. Despite what Elhassan and coauthors claim in their work [48], the constraint in Eq. (28) does not "remove any inconsistencies between thermodynamic stability and physical reality". Even if Eq. (28) guarantees that both the Helmholtz energy and the Gibbs energy of the vapor-liquid coexistence state is lower than the Gibbs energy of a pseudo-stable state coming from a second Maxwell loop [48], the pseudo-stable state can still be stable in other ensembles such as in an isolated system. We have elaborated in detail on this in Ref. [16].

3.2. Inequality constraints to avoid inadmissible pseudo-stable states between the spinodals

Since the inequality in Eq. (28) is insufficient for constraining EoS to avoid inadmissible pseudo-stable states in the unstable-region of the single-phase fluid (between the spinodals), we shall next discuss which inequality constraints that can be used instead. The derivatives in Eqs. (16–18) are natural candidates for such inequality constraints for the single-component fluid, since they reach zero before any other thermodynamic identities at the spinodals. We note that similar thermodynamic quantities can be defined for multicomponent fluids [39], and exploited in the fitting of multiparameter EoS for mixtures, such as GERG2008. We shall now evaluate Eqs. (16–18) for an EoS that is considered, from a qualitative perspective, to have a physically admissible behavior in the two-phase region: the Van der Waals cubic (VdW) EoS.

Fig. 2 plots Eqs. (16–18) for methane at 92 K through the metastable and unstable regions of the single-phase fluid, as predicted by the VdW EoS. The figure shows that all six of the thermodynamic quantities in Eqs. (16–18) reach zero at exactly the same two densities ($\rho = 32$ kg/m^3 and $\rho = 251$ kg/m^3), as shown by the vertical red dashed lines. These two densities define the vapor and liquid spinodals. At constant temperature, these are the only two densities where the thermodynamic quantities in Eqs. (16–18) equal zero.

If we examine the sign of the thermodynamic relations in Eqs. (16) and (18), only four of them remain negative between the vapor and liquid spinodals (vertical red dashed lines). The two thermodynamic relations that represent the diagonal entries of the Hessian matrix of the enthalpy, $(\partial\mu/\partial N)_{P,S}$ and $(\partial T/\partial S)_{P,N}$ shown in Figs. 2e and f, have asymptotes at densities just after the vapor spinodal and right before the liquid spinodal, and are positive in a region between the asymptotes. One of these thermodynamic relations has a clear physical interpretation:

$$\left(\frac{\partial T}{\partial S}\right)_{P,N} = \frac{T}{N\left(C_p^0 + C_p^{\text{r}}\right)}, \tag{29}$$

where the isobaric heat capacity, C_p, is split into an ideal gas contribution (superscript 0) and a residual contribution (superscript r). While C_p^{r} goes to $\pm\infty$ at the spinodals, C_p^0 is positive and depends only on the temperature. It is thus constant in Figs. 2 and 3. While $C_p^0(T)$ can be determined experimentally and is well-known for methane, $C_p^{\text{r}}(T,\rho)$ is unknown between the spinodals. The asymptotes of Eq. (29) correspond to the points where

$$C_p^{\text{r}}(T,\rho) = -C_p^0(T), \tag{30}$$

which can occur only between the spinodals. Interestingly, whether Eq. (30) is satisfied between the spinodals depends on which parameters that are used in the VdW EoS, and at which temperature the EoS is used. For instance, for methane at 92 K, Eq. (30) is clearly satisfied at two densities (see the asymptotes in Figs. 2e and f). However, for methane at 157 K, the same EoS predicts that $C_p^{\text{r}}(T,\rho) < -C_p^0(T)$ for all densities between the spinodals, where both of the thermodynamic relations in Eq. (18) remain negative between the spinodals, as shown in Fig. 3.

We shall next discuss if there are any physical arguments for why the thermodynamic quantities in Eqs. (16–18) should remain negative between the spinodals. To examine thermodynamic stability, we evaluate the sign of the eigenvalues of the Hessian matrices, since they define whether a stationary point of the energy state function is a minimum (only positive eigenvalues), a

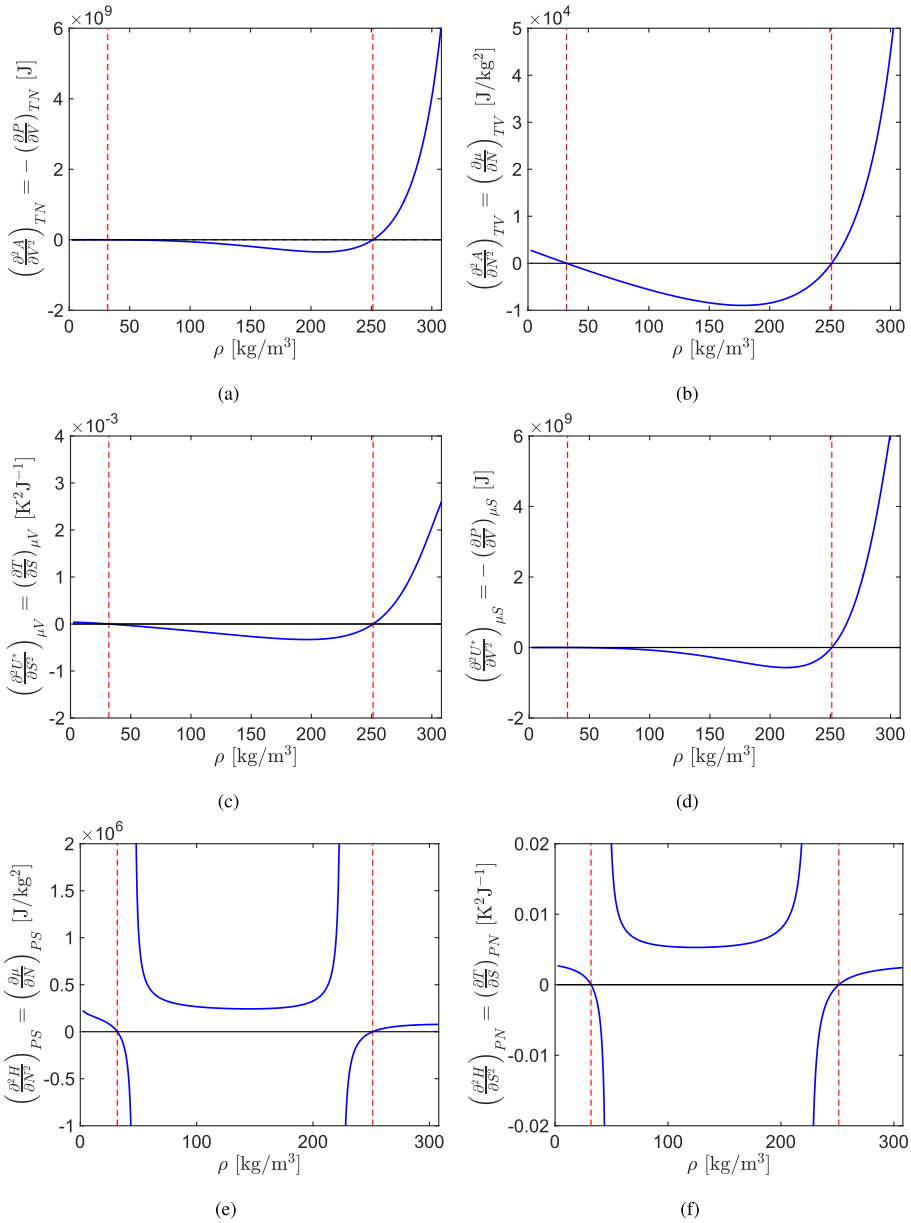

Fig. 2. A plot of Eqs. (16–18) through the two-phase region in the case of methane at 92 K as predicted by the Van der Waals cubic EoS (blue solid lines). The vertical red dashed lines show where the quantities pass through zero. The reported values are for 1 kmol of fluid. (For interpretation of the references to colour in this figure legend, the reader is referred to the web version of this article.)

maximum (only negative eigenvalues) or a saddle point (positive and negative eigenvalues).

First, let us discuss the rank of Hessian matrices and hence how many non-zero eigenvalues we expect. Since the energy state functions are Euler homogeneous functions of first degree in their extensive variables, the highest possible rank of their Hessian matrices is $r - 1$, where r is the number of extensive variables (we refer to Sec. 1.3 in Ref. [41] for details). Thus, for all the Hessian matrices, we expect at least one eigenvalue to be zero since they are singular [41]. For a single-component fluid, this gives a maximum

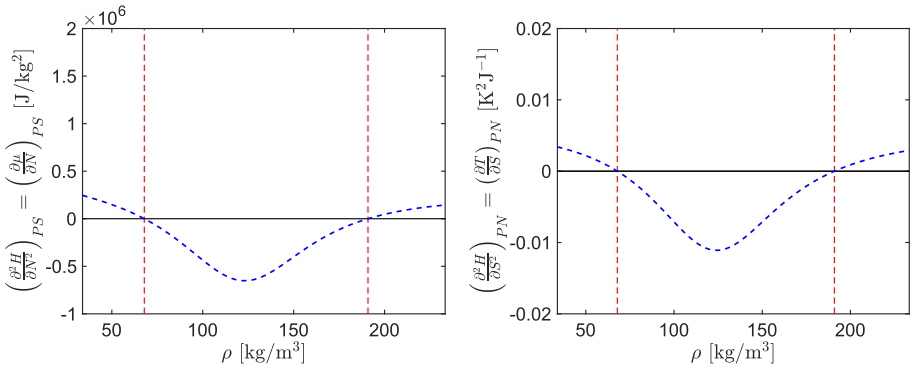

Fig. 3. A plot of two of the thermodynamic relations in Eq (18) through the two-phase region in the case of methane at 157 K as predicted by the VdW EoS (blue dashed lines). The vertical red dashed lines show where the quantities pass through zero. The reported values are for 1 kmol^3 of fluid. (For interpretation of the references to colour in this figure legend, the reader is referred to the web version of this article.)

of two non-zero eigenvalues for U and one non-zero eigenvalue for U^*, H and A. We have plotted the non-zero eigenvalues in Fig. 4 for methane, as described by the VdW EoS at 92 K (solid lines). In the figure, the eigenvalues have been divided by the eigenvalue of the liquid phase at saturation, and the subscripts refer to which energy state function the eigenvalues come from.

Fig. 4 shows that except for one of the eigenvalues of the Hessian matrix of U, $\lambda_{U,1}$, all eigenvalues go from positive to negative at the spinodals. This means that the internal energy goes from being a *local* minimum to a saddle point at the spinodals (one positive and one negative eigenvalue), while U^*, H and A go from local minima to maxima at the spinodals. Except for the eigenvalue of the Hessian matrix of the enthalpy displayed in Fig. 4c, the eigenvalues look very similar at 157 K and have not been plotted.

The asymptotes in the diagonal elements of the Hessian matrix of H at 92 K displayed in Fig. 2e and f are also reflected in asymptotes at the same densities in λ_H. In fact, Fig. 4c shows that the eigenvalue of $\nabla_{S,N}\nabla_{S,N}$ H goes from negative to positive in a region between the spinodals. When the asymptotes in the diagonal elements of the Hessian matrix of H disappear, such as at 157 K (see Fig. 3), then λ_H remains negative between the spinodals, similar to $\lambda_{U,2}$, λ_{U^*} and λ_A, as shown by the blue dashed lines in Fig. 4d.

Since all eigenvalues of the Hessian matrix of the enthalpy are non-negative in a region between the spinodals, the energy state function is a minimum. The VdW EoS thus predicts a uniform phase between the spinodals to be "pseudo-stable" in an adiabatic system kept at constant pressure, since the enthalpy is then the appropriate energy state function to examine.

In a macroscopic, single-phase system of arbitrary size, the thermodynamic stability of a sub-volume within the fluid should be independent of the choice of surroundings. Moreover, a pseudo-stable phase has never been observed experimentally between the spinodals, regardless of which experimental conditions that have been chosen. Therefore, the positive value of λ_H between the spinodals is an artifact of the VdW EoS and its parameters. We find a similar behavior of other cubic EoS, such as SRK and PR, where λ_H becomes positive between the spinodals at low temperatures. This is surprising, as its shows that even cubic EoS that have been considered to have a "physically admissible" behavior between the spinodals exhibit inconsistencies in the unstable domain of the single-phase fluid. To summarize: If one can find a state between the spinodals where, for any choice of energy state function, all eigenvalues of the Hessian are positive (one eigenvalue is always zero), one has found a pseudo-stable phase in that region. On the contrary, if at least one eigenvalue stays negative, such states are thermodynamically unstable. Thus, if we assume that such states are physically inadmissible, we arrive at the following statement:

> A sufficient condition for EoS to avoid inadmissible pseudo-stable states between the vapor and liquid spinodals is that at least one eigenvalue of the Hessian of the energy state function goes from positive to negative at, and remains negative between, the spinodals, for any choice of energy state function.

Fig. 2 shows that even if the EoS exhibits a physically admissible behavior for many of the state functions, this does not guarantee a physically admissible behavior for all energy state functions, unlike what is suggested in the work by Elhassan and coauthors [48]. We can also make some statements about the suitability of using Eqs. (16–18) as inequality constraints in fitting an EoS for a single-component fluid (similar statements can be made about multi-component fluids).

We know the following about the Hessian matrices of the energy state functions: They are singular, meaning that one of the eigenvalues is always zero and they are symmetric. Since the sum of the eigenvalues of a matrix equals the sum of the diagonal elements, one can prove mathematically that the two thermodynamic quantities in each of Eqs. (16–18) will always have the same sign for a single-component fluid. Therefore, it is only necessary to use one thermodynamic relation in each of the pairs in Eqs. (16–18) as an inequality constraint between the spinodals, where they have to be negative for a physically admissible behavior in the unstable region of the single-component fluid.

3.3. The spinodals and the limit of homogeneous nucleation

In Sec. 3.1 we argue that it is important to determine the spinodal precisely to arrive at EoS that are accurate in the metastable domain. In what follows, we investigate to which extent the EoS that are available today differ in their predictions of the spinodal.

Solving phase equilibrium calculations has received much attention in the literature. This can be challenging, in particular for multicomponent mixtures and multiparameter EoS [49]. Determining the spinodal has a comparable degree of complexity to phase equilibrium calculations, where a set of algebraic equations have to be solved based on the underlying EoS. However, robust

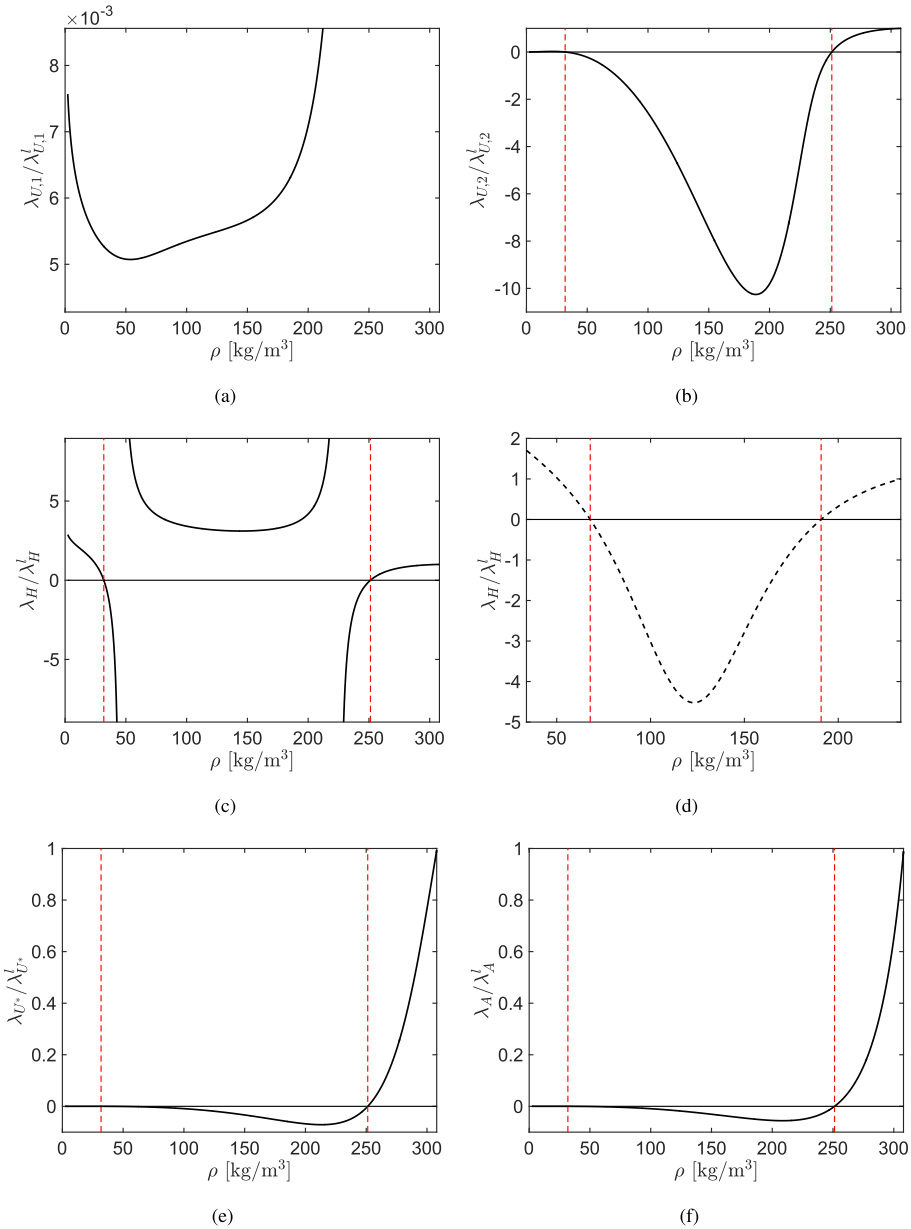

Fig. 4. A plot of the normalized eigenvalues of the energy state functions through the two-phase region in the case of methane at 92 K as predicted by the Van der Waals cubic EoS (black solid lines). The dashed line represents the eigenvalue the Hessian matrix of the enthalpy at 157 K. The vertical red dashed lines show where the quantities pass through zero. (For interpretation of the references to colour in this figure legend, the reader is referred to the web version of this article.)

and accurate methods for obtaining the spinodal have received far less attention in the literature than phase equilibrium calculations, partly due to the spinodal being less needed in engineering calculations. Previous work on the topic has mainly been limited to simple cubic EoS and pure substances [9,20–24].

In Fig. 5 we have used the methodology described in Sec. 2.2.3 to obtain the spinodal curve of a multicomponent natural gas mixture with one of the most accurate EoS available today, GERG2008 [50].

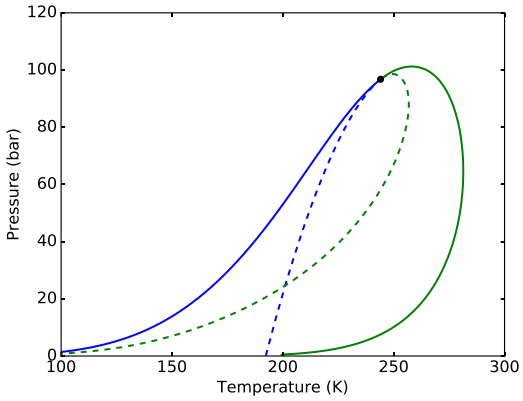

Fig. 5. Illustration of the phase envelope and spinodal curves obtained with the GERG2008 EoS for a five-component mixture of methane (75 mol-%), ethane (10 mol-%), propane (7 mol-%), butane (3 mol-%) and nitrogen (5 mol-%). The bubble line (solid blue), the dew line (solid green), the liquid spinodal (dashed blue) and the gas spinodal (dashed green) all meet in the critical point (black dot). (For interpretation of the references to colour in this figure legend, the reader is referred to the web version of this article.)

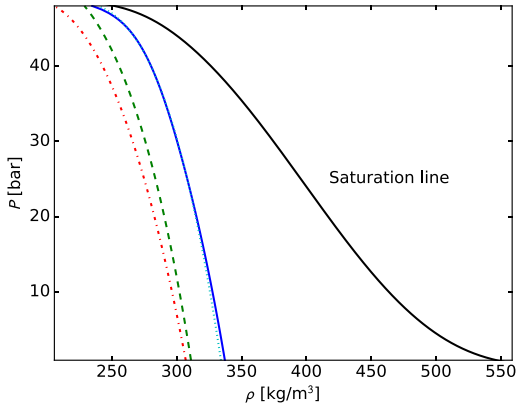

Fig. 6. The liquid density and pressure at the liquid spinodal curve for ethane, calculated using GERG2008 (solid blue), PC-SAFT (dashed green), PR (dash-dot red) and extended CSP (dotted cyan). The saturation line is given by the solid black line. (For interpretation of the references to colour in this figure legend, the reader is referred to the web version of this article.)

The figure demonstrates that the method we have presented is robust, even in the vicinity of the critical point, scalable to multi-component mixtures and applicable to complex non-analytical EoS. We observe, from a comparison of the solid and the dashed lines in Fig. 5, that there is a significant distance in the *TP* -space between the coexistence limits (solid lines) and the spinodal curves (dashed lines).

In what follows, we discuss the predicted spinodal for hydrocarbons with a selection of EoS representative of what is used in modern applications. Herein, we mainly focus on the pressure and temperature. In this discussion it is however crucial to recognize that the liquid density can change dramatically within the metastable region, even though it might only span a few degrees kelvin. An illustrative example of this is given in Fig. 6, showing the density and pressure of the liquid spinodal of ethane compared to the saturation line. At low pressures, the liquid density of the metastable fluid near the spinodal curve can be half of that at the saturation curve. Moreover, the difference in liquid density at the spinodal for different EoS can also be significant.

Fig. 7 shows the spinodal curve in the *TP* -space compared to the corresponding homogeneous nucleation limit and available experimental data for the limit of superheat for a selection of pure species. For all three substances considered here, there is a clear agreement between the limit of superheat predicted by nucleation theory and experimental data obtained from the droplet explosion method. Table 1 shows the absolute average deviation (AAD) of the experimental data points relative to the limit of superheat from classic nucleation theory for pure components and binary mixtures. The overall AAD between the predictions from CNT and the experimental measurements for the limit of superheat is only 1.0 K for pure species and 2.4 K for mixtures. Thus, even though CNT does not accurately predict the exact nucleation rates of fluids [1], it accurately reproduces the superheat limit.

The gap between the limit of superheat predicted by CNT and the liquid spinodal curve thus accurately represents the experimentally unobtainable part of the metastable region, caused by thermal fluctuations in the liquid. Overall, the liquid spinodal curves predicted using GERG2008, PC-SAFT, PR, and CSP agree within 2–3 K in the range from atmospheric to critical pressure. A notable exception is the liquid and vapor spinodals for n-pentane calculated using the PC-SAFT EoS (Fig. 7b). Here, a significant inaccuracy in the predicted critical point seems to offset the entire liquid spinodal curve by 5–10 K. This suggests that it is imperative for the EoS to reproduce the critical point of the fluid to provide reliable predictions of the spinodal. Note that while the CNT predictions depend on an estimated liquid density, surface tension, as well as the value of J_{crit}, a sensitivity analysis showed that the predicted limit of superheat matched experimental data for reasonable perturbations of ρ and σ, and for J_{crit} differing by orders of magnitude.

For the vapor spinodal there is a significantly larger span in the predicted spinodal curves from the four EoS than for the liquid spinodal. In particular, at a pressure of 0.9 bar, the difference in the vapor spinodal ranges from 42.4–85.1 K for methane, 135.5–213.6 K for n–pentane and 32.6–59.7 K for nitrogen. Table 2 shows the pressure-averaged standard deviation (with regard to EoS) in kelvin for a number of light hydrocarbons and nitrogen. The spread in predictions is higher for the vapor spinodal than the liquid spinodal, with an average standard deviation of 6.29 K for the former.

Fig. 8 shows the binary mixture liquid and vapor spinodal temperature at atmospheric pressure for the GERG2008, PC-SAFT, PR and extended CSP EoS, as a function of the second component mole fraction. The spinodal curves are compared to the bubble and dew lines, the superheat and supersaturation limits predicted by CNT, as well as available experimental data for the limit of superheat. Again, there is a good agreement between liquid superheat limit obtained in droplet explosion experiments and the limit predicted by classic nucleation theory. The predicted liquid spinodals mostly agree within 5 K. Moreover, the results indicate that for these species, a mole-weighted average of pure specie spinodal can provide an accurate estimate of the mixture spinodal.

The binary mixture vapor spinodals (Fig. 8, right) demonstrates a larger internal spread than what is the case for the liquid spinodal curves. Specifically, for an even mixture, the vapor spinodal temperature ranges from 85.9–154.7 K for ethane/propane, 108.9–177.0 K for propane/n–butane and 154.4–227.3 K for n–pentane/n–hexane. This behavior is consistent with what was

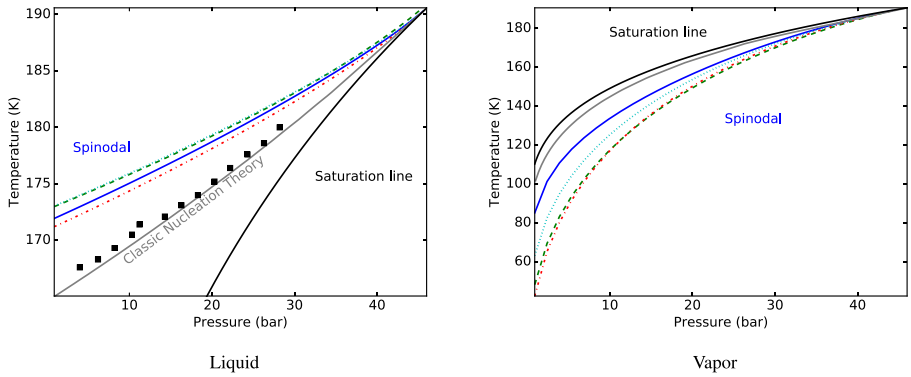

(a) Methane

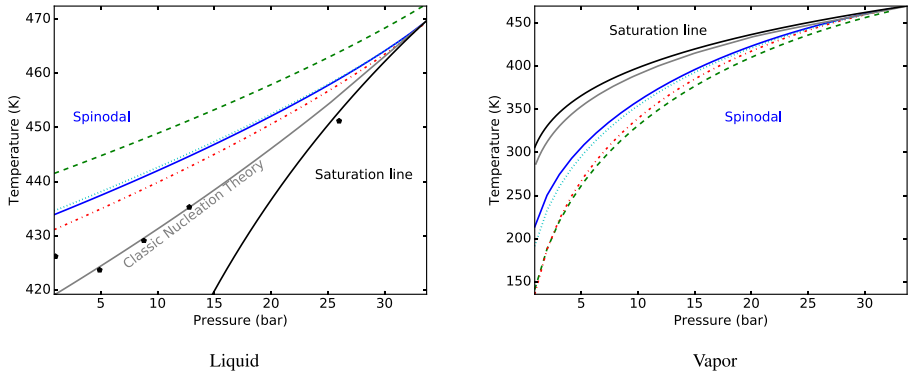

(b) n-Pentane

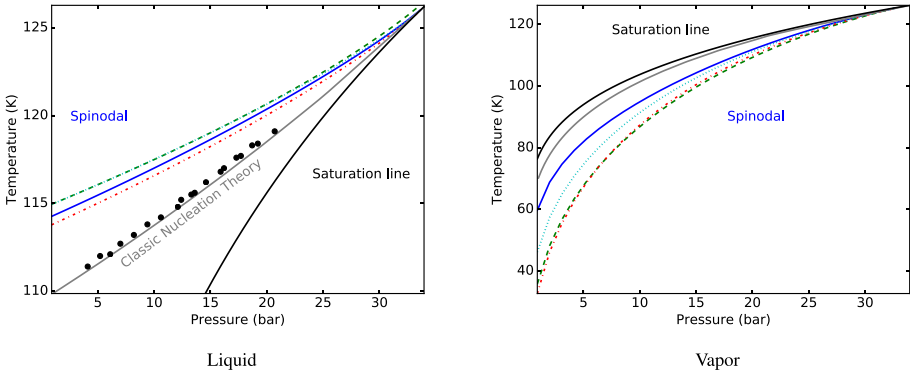

(c) Nitrogen

Fig. 7. Comparison of pure-component spinodal curves (liquid and vapor), superheat and subcool limits predicted using CNT (solid gray) and saturation line (solid black). The saturation lines are calculated with GERG2008. Spinodal curves are shown for four different EoS: GERG2008 (solid blue), PC-SAFT (dashed green), PR (dash-dot red) and extended CSP (dotted cyan). Experimental data from various studies of the limit of superheat are also shown: methane by Baidakov and Skripov [51] (squares), n-pentane compiled by Avedisian [8] (pentagons), nitrogen by Baidakov and Skripov [51] (circles). (For interpretation of the references to colour in this figure legend, the reader is referred to the web version of this article.)

Table 1
The average absolute deviation (AAD) in the temperature for the experimental data for the limit of superheat compared to classic nucleation theory for pure components and mixtures at pressure ranging from 0.9 bar to the critical pressure.

	AAD (K)
Methane	0.62
n-Pentane	0.28
Nitrogen	2.21
Ethane/Propane	4.5
Propane/n-Butane	1.2
n-Pentane/n-Hexane	1.6

Table 2
The standard deviation in the temperature with regard to EoS for the predicted spinodal. For the GERG2008, PC-SAFT, PR, and CSP EoS. Standard deviations are averaged for pressures ranging from 0.9 bar to the critical pressure.

	Liquid (K)	Vapor (K)
Methane	0.44	4.07
Ethane	1.13	6.62
Propane	1.60	7.15
n-Butane	2.19	7.99
n-Pentane	2.86	9.31
Nitrogen	0.30	2.61
Overall	1.42	6.29

observed for pure species (Fig. 7 right). The highest predictions for the vapor spinodal all come from the multiparameter GERG2008 equation, while the lowest come from the simple cubic Peng–Robinson EoS. This further illustrates the inconsistency of widely used EoS when used in the metastable domain. Table 3 shows the average (over mole fractions) standard deviation (with regard to EoS) of the predicted liquid and vapor spinodal temperatures for mixtures. Again, as for pure species, the spread in predicted spinodal temperatures is significant, especially for the vapor spinodal.

3.4. How close to the spinodals can experiments bring us?

We showed in Sec. 3.3 that the limit of superheat from experiments agreed very well with predictions from CNT, both for single-component liquids (Fig. 7) and mixtures (Fig. 8). This does not contradict that CNT is unable to reproduce experimental nucleation rates, since the limit of superheat is insensitive to the exact choice of the critical nucleation rate in Eq. (27). We can therefore use CNT to estimate the limits for how close to the spinodal it is possible to get experimentally before homogeneous nucleation occurs spontaneously. In Fig. 9, we have used methane as example and plotted the phase envelope that encloses the two-phase region (blue solid line), the limit of homogeneous nucleation as predicted by CNT (green dashed line) and the spinodals (red solid line). The spinodals, the coexistence line and the homogeneous nucleation limit all merge in the critical point.

In the following, we shall refer to the function $P = P(T, \rho)$ as the thermodynamic surface of methane. Fig. 9 shows that:

1 On a curve on the thermodynamic surface that goes from the spinodal to the coexistence limit, the distance between the spinodal and the nucleation limit relative to the corresponding distance to the coexistence limit is significant.
2 The relative distance on this curve is much larger for metastable vapor than for metastable liquid.

Point number 1 means that there is large part of the thermodynamic surface where the properties of the metastable fluid are currently experimentally unavailable, in particular for metastable vapor. In the literature, some suggestions have been put forward on how to enter the region of the thermodynamic surface that is currently experimentally unavailable.

A recent work [56] shows how small closed containers can be used to completely prevent nucleation, achieving infinitely long-lived metastable states, referred to as superstable. Experiments can be carried out in quartz inclusions, similar to Ref. [6], where speed of sound measurements in the inclusion give information about the slope of $P(\rho)$ at constant entropy, similar to Ref. [57]. Since such experiments are very challenging, the perhaps most available methodology to study the properties of highly metastable states is to use molecular dynamics simulations in the canonical ensemble. For many fluids like alkanes, carbon dioxide and nitrogen, force fields have been developed that reproduce the thermodynamic properties from experiments very accurately [58]. Molecular Dynamics simulations are then capable of generating pseudo-experimental data in the metastable regions, or to estimate the spinodals of the fluid. Eventually, hybrid data sets with both experimental data and data from computations can be exploited in the fitting of the next generation multiparameter EoS, following a procedure similar to Rutkai et al. [59]. This represents a largely unexplored research topic for the future.

Bullet point 2 agrees with the results in Figs. 7 and 8, and shows that CNT predicts the nucleation limit to be closer to the spinodal for liquids than for vapor.

4. Conclusion

In this work, we have presented a method that can be used to obtain the thermodynamic stability limit of a single-phase fluid, called the spinodal. We demonstrated that the method was robust in vicinity of the critical point, scalable to multicomponent mixtures and applicable to complex non-analytical EoS.

We next discussed the role of the spinodal, the metastable and the unstable regions of the phase diagram of the single-phase fluid in the development of modern equations of state (EoS). Since the spinodal provides a reference for an extrapolation into the metastable domain from the saturation curve, and since much is known about the thermodynamic properties of the fluid at the spinodal, information about the spinodal can be used to characterize the properties or to estimate the uncertainty of the properties of fluids in the metastable domain.

A future goal should be to develop EoS without inadmissible pseudo-stable states in the unstable domain. This is of importance, both for combining them with mass based density functional theory and to develop thermodynamically consistent mixing rules with a physical interpretation. We proposed and evaluated a set of inequality constraints that can be used for this purpose in the fitting of modern EoS for single-component fluids.

We showed that there were large inconsistencies in predicted spinodals from a wide range of EoS such as cubic EoS, extended corresponding state EoS, SAFT and multiparameter EoS. The overall standard deviation in the prediction of the spinodal temperatures were 1.4 K and 2.7 K for single- and multi-component liquid-spinodals and 6.3 K and 26.9 K for single- and multi-component vapor spinodals. However, the range between the smallest and the largest predictions were significantly larger. For example, for an even mixture of hydrocarbons, the vapor spinodal temperature ranged from 85.9–154.7 K for ethane/propane, 108.9–177.0 K for propane/n–butane and 154.4–227.3 K for n–pentane/n–hexane. In general, there was a much larger spread in the prediction of the vapor-spinodal than the liquid-spinodal.

We also discussed the relationship between the measurable limit of superheat or supersaturation and the theoretical concept of

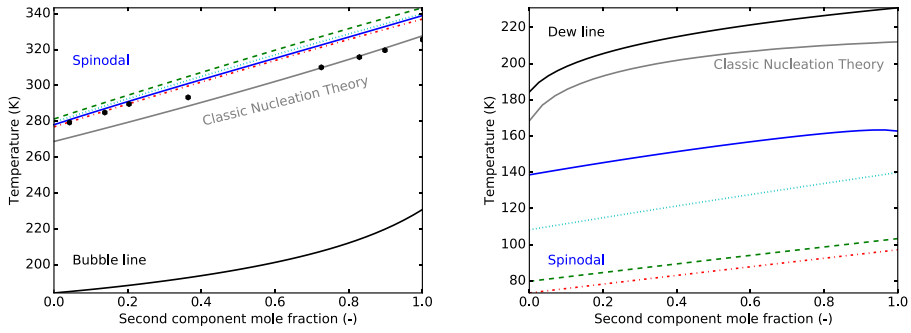

Liquid Vapor

(a) Ethane + Propane

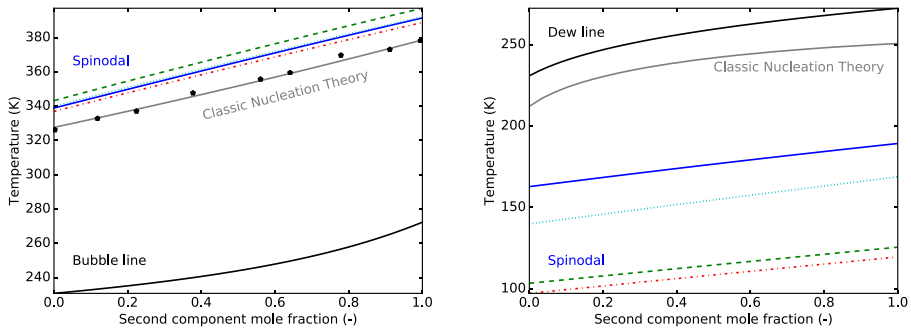

Liquid Vapor

(b) Propane + n-Butane

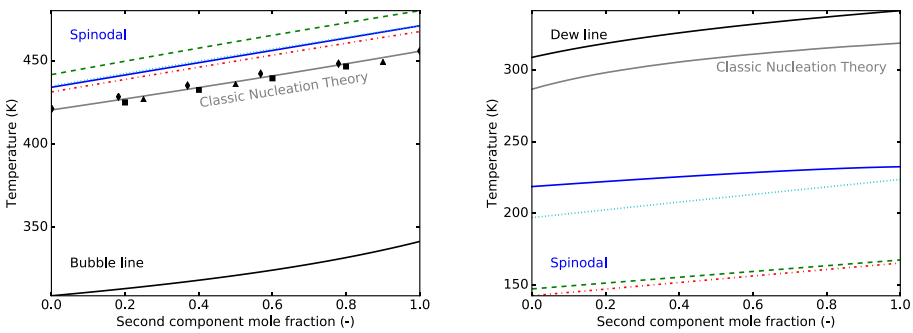

Liquid Vapor

(c) n-Pentane + n-Hexane

Fig. 8. Comparison of the spinodal curve (liquid and vapor), superheat and subcool limits predicted using CNT (solid gray), and bubble and dew lines (solid black) for some binary mixtures at 1 bar. The bubble and dew lines are computed using GERG2008. Spinodals are shown for four different EoS: GERG2008 (solid blue), PC-SAFT (dashed green), PR (dash-dot red) and extended CSP (dotted cyan). Experimental data from various studies of the limit of superheat are also shown: ethane + propane by Porteous and Blander [52] (hexagons), propane + n-butane by Renner et al. [53] (pentagons), n-pentane + n-hexane by Holden and Katz [54] (squares), Park et al. [24] (diamonds) and Skripov [55] (triangles). (For interpretation of the references to colour in this figure legend, the reader is referred to the web version of this article.)

Table 3
The standard deviation in the temperature for the predicted spinodal limit for binary mixtures at atmospheric pressure using the GERG2008, PC-SAFT, PR, and CSP EoS. Standard deviations are averaged over all mole fractions.

	Liquid (K)	Vapor (K)
Methane/Ethane	1.85	21.51
Methane/Propane	2.62	23.34
Ethane/Propane	2.05	27.22
Ethane/n-Butane	2.67	28.92
Propane/n-Butane	2.70	28.13
n-Pentane/n-Hexane	4.31	31.97
Overall	2.70	26.85

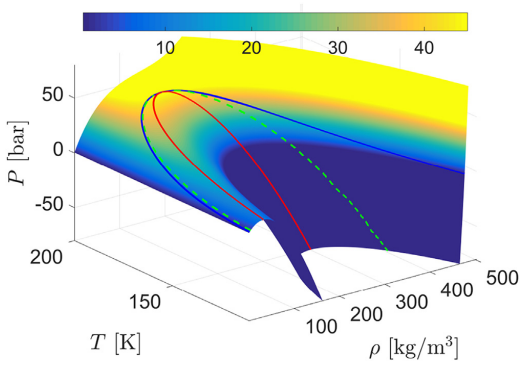

Fig. 9. A three-dimensional representation of the thermodynamic landscape of methane (relation between P, T and ρ) as predicted by the PR EoS. Here, the blue solid line encloses the two-phase region, the green dashed lines denote the states where Eq. (27) is satisfied and the homogeneous nucleation rate as predicted by CNT is so fast that the single-phase fluid appearers to decompose spontaneously into two phases. The red solid lines denote the spinodal, and enclose a region in which the single-phase fluid is unstable. (For interpretation of the references to colour in this figure legend, the reader is referred to the web version of this article.)

the spinodal. While nucleation rates from CNT can deviate orders of magnitude from experiments, we found that the limit of superheat experiments agreed within 1.0 K and 2.4 K with predictions from CNT for single- and multi-component fluids respectively.

At present, a large part of the metastable domain of the phase diagram is experimentally unavailable, in particular for metastable vapor. Novel techniques, with experimental or computational methods, should be developed to characterize the thermodynamic properties in these regions, and to identify the thermodynamic states that define the spinodal.

Acknowledgment

The authors acknowledge the support from the Research Council of Norway (project number 244076). The authors thank “The Gas Technology Centre NTNU-SINTEF” for the support.

References

[1] P.G. Debenedetti, Metastable Liquids: Concepts and Principles, Princeton University Press, Princeton, 1996.
[2] F. Caupin, E. Herbert, Cavitation in water: a review, Comptes Rendus Phys. 7 (9) (2006) 1000–1017, http://dx.doi.org/10.1016/j.crhy.2006.10.015.
[3] K. Davitt, A. Arvengas, F. Caupin, Water at the cavitation limit: density of the metastable liquid and size of the critical bubble, Europhys. Lett. 90 (2010) 16002, http://dx.doi.org/10.1209/0295-5075/90/16002.
[4] F. Caupin, A. Arvengas, K. Davitt, M. El Mekki Azouzi, K.I. Shmulovich, C. Ramboz, D.A. Sessoms, A.D. Stroock, Exploring water and other liquids at negative pressure, J. Phys. Condens. Matter 24 (28) (2012) 284110, http://dx.doi.org/10.1088/0953-8984/24/28/284110.
[5] Q. Zheng, D.J. Durben, G.H. Wolf, C.A. Angell, Liquids at large negative pressures: water at the homogeneous nucleation limit, Science 254 (5033) (1991) 829–832, http://dx.doi.org/10.1126/science.254.5033.829.
[6] M. El Mekki Azouzi, C. Ramboz, J.F. Lenain, F. Caupin, A coherent picture of water at extreme negative pressure, Nat. Phyics 9 (2013) 38–41, http://dx.doi.org/10.1038/nphys2475.
[7] A. C. Hack, A. B. Thompson, Density and viscosity of hydrous magmas and related fluids and their role in subduction zone processes, J. Petrology 52 (1333–1362). doi:10.1093/petrology/egq048.
[8] C. Avedisian, The homogeneous nucleation limits of liquids, J. Phys. Chem. Reference Data 14 (3) (1985) 695–729, http://dx.doi.org/10.1063/1.555734.
[9] J. Salla, M. Demichela, J. Casal, BLEVE: a new approach to the superheat limit temperature, J. Loss Prev. Process Industries 19 (6) (2006) 690–700, http://dx.doi.org/10.1016/j.jlp.2006.04.004.
[10] R. Bubbico, E. Salzano, Acoustic analysis of blast waves produced by rapid phase transition of LNG released on water, Saf. Sci. 47 (4) (2009) 515–521, http://dx.doi.org/10.1016/j.ssci.2008.07.033.
[11] R.K. Eckhoff, Boiling liquid expanding vapour explosions (BLEVEs): a brief review, J. Loss Prev. Process Industries 32 (2014) 30–43, http://dx.doi.org/10.1016/j.jlp.2014.06.008.
[12] H. Vehkamäki, Classical Nucleation Theory in Multicomponent Systems, Springer Verlag, Berlin, 2006.
[13] A. Obeidat, J.S. Li, G. Wilemski, Nucleation rates of water and heavy water using equations of state, J. Chem. Phys. 121 (19) (2004) 9510–9516, http://dx.doi.org/10.1063/1.1806400.
[14] A. Obeidat, G. Wilemski, Gradient theory of nucleation in polar fluids, Atmos. Res. 82 (2006) 481–488, http://dx.doi.org/10.1016/j.atmosres.2006.02.005.
[15] W. Wagner, A. Pruß, The IAPWS formulation 1995 for the thermodynamic properties of ordinary water substance for general and scientific use, J. Phys. Chem. Reference Data 31 (2002) 387–535, http://dx.doi.org/10.1063/1.1461829.
[16] Ø. Wilhelmsen, A. Aasen, G. Skaugen, P. Aursand, A. Austegard, E. Aursand, M.Aa. Gjennestad, H. Lund, G. Linga, M. Hammer, Thermodynamic Modeling with Equations of State: present Challenges for Established Models, Under Revision.
[17] H. Wakeshima, K. Takata, On the limit of superheat, J. Phys. Soc. Jpn. 13 (11) (1958) 1398–1403, http://dx.doi.org/10.1143/JPSJ.13.1398.
[18] G.R. Moore, Vaporization of superheated drops in liquids, AIChE J. 5 (4) (1959) 458–466, http://dx.doi.org/10.1002/aic.690050412.
[19] J.H. Lienhard, A. Karimi, Homogeneous nucleation and the spinodal line, J. Heat Transf. 103 (1981) 61–64, http://dx.doi.org/10.1115/1.3244431.
[20] J.H. Lienhard, N. Shamsundar, P.O. Biney, Spinodal lines and equations of state: a review, Nucl. Eng. Des. 95 (1986) 297–314, http://dx.doi.org/10.1016/0029-5493(86)90056-7.
[21] N. Shamsundar, J.H. Lienhard, Equations of state and spinodal lines – a review, Nucl. Eng. Des. 141 (1) (1993) 269–287, http://dx.doi.org/10.1016/0029-5493(93)90106-J.
[22] P.O. Biney, W.-G. Dong, J.H. Lienhard, Use of a cubic equation to predict surface tension and spinodal limits, J. Heat Transf. 108 (2) (1986) 405–410, http://dx.doi.org/10.1115/1.3246938.
[23] C. Liu, D. Zeng, K. Xing, Superheat limit of liquid mixtures, Proc. Symposium Energy Eng. 21st Century 1 (2000) 373–378.
[24] H.-C. Park, K.-T. Byun, H.-Y. Kwak, Explosive boiling of liquid droplets at their superheat limits, Chem. Eng. Sci. 60 (7) (2005) 1809–1821, http://dx.doi.org/10.1016/j.ces.2004.11.010.
[25] G. Soave, Equilibrium constants from a modified Redlich–Kwong equation of state, Chem. Eng. Sci. 27 (6) (1972) 1197–1203, http://dx.doi.org/10.1016/0009-2509(72)80096-4.
[26] D.-Y. Peng, D.B. Robinson, A new two-constant equation of state, Industrial Eng. Chem. Fundam. 15 (1) (1976) 59–64, http://dx.doi.org/10.1021/i160057a011.
[27] J. F. Ely, I. M. F. Marrucho, Equations of State for Fluid Mixtures, IUPAC, 2000, Ch. The Corresponding-states Principle, pp. 289–320.
[28] Ø. Wilhelmsen, G. Skaugen, O. Jørstad, H. Li, Evaluation of SPUNG and other equations of state for use in carbon capture and storage modelling, Energy Procedia 23 (2012) 236–245, http://dx.doi.org/10.1016/j.egypro.2012.06.024.
[29] M.L. Michelsen, J.M. Mollerup, Thermodynamic Models: Fundamentals and Computational Aspects, second ed., Tie-Line Publictions, Holte, Denmark, 2007.
[30] W.G. Chapman, K.E. Gubbins, G. Jackson, M. Radosz, SAFT: equation-of-state solution model for associating fluids, Fluid Phase Equilibria 52 (1989) 31–38, http://dx.doi.org/10.1016/0378-3812(89)80308-5.
[31] J. Gross, G. Sadowski, Perturbed-chain SAFT: an equation of state based on a perturbation theory for chain molecules, Industrial Eng. Chem. Res. 40 (4) (2001) 1244–1260, http://dx.doi.org/10.1021/ie0003887.
[32] U. Setzmann, W. Wagner, A new equation of state and tables of thermodynamic properties for methane covering the range from the melting line to 625 K at pressures up to 100 MPa, J. Phys. Chem. Reference Data 20 (6) (1991) 1061–1155, http://dx.doi.org/10.1063/1.555898.
[33] R. Span, W. Wagner, A new equation of state for carbon dioxide covering the fluid region from the triple-point temperature to 1100 K at pressures up to 800 MPa, J. Phys. Chem. Reference Data 25 (6) (1996) 1509–1596, http://

dx.doi.org/10.1063/1.555991.
[34] R. Span, E.W. Lemmon, R.T. Jacobsen, W. Wagner, A reference quality equation of state for nitrogen, Int. J. Thermophys. 19 (4) (1998) 1121–1132, http://dx.doi.org/10.1023/A:1022689625833.
[35] C. Tegeler, R. Span, W. Wagner, A new equation of state for argon covering the fluid region for temperatures from the melting line to 700 K at pressures up to 1000 MPa, J. Phys. Chem. Reference Data 28 (3) (1999) 779–850, http://dx.doi.org/10.1063/1.556037.
[36] J. Smukala, R. Span, W. Wagner, New equation of state for ethylene covering the fluid region for temperatures from the melting line to 450 K at pressures up to 300 MPa, J. Phys. Chem. Reference Data 29 (5) (2000) 1053–1121, http://dx.doi.org/10.1063/1.1329318.
[37] O. Kunz, W. Wagner, The GERG-2008 wide-range equation of state for natural gases and other mixtures: an expansion of GERG-2004, J. Chem. Eng. Data 57 (11) (2012) 3032–3091, http://dx.doi.org/10.1021/je300655b.
[38] H.B. Callen, Thermodynamics and an Introduction to Thermostatistics, second ed., Wiley, New York, 1985.
[39] J.W. Tester, M. Modell, Thermodynamics and its Applications, Prentice Hall PTR, New Jersey, 1996.
[40] B.L. Beegle, M. Modell, R.C. Reid, Thermodynamic stability criterion for pure substances and mixtures, AIChe J. 20 (1974) 1200–1206, http://dx.doi.org/10.1002/aic.690200621.
[41] E.H. Chimowitz, Introduction to Critical Phenomena in Fluids, Oxford University Press, New York, 2005.
[42] R.A. Heidemann, A.M. Khalil, The calculation of critical points, AIChE J. 26 (5) (1980) 769–779, http://dx.doi.org/10.1002/aic.690260510.
[43] M.L. Michelsen, Calculation of critical points and phase boundaries in the critical region, Fluid Phase Equilibria 16 (1) (1984) 57–76, http://dx.doi.org/10.1016/0378-3812(84)85021-9.
[44] Ø. Wilhelmsen, D. Reguera, Evaluation of finite-size effects in cavitation and droplet formation, J. Chem. Phys. 142 (2015) 064703, http://dx.doi.org/10.1063/1.4907367.
[45] R.C. Reid, J.M. Prausnitz, B.E. Poling, The Properties of Gases and Liquids, McGraw Hill Book Co., New York, NY, 1987.
[46] E.W. Lemmon, R.T. Jacobsen, A new functional form and new fitting techniques for equations of state with application to pentafluoroethane (HFC-125), J. Phys. Chem. Reference Data 34 (2005) 69–108, http://dx.doi.org/10.1063/1.1797813.
[47] E.W. Lemmon, M.O. McLinden, W. Wagner, Thermodynamic properties of propane. III. a reference equation of state for temperatures from the melting line to 650 K and pressures up to 1000 MPa, J. Phys. Chem. Reference Data 54 (2009) 3141–3180, http://dx.doi.org/10.1021/je900217v.
[48] A.E. Elhassan, R.J.B. Craven, K.M. de Reuck, The area method for pure fluids and an analysis of the two-phase region, Fluid Phase Equilibria 130 (1997) 167–187, http://dx.doi.org/10.1016/S0378-3812(96)03222-0.
[49] J. Gernert, A. Jäger, S. R, Calculation of phase equilibria for multi-component mixtures using highly accurate helmholtz energy equation of state, Fluid Phase Equilibria 375 (2014) 209–218, http://dx.doi.org/10.1016/j.fluid.2014.05.012.
[50] Software for the Reference Equation of State GERG-2008 for Natural Gases and Other Mixtures, 2016, http://www.thermo.rub.de/en/prof-w-wagner/software/gerg-2004-gerg-2008.html.
[51] V.G. Baidakov, V.P. Skripov, Superheating and surface tension of vapor nuclei in nitrogen, oxygen, and methane, Russ. J. Phys. Chem. 56 (1982) 499–501.
[52] W. Porteous, M. Blander, Limits of superheat and explosive boiling of light hydrocarbons, halocarbons, and hydrocarbon mixtures, AIChE J. 21 (3) (1975) 560–566, http://dx.doi.org/10.1002/aic.690210319.
[53] T.A. Renner, G.H. Kucera, M. Blander, Explosive boiling in light hydrocarbons and their mixtures, J. Colloid Interface Sci. 52 (2) (1975) 391–396, http://dx.doi.org/10.1016/0021-9797(75)90215-5.
[54] B.S. Holden, J.L. Katz, The homogeneous nucleation of bubbles in superheated binary liquid mixtures, AIChE J. 24 (2) (1978) 260–267, http://dx.doi.org/10.1002/aic.690240215.
[55] V.P. Skripov, Metastable Liquids, John Wiley & Sons, 1974.
[56] Ø. Wilhelmsen, D. Bedeaux, S. Kjelstrup, D. Reguera, Communication: superstabilization of fluids in nanocontainer, J. Chem. Phys. 141 (2014) 071103, http://dx.doi.org/10.1063/1.4893701.
[57] A.D. Alvarenga, M. Grimsditch, R.J. Bodnar, Elastic properties of water under negative pressures, J. Chem. Phys. 98 (1993) 8392–8396, http://dx.doi.org/10.1063/1.464497.
[58] J.J. Potoff, J. Ilja Siepmann, Vapor-liquid equilibria of mixtures containing alkanes, carbon dioxide, and nitrogen, AIChE J. 47 (2001) 1676–1682, http://dx.doi.org/10.1002/aic.690470719.
[59] G. Rutkai, M. Thol, R. Lustig, R. Span, J. Vrabec, Communication: fundamental equation of state correlation with hybrid data sets, J. Chem. Phys. 139 (2013) 041102, http://dx.doi.org/10.1063/1.4817203.